International Journal of Engineering (IJE)

ISSN : 1985-2312

VOLUME 4, ISSUE 5

PUBLICATION FREQUENCY: 6 ISSUES PER YEAR

International Journal of Engineering (IJE)

Volume 4, Issue 5, 2010

Edited By

Computer Science Journals

www.cscjournals.org

Editor in Chief Dr. Kouroush Jenab

International Journal of Engineering (IJE)

Book: 2010 Volume 4, Issue 5

Publishing Date: 20-12-2010

Proceedings

ISSN (Online): 1985-2312

IJE Journal is a part of CSC Publishers

http://www.cscjournals.org

Published in Malaysia

Typesetting: Camera-ready by author, data conversation by CSC Publishing Services – CSC Journals, Malaysia

CSC Publishers

Editorial Preface

This is the fifth issue of volume four of International Journal of Engineering (IJE). The Journal is published bi-monthly, with papers being peer reviewed to high international standards. The International Journal of Engineering is not limited to a specific aspect of engineering but it is devoted to the publication of high quality papers on all division of engineering in general. IJE intends to disseminate knowledge in the various disciplines of the engineering field from theoretical, practical and analytical research to physical implications and theoretical or quantitative discussion intended for academic and industrial progress. In order to position IJE as one of the good journal on engineering sciences, a group of highly valuable scholars are serving on the editorial board. The International Editorial Board ensures that significant developments in engineering from around the world are reflected in the Journal. Some important topics covers by journal are nuclear engineering, mechanical engineering, computer engineering, electrical engineering, civil & structural engineering etc.

The coverage of the journal includes all new theoretical and experimental findings in the fields of engineering which enhance the knowledge of scientist, industrials, researchers and all those persons who are coupled with engineering field. IJE objective is to publish articles that are not only technically proficient but also contains information and ideas of fresh interest for International readership. IJE aims to handle submissions courteously and promptly. IJE objectives are to promote and extend the use of all methods in the principal disciplines of Engineering.

IJE editors understand that how much it is important for authors and researchers to have their work published with a minimum delay after submission of their papers. They also strongly believe that the direct communication between the editors and authors are important for the welfare, quality and wellbeing of the Journal and its readers. Therefore, all activities from paper submission to paper publication are controlled through electronic systems that include electronic submission, editorial panel and review system that ensures rapid decision with least delays in the publication processes.

To build its international reputation, we are disseminating the publication information through Google Books, Google Scholar, Directory of Open Access Journals (DOAJ), Open J Gate, ScientificCommons, Docstoc and many more. Our International Editors are working on establishing ISI listing and a good impact factor for IJE. We would like to remind you that the success of our journal depends directly on the number of quality articles submitted for review. Accordingly, we would like to request your participation by submitting quality manuscripts for review and encouraging your colleagues to submit quality manuscripts for review. One of the great benefits we can provide to our prospective authors is the mentoring nature of our review

process. IJE provides authors with high quality, helpful reviews that are shaped to assist authors in improving their manuscripts.

Editorial Board Members
International Journal of Engineering (IJE)

Editorial Board

Table of Content

Volume 4, Issue 5, December 2010

Pages

Experimental Investigation and Numerical Modeling of the Effect of Natural and Steel Fibers on the Performance of Concrete

Hossam Hodhod hossamhodhod@hotmail.com
Faculty of Engineering/Dept. of structural Engineering Cairo University
Giza, 12211, Egypt

Mostafa A. M. Abdeen mostafa_a_m_abdeen@hotmail.com
Faculty of Engineering/Dept. of Engineering Mathematics and Physics
Cairo University Giza, 12211, Egypt

Abstract

The application of fibers to concrete industry is growing due to the demanding needs of concrete with better structural performance. Environmental considerations urge this application since many of the fiber types (especially natural ones) results as by products from different industrial and agricultural processes. In this study, the application of metallic steel fibers and natural (Linen) fibers in concrete industry is investigated. Twenty one mixes are made with different mix proportions and with different types of fibers. The mixes were designed first to give strengths in the range from 150 to 450 Kg/cm2, without fiber inclusion. The two types of fibers are added to each of the basic control mixes. Standard specimens in forms of cubes and cylinders were cast from each mix. The specimens were tested in compression, tension and impact. Measurements were also made using two NDT techniques. The specimens were tested at ages of 7 and 28 days and after exposure to elevated temperatures of 400 and 450°C . The results were compared and showed the enhancement level obtained by including steel and natural fibers. Following this experimental effort, the Artificial Neural Network (ANN) technique was applied for predicting the performance of concrete with different mix proportions. The current paper introduced the (ANN) technique to investigate the effect of natural and steel fibers on the performance of concrete. The results of this study showed that the ANN method with less effort was very efficiently capable of simulating and predicting the performance of concrete with different mix proportions and different types of fibers.

Keywords: Concrete, Fibers, Ultrasonic Pulse Velocity, Modeling, Artificial Neural Network.

1. INTRODUCTION

The engineering ambition represents the main motivation for producing new materials that comply with the demands of engineers and structures. Concrete is the main structural material of the majority of structures in the world. Therefore, the enhancement of its properties represents the shortest way to get new superior construction material. Also, fibers represent the best method for enhancing concrete properties since it has the advantage of increasing tensile strength and

ductility which are the main disadvantages of concrete. Fibers have mainly two types: metallic and non-metallic. Steel is the main source for the first type; whereas natural fibers (vegetal type) represent a main and cheap source of the second type, Parret and Ramachandran, [15] and [16]. A continuous research oriented towards the evaluation of material (pure and composite) properties is the direct way to identify the efficiency of local resources of material. This appears in the continuous published work concerning the potential of applying many types of natural fibers, Gorillo and Silva, [10] and [18].

In this paper, the effect of applying local natural fibers (linen) to concrete is investigated experimentally. A comparison is made with two extremes of plain concrete and steel fiber reinforced concretes. The investigation is made at 7 different concrete mixes and comprehensive evaluation is made. Evaluation includes the compressive and tensile strengths, impact strength, stiffness, readings of non-destructive techniques, and effect of elevated temperatures.

Since the experimental work needs a lot of effort, time and money, the need for utilizing new methodologies and techniques to reduce this effort, save time and money (and at the same time preserving high accuracy) is urged.

Artificial intelligence has proven its capability in simulating and predicting the behavior of the different physical phenomena in most of the engineering fields. Artificial Neural Network (ANN) is one of the artificial intelligence techniques that have been incorporated in various scientific disciplines. Minns [14] investigated the general application of ANN in modeling rainfall runoff process. Kheireldin [11] presented a study to model the hydraulic characteristics of severe contractions in open channels using ANN technique. The successful results of his study showed the applicability of using the ANN approach in determining relationship between different parameters with multiple input/output problems. Abdeen [1] developed neural network model for predicting flow characteristics in irregular open channels. The developed model proved that ANN technique was capable with small computational effort and high accuracy of predicting flow depths and average flow velocities along the channel reach when the geometrical properties of the channel cross sections were measured or vice versa. Tahk and Shin [19] presented a study on the fault diagnosis of Roller-Shape using frequency analysis of tension signals and Artificial Neural Network (ANN) based approach in a web transport system. ALLAM [7] used the artificial intelligence technique to predict the effect of tunnel construction on nearby buildings which is the main factor in choosing the tunnel route. Park and Azmathullah et. al. [9] presented a study for estimating the scour characteristics downstream of a ski-jump bucket using Neural Networks (NN). Abdeen [2] presented a study for the development of ANN models to simulate flow behavior in open channel infested by submerged aquatic weeds. Mohamed [13] proposed an artificial neural network for the selection of optimal lateral load-resisting system for multi-story steel frames.

It is quite clear from the previously presented literature that ANN technique showed its applicability in simulating and predicting the behavior of different engineering problems. However, the utilization of ANN technique in simulating and predicting the effect of fibers on concrete properties is very limited. Therefore, one of the aims of the presented study is utilizing the ANN technique in modeling the behavior of concrete after applying fibers.

2. PROBLEM DESCRIPTION

To study the effect of fibers (linen and steel) as well as elevated temperature on the performance of concrete (compressive, tensile, impact, stiffness, rebound number, ultrasonic pulse velocity), experimental and numerical techniques will be presented in this study. The experimental program and its results will be described in detail in the following sections. The numerical models presented in this study utilized Artificial Neural Network technique (ANN) using the data of the experiments and then can predict the performance of concrete for different mix proportions.

3. EXPERIMENTAL PROGRAM

In order to evaluate the effect of adding linen fibers to concrete, it was decided to test three sets of specimens: one including linen fibers and one without any fibers and the third with steel fibers. Concrete strength was considered as a parameter. Therefore, for each set, the strength was changed in the range of 150 to 450 kg/cm^2. Fiber content was kept constant at .0.5 % volume fraction. This value was selected based on preliminary tests to check that concrete can have a workable consistency.

Compressive, splitting tensile, impact strengths, and modulus of elasticity were selected to be the criteria for evaluating effect of adding fibers to concrete mixes. Measurements of rebound hammer and PUNDIT ultrasonic testers were also planned. These two techniques were selected as being the most easy-to-apply ones, Malhorta, ACI 228, ACI 437 and ACI 544 [12], [3], [4] and [5].

The experimental program also includes the evaluation of concrete performance after exposure to elevated temperature for one hour.

4. MATERIALS AND SPECIMENS

Concrete materials were: locally produced CEM I 32.5R conforming to ES 4756-2007, tap water, sand with fineness modulus of 3.0, and gravel with maximum nominal size of 25 mm. Steel fibers with 5400 kg/cm2 tensile strength, 0.8 mm diameter and aspect ratio of 50 were used. Linen fibers were locally produced fibers and applied in decorative elements of buildings. Their properties vary in a wide range. However, they have a mean diameter of about 0.5 mm and length of 40 mm. Linen fibers are usually delivered in spools. Fibers were cut manually to the required length.

In order to get the mix proportions for concretes with different compressive strength, the database of the British method were used. In order to eliminate the effect of compaction on results, water content was kept constant at 200 litre/m^3. The strength was varied by changing the water/ cement ratio (w/c) via changing cement content. Seven mix proportions were calculated to get concrete mixes with strengths from 150 to 450 kg/cm^2 in an increment of 50 kg/cm^2. The fibers were added to each of these mixes (0.5 % by volume) to get the two other sets of concrete mixes. Table (1) shows mix proportions of different concretes.

Constituents were mixed mechanically in a tilting type mixer with 140 liter capacity. Dry materials were mixed first for about 1 minute and then water was added gradually and mixing continued till a homogeneous mix was obtained. When fibers were used, they were spread uniformly by hand during mixing other materials, as per recommendation of ACI 544 [5]. Steel molds were used to cast set of (15*30 cm) cylinders and cubes (15 cm). Specimens were covered by plastic sheets for 24 hours. Then, specimens were demolded and immersed in water till day of testing.

5. TEST RESULTS

Unless noted otherwise, each of the data points shown below represents the average of test results of testing two concrete specimens.

5.1 Compressive Strength

Compression test was made on cube specimens at ages of 7 and 28 days. Figs. (1,2) show the compressive strength values plotted versus w/c ratio at both 7 and 28 days. One can see that the addition of fibers increases compressive strength insignificantly.

Mix No	Content – kg/m^3					
	Water	Cement	Sand	Gravel	Steel Fibers	Linen Fibers
1	200	322.5	581.3	1162.6	0	0
2	200	344.8	575.4	1150.8	0	0
3	200	377.3	566.8	1133.7	0	0
4	200	416.6	556.4	1112.9	0	0
5	200	454.5	546.4	1092.8	0	0
6	200	487.8	537.6	1075.2	0	0
7	200	526.3	527.4	1054.8	0	0
8	200	322.5	581.3	1162.6	0	0.4
9	200	344.8	575.4	1150.8	0	0.4
10	200	377.3	566.8	1133.7	0	0.4
11	200	416.6	556.4	1112.9	0	0.4
12	200	454.5	546.4	1092.8	0	0.4
13	200	487.8	537.6	1075.2	0	0.4
14	200	526.3	527.4	1054.8	0	0.4
15	200	322.5	581.3	1162.6	3.9	0
16	200	344.8	575.4	1150.8	3.9	0
17	200	377.3	566.8	1133.7	3.9	0
18	200	416.6	556.4	1112.9	3.9	0
19	200	454.5	546.4	1092.8	3.9	0
20	200	487.8	537.6	1075.2	3.9	0
21	200	526.3	527.4	1054.8	3.9	0

TABLE 1: Mix Proportions (by weight) for one cubic meter of Concrete

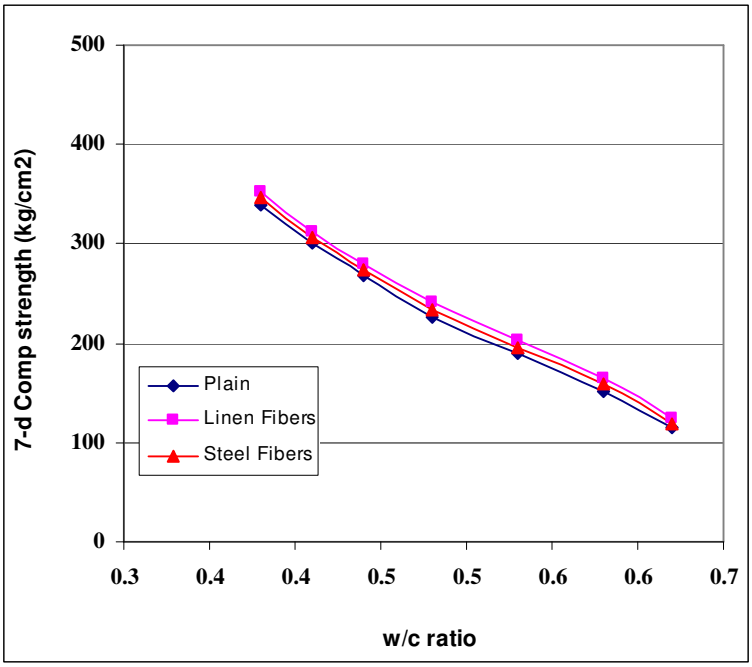

FIGURE 1: 7-day Compressive Strength

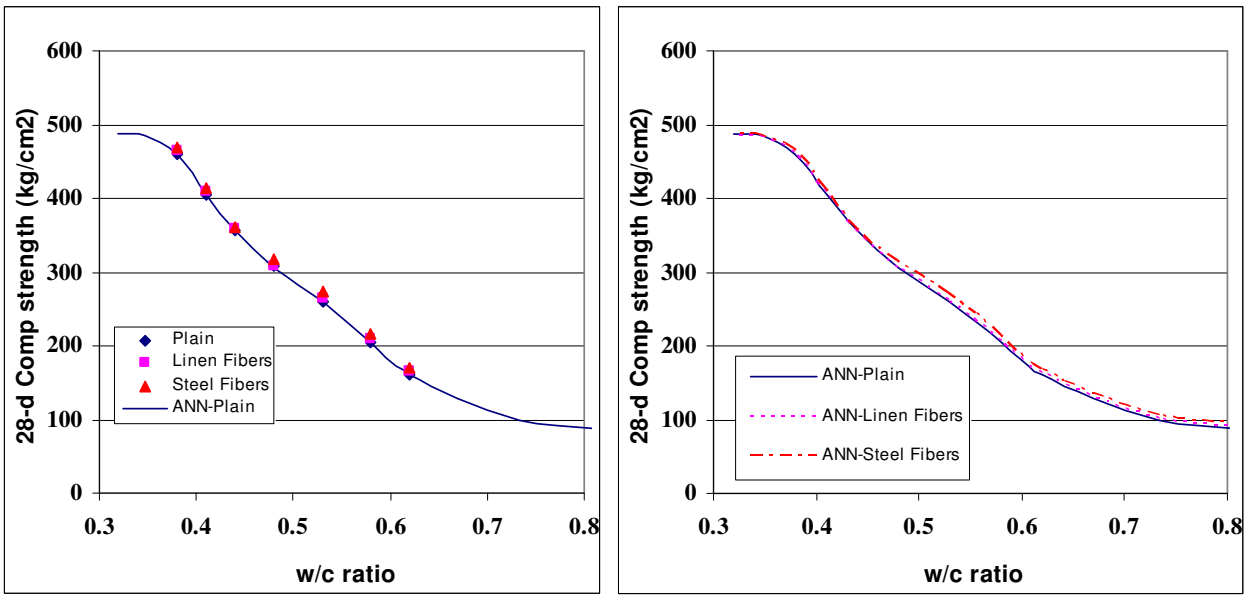

FIGURE 2: 28-day Compressive Strength

5.2 Tensile Strength

Indirect (splitting) tension test was made on cylindrical specimens at 28 days. Fig. (3) shows the Compressive strength values plotted versus the corresponding splitting tensile strengths. One can see that the addition of fibers increases tensile strength significantly. This is expected since fibers improve tensile behavior of brittle materials via crack arrest and crack bridging, Ramachandran [16]. Role of fiber tensile strength appears when observing that linen fibers improves tensile strength by about 11 %, in average, while steel fibers increases tensile strength by about 29 % in average.

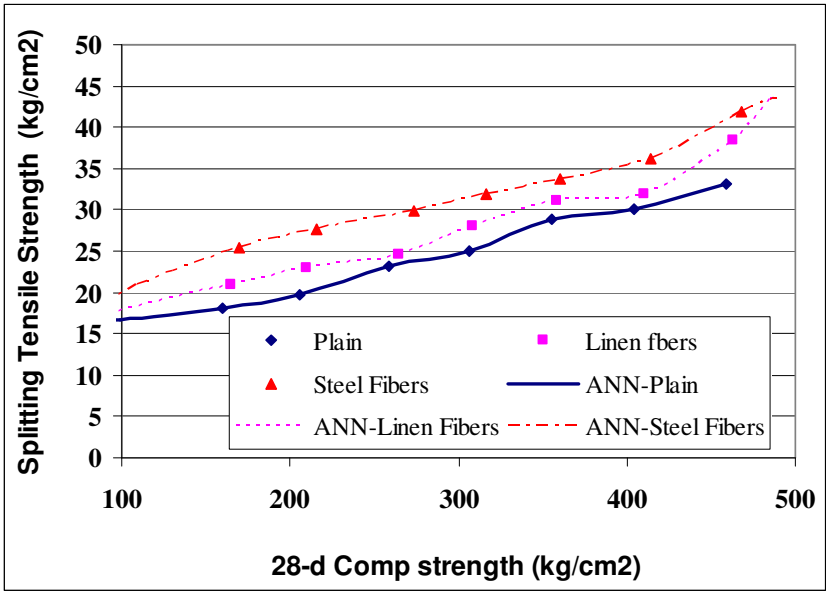

FIGURE 3: 28-day Tensile Strength

5.3 Impact Strength

Impact test was made on concrete discs (15*10 cm) cut from the standard concrete cylinders (15*30 cm). Test was made according to test method described in ACI 544 [6]. Figure (4) shows number of blows (drops of standard hammer) till the appearance of first crack. Fibers increase impact strength mainly via the fiber pull-out mechanism, Parret and Ramachandran, [15] and [16]. One can see that the improvement of impact strength due to linen fibers (34% in average) is almost half of that made by steel fibers (68% in average). There is no trend on variation of this value with concrete compressive strength.

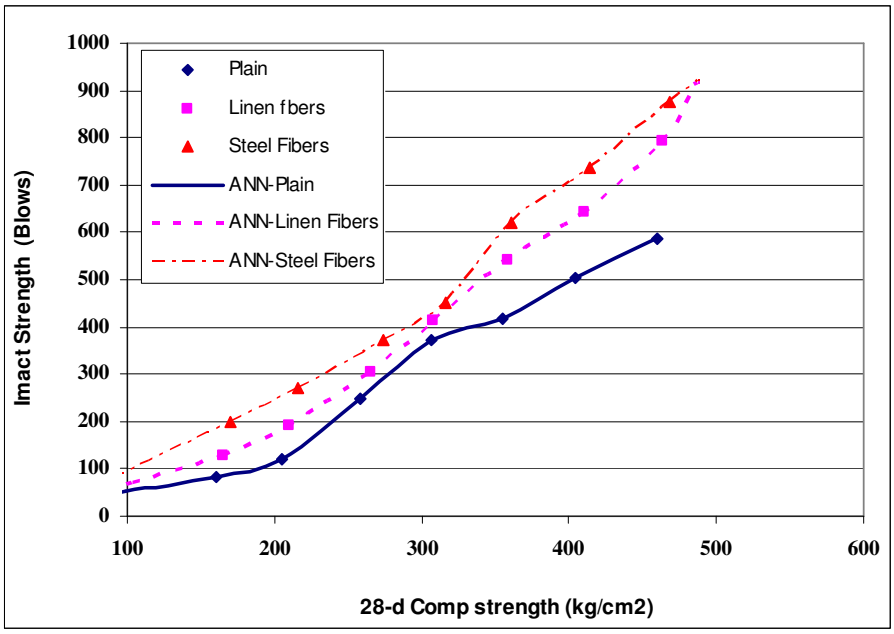

FIGURE 4: 28-day Impact Strength

5.4 Stiffness (Modulus of Elasticity)

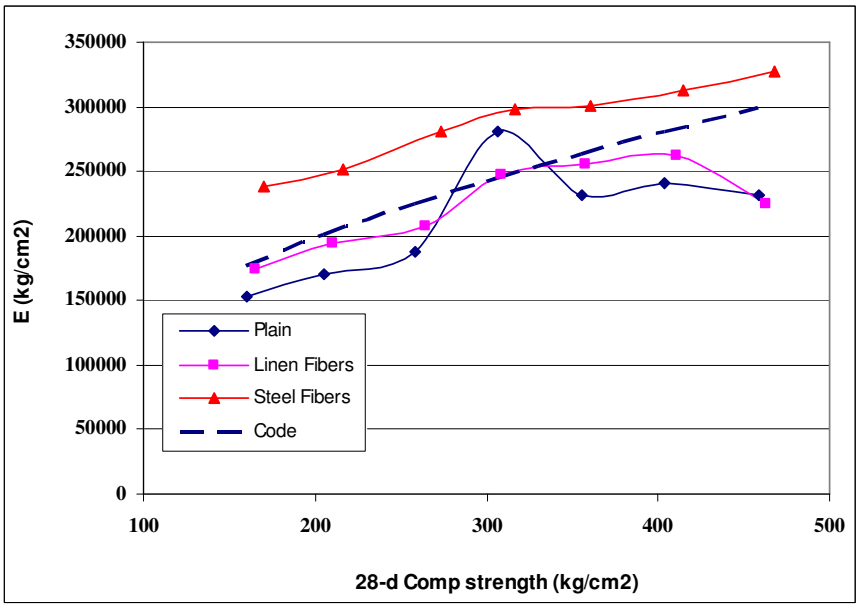

FIGURE 5: Modulus of Elasticity of Different Concretes

The stiffness of concrete was measured applying the method described by ASTM C0469-02E01 [8]. A compressometer with mechanical dial gage (accuracy of 0.001 mm) was used to measure deformations of the tested cylinders. Measurements were made on one specimen for each mix. Results are shown in Fig (5). Direct proportion can be seen in the figure. The dashed line shows the relationship given by Egyptian code of practice ECP 203/2007 $E = 14000 (f_{cu})^{0.5}$. One can see that addition of fibers increases stiffness, since it reduces strains. Also, code equation represents an upper bound of stiffness for plain and linen fiber reinforced concrete. However, code equation represents a lower bound for steel fiber reinforced concrete.

5.5 Rebound Hammer Reading

The rebound hammer is one of the most common tools used for evaluating uniformity of concrete, and sometimes its strength. The hammer readings were taken on concrete cubes while supported in compression testing machines under 5 ton load. Angle of hammer axis was zero. Ten readings were taken on each cube (5 for each of the accessible faces). Average value of rebound number (Rn) is plotted vs. actual compressive strength measured from loading cube till failure, in Fig (6). One can see that hardness of concrete increases with inclusion of fibers. This effect is more pronounced for steel fibers, and at later ages. This is an expected effect due to the stiffening effect of fibers that is increased with stiffness of material of fiber. The range of variation of strength, at the same rebound number, reaches 25% with steel fiber reinforced concrete in the lower bound. This range, however, is identical to that known for rebound hammer readings on surfaces made from same concrete mix, Malhotra, [12].

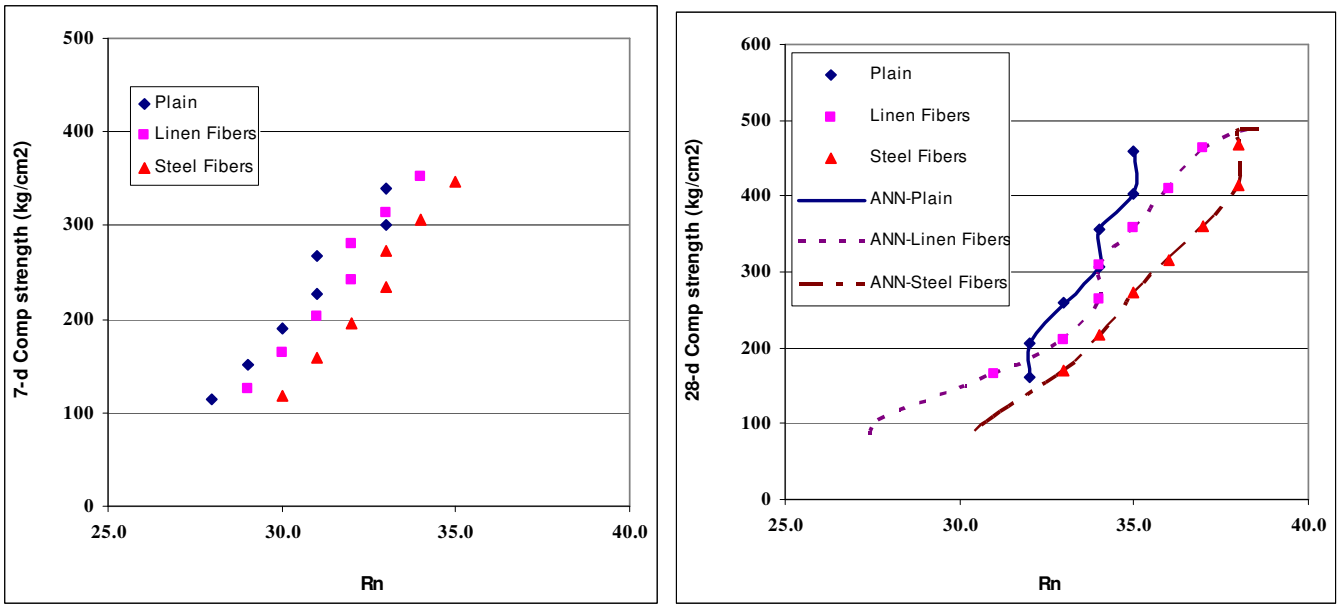

FIGURE 6: 7-d and 28-d Compressive Strength vs. Rebound Number

5.6 Ultrasonic Pulse Velocity

Another common technique applied for evaluating uniformity of concrete, and sometimes its strength. Ultrasonic pulse velocity was measured on concrete cubes using PUNDIT tester in a direct transmission. Measurements were made in two directions (using four faces of concrete cube). Average velocity (v) is plotted vs. concrete compressive strength measured from lading tested cube till failure. Data are shown in Fig (7). One can see that data is more scattered at 7-days where concrete is less mature and the effect of fibers is more pronounced.

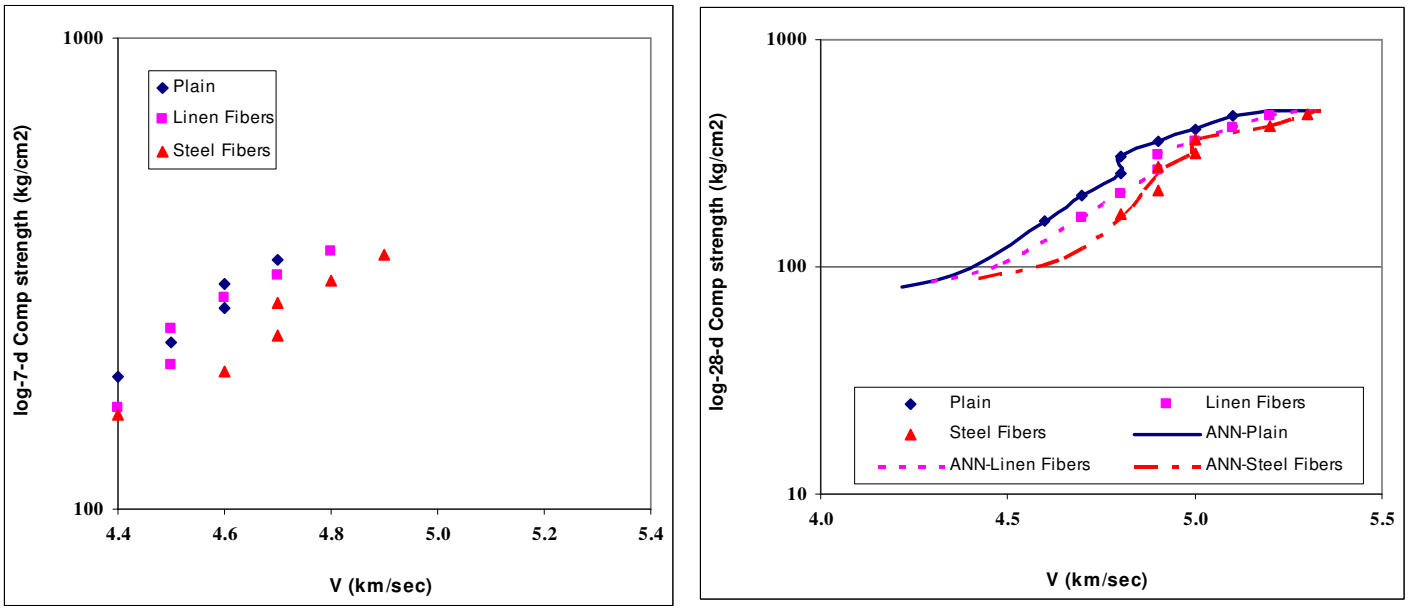

FIGURE 7: 7-d and 28-d Compressive Strength vs. Ultrasonic pulse Velocity

5.7 Effect of Elevated Temperature

The fire redundancy is one of the main requirements in structures after increasing safety precautions. In order to investigate effect of elevated temperature on mixes, concrete cubes were subjected to elevated temperature at two levels (400 and 450°C), in an electric oven, for one hour. Cubes were taken out of the furnace and cooled in ambient air. Then, measurements of rebound and ultrasonic pulse velocity were made. Later, cubes were loaded in compression till failure and residual compressive strength was measured. Results are plotted in Figs.(8-10). It shall be mentioned that tests were made at ages later than 28 days, and earlier than 56 days. One can see that the effect of elevated temperature on strength is more pronounced at 450°C. Also, inclusion of fibers improves significantly heat resistance of concrete. Steel and linen fibers have almost equal effect in the improvement of concrete heat resistance. One can also see from Fig.(8) that strength reduction is more obvious for concrete with higher rank (28-d strength). It can also be seen, from Fig.(9) that correlation between strength and Rn becomes closer for plain and fiber reinforced concretes. However, damage in surface layer for exposure at 450° C makes Rn smaller, especially for concrete with small rank. In case of exposure to 400° C, drying effect causes an increase in surface hardness as can be seen from the range of readings.

Measurements of ultrasonic pulse velocity appear to be more sensitive to heat damage. This is expected since wave propagation is more interrupted by heat induced cracks. Effect of fibers is significant since it allows transmission across cracks by bridging mechanism they offer. This is more obvious for high residual strength range; where the number of internal cracks from thermal damage is less.

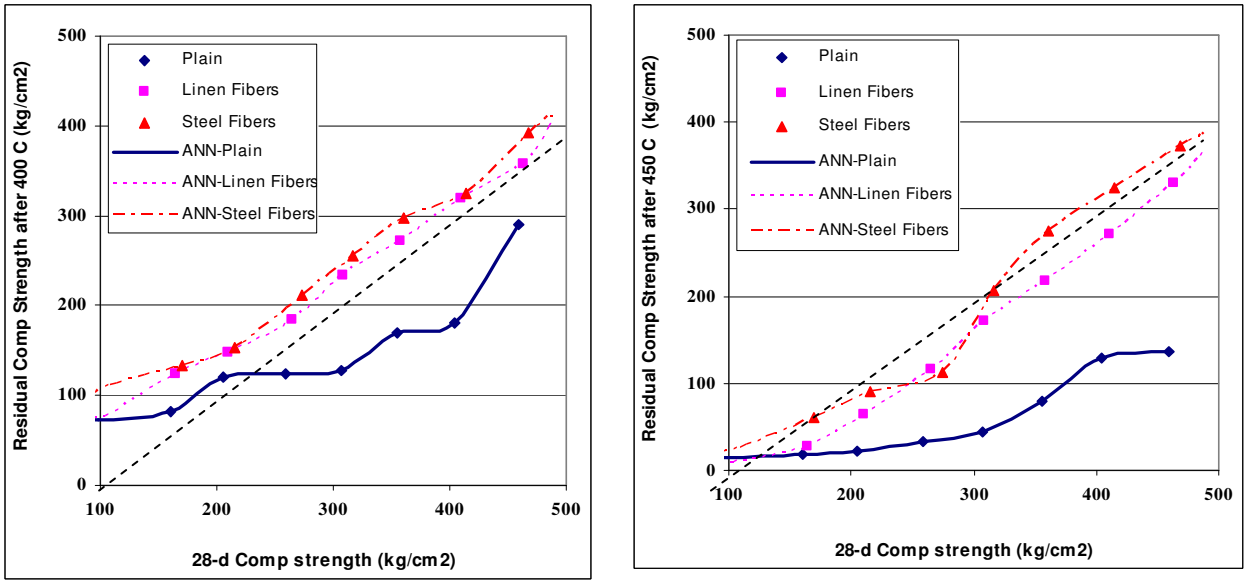

FIGURE 8: Residual Compressive Strength vs. 28-d Compressive Strength

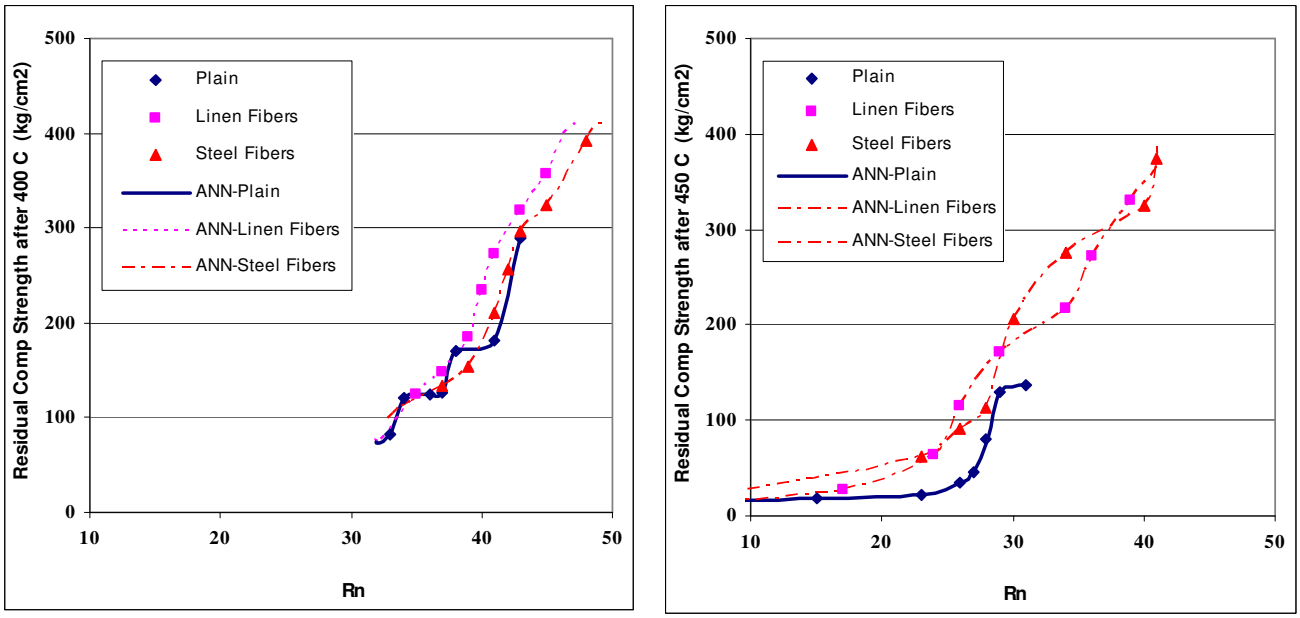

FIGURE 9: Residual Compressive Strength vs. Rebound Number

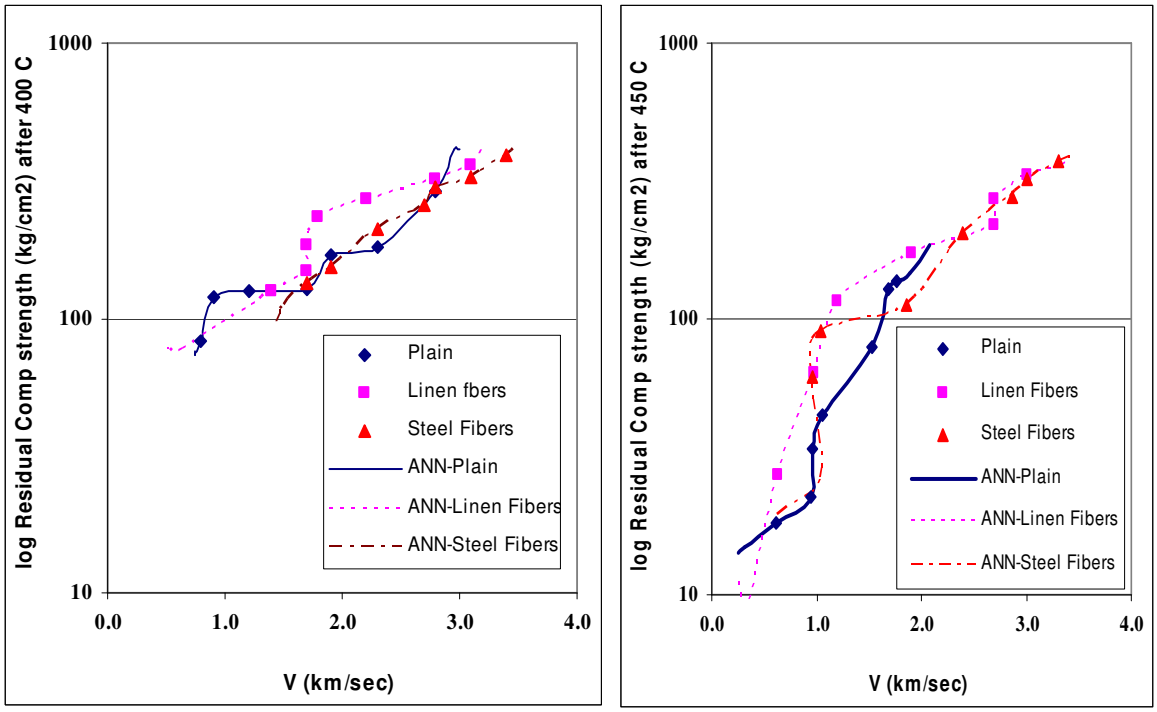

FIGURE 10: Residual Compressive Strength vs. Ultrasonic Pulse Velocity

6. NUMERICAL MODEL STRUCTURE

Neural networks are models of biological neural structures. Briefly, the starting point for most networks is a model neuron as shown in Fig. (11). This neuron is connected to multiple inputs and produces a single output. Each input is modified by a weighting value (w). The neuron will combine these weighted inputs with reference to a threshold value and an activation function, will determine its output. This behavior follows closely the real neurons work of the human's brain. In the network structure, the input layer is considered a distributor of the signals from the external world while hidden layers are considered to be feature detectors of such signals. On the other hand, the output layer is considered as a collector of the features detected and the producer of the response.

It is quite important for the reader to understand how the neural network operates to simulate different physical problems. The output of each neuron is a function of its inputs (X_i). In more details, the output (Y_j) of the j^{th} neuron in any layer is described by two sets of equations as follows:

$$U_j = \sum\left(X_i w_{ij} \right) \quad (1)$$

And

$$Y_j = F_{th}\left(U_j + t_j \right) \quad (2)$$

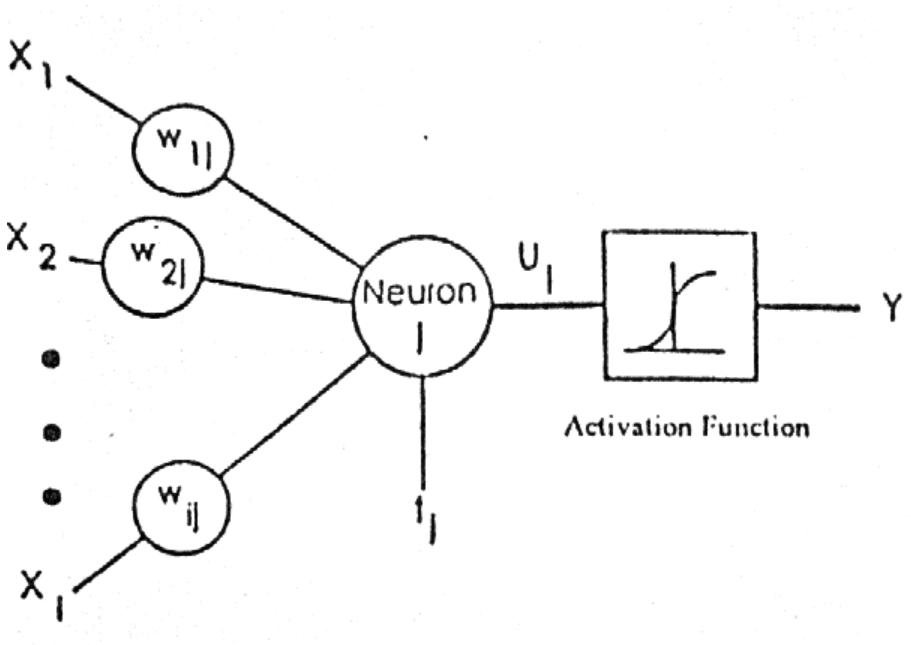

FIGURE 11: Typical picture of a model neuron that exists in every neural network

For every neuron, *j*, in a layer, each of the *i* inputs, X_i, to that layer is multiplied by a previously established weight, w_{ij}. These are all summed together, resulting in the internal value of this operation, U_j. This value is then biased by a previously established threshold value, t_j, and sent through an activation function, F_{th}. This activation function can take several forms such as Step, Linear, Sigmoid, Hyperbolic, and Gaussian functions. The Hyperbolic function, used in this study, is shaped exactly as the Sigmoid one with the same mathematical representation, as in equation 3, but it ranges from – 1 to + 1 rather than from 0 to 1 as in the Sigmoid one.

$$f(x) = \frac{1}{1+e^{-x}} \tag{3}$$

The resulting output, Y_j, is an input to the next layer or it is a response of the neural network if it is the last layer. In applying the Neural Network technique, in this study, Neuralyst Software, Shin [17], was used.

The next step in neural network procedure is the training operation. The main purpose of this operation is to tune up the network to what it should produce as a response. From the difference between the desired response and the actual response, the error is determined and a portion of it is back propagated through the network. At each neuron in the network, the error is used to adjust the weights and the threshold value of this neuron. Consequently, the error in the network will be less for the same inputs at the next iteration. This corrective procedure is applied continuously and repetitively for each set of inputs and corresponding set of outputs. This procedure will decrease the individual or total error in the responses to reach a desired tolerance. Once the network reduces the total error to the satisfactory limit, the training process may stop. The error propagation in the network starts at the output layer with the following equations:

$$w_{ij} = w_{ij}^{'} + LR\left(e_j X_i\right) \tag{4}$$

And,

$$e_j = Y_j\left(1 - Y_j\right)\left(d_j - Y_j\right) \tag{5}$$

Where, w_{ij} is the corrected weight, w'_{ij} is the previous weight value, LR is the learning rate, e_j is the error term, X_i is the i^{th} input value, Y_j is the ouput, and d_j is the desired output.

7. SIMULATION CASES

To fully investigate the effect of natural and steel fibers on the performance of concrete, several simulation cases are considered in this study. These simulation cases can be divided into two groups. The first group simulates the impact of fibers on the performance of concrete: compressive, tensile, impact strengths, rebound hammer reading and ultra sonic pulse velocity. The second group simulates the effect of elevated temperature on the performance of plain concrete as well as concrete with fibers: residual strength, rebound hummer reading and ultra sonic pulse velocity.

8. NEURAL NETWORK DESIGN

To develop a neural network model to simulate the effect of fibers on the performance of concrete, first input and output variables have to be determined. Input variables are chosen according to the nature of the problem and the type of data that would be collected in the field. To clearly specify the key input variables for each neural network simulation groups and their associated outputs, Tables (2) and (3) are designed to summarize all neural network key input variables and outputs for these two groups respectively.

It can be noticed from Table (2) that the first simulation group consists of five simulation cases (five neural network models) to study the effect of fibers on the compressive strength, splitting tensile strength, impact strength, rebound hammer reading and ultrasonic velocity. Table (3), for the second simulation group, consists of six simulation cases (six neural network models) to study the effect of fibers on the residual compressive strength, rebound hammer reading and ultrasonic velocity in case of elevated temperature to 400^{o}C and 450^{o}C.

Several neural network architectures are designed and tested for all simulation cases investigated in this study to finally determine the best network models to simulate, very accurately, the effect of fibers as well as elevated temperature on the performance of concrete based on minimizing the Root Mean Square Error (RMS-Error). Fig. (12) shows a schematic diagram for a generic neural network.

Simulation Case	**Input Variables - Kg/m^3**						**Output**
Compressive Strength	Water	Cement	Sand	Gravel	Steel Fibers	Linen Fibers	28-days Comp. Strength
Tensile Strength							Splitting Tensile Strength
Impact Strength							Impact Strength
Rebound Hammer Reading							Rebound Number 28-days
Ultrasonic Velocity							Velocity 28-days

TABLE 2: Key input variables and output for the first neural network simulation group

Simulation Case	Input Variables - Kg/m^3						Output
Residual Comp. Strength	Water	Cement	Sand	Gravel	Steel Fibers	Linen Fibers)	Strength at 400^{o}C
Residual Comp. Strength							Strength at 450^{o}C
Rebound Hammer Reading							Rn at 400^{o}C
Rebound Hammer Reading							Rn at 450^{o}C
Ultrasonic Velocity							Velocity at 400^{o}C
Ultrasonic Velocity							Velocity. at 450^{o}C

TABLE 3: Key input variables and output for the second neural network simulation group (elevated temperature)

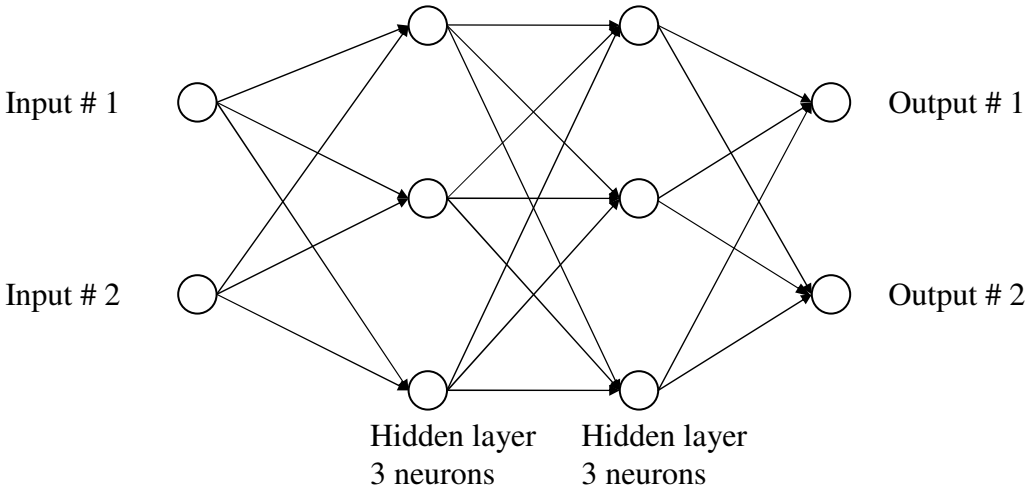

FIGURE 12: General schematic diagram of a simple generic neural network

Table (4) shows the final neural network models for all the simulated cases and their associated number of neurons. The input and output layers represent the key input and output variables described previously for each simulation case. The term PRE showed in the table referred to percentage relative error and is computed based on equation 6 as follows:

PRE = (Absolute Value (ANN_PR - AMV)/AMV)*100 (6)
Where:
ANN_PR: Predicted results using the developed ANN model
AMV : Actual Measured Value

The parameters of the various network models developed in the current study for the different simulation cases are presented in Table (5), where: (**Comp. St.**) denotes for compressive strength, (**Ten. St.**) for tensile strength and (**Rn**) for rebound number,. These parameters can be described with their tasks as follows:

Learning Rate (LR): determines the magnitude of the correction term applied to adjust each neuron's weights during training process = 1 in the current study.
Momentum (M): determines the "life time" of a correction term as the training process takes place = 0.9 in the current study.
Training Tolerance (TRT): defines the percentage error allowed in comparing the neural network output to the target value to be scored as "Right" during the training process.
Testing Tolerance (TST): it is similar to Training Tolerance, but it is applied to the neural network outputs and the target values only for the test data.
Input Noise (IN): provides a slight random variation to each input value for every training epoch = 0 in the current study.
Function Gain (FG): allows a change in the scaling or width of the selected function = 1 in the current study.
Scaling Margin (SM): adds additional headroom, as a percentage of range, to the rescaling computations used by Neuralyst Software, Shin [17], in preparing data for the neural network or interpreting data from the neural network = 0.1 in the current study.

Simulation Case	No. of Layers	No. of Neurons in each Layer						Max PRE
		Input Layer	First Hidden	Second Hidden	Third Hidden	Fourth Hidden	Output Layer	
Compressive Strength	6	6	6	5	4	3	1	0.122
Tensile Strength	5	6	5	5	4	-	1	0.151
Impact Strength	5	6	6	5	4	-	1	0.08
Rebound Hammer Reading	6	6	6	5	4	3	1	0.118
Ultrasonic Pulse Vel.	5	6	5	4	3	-	1	0.693
Strength at 400°C	5	6	6	5	4	-	1	0.014
Strength at 450°C	5	6	5	4	3	-	1	0.697
Rn at 400°C	5	6	5	4	3	-	1	0.154
Rn at 450°C	6	6	6	6	5	6	1	0.078
Velocity at 400°C	5	6	5	4	3	-	1	0.294
Velocity at 450°C	5	6	5	4	3	-	1	0.207

TABLE 4: The developed neural network models for all the simulation cases

Simulation Case	Comp. St.	Ten. St.	Impact St.	Rn	V	St. 400° C	St. 450° C	Rn 400° C	Rn 450° C	V 400° C	V 450° C
TRT	0.0005	0.001	0.0001	0.001	0.001	0.0001	0.0001	0.001	0.0005	0.0005	0.001
TST	0.001	0.003	0.0003	0.003	0.003	0.0001	0.001	0.003	0.001	0.001	0.003

TABLE 5: Parameters used in the developed neural network models

9. RESULTS AND DISCUSSIONS

Numerical results using ANN technique are plotted with the experimental results for the first neural network simulation group : compressive strength, tensile strength, impact strength, rebound hammer reading and ultrasonic pulse velocity as shown in Figs. (2 – 7) respectively. It can be noticed from these figures that ANN technique can accurately simulate the effect of fibers on the performance of concrete.

To study the effect of elevated temperature as well as fibers on the performance of concrete (residual strength, rebound hammer reading and ultrasonic velocity) numerically, the second neural network simulation group are prepared as shown in Table (3). The results of this group are plotted with the experimental results in Figs. (8 – 10) for both 400°C and 450°C. One can see from these Figs. that ANN technique can accurately simulate the effect of elevated temperature and existence of fibers on the performance of concrete.

To check the accuracy of neural network the term PRE is calculated as in equation 6 for each data point in each model. Then the Max PRE is calculated through each model and reported in Table 4. It is very clear from the column of Max PRE that this value doesn't exceed 0.7 % for all the simulation cases presented in this study.

To check the trend of the model before and after the experimental data, two mixes were chosen by reducing the cement content by 50 Kg/m^3 and 100 Kg/m^3 respectively and increasing the weights of sand and gravel content using their corresponding specific gravity. Also, in some cases, other two mixes were chosen by increasing the cement content by the same values as before and reducing the weights of sand and gravel content using their specific gravity. The numerical data resulted from neural network models for these extrapolation points are shown in Figs. (2 – 10). The trend achieved from these figures shows the power of ANN technique to simulate the behavior of concrete under the effect of fibers and elevated temperature.

10. CONCLUSIONS

Application of linen fibers to concrete yields behavior and properties close to that of plain concrete of same rank. Significant improvements were observed for tensile, stiffness, impact and fire resistance. Although an increase of surface hardness and ultrasonic pulse velocity was observed upon use of fibers, almost same calibration curves can be applied for non-destructive testing techniques of rebound hammer and ultrasonic pulse velocity. This can be done considering the range of accuracy of both techniques in evaluating compressive strength of hardened concrete.

The results of implementing the ANN technique in this study showed that this approach was capable of identifying relationship between different uncertain parameters with multiple input/output criterions. The ANN presented in this study was very successful in simulating and predicting the effect of fibers and elevated temperature on the performance of concrete.

11. ACKNOLEDGEMENT

The Authors would like to express their gratitude towards Prof. Dr. Farouk El-Hakim of 15th May institute for Civil and Arch. Engineering, and undergraduate students (4th year– civil) for the help they provided during the experimental part of this research.

12. REFERENCES

1. Abdeen, M. A. M. "*Neural Network Model for predicting Flow Characteristics in Irregular Open Channel*". Scientific Journal, Faculty of Engineering-Alexandria University, Alexandria, Egypt, 40(4):539-546, 2001

2. Abdeen, M. A. M. "*Development of Artificial Neural Network Model for Simulating the Flow Behavior in Open Channel Infested by Submerged Aquatic Weeds*". Journal of Mechanical Science and technology, KSME Int. J., Soul, Korea, 20(10): 2006

3. ACI 228.1 R89. "*In-Place Methods for Determination of Strength of Concrete*". American Concrete Institute, 1989

4. ACI 437 R91. "*Strength Evaluation of Existing Concrete Buildings*". American Concrete Institute, 1991

5. [ACI 544.1 R82-96. "*State of the Art Report on Fiber Reinforced Concrete*". American Concrete Institute, 1996

6. ACI 544.2R-99. "*Measurement of Properties of Fiber Reinforced Concrete*". American Concrete Institute, 1999

7. ALLAM, B. S. M. "*Artificial Intelligence Based Predictions of Precautionary Measures for building adjacent to Tunnel Rout during Tunneling Process*". Ph.D. Thesis, Faculty of Engineering, Cairo University, Giza, Egypt, 2005

8. ASTM C0469-02E01. "*Test Method for Static Modulus of Elasticity and Poisson's Ratio of Concrete in Compression*", 2001

9. Azmathullah, H. Md., Deo, M. C., Deolalikar, P. B. "*Neural Networks for Estimation of Scour Downstream of a Ski-Jump Bucket*". Journal of Hydrologic Engineering*, ASCE*, 131(10), 898-908, 2005

10. Gorillo, P., Shimizu, G. "*Study of the Properties of Coir Fiber Mortar and Concrete*". Proc. of the Annual Meeting of Japan Concrete Institute JCI, 14(1):1143-1148, 1992

11. Kheireldin, K. A. "*Neural Network Application for Modeling Hydraulic Characteristics of Severe Contraction*". *Proc*. of the 3rd Int. Conference*, Hydroinformatics*, Copenhagen - Denmark August 24-26, 1998

12. Malhotra, V.M. "*Testing Hardened Concrete: Nondestructive Methods*". ACI Monograph, No. 9, 1986

13. Mohamed, M. A. M. "*Selection of Optimum Lateral Load-Resisting System Using Artificial Neural Networks*". M. Sc. Thesis, Faculty of Engineering, Cairo University, Giza, Egypt, 2006

14. Minns. "*Extended Rainfall-Runoff Modeling Using Artificial Neural Networks*". Proc. of the 2nd Int. Conference on Hydroinformatics, Zurich, Switzerland, 1996

15. Parrett, N. J.. "*Fiber Reinforced Materials Technology*". Van Nostrand Reinhold Company*,* London, 1972

16. Ramachandran, V.,J. et al. "*Concrete Science*". Heyden & Sons Ltd*.,* London, (1981)

17. Shin, Y. "*Neuralyst*^{TM} *User's Guide". "Neural Network Technology for Microsoft Excel*". Cheshire Engineering Corporation Publisher, (1994)

18. Silva, R. V., Aquino, E. M. F.,"*Curaua Fiber: A New Alternative to Polymeric Composites*". Journal of Reinforced Plastics and Composites, 27(1):2008

19. Tahk, K. Mo, K. H. Shin. "*A study on the Fault Diagnosis of Roller-Shape Using Frequency Analysis of Tension Signals and Artificial Neural Networks Based Approach in a Web Transport System*". Journal of Mechanical Science and technology, KSME Int. J., Soul, Korea, 16(12):2002

Verification of the Thermal Buckling Load in Plates Made of Functional Graded Materials

Hamid Mozafari mozafari.h@gmail.com
Faculty of Mechanical Engineering
Technical University of Malaysia-UTM
81310 UTM, Skudai, Johor, Malaysia

Amran Ayob amran@fkm.utm.my
Faculty of Mechanical Engineering
Technical University of Malaysia-UTM
81310 UTM, Skudai, Johor, Malaysia

Amran Alias amran_al @fkm.utm.my
Faculty of Mechanical Engineering
Technical University of Malaysia-UTM
81310 UTM, Skudai, Johor, Malaysia

Abstract

In this study, thermal buckling of thin plate made of Functionally Graded Materials (FGM) with linearly varying thickness is considered. The material properties are also graded in the thickness direction according to a simple power law distribution in which the properties are stated in terms of the volume fractions of the constituents. All edges of the plate are simply supported. The equilibrium and stability equations of a FGM plate under thermal loads can be derived based on higher order plate theories via variation formulation, and are then used to determine the governing deferential equation of the plate and the pre-buckling forces. The buckling analysis of a FGM plate is conducted by assuming a uniform temperature rise, temperature gradient through the thickness, and linear temperature variation in the thickness. Closed–form solutions are obtained the buckling load defined in a weighted residual approach. In a special case the obtained results are compared with the results of FGM plates with uniform thickness. The influences of the plate thickness variation and the edge ratio on the critical loads are investigated. Different gradient exponent *k*, different geometries and loading conditions were studied.

Keywords: Thermal buckling; FGM plates; Thin plate; Higher Order plate theories; Variable thickness plate.

1. INTRODUCTION

Functionally graded materials (FGMs) have received considerable attention in many engineering applications since they were first reported in 1984 in Japan [23]. The main advantage of such materials is the possibility of tailoring desired properties to needs. Obviously, FGM's can be used in a variety of applications which have made them very attractive. Theories of plates and shells have already been applied to high extent, and there are many text books available, such as [1- 3]. Later on, the concept of FGM was proposed in [4] and [5]. The main advantage of FGMs is their high resistance to environments with extremely high temperature and extreme changes in temperature. Ceramic due to low thermal

conductance constituents causes resistance to high temperature. One of the main applications of Functionally Graded Materials is their use in power reactors, electronic and magnetic sensors, medical engineering of artificial bones and teeth, chemical industry and in new technologies such as ceramic engines and as resistant covers and protection against corrosion.

Chi and Chung [9, 10] examined the mechanical behavior of FGM plates under transverse load. Najafizadeh and Eslami [14] studied the buckling behavior of circular FGM plates under uniform radial compression. Shariat and Eslami [16] investigated thermal buckling of imperfect FGM plates. Huang and Chang [13] carried out studies on corner stress singularities in an FGM thin plate. Nonlinear analysis, such as nonlinear bending, nonlinear vibration and post-bucking analysis of homogeneous isotropic or FGM plates and shells can be found in the articles by Sundararajan et al. [17], Chen et al. [7], Hsieh and Lee [12], Ghannadpour and Alinia [11]. Further research can be found in the articles by Navazi et al. [15], Woo et al. [18], Chen and Tan [8] and Li et al. [20]. Morimoto et al. [19] and Abrate [6] noticed that there is no stretching–bending coupling in constitutive equations if the reference surface is properly selected. Classical nonlinear laminated plate theory and the concept of physical neutral surface are employed to formulate the basic equations of the FGM thin plate.
Da-Guang Zhanga and You-He Zhou studied functionally graded materials as thin plates in 2008 [27], whereas Wu [21] has examined the effect of shear deformation on the thermal buckling of FGM plates. Chen and Liew [22] have examined the buckling of rectangular FGM plates subjected to in-plane edge loads. Based on third order shear deformation theory, Shariat and Eslami [27] studied the buckling of *thick* functionally graded material under mechanical and thermal load and Javaheri and Eslami [28] studied the buckling of functionally graded plate under in-plane compressive loading based on classical plate theory. Previous studies reported that critical buckling temperature differences for the functionally graded plates are generally lower than the corresponding values for homogeneous plates. They used classical plate theory for the buckling analysis of functionally graded plates under in–plane compressive loading.

In the present study, equilibrium and stability equations for functionally graded *thin* plates are derived based on higher order shear deformation plate theory. The resulting equations are employed to obtain closed–form solutions for the critical buckling loads. In order to establish the fundamental system of equations for the buckling analysis, it is assumed that the non-homogeneous mechanical properties of the material are given by a power law formulated in Cartesian coordinates.

2. FGM PLATE AND ITS PROPERTIES

Consider a FG thin plate made from a mixture of ceramics and metals and subjected to a kind of thermal load. The plate coordinate system (*x, y, z*) is chosen such that, *x* and *y* are in-plane coordinates and *z* is in the direction through the thickness and normal to the middle plane. The corresponding displacements in the x-, y- and z-directions are designated by *u*, *v* and *w*, respectively. The origin of the coordinate system is located at the corner of the plate on the middle plane. The plate side lengths in the *x*- and y-directions are designated as *a*, and *b* respectively. The thickness of the plate, *h*, varies the *x* and *y* directions such that (see Fig. 1);

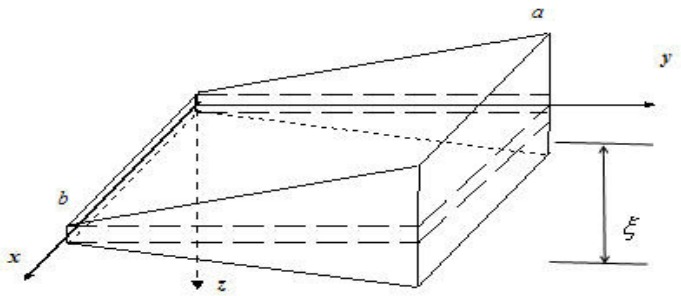

FIGURE 1: Geometry and coordinate system of rectangular plate (a ×b)

$$h = h(x) = \xi = c_1 x + c_2 \quad \& \quad h = h(y) = \xi = c_1 y + c_2. \tag{1}$$

in which ξ is a general parameter indicating the thickness change in either of *x* or *y* directions, c_2 is the nominal thickness of the plate at the origin and c_1 is a variable parameter called the non-dimensional parameter. When c_1=0, it means that the plate has a constant thickness. When *x* = 0, one has $\xi = c_2 = h$ and for the case of $x = a$, $\xi(a) = c_1 a + c_2$

To get the change in through thickness properties, it is assumed that the plate composition is varied from the outer (top) to the inner (bottom) surface; i.e. the outer surface of the plate is ceramic rich whereas the inner surface is metal-rich. The material properties of the FGM plate, are such that the coefficient of thermal expansion, α, modulus of elasticity *E*, and coefficient of thermal conduction *k* are assumed to be functions of the constituent materials, while the Poisson's ratio *v* is assumed to be constant across the plate thickness such that:

$$\begin{aligned} E(z) &= E_c V_c + E_m (1 - V_{c),} \\ \alpha(z) &= \alpha_c V_c + \alpha_m (1 - V_c), \\ K(z) &= K_c V_c + K_m (1 - V_c), \\ v(z) &= v, \end{aligned} \tag{2}$$

where subscripts *m* and *c* refer to the metal and ceramic constituents, respectively. The volume fractions of ceramic v_c and metal v_m are related by

$$\begin{aligned} V_c &= (z/h + 1/2)^k, \quad k \geq 0, \quad k = \infty, \\ V_m(z) + V_c(z) &= 1, \end{aligned} \tag{3}$$

where volume fraction exponent *k* dictates the material metal-ceramic variation profile through the plate thickness. *k* assumes values greater than or equal to zero. *K* = 0 represents a fully ceramic plate. From Eqns. (2) and (3) material properties of the FGM plate are determined, which are the same as the equations proposed by many references.

$$\begin{aligned} E(z) &= E_m + E_{cm}(z/h + 1/2)^k, \\ \alpha(z) &= \alpha_m + \alpha_{cm}(z/h + 1/2)^k, \\ K(z) &= K_m + K_{cm}(z/h + 1/2)^k, \\ v(z) &= v, \end{aligned} \tag{4}$$

in which;

$$E_{cm} = E_c - E_m, \qquad \alpha_{cm} = \alpha_c - \alpha_m, \qquad K_{cm} = K_c - K_m, \tag{5}$$

3. BASIC AND EQUILIBRIUM EQUATIONS

The higher order plate theories which is considered in the present work is based on the assumption of the displacement field in the following form:

$$u(x, y, z) = u_0(x, y) - z w_{0,x,}$$

$$v(x,y,z) = v_0(x,y) - zw_{0,y,} \qquad (6)$$

$$w(x,y,z) = w_0(x,y)$$

in which *u, v, w* are the total displacement and (u_0, v_0, w_0) are the mid-plane displacements in the *x*, *y* and *z* directions, respectively. For the thin plate i.e. $(h/b) \leq (1/20)$, where *h* and *n* are the thickness and smaller edge side of the plate, respectively.
Hook's law for a plate with thermal effects is defined as:

$$\bar{\sigma}_{xx} = \frac{E(z)}{1-v^2}\left[\bar{\varepsilon}_{xx} + v\bar{\varepsilon}_{yy} - (1+v)\alpha T\right],$$

$$\bar{\sigma}_{yy} = \frac{E(z)}{1-v^2}\left[\bar{\varepsilon}_{yy} + v\bar{\varepsilon}_{xx} - (1+v)\alpha T\right], \qquad (7)$$

$$\bar{\sigma}_{xy} = \frac{E(z)}{2(1+v)}\bar{\gamma}_{xy}$$

The plate is assumed to be comparatively thin and according to the Love-Kirchhoff assumption, planes which are normal to the median surface are assumed to remain plane and normal during deformation, thus out-of-plane shear deformations $(\gamma_{xz}, \gamma_{yz})$ are disregarded. Strain components at distance z from the middle plane are then given by:

$$\bar{\varepsilon}_{xx} = \varepsilon_{xx} + zk_{xx},$$

$$\bar{\varepsilon}_{yy} = \varepsilon_{yy} + zk_{yy}, \qquad (8)$$

$$\bar{\gamma}_{xy} = \gamma_{xy} + 2zk_{xy.}$$

Here, $\varepsilon_{xx}, \varepsilon_{yy}, \gamma_{xy}$ denote the corresponding quantities at points on the mid-plane surface only, and k_{xx}, k_{yy}, k_{xy} are the curvatures which can be expressed in term of the displacement components. The relations between the mid-plane strains and the displacement components according to the Sander's assumption are;

$$\varepsilon_{xx} = u_{,x} + \frac{1}{2}w_{,x}^2,$$

$$\varepsilon_{yy} = v_{,y} + \frac{1}{2}w_{,y}^2, \qquad (9)$$

$$\gamma_{xy} = u_{,y} + v_{,x} + w_{,x}w_{,y}.$$

and

$$k_{xx} = -w_{,xx}, \qquad k_{yy} = -w_{,yy}, \qquad k_{xy} = -w_{,xy} \qquad (10)$$

Substituting Eqns. (9) and (10) into Eqns. (8), the following expressions for the strain components are obtained:

$$\bar{\varepsilon}_{xx} = u_{,x} + \frac{1}{2}w_{,x}^2 - zw_{,xx},$$

$$\bar{\varepsilon}_{yy} = v_{,y} + \frac{1}{2}w_{,y}^2 - zw_{,yy}, \qquad (11)$$

$$\bar{\gamma}_{xy} = u_{,y} + v_{,x} + w_{,x}w_{,y} - 2zw_{,xy}.$$

A loaded plate is in equilibrium if its total potential energy *V* remains stationary (δV =0), and *V* is stationary if the integrand in expression for *V* satisfies the Euler equations.

The total potential energy *V* of a plate subjected to thermal loads is defined as:

$$V = U_m + U_b + U_c + U_T, \tag{12}$$

where U_m is the membrane strain energy, U_b is the bending strain energy, U_c is the coupled strain energy, and U_T is the thermal strain energy. The strain energy for thin plate based on classical plate theory is defined as;

$$U = \frac{1}{2}\iiint\left[\overline{\sigma}_{xx}(\overline{\varepsilon}_{xx} - \alpha T) + \overline{\sigma}_{yy}(\overline{\varepsilon}_{yy} - \alpha T) + \overline{\tau}_{xy}\overline{\gamma}_{xy}\right]dxdydz. \tag{13}$$

Substituting Eqns. (7) and (8) into Eqn. (13), and integrating with respect to *z* from- ξ*/2 to* ξ*/2,* the total potential energy results in;

$$V = \iint F dxdy. \tag{14}$$

where, the function *F* is;

$$\begin{aligned} F = {} & \frac{A}{2(1-v^2)}\left[\varepsilon_{xx}^2 + \varepsilon_{yy}^2 + 2v\varepsilon_{xx}\varepsilon_{yy} + \frac{1-v}{2}\gamma_{xy}^2\right] + \\ & \frac{C}{2(1-v^2)}\left[k_{xx}^2 + k_{yy}^2 + 2vk_{xx}k_{yy} + 2(1-v)k_{xy}^2\right] + \\ & \frac{B}{2(1-v^2)}\left[\varepsilon_{xx}k_{xx} + \varepsilon_{yy}k_{yy} + v(\varepsilon_{xx}k_{yy} + \varepsilon_{yy}k_{xx}) + (1-v)\gamma_{xy}k_{xy}\right] - \\ & \frac{1}{1-v}\left[\Theta(\varepsilon_{xx} + \varepsilon_{yy}) + \Phi(k_{xx} + k_{yy}) - \psi\right] \end{aligned} \tag{15}$$

where

$$\begin{aligned} A &= \int_{-\xi/2}^{\xi/2} E(z)dz = E_m\xi + E_{cm}\frac{\xi}{k+1}, \\ B &= \int_{-\xi/2}^{\xi/2} E(z)zdz = E_{cm}\frac{k\xi^2}{(2k+2)(k+2)}, \\ C &= \int_{-\xi/2}^{\xi/2} E(z)z^2dz = E_m\frac{\xi^3}{12} + E_{cm}\xi^3\left[\frac{1}{k+3} - \frac{1}{k+2} + \frac{1}{4k+4}\right], \\ (\Theta,\Phi) &= \int_{\xi/2}^{\xi/2} (1,z)E(z)\alpha(z)T(x,y,z)dz, \\ \psi &= \int_{\xi/2}^{\xi/2} E(z)\alpha^2(z)T^2(x,y,z)dz. \end{aligned} \tag{16}$$

The total potential energy is a function of the displacement components and their derivatives. Hence, minimization of total potential energy in terms of the function *F* yields the following Euler Equations:

$$\begin{aligned} &\frac{\partial F}{\partial u} - \frac{\partial}{\partial x}\cdot\frac{\partial F}{\partial u_{,x}} - \frac{\partial}{\partial y}\cdot\frac{\partial F}{\partial u_{,y}} = 0 \\ &\frac{\partial F}{\partial v} - \frac{\partial}{\partial x}\cdot\frac{\partial F}{\partial v_{,x}} - \frac{\partial}{\partial y}\cdot\frac{\partial F}{\partial v_{,y}} = 0 \\ &\frac{\partial F}{\partial w} - \frac{\partial}{\partial x}\cdot\frac{\partial F}{\partial w_{,x}} - \frac{\partial}{\partial y}\cdot\frac{\partial F}{\partial w_{,y}} + \frac{\partial^2}{\partial x^2}\cdot\frac{\partial F}{\partial w_{,xx}} + \frac{\partial^2}{\partial x\partial y}\cdot\frac{\partial F}{\partial w_{,xy}} + \frac{\partial^2}{\partial y^2}\cdot\frac{\partial F}{\partial w_{,yy}} = 0 \end{aligned} \tag{17}$$

Substituting Eqns. (9) and (10) into Eqn. (15) and using Eqns. (17), the equilibrium equations for general rectangular plate made of functionally graded material are given by;

$$N_{x,x} + N_{xy,y} = 0$$

$$N_{xy,x} + N_{y,y} = 0 \tag{18}$$

$$M_{x,xx} + 2M_{xy,xy} + M_{y,yy} + N_x w_{,xx} + 2N_{xy} w_{,xy} + N_y w_{,yy} + P_n = 0$$

where stress resultant N_i, M_i are given by:

$$(N_i, M_i) = \int_{\xi/2}^{\xi/2} (1, z).\overline{\sigma}_i.dz, \qquad i = x, y, xy \tag{19}$$

By substituting Eq. (7) into Eq. (19), one can arrive to the following constitutive relation is obtained;

$$\begin{aligned}
(N_x, M_x) &= \frac{1}{1-v^2}\left[(A,B)(\varepsilon_{xx} + v\varepsilon_{yy}) + (B,C)(k_{xx} + vk_{yy}) - (1+v)(\Theta,\Phi)\right], \\
(N_y, M_y) &= \frac{1}{1-v^2}\left[(A,B)(\varepsilon_{yy} + v\varepsilon_{xx}) + (B,C)(k_{yy} + vk_{xx}) - (1+v)(\Theta,\Phi)\right], \\
(N_{xy}, M_{xy}) &= \frac{1}{2(1+v)}\left[(A,B)\gamma_{xy} + 2(B,C)k_{xy}\right]
\end{aligned} \tag{20}$$

4. PLATE STABILITY EQUATIONS

Stability equations of thin plates are derived using the energy method. If *V* is the total potential energy of the plate, then expanding *V* about the equilibrium state using Taylor series yields;

$$\Delta V = \delta V + \frac{1}{2!}\delta^2 V + \frac{1}{3!}\delta^3 V + ... \tag{21}$$

The first variation δV is associated with the state of equilibrium. The stability of the plate in the neighborhood of equilibrium condition may be determined by the sign of second variation. The condition $\delta^2 V = 0$ is used to derive the stability equations for buckling problems [16]. Assume that $\hat{u}_i$ denotes the displacement component of the equilibrium state and $\delta\hat{u}_i$ the virtual displacement corresponding to a neighboring state. Denoting $\overline{\delta}$ the variation with respect to $\hat{u}_i$, the following rule, known as the Trefftz rule, is adopted for the determination of the critical load. The external load acting on the plate is considered to be the critical buckling load if the following variation equation is satisfied $\overline{\delta}(\delta^2 V) = 0$. The state of primary equilibrium of a rectangular plate under general loading is designated by u_0, v_0, w_0. In deriving the stability equations, virtual displacements are defined as:

$$\begin{aligned}
u &\to u_0 + u_1, \\
v &\to v_0 + v_1, \\
w &\to w_0 + w_1,
\end{aligned} \tag{22}$$

where u_1, v_1, w_1 are the virtual displacement increments. Substituting Eqns. (22) into Eqn. (15) and collecting the second–order terms, the second variation of the potential energy are obtained as;

$$\frac{1}{2}\delta^2 V = \iint \left\{ \frac{A}{2(1-v^2)}\left[u_{1,x}^2 + v_{1,y}^2 + 2v u_{1,x} v_{1,y} + \frac{1-v}{2}(u_{1,y} + v_{1,x})^2 \right] - \right.$$
$$\frac{B}{1-v^2}\left[u_{1,x} w_{1,xx} + v_{1,y} w_{1,yy} + v(u_{1,x} w_{1,yy} + v_{1,y} w_{1,xx}) + (1-v)(u_{1,y} + v_{1,x}) w_{1,xy} \right] +$$
$$\frac{C}{2(1-v^2)}\left[w_{1,xx}^2 + w_{1,yy}^2 + 2v w_{1,xx} w_{1,yy} + 2(1-v) w_{1,xy}^2 \right] + \qquad (23)$$
$$\left. \frac{1}{2}\left[N_x^0 w_{1,x}^2 + 2N_{xy}^0 w_{1,x} w_{1,y} + N_y^0 w_{1,y}^2 \right] \right\} dxdy$$

Applying the Euler equations (17) to the functional of Eq. (23), the stability equations are obtained as;

$$N_{x1,x} + N_{xy1,y} = 0$$
$$N_{xy1,x} + N_{y1,y} = 0 \qquad (24)$$
$$M_{x/,xx} + 2M_{xy1,xy} + M_{y1,yy} + (N_x^0 w_{1,xx} + 2N_{xy}^0 w_{1,xy} + N_y^0 w_{1,yy}) = 0$$

where

$$(N_{x1}, M_{x1}) = \frac{1}{1-v^2}\left[(A,B)(u_{1,x} + w_{1,y}) - (B,C)(w_{1,xx} + v w_{1,yy}) \right],$$
$$(N_{y1}, M_{y1}) = \frac{1}{1-v^2}\left[(A,B)(v_{1,x} + v u_{1,x}) - (B,C)(w_{1,yy} + v w_{1,xx}) \right],$$
$$(N_{xy1}, M_{xy1}) = \frac{1}{2(1+v)}\left[(A,B)(u_{1,y} + v_{1,x}) - 2(B,C) w_{1,xy} \right], \qquad (25)$$
$$N_x^0 = \frac{1}{1-v^2}\left[A(u_{0,x} + w_{0,y}) - B(w_{0,xx} + v w_{0,yy}) \right] - \frac{\Theta}{1-v},$$
$$N_y^0 = \frac{1}{1-v^2}\left[A(v_{0,y} + v u_{0,x}) - B(w_{0,yy} + v w_{0,xx}) \right] - \frac{\Theta}{1-v},$$
$$N_{xy}^0 = \frac{A}{2(1+v)}(u_{0,y} + v_{0,x}) - \frac{B}{1+v} w_{0,xy}.$$

4.1 Governing Differential Equation for FGM

By substituting Eq. (25) into Eq. (24), the stability equations in terms of displacement components become;

$$A_{,x}(u_{1,x} + v v_{1,y}) + A(u_{1,xx} + v v_{1,xy}) - B_{,x}(w_{1,xx} + v w_{1,yy}) - B(w_{1,xxx} + v w_{1,xyy})$$
$$+ \frac{A(1-v)}{2}(u_{1,yy} + v_{1,xy}) - B(1-v) w_{1,xy} = 0,$$
$$\frac{1-v}{2} A_{,x}(u_{1,y} + v_{1,x}) + A\frac{1-v}{2}(u_{1,xy} + v_{1,xx}) - (1-v) B_{,x} w_{1,xy} - (1-v) B w_{1,xxy}$$
$$+ A(v_{1,yy} + v u_{1,xy}) - B(w_{1,yyy} + v w_{1,xxy}) = 0, \qquad (26)$$
$$B_{,xx}(u_{1,x} + v v_{1,y}) + 2B_{,x}(u_{1,xx} + v v_{1,xy}) + B(u_{1,xxx} + v v_{1,xxy}) + B(v_{1,yyy} + v u_{1,xyy})$$

$$+(1-v)B_{,x}(u_{1,yy}+v_{1,xy})+(1-v)B(u_{1,xyy}+v_{1,xxy})-C_{,xx}(w_{1,xx}+vw_{1,yy})$$

$$-2C_{,x}(w_{1,xxx}+vw_{1,xyy})-2C_{,x}(1-v)w_{1,xyy}-2(1-v)Cw_{1,xxyy}-C(w_{1,xxxx+}$$

$$vw_{1,xxyy})-C(w_{1,yyyy}+vw_{1,xxyy})+(1-v^2)\left[N_x^0 w_{1,xx}+N_y^0 w_{1,yy}+2N_{xy}^0 w_{1,xy}\right]=0$$

In the next step variables *u*, *v* are eliminated in above relation, then the equations of stability Eqn. (26) can be merged into one equation in terms of deflection component *w* and pre-buckling forces only for linear thickness variation, as:

$$(\frac{B^2}{A}-C)\Delta\Delta w_1+(3\frac{B}{A}B_{,x}-2C_{,x})\frac{\partial}{\partial x}\Delta w_1+(\frac{B}{A}B_{,xx}+\frac{B_{,x}^2}{A}-C_{,xx})(w_{1,xx}+$$

$$vw_{1,yy})+(1-v^2)(N_x^0 w_{1,xx}+N_y^0 w_{1,yy}+2N_{xy}^0 w_{1,xy})=0. \quad (27)$$

where

$$\Delta=\frac{\partial^2}{\partial x^2}+\frac{\partial^2}{\partial y^2}. \quad (28)$$

4.2 Solution Method

The method of solving Eq. (27) is based on the series expansion developed by Galerkin [16]. It was originally proposed by Bubnov and sometimes is referred to as the Bubnov-Galerkin method. If the FGM plate is simply supported at all four edges, then the boundary condition are:

$$w_1=0, \quad w_{1,xx}=0 \quad \text{at} \quad x=0,\ a$$

$$w_1=0, \quad w_{1,yy}=0 \quad \text{at} \quad x=0,\ b \quad (29)$$

The proposed deflection function w_1 for this case is assumed to be in the following series form;

$$w_1=B_{mn}\sin(m\pi x/a)\sin(n\pi y/b), \quad (m, n)=1, 2, 3,\ldots \quad (30)$$

where B_{mn} are constant coefficients, and *m*, *n* are the half wave numbers in the *x*, *y* directions, respectively.

In this study, in order to determine the critical load, the Galerkin method is used. According to this method,

$$\iint_{\Omega}\phi(w)R(x,y)dxdy=0, \quad (31)$$

in which R(*x*, *y*) is the residue function and $\phi(w)$ is the weight function.

5. THERMAL BUCKLING ANALYSIS

Consider a plate made of functionally graded material with simply supported edge conditions and subjected to an induced in-plane loading in two directions, as shown in Fig. 1. To obtain the critical thermal loading, the pre-buckling forces should be found. Solving the membrane form of equilibrium equations, results in the following force resultants.

$$N_{x_c}=\frac{E_1}{1-\upsilon_0^2}[\Delta T(E_m\alpha_m+\frac{1}{n+1}(E_m\alpha_{cm}+E_{cm}\alpha_m)+\frac{1}{2n+1}E_{cm}\alpha_{cm})](\frac{1+\upsilon_0}{E_1}c_1x-$$

$$\frac{1+\upsilon_0}{2E_1}c_1a)-\frac{1}{1-\upsilon_0}[\Delta T(E_m\alpha_m+\frac{1}{n+1}(E_m\alpha_{cm}+E_{cm}\alpha_m)+\frac{1}{2n+1}E_{cm}\alpha_{cm})](c_1x+c_2)$$

$$N_{y_c} = \frac{E_1}{1-\upsilon_0^2}\upsilon_0[\Delta T(E_m\alpha_m + \frac{1}{n+1}(E_m\alpha_{cm} + E_{cm}\alpha_m) + \frac{1}{2n+1}E_{cm}\alpha_{cm})](\frac{1+\upsilon_0}{E_1}c_1 x - \frac{1+\upsilon_0}{2E_1}c_1 a) - \frac{1}{1-\upsilon_0}[\Delta T(E_m\alpha_m + \frac{1}{n+1}(E_m\alpha_{cm} + E_{cm}\alpha_m) + \frac{1}{2n+1}E_{cm}\alpha_{cm})](c_1 x + c_2)$$

$$N_{xy_0} = 0 \tag{32}$$

where R is a non-dimensional constant. The resulting equation then may be solved for a series of selected values of R. The simply supported boundary conditions are defined as

$$w_0(x,0) = w_0(x,b) = w_0(0,y) = w_0(a,y) = 0$$

$$p_y(x,0) = p_y(x,b) = p_x(0,y) = p_x(a,y) = 0$$

$$M_y(x,0) = M_y(x,b) = M_x(0,y) = M_x(a,y) = 0 \tag{33}$$

$$u_0^1(x,0) = u_0^1(x,b) = v_0^1(0,y) = v_0^1(a,y) = 0$$

$$v_1^1(x,0) = u_1^1(x,b) = v_1^1(0,y) = v_1^1(a,y) = 0$$

The following approximate solutions are found to satisfy both the differential equations and the boundary conditions

$$u_0^1 = u_{0mn}\cos\frac{m\pi}{a}x\sin\frac{n\pi y}{b}$$

$$u_1^1 = u_{1mn}\cos\frac{m\pi}{a}x\sin\frac{n\pi y}{b} \qquad m, n = 1, 2, 3\ldots.$$

$$v_0^1 = v_{0mn}\sin\frac{m\pi}{a}x\cos\frac{n\pi y}{b} \tag{34}$$

$$v_1^1 = v_{1mn}\sin\frac{m\pi}{a}x\cos\frac{n\pi}{b}y$$

$$w_0^1 = w_{0mn}\sin\frac{m\pi}{a}x\sin\frac{n\pi y}{b}y$$

where m and n are number of half waves in x and y directions, respectively, and $(u_{0mn}, u_{1mn}, \upsilon_{0mn}, \upsilon_{1mn}, \omega_{0mn})$ are constant coefficients. Substituting Eqns. (34) into the stability equations (24) and using the kinematic and constitutive relations yields a system of five homogeneous equations for $u_{0mn}, u_{1mn}, \upsilon_{0mn}, \upsilon_{1mn}$, and $\omega_{0mn,}$ i. e.

$$[k_{ij}]\begin{pmatrix} u_{0mn} \\ v_{0mn} \\ w_{0mn} \\ u_{1mn} \\ v_{1mn} \end{pmatrix} = 0 \tag{35}$$

in which K_{ij} is a symmetric matrix with the components

$$k_{11} = E_1[(\frac{m\pi}{a})^2 + \frac{1-\upsilon_0}{2}(\frac{n\pi}{b})^2]$$

$$k_{12} = E_1\frac{(1+\upsilon_0)}{2}(\frac{m\pi}{a})(\frac{n\pi}{b})$$

$$k_{14} = (E_2 - \frac{4E_4}{3h^2})[(\frac{m\pi}{a})^2 + \frac{1-\upsilon_0}{2}(\frac{n\pi}{b})^2]$$

$$k_{15} = (\frac{E_2}{2} - \frac{2E_4}{3h^2})(1+\upsilon_0)(\frac{m\pi}{a})(\frac{n\pi}{b})$$

$$k_{21} = k_{12}$$

$$k_{22} = E_1[\frac{1-\upsilon_0}{2}(\frac{m\pi}{a})^2 + (\frac{n\pi}{b})^2]$$

$$k_{23} = -\frac{4E_4}{3h^2}[((\frac{m\pi}{a})^2(\frac{n\pi}{b}) + (\frac{n\pi}{b})^3]$$

$$k_{24} = (\frac{E_2}{2} - \frac{2E_4}{3h^2})(1+\upsilon_0)(\frac{m\pi}{a})(\frac{n\pi}{b})$$

$$k_{25} = (2 - \frac{4E_4}{3h^2})[\frac{1-\upsilon_0}{2}(\frac{m\pi}{a})^2 + (\frac{n\pi}{b})^2]$$

$$k_{31} = k_{13}$$

$$k_{32} = k_{23}$$

$$\bar{k}_{33} = \frac{16E_7}{9h^4}[(\frac{m\pi}{a})^2 + (\frac{n\pi}{b})^2]^2 - (\frac{4E_3}{h^2} - \frac{E_1}{2} - \frac{8E_5}{h^2})$$

$$(1-\upsilon_0)[(\frac{m\pi}{a})^2 + (\frac{n\pi}{b})^2] + (1-\upsilon_0^2)]N_{x_0}(\frac{m\pi}{a})^2 + N_{y_0}(\frac{n\pi}{b})^2]$$

$$k_{34} = -(\frac{4E_3}{h^2} - \frac{E_1}{2} - \frac{8E_5}{h^4})(1-\upsilon_0)(\frac{m\pi}{a}) +$$

$$(\frac{16E_7}{9h^4} - \frac{4E_5}{3h^2})[(\frac{m\pi}{a})^3 + (\frac{m\pi}{a})(\frac{n\pi}{b})^2] \quad (36)$$

$$k_{35} = -(\frac{4E_3}{h^2} - \frac{E_1}{2} - \frac{8E_5}{h^4})(1-\upsilon_0)(\frac{n\pi}{b}) + (\frac{16E_7}{9h^4} - \frac{4E_5}{3h^2})$$

$$[(\frac{m\pi}{a})^2(\frac{m\pi}{b}) + (\frac{n\pi}{b})^3]$$

$$k_{41} = -k_{14}$$

$$k_{42} = -k_{24}$$

$$k_{43} = -k_{34}$$

$$k_{44} = (\frac{8E_5}{3h^2} - \frac{16E_7}{9h^4} - E_3)[(\frac{m\pi}{a})^2 + \frac{1-\upsilon_0}{2}(\frac{n\pi}{b})^2] - (\frac{E_1}{2} - \frac{4E_3}{h^2} + \frac{8E_5}{h^4})(1-\upsilon_0)$$

$$k_{45} = (\frac{4E_5}{3h^2} - \frac{E_3}{2} - \frac{8E_7}{9h^2}E_3)(\frac{m\pi}{a})(\frac{n\pi}{b})$$

$$k_{52} = -k_{25}$$

$$k_{53} = -k_{35}$$

$$k_{51} = -k_{15}$$

$$k_{54} = k_{45}$$

$$k_{55} = (\frac{8E_5}{3h^2} - \frac{16E_7}{9h^4} - E_3)[\frac{1-\upsilon_0}{2}(\frac{m\pi}{a})^2 + (\frac{n\pi}{b})^2] (\frac{E_1}{2} - \frac{4E_3}{h} + \frac{8E_5}{h^4})(1-\upsilon_0)$$

Substituting pre-bucking forces from Eqs. The relation of K_{33} and setting $\left| K_{ij} \right| = 0$ to obtain the nonzero solution, the value of the F_x is found as

$$\Delta T = \frac{2b^2 k_d}{\pi^2 (1+\upsilon_0)(c_1 a + 2c_2)\eta^*[(\frac{mb}{a})^2 + n^2]k_c} \tag{37}$$

where

$$\eta^* = [E_m\alpha_m + (E_m\alpha_{cm} + \alpha_m E_{cm})/(n+1) + E_{cm}\alpha_{cm}/(2n+1)] \tag{38}$$

$$k_d = \det\left|k_{ij}\right|$$

$$k_c = k_{15}k_{24}k_{42}k_{51} + k_{12}k_{25}k_{44}k_{51} + k_{14}k_{22}k_{45}k_{51} + k_{14}k_{25}k_{41}k_{52} + k_{15}k_{21}k_{44}k_{52}$$

$$k_{15}k_{21}k_{44}k_{52} + k_{11}k_{24}k_{45}k_{52} + k_{15}k_{22}k_{41}k_{54} + k_{11}k_{25}k_{42}k_{54} + k_{12}k_{21}k_{45}k_{54}$$

$$k_{12}k_{24}k_{41}k_{55} + k_{14}k_{21}k_{42}k_{55} + k_{11}k_{22}k_{44}k_{55} - k_{14}k_{25}k_{42}k_{51} - k_{15}k_{22}k_{44}k_{51}$$

$$k_{12}k_{24}k_{45}k_{51} - k_{15}k_{24}k_{41}k_{52} - k_{11}k_{25}k_{44}k_{52} - k_{14}k_{21}k_{45}k_{52} - k_{12}k_{25}k_{41}k_{54}$$

$$- k_{15}k_{21}k_{42}k_{54} - k_{11}k_{22}k_{45}k_{54} - k_{14}k_{22}k_{41}k_{55} - k_{11}k_{24}k_{42}k_{55} - k_{12}k_{21}k_{44}k_{55}$$

In this section, the closed form solutions of Eq. (27) for three types of thermal loading conditions are presented. The plate is assumed to be simply supported in all edges and rigidity fixed against any extension.

Case A. *Uniform Temperature Rise*

The initial uniform temperature of the plate T_i is uniformly raised to a final value T_f, such that the plate buckles. To find the critical buckling temperature difference i.e., $\Delta T_A = T_f - T_i$, the pre- buckling thermal forces, should be found. Solving the membrane form of equilibrium equations i.e., Eq. (18), gives the pre- buckling force resultants as;

$$N_x^0 = -\frac{\Delta T_A G_1}{2(1-v)}(c_1 a + 2c_2),\ N_y^0 = -\frac{\Delta T_A G_1}{2(1-v)}(c_1 a + 2c_2) - \Delta T_A G_1 c_1 x, \qquad N_{xy}^0 = 0. \tag{39}$$

where

$$G_1 = \left[E_m \alpha_m + (E_m \alpha_{cm} + E_{cm} \alpha_m)/(k+1) + E_{cm} \alpha_{cm}/(2k+1)\right], \tag{40}$$

By substituting this type of loading condition into Eqns. (16), one can get;

$$\Theta = \Delta T_A . \xi . G_1 \tag{41}$$

Substituting Eqn. (39) into Eqn. (27), the buckling equation for this type of loading is obtained as;

$$\begin{aligned}&(\frac{B^2}{A} - C)\Delta\Delta w_1 + (3\frac{B}{A}B_{,x} - 2C_{,x})\frac{\partial}{\partial x}\Delta w_1 + (\frac{B}{A}B_{,xx} + \frac{B_{,x}^2}{A} - C_{,xx})(w_{1,xx} + v w_{1,yy})\\ &-(1-v^2)\Delta T_A G_1\left[(\frac{c_1 a}{2(1-v)} + \frac{c_2}{1-v})w_{1,xx} + (c_1 x + \frac{v c_1 a}{2(1-v)} + \frac{c_2}{1-v})w_{1,yy})\right] = 0.\end{aligned} \tag{42}$$

For the assumed displacement field given by Eqn. (30) the result of Eqns. (31), (42) becomes;

$$\begin{aligned}&\frac{\pi^2 B_{mn}}{a^4 b^4}\int_0^b \int_0^a \left\{\pi^2 (m^2 b^2 + n^2 a^2)^2 (\tilde{B}^2/\tilde{A} - \tilde{C})(c_1 x + c_2)^3 \sin(m\pi x/a)\sin(n\pi y/b) + \right.\\ &6(\tilde{B}^2/\tilde{A} - \tilde{C})mab^2(m^2 b^2 + n^2 a^2)c_1(c_1 x + c_2)^2 \cos(m\pi x/a)\sin(n\pi y/b) +\\ &6(\tilde{B}^2/\tilde{A} - \tilde{C})(m^2 b^2 + v n^2 a^2)a^2 b^2 (c_1^3 x + c_1^2 c_2)\sin(m\pi x/a)\sin(n\pi y/b) +\\ &(1-v^2)\Delta T_A G_1\left[(c_1 a/2(1-v^2) + c_2/(1-v))(m/a)^2 + (c_1 x + v c_1 a/2(1-v) + c_2/(1-v))\right.\\ &\left.\left.(n/b)^2\right]a^4 b^4 \sin(m\pi x/a)\sin(n\pi y/b)\right\}\sin(m\pi x/a)\sin(n\pi y/b)dxdy = 0\end{aligned} \tag{43}$$

After carrying out the integration, one would get;

$$\Delta T_A = H.\left[(mb/a)^2 + n^2\right] \tag{44}$$

in which,

$$\begin{aligned}H = \frac{\pi^2}{b^2(1+v)(c_1 a/2 + c_2)G_1}&\left\{(\tilde{C} - \tilde{B}^2/\tilde{A})(c_1^3 a^3/4 + c_1^2 c_2 a^2 + 3c_1 c_2^2 a/2 + c_2^3)\right.\\ &\left.+ 6(\tilde{C} - \tilde{B}^2/\tilde{A})\frac{a^2 b^2 (m^2 b^2 + v n^2 a^2)}{\pi^2 (m^2 b^2 + n^2 a^2)^2}(c_1^3 a/2 + c_1^2 c_2)\right\}.\end{aligned} \tag{45}$$

where,

$$\tilde{A} = E_m + E_{cm}/(k+1), \qquad \tilde{B} = E_{cm}k/(2k+2)(2k+1), \tag{46}$$
$$\tilde{C} = E_m/12 + E_{cm}\left[1/(k+3) - 1/(k+2) + 1/(4k+4)\right].$$

The critical buckling load ΔT_A^{cr} can be obtained for different values of *m*, *n* such that it minimizes Eq.(44). Apparently, when minimization methods are used, the critical buckling load, ΔT_A^{cr}, is obtained for $m = n = 1$, thus;

$$\Delta T_A^{cr} = \frac{\pi^2\left[(b/a)^2+1\right]}{b^2(1+v)(c_1 a/2 + c_2)G_1}\left\{(\tilde{C} - \tilde{B}^2/\tilde{A})(c_1^3 a^3/4 + c_1^2 c_2 a^2 + 3c_1 c_2^2 a/2 + c_2^3)\right.$$
$$\left. + 6(\tilde{C} - \tilde{B}^2/\tilde{A})\frac{a^2 b^2 (b^2 + v a^2)}{\pi^2 (b^2+a^2)^2}(c_1^3 a/2 + c_1^2 c_2)\ \right\}. \tag{47}$$

When $c_1 = 0$, Eq. (40) represents the critical thermal buckling load, ΔT_A^{cr} of a FGM plate with constant thickness $c_2 = h$, i.e. ;

$$\Delta T_{Ai}^{cr.} = \frac{\pi^2\left[(\frac{b}{a})^2+1\right]}{b^2(1+v)hG_1}\left(\frac{A.C - B^2}{A}\right). \tag{48}$$

The result given in Eq. (41) is exactly the same as the one obtained by reference [9].

Case B. *Linear Temperature variation across the thickness*

For a functionally graded plate, usually the temperature change is not uniform where the temperature level is much higher at the ceramic side than that in the metal side of the plate. In this case, the temperature variation through the thickness is given by;

$$T(z) = \frac{\Delta T_B}{\xi}(z + \frac{\xi}{2}) + T_m \tag{49}$$

in which

$$T\Big|_{z=\frac{\xi}{2}} = T_c,$$
$$T\Big|_{z=-\frac{\xi}{2}} = T_m,$$
$$\Delta T_B = T_c - T_m \tag{50}$$

T_c and T_m denote the temperature level at the top (ceramic side) and the bottom (metal side) surfaces, respectively. The pre-buckling forces now can be obtained by solving the membrane form of equilibrium equations, i.e. Eqn. (18) and this gives;

$$N_x^0 = -\frac{c_1 a/2 + c_2}{1-v}(\Delta T_B G_2 + T_m G_1),$$
$$N_y^0 = -[c_1 x + \frac{v c_1 a}{2(1-v)} + \frac{c_2}{1-v}](\Delta T_B G_2 + T_m G_1), \qquad N_{xy}^0 = 0. \tag{51}$$

in which

$$G_2 = [E_m\alpha_m / 2 + (E_m\alpha_{cm} + E_{cm}\alpha_m)/(k+2) + E_{cm}\alpha_{cm}/(2k+2)], \quad (52)$$

Substituting Eqn. (51) into Eqn. (27), the buckling equation for this case of loading is obtained;

$$(\frac{B^2}{A} - C)\Delta\Delta w_1 + (3\frac{B}{A}B_{,x} - 2C_{,x})\frac{\partial}{\partial x}\Delta w_1 + (\frac{B}{A}B_{,xx} + \frac{B_{,x}^2}{A} - C_{,xx})(w_{1,xx} + vw_{1,yy)}$$
$$-(1-v^2)[(\frac{c_1 a}{2(1-v)} + \frac{c_2}{1-v})w_{1,xx} + (c_1 x + \frac{vc_1 a}{2(1-v)} + \frac{c_2}{1-v})w_{1,yy})](\Delta T_B G_2 + T_m G_1) = 0 \quad (53)$$

Following similar steps to that given in case A, the buckling load for case B is;

$$\Delta T_B^{cr} = \frac{\pi^2[(b/a)^2+1]}{b^2(1+v)(c_1 a/2 + c_2)G_2}\{(\tilde{C} - \tilde{B}^2/\tilde{A})(c_1^3 a^3/4 + c_1^2 c_2 a^2 + 3c_1 c_2^2 a/2 + c_2^3)$$
$$+6(\tilde{C} - \tilde{B}^2/\tilde{A})\frac{a^2 b^2(b^2 + va^2)}{\pi^2(b^2+a^2)^2}(c_1^3 a/2 + c_1^2 c_2)\ \} - \frac{T_m G_1}{G_2} \quad (54)$$

When $c_1 = 0$, Eq. (47) is reduced to the critical buckling load, $\Delta T_{B_i}^{cr}$ of a FGM plate, with constant thickness $c_2 = h$, which is;

$$\Delta T_B^{cr} = \frac{\pi^2[(b/a)^2+1]}{b^2(1+v)hG_2}(\frac{A.C - B^2}{A}) - \frac{T_m G_1}{G_2} \quad (55)$$

The result given in Eq. (55) is exactly the same as the one obtained by reference.

Case C. *Buckling of FGM plate under Non-linear temperature variation across the Thickness*
In this section, the governing differential equation for the temperature distribution through the thickness is given by one- dimensional Fourier equation under steady state heat condition as;

$$\frac{d}{dz}\left[k(z)\frac{dT}{dz}\right] = 0, \quad (56)$$

where $k(z)$ is the coefficient of thermal conduction. Similar to what was considered for the variation of the elastic modulus and coefficient of thermal expansion, here the coefficient of the heat conduction is also assumed to change according to a power law in terms of *z* as represented by Eq. (49).

By inserting Eq. (49) into Eq. (56) one would get;

$$\frac{d^2T}{dm^2} + \frac{kK_{cm}m^{k-1}}{K_m + K_{cm}m^k}\frac{dT}{dm} = 0, \quad (57)$$

in which

$$m = \frac{2z + \xi}{2\xi} \quad (58)$$

and the boundary conditions across the plate thickness are;

$$T = T_{c,} \qquad m = 1, \tag{59}$$

$$T = T_{m,} \qquad m = 0,$$

The solution of Eq. (50) can be obtained by means of polynomial series. Taking the first seven terms of the series;

$$T = \hat{C}_0 + \hat{C}_1 m + \hat{C}_2 m^2 + \hat{C}_3 m^3 + \hat{C}_4 m^4 + \hat{C}_5 m^5 + \hat{C}_6 m^6, \tag{60}$$

In which $\hat{C}_i$ are constant coefficients to be evaluated. After substituting Eqn. (60) Into Eqn. (57), imposing the boundary conditions and repeating similar above mathematical manipulations, one can get;

$$T(z) = T_m + \frac{\Delta T_c}{\hat{C}_0} L(z). \tag{61}$$

in which

$$\hat{C}_0 = 1 - \frac{K_{cm}}{(k+1)K_m} + \frac{K_{cm}^2}{(2k+1)K_m^2} - \frac{K_{cm}^3}{(3k+1)K_m^3} + \frac{K_{cm}^4}{(4k+1)K_m^4} - \frac{K_{cm}^5}{(5k+1)K_m^5},$$

$$L(z) = (\frac{2z+\xi}{2\xi}) - \frac{K_{cm}}{(k+1)K_m}(\frac{2z+\xi}{2\xi})^{k+1} + \frac{K_{cm}^2}{(2k+1)K_m^2}(\frac{2z+\xi}{2\xi})^{2k+1}$$

$$- \frac{K_{cm}^3}{(3k+1)K_m^3}(\frac{2z+\xi}{2\xi})^{3k+1} + \frac{K_{cm}^4}{(4k+1)K_m^4}(\frac{2z+\xi}{2\xi})^{4k+1} - \frac{K_{cm}^5}{(5k+1)K_m^5}(\frac{2z+\xi}{2\xi})^{5k+1} \tag{62}$$

$$\Delta T_c = T_c - T_m$$

The pre-buckling resultants loads for this case can be obtained by solving the membrane effects of the equilibrium equations i.e., (Eq. (18)) which yields;

$$N_x^0 = -\frac{c_1 a/2 + c_2}{1-v}(\Delta T_c G_3 + T_m G_1)$$

$$N_y^0 = -[c_1 x + \frac{v c_1 a}{2(1-v)} + \frac{c_2}{1-v}](\Delta T_c G_3 + T_m G_1)$$

$$N_{xy}^0 = 0 \tag{63}$$

Substituting $T(z)$ in Eqns. (16) and calculating for Θ ;

$$\Theta = T_m \int_{-\xi/2}^{\xi/2} E(z).\alpha(z)dz + \frac{\Delta T_c}{\hat{C}_0} \int_{-\xi/2}^{\xi/2} L(z).E(z).\alpha(z)dz \tag{64}$$

By substituting Eqn. (63) into Eqn. (27) the buckling for this case of loading is obtained. By performing an analysis similar to that done for the case A, the thermal critical buckling load, ΔT_c^{cr} for case C is determined to be.

$$\Delta T_C^{cr} = \frac{\pi^2[)b/a)^2 + 1]}{b^2(1+v)(c_1 a/2 + c_2)G_3}\Big\{(\tilde{C} - \hat{B}^2/\tilde{A})(c_1^3 a^3/4 + c_1^2 c_2 a^2 + 3c_1 c_2^2 a/2 + c_2^3)$$

$$+ 6(\tilde{C} - \tilde{B}^2/\tilde{A})\frac{a^2 b^2 (b^2 + v a^2)}{\pi^2 (b^2 + a^2)^2}(c_1^3 a/2 + c_1^2 c_2)\ \Big\} - \frac{T_m G_1}{G_3}, \tag{65}$$

in which

$$G_3 = 1/\hat{C}_0\{E_m\alpha_m[1/2 - K_{cm}/(k+2)(k+1)K_m + K_{cm}^2/(2k+2)(2k+1)K_m^2 - K_{cm}^3/(3k+1)(3k+2)K_m^3 + K_{cm}^4/(4k+2)(4k+1)K_m^4 - K_{cm}^5/(5k+2)(5k+1)K_m^5] + (E_m\alpha_{cm} + E_{cm}\alpha_m)[1/(k+2) - K_{cm}/(2k+2)(k+1)K_m + K_{cm}^2/(3k+2)(2k+1)K_m^2 - K_{cm}^3/(4k+2)(3k+1)K_m^3 + K_{cm}^4/(5k+2)(4k+1)K_m^4 - K_{cm}^5/(6k+2)(5k+1)K_m^5] + E_{cm}\alpha_{cm}[1/(2k+2) - K_{cm}/(3k+2)(k+1)k_m + K_{cm}^2/(2k+1)(4k+2)K_m^2 - K_{cm}^3/(5k+2)(3k+1)K_m^3 + K_{cm}^4/(6k+2)(4k+1)K_m^4 - K_{cm}^5/(7k+2)(5k+1)K_m^5]\} \quad (66)$$

When $c_1 = 0$, Eq. (65) will be reduced to the critical buckling load, $\Delta T_{C_i}^{cr}$ of a FGM plate with constant thickness $c_2 = h$, which is;

$$\Delta T_{C_i}^{cr} = \frac{\pi^2(A.C - B^2)}{b^2(1+v)A.h.G_3}[(b/a)^2 + 1] - \frac{T_m G_1}{G_3} \quad (67)$$

The result given in Eq. (67) is exactly the same as the one obtained by reference

6. RESULTS AND DISCUSSIONS

In this paper, the pre-buckling and critical thermal buckling loads of a thin FGM plate with variable thickness are obtained. The analysis on thickness variation of the plate is carried out for two different types of linear heat conduction variations both in *x*- and *y*-directions. In order to conduct further calculations, a functionally graded material consisting of aluminum and alumina is considered in which the Young's modulus, conductivity, and the coefficient of thermal expansion, are: for aluminum, $K_m = 204w/mk$, $\alpha_m = 23\times10^{-6}(1/^0C)$ $E_m = 70GPa$ and for alumina, $E_c = 380GPa$, $K_c = 10.4w/mk$, $\alpha_c = 7.4\times10^{-6}(1/^0C)$. The Poisson's ratio $\nu_m = \nu_c = 0.3$ are taken for both.

The graphs of critical temperature change ΔT^{cr} versus the aspect ratio b/a , c_1, and volume fraction exponent *k* for two types of linear change of thickness at *x*, *y* directions and three types of thermal loading are shown in Figs. (2- 4). To begin with, the variation of the critical temperature difference ΔT_A^{cr} of FGM plate under uniform temperature rise vs. different geometric parameter (b/a), for different volume fraction exponents is analyzed. The variations are plotted in Fig. (2). By comparing the values of the critical temperature differences ΔT_A^{cr} calculated with using linear change in the plate thickness in the *x*-direction are lower than in *y*-direction. For the plate of FGM material ($k > 0$), the critical temperature difference of buckling for thickness variation in the *y*-direction is higher than in *x*-direction. Therefore, the plate resistance against buckling for all kinds of thermal loads is higher in the *y*-direction when the plate has a variable thickness.

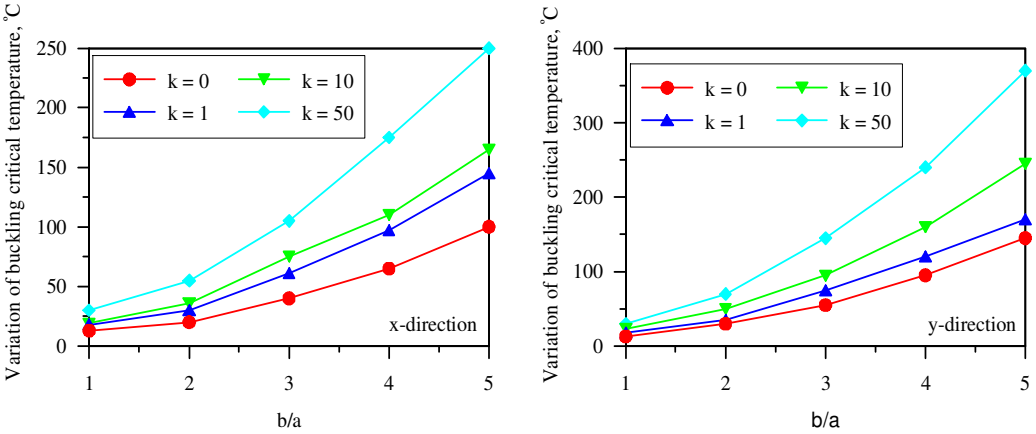

FIGURE 2: Variation of buckling critical temperature (Case A)

Figure 2 is shown the variation of buckling critical temperature gradient against *b*/*a* for different functionally graded material plate with linear thickness change in *x*-direction and *y*-direction under uniform temperature rise.

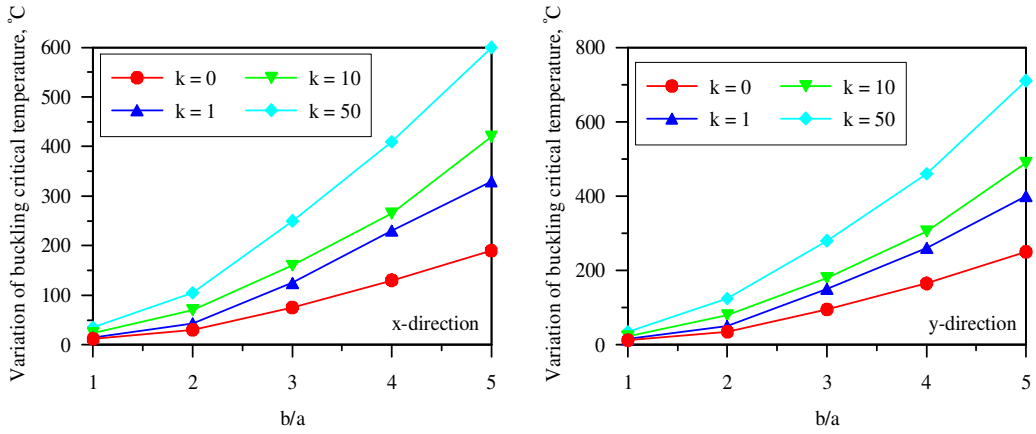

FIGURE 3: Variation of buckling critical temperature (Case B)

Figure 3 is illustrated the variation of buckling critical temperature gradient against material index *k* for different FGM plate with linear thickness change in both *x* and *y* directions under linear temperature across thickness.

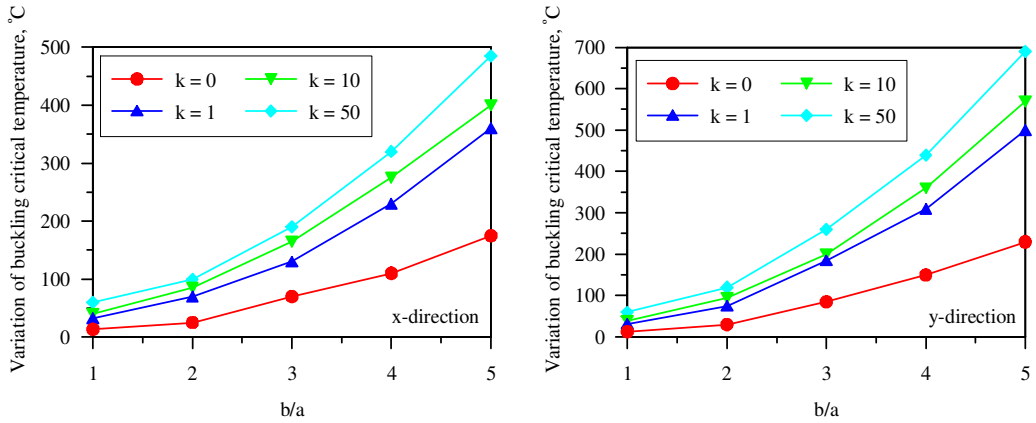

FIGURE 4: Variation of buckling critical temperature (Case C)

Figure 4 is shown the variation of the buckling critical temperature gradient against material index *k* for different FGM plate with linear thickness change in both *x* and *y* directions under non-linear temperature across thickness.

As an overview of all the above cases, one can say that the critical buckling temperature gradient of a homogeneous ceramic plate ($k = 0$), is higher than the FGM plate. This result is justifiable, because the coefficient of the thermal expansion of ceramic plate is lower than the FGM plate. Referring to Figs. (2- 4) it can be said that the difference between variation of critical buckling temperature gradient of the homogeneous ceramic plate ($k = 0$) and the FGM plate ($k > 0$) is not significantly high. Contrary to this, for the other types of loading the difference is much higher; therefore, this type of loading results in a more acceptable low thermal stress distribution in the plate.

In Figs. 2- 4, it is found that the critical temperature difference of FGM plate is higher than that of the fully metallic isotropic plate but lower than that of the fully ceramic isotropic plate. In addition, the critical temperature change decreases as the volume fraction exponent *k* is increased. In all cases, the critical temperature difference increases, when the geometric parameter *b*/*a* is increased.

7. CONCLUSIONS

In the present paper, equilibrium and stability equations for a simply supported rectangular functionally graded plate with its thickness varying along both the *x*- and y-axis as a linear function, under thermal loading are obtained according to the classical plate theory. The critical buckling temperature gradient for three different types of thermal loading is derived using Galerkin method. From the results, primarily one can conclude that the thickness change causes reinforcement of resistance of buckling.

8. REFERENCES

1. Brush DO, Almroth BO. Bucking of Bars, Plates and Shells. New York: McGraw-Hill, 1975.

2. Timoshenko S, Woinowsky-Krieger S. Theory of plates and shells (second ed). New York: McGraw-Hill, 1959.

3. Zheng XJ. The theory and application for large deflection of Circular plate. Ji-Lin Science Technology press. Chinese: Chang-Chun, 1990.

4. Yamanouchi M, Koizumi M, Shiota I. Proceedings of the First International Symposiumon Functionally Gradient Materials. Japan, 1990; 273-281.

5. Koizumi M. The concept of FGM, Ceram:Trans., Funct. Grad Mater 1993;34:3-10.

6. Abrate S. Functionally graded material behave like homogeneous plates. Composites Part B: Engineering 2008;39(1):151–158.

7. Chen CS, Chen TJ, Chien RD. Nonlinear vibration analysis of an initially stressed functionally graded plate. Thin-Walled Structures 2006;44(8):844–851.

8. Chen CS, Tan AH. Imperfection sensitivity in the nonlinear vibration of initially stresses functionally graded plates. Composite Structures 2007;78(4):529–536.

9. Chi SH, Chung YL. Mechanical behavior of functionally graded material under transverse load. International Journal of Solids and Structures 2006;43(13):3657–3674.

10. Chi SH, Chung YL. Mechanical behavior of functionally graded material. International Journal of Solids and Structures 2006;43(13):3675–3691.

11. Ghannadpour SAM, Alinia MM. Large deflection behavior of functionally graded plates under pressure loads. Composite Structures 2006;75(1–4):67–71.

12. Hsieh JJ, Lee LT. An inverse problem for a functionally graded elliptical. International Journal of Solids and Structures 2006;43(20):5981–5993.

13. Huang CS, Chang MJ. Corner stress singularities in an FGM thin plate. International Journal of Solids and Structures 2007;44(9):2802–2819.

14. Najafizadeh MM, Eslami MR. Thermoelastic stability of circular plates composed of functionally graded materials under uniform radial compression. International Journal of Mechanical Sciences 2002;44(12):2479–93.

15. Navazi HM, Haddadpour H, Rasekh M. An analytical solution for nonlinear cylindrical bending of functionally graded plates. Thin-Walled Structures 2006;44(11):1129–1137.

16. Shariat BAS, Eslami MR. Thermal buckling of imperfect functionally graded plates. International Journal of Solids and Structures 2006;43(14–15):4082–4096.

17. Sundararajan N, Prakash T, Ganapathi M. Influence on functionally graded material on buckling of skew plates under mechanical loads. Finite elements in analysis and design 2005;42(2):152–168.

18. Woo J, Meguid SA, Ong LS. Nonlinear free vibration behavior of functionally graded plates. Journal of Sound and Vibration 2006;289(3):595–611.

19. Morimoto T, Tanigawa Y, Kawamura R. Thermal buckling analysis of in homogeneous rectangular plate. International Journal of Mechanical Sciences 2006;48(9):926–937.

20. Li SR, Zhang JH, Zhao YG. A theoretical analysis of FGM thin plates. Thin-Walled Structures 2007;45(5):528–536.

21. Wu L. Thermal buckling of a simply supported moderately thick rectangular FGM plate. Composite Structures 2004;64:21–8.

22. Chen XL, Liew KM. Buckling of rectangular functionally graded material plates subjected to nonlinearly distributed in-plane edge loads. Smart Materials and Structures 2004;13:1430–7.

23. Yamanouchi M., Koizumi M, Shiota I. in: Proc. First Int. Symp.Functionally Gradient Materials, Sendai, Japan 1990.

24. Fukui Y. Fundamental investigation of functionally gradient material manufacturing system using centrifugal force. Int. J. Japanese Soci. Mech. Eng. 1991;3:144-148.

25. Koizumi M. FGM Activites in Japan, Composite: 1997;28(1):1-4.

26. Praveen GN, Reddy J N. Nonlinear transient thermo elastic analysis of functionally graded ceramic metal plates. International Journal of Solids and Structures 1998;35:4457-4476.

27. Shariat BAS, Eslami MR. Buckling of thick functionally graded plates under mechanical and thermal load. Compos Struct 2007;78(3):433-439

28. Javaheri R, Eslami MR. Buckling of functionally graded plates under in-plane compressive loading. ZAMM 2002;82(4):277-283.

Transient Stability Assessment of the Nigerian 330kV Network

Prof Anthony O. Ibe aoibeofuniport@yahoo.com
Faculty of Engineering Department of Electrical/Electronic
University of Port Harcourt.
Port Harcourt, 00234, Nigeria

Ameze Odia amezeodia@yahoo.com
Faculty of Engineering/Department of Electrical/Electronic
University of Port Harcourt.
Port Harcourt, 00234, Nigeria

Abstract

Transient stability limit of the Nigerian 330kV power system was assessed in terms of its ability to maintain synchronism among the generating units. The Power (angle) stability limit and voltage stability limit, before, during and after system changes or disturbances were also assessed. The 330kV transmission network was analyzed using the Runge Kutta Method to determine the critical clearing angle and the corresponding critical clearing time. It was observed that a critical clearing angle of 12.85˚ with critical clearing time of 0.1s gave a more stable result than a critical clearing angle of 166.376˚ with a corresponding critical clearing time of 0.363s. It was therefore recommended that faults on the network be cleared as quickly as possible so as to maintain the system stability.

Keywords: Power (angle) stability limit, voltage stability limit, synchronism, 330kV Power System, Runge Kutta Method.

1. INTRODUCTION

The 330kV transmission system connects the generating stations and major load centers [4]. Interruptions in this network may hinder the flow of power to the load. Also, the cost of losing synchronism through transient instability is extremely high. This makes transient stability studies significant because it deals with the effects of large, sudden disturbances such as the occurrence of a fault, sudden outage of a line or the sudden application or removal of load.

Consequences of power system instability can be seen in the scenario that occurred in Lagos Nigeria at Murtala Mohammed international airport on the 10th of May 2010. Hundreds of passengers were stranded at the international wing due to power outages that paralyzed operations. This problem was as a result of short circuit fault, which led to the tripping of power supply to some of the areas in the terminal building. The fault lasted for more than three hours. Finally, power was restored after the fault had been cleared [2].

The quality of electricity supply is measured in terms of the voltage, frequency, lack of interruptions to supply of power and ability to withstand faults and recover quickly. It is a well known fact that the Nigerian power supply is inadequate and epileptic in nature and suffers a lot of outages. It is therefore important to assess the Transient and Voltage stability limits of the Nigerian 330kV power system before, during and after system changes or disturbances.

2. MATERIALS AND METHOD

The equation of central importance in power system stability analysis is the rotational inertia equation that describes the effect of unbalance between the electromagnetic torque and the mechanical torque of the individual machines. This equation is known as the *swing equation* and it is given by:

$$M\frac{d^2\delta}{dt^2} = P_m - P_e = P_a$$

Where

M = angular momentum (Joule-sec/rad)
P_{mec} = Input mechanical power (W)
P_{elec} = Output electrical power (W)
P_a = Net accelerating power (W)

This equation is a non linear differential equation that can be solved using Runge Kutta method [5]. Analysis of transient stability of the Nigerian 330kV network involves the computation of nonlinear dynamic responses to large disturbances. The occurrence of fault is followed by the isolation of the faulted element by a protective device.

Determination of Time Response Using the Runge-Kutta Method:
The general formula for Runge Kutta method is

$$\delta_{n+1} = \delta_n + \Delta\delta$$
$$= \delta_n + \frac{k_1 + k_2}{2} \ldots\ldots\ldots (3.1)$$

Where

$$k_1 = f(\delta_n, t_n)\Delta t$$
$$k_2 = f(\delta_n + k_1, t_n + \Delta t)\Delta t$$

This method is equivalent to considering first and second derivative terms in the Taylor series. Hence it is a second order Runge Kutta Method.
The system operating condition with quantities expressed in per unit is specified as follows:

$\Delta t = 1.0s$, and $\Delta\omega = 0$ at pre fault. Let the turbine power P_m = 1.0, and H = *3.5 MW.s/MVA*

The critical clearing angle was found to be $\delta_{cr} = 166.376^{\circ}$
The corresponding critical clearing time is derived from the swing equations and is given by:

$$t_{cr} = \sqrt{(\delta_{cr} - \delta_0)\frac{4H}{\omega_0 P_m}}$$

Thus, the corresponding critical clearing time gotten from this equation is 0.363secs.

One Machine System connected to the National grid.
A one machine system connected to an infinite bus bar is first considered, using Jebba power station as a case study. The power transfer can be formulated as follows:

$$P_e = \frac{|E||V|}{X_e}\sin\delta \quad (MW) \ldots\ldots 3.2$$

and

$$P_m = P_{mo} = constant \ldots\ldots\ldots (3.3)$$

At

$$\delta = 90^{\circ}$$
$$P_e = P_{e,max}$$

Therefore,

$$P_{e,max} = \frac{|E||V|}{X_{eq}} \ldots\ldots\ldots (3.4)$$

3. RESULTS AND DISCUSSIONS

Two fault clearing times are specified in this study:
1. A fault clearing time of 0.363secs with a corresponding critical clearing angle of 166.376° is specified.
2. A fault clearing time of 0.1sec with a corresponding critical clearing angle of 12.85° is specified.

Voltage Stability Limit
According to the Grid Code [3], the power system operator endeavours to control the different bus bar voltages to be within the voltage control range of $330kV \pm 5\%$. Therefore, generators must be adjusted during the day to maintain voltages within this secure range. In fact, most generators are designed to have automatic voltage regulators [1]. Also, transmission lines should not be operated too close to their stability limit. There must be a margin to allow for disturbances.

The following plots in figures 1 and 2 demonstrate this.

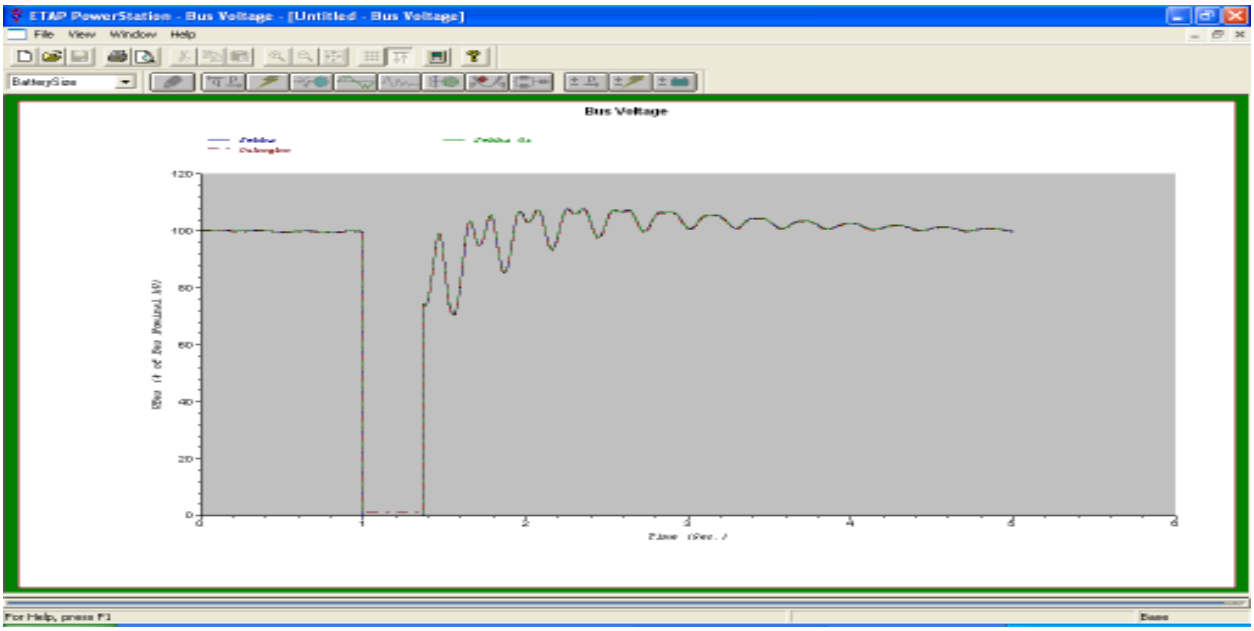

FIGURE 1: Bus Voltage at 0.363 secs

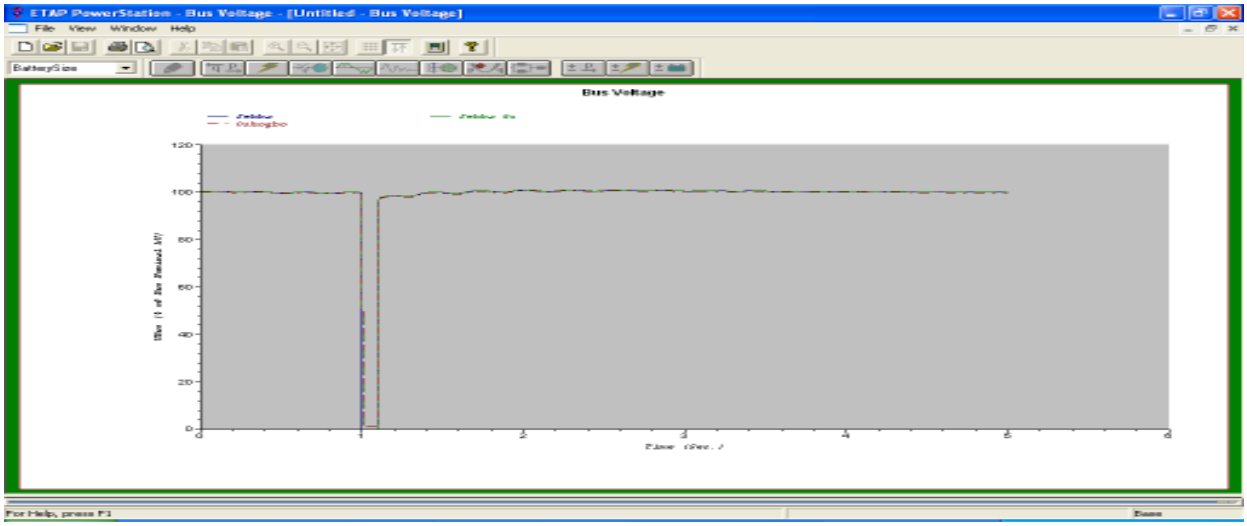

FIGURE 2: Bus Voltage at 0.1 secs

The Voltage stability limit, before, during and after system changes or disturbances is demonstrated in tables 1-3.

Time (s)	Bus Voltage (%) at t_{cr} 0f 0.363s	Bus Voltage (%) at t_{cr} of 0.1s
0.000	100.22	100.22
0.050	100.27	100.27
0.100	100.42	100.42
0.150	100.38	100.38
0.200	100.12	100.12
0.250	100.09	100.09
0.300	100.21	100.21
0.350	100.24	100.24
0.400	100.13	100.13
0.450	99.87	99.87
0.500	99.68	99.68
0.550	99.79	99.79
0.600	99.98	99.98
0.650	100.03	100.03
0.700	99.91	99.91
0.750	99.70	99.70

0.800	99.62	99.62
0.850	99.77	99.77
0.900	99.94	99.94

TABLE1: Transient Stability Analysis for Bus Voltages at Pre Fault

Time (s)	**Bus Voltage (%) at t_{cr} 0f 0.363s**	**Bus Voltage (%) at t_{cr} of 0.1s**
1.000	99.85	99.85
1.050	0.00	0.00
1.100	0.00	0.00
1.150	0.00	98.29
1.200	0.00	98.67
1.250	0.00	98.34
1.300	0.00	98.26
1.350	0.00	99.08
1.363	0.00	99.32

TABLE 2: Transient Stability Analysis for Bus Voltages during Fault

Time (s)	**Bus Voltage (%) at t_{cr} 0f 0.363s**	**Bus Voltage (%) at t_{cr} of 0.1s**
1.400	76.64	99.81
1.450	96.29	100.06
1.500	87.64	99.90
1.550	70.76	99.42
1.600	83.16	99.45
1.650	103.21	100.09
1.700	96.15	100.58
1.750	100.18	100.67
1.800	103.40	100.38
1.850	87.35	100.01
1.900	90.99	100.14
1.950	106.14	100.64

2.000	103.83	100.94
2.100	104.69	100.56
2.200	99.18	100.52
2.300	100.20	101.03
2.400	100.65	100.58
2.500	104.00	100.67
2.600	106.93	100.97
2.700	99.00	100.55
2.800	105.63	100.70
2.900	106.48	100.82
3.000	100.87	100.47
3.100	105.40	100.64
3.500	103.43	100.50
3.600	101.30	100.31
3.700	103.62	100.44
3.800	102.04	100.35
3.900	101.36	100.23
4.000	100.00	100.34
4.100	101.08	100.23

TABLE 3: Transient Stability Analysis for Bus Voltages at Post Fault

The maximum power that the machine can deliver occurs when $\delta = 90^{\circ}$. Any further increase in δ will result in a decrease in the electrical power output. Hence, based on the result gotten, it can be deduced that the system is unstable at a critical clearing time of 0.363s but is stable at a critical clearing time of 0.1s.

Electrical appliances are designed to operate best at its rated voltage. Efficiency and operating characteristics are adversely affected when they are operated at voltages other than their rated values. For example, with a lighting load, a small decrease in voltage causes a great decrease in light output. Motors subject to reduced voltage have poor starting torque and poor speed regulation. They draw more current than they would at their rated voltage. This causes overheating, thus, making them inefficient [6].

Transient Stability Assessment of the Nigerian 330kV Network.
Figure 3 shows the complete Nigeria 330kV Transmission Network with synchronous generators, transformers, transmission lines and loads.

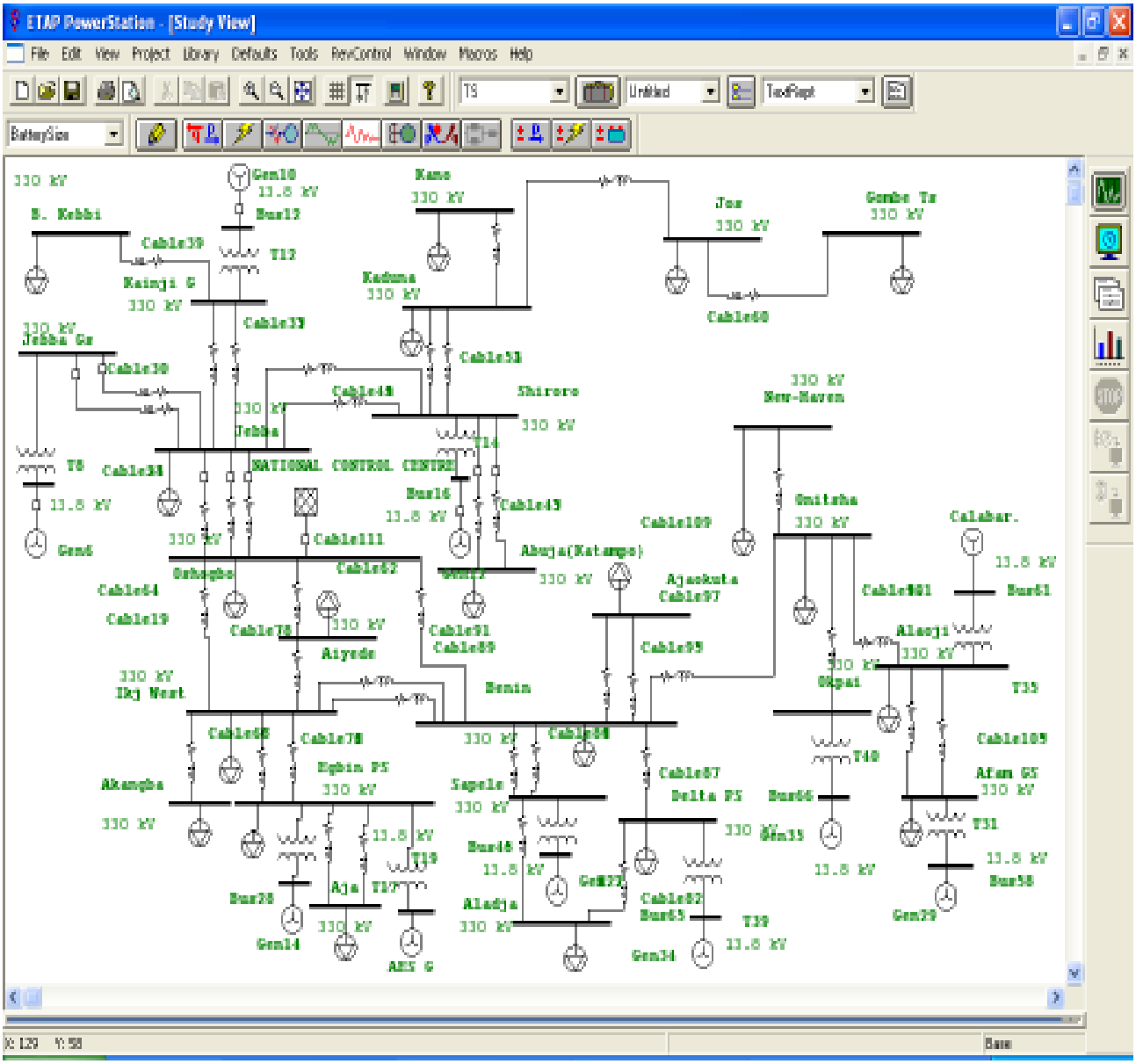

Synchronism

The Nigerian 330kV network consists of synchronous machines connected by transmission links. In order to maintain stability, these machines must rotate at the same speed and frequency of 50Hz. The phase angles between them must not vary appreciably.

Also, if the oscillatory response of the power system during the transient period is damped and the system settles in a finite time to a new steady operating condition, then the system is stable. If the system is not settled in a finite time, then it is considered unstable.

The following plots in figures 1-6 are generated for the 330kV Network with fault clearing times of 0.363s and 0.1s

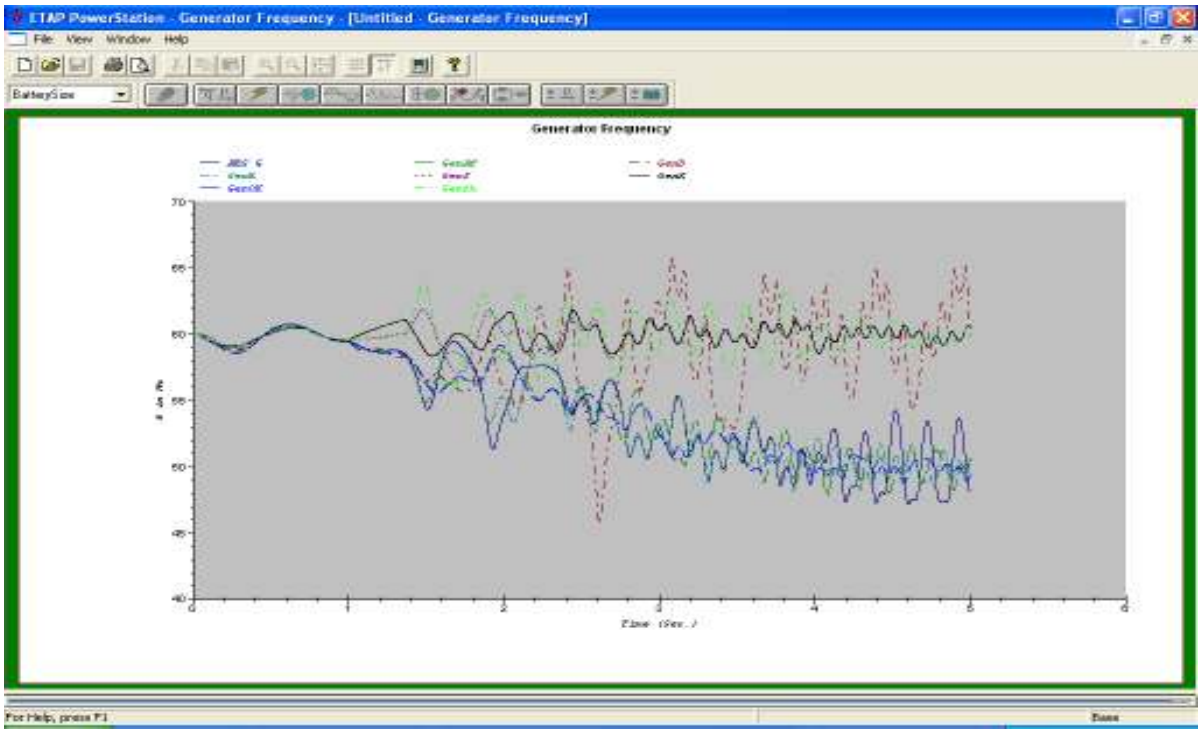

FIGURE 4: Frequency of the various generators at 0.363s fault clearing time

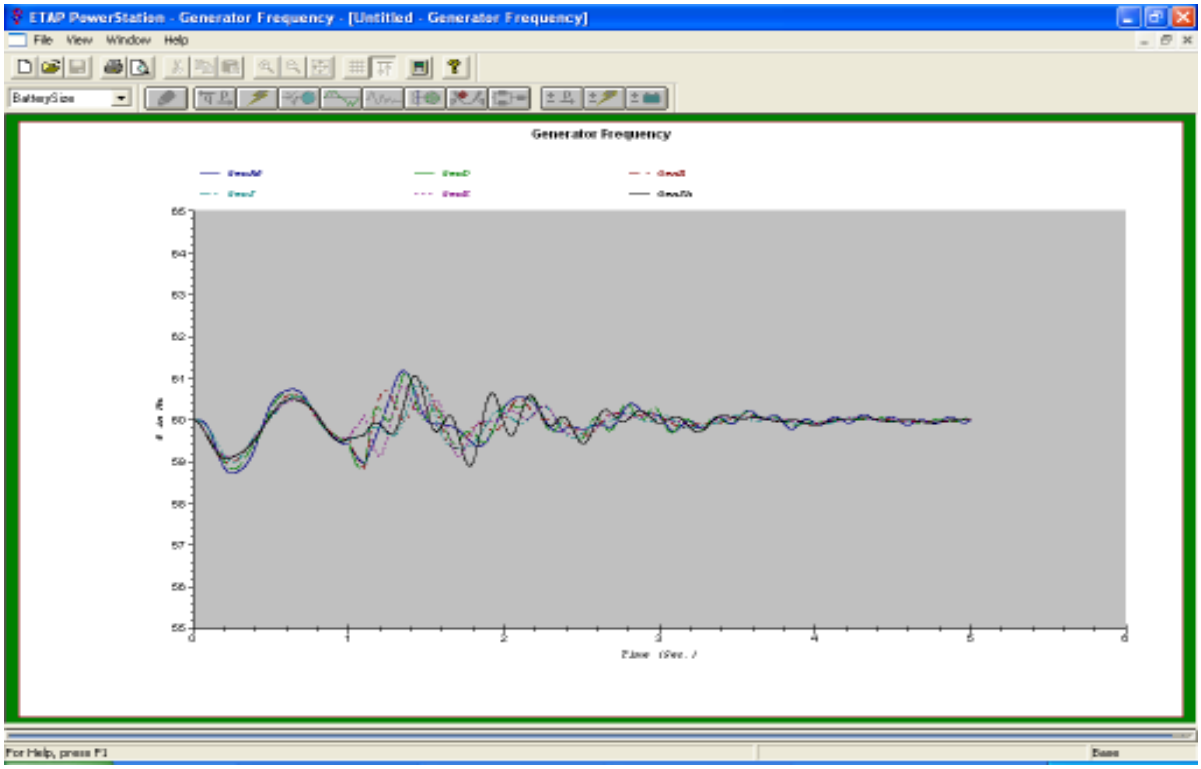

FIGURE 5: Frequency of the various generators at 0.1s fault clearing time

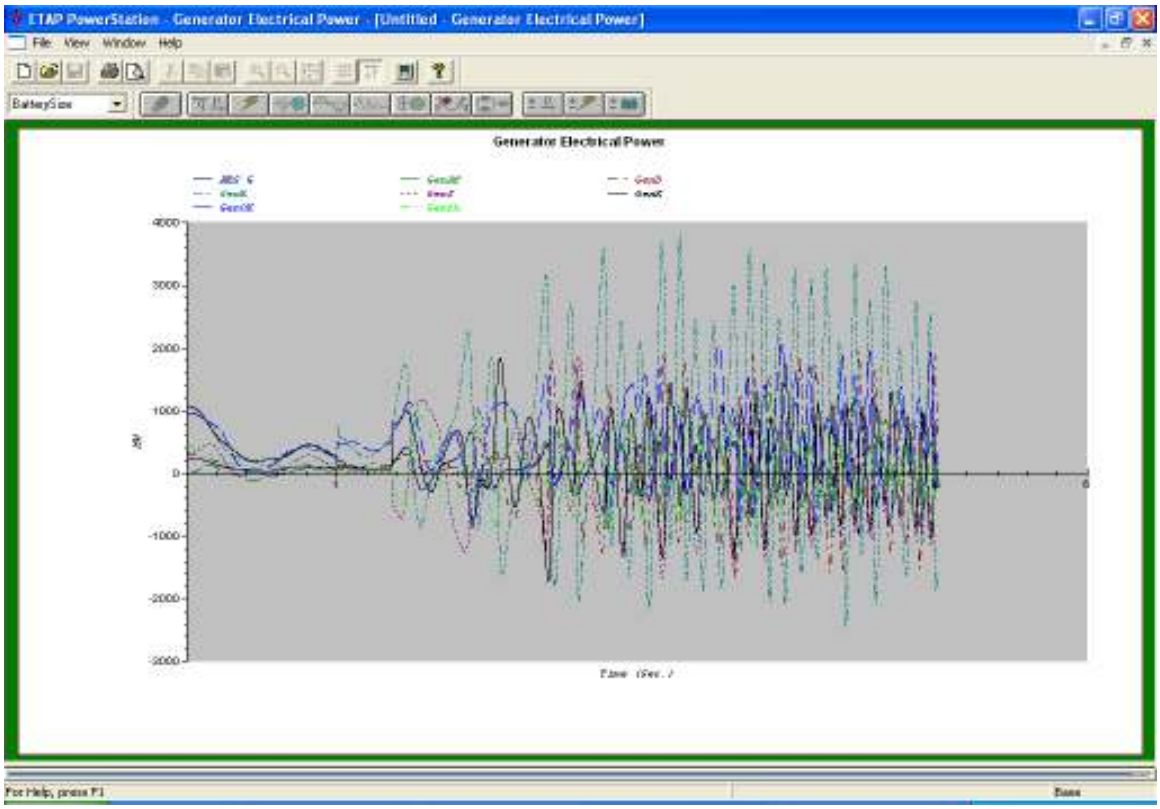

FIGURE 6: Electrical Power for the various generators at 0.363s fault clearing time

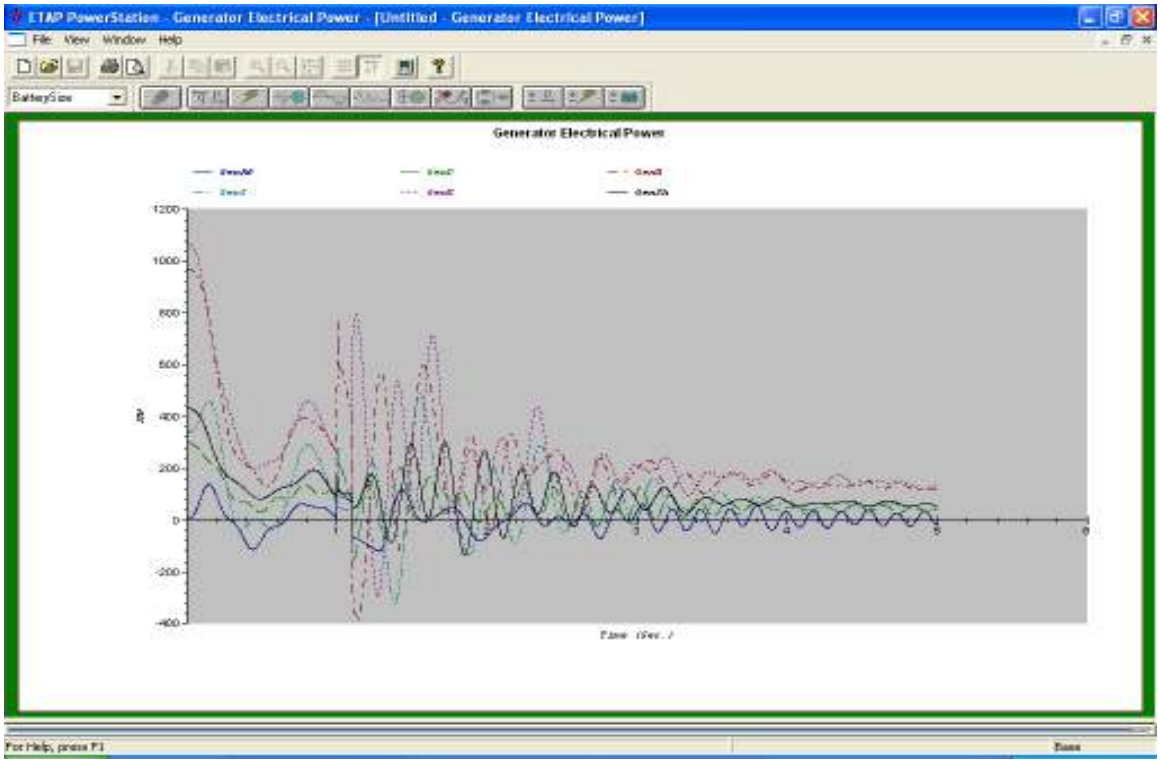

FIGURE 7: Electrical Power for the various generators at 0.1s fault clearing time

ACHIEVEMENTS:

This study has been able to show the urgent need for upgrading and expanding the Nigerian 330kV network. It has been established that faults should be cleared as quickly as possible. This will save the system from total collapse. Analysis of this study showed that a fault clearing time of 0.1s gave a more stable result than a fault clearing time of 0.363s.

CONSLUSION & FUTURE WORK

In summary, this study has assessed the stability limits of the Nigerian 330kV transmission network in terms of its ability to maintain synchronism among the generating units. Also, the Voltage stability limit for a one machine system, before, during and after system disturbances was assessed. A short circuit fault was simulated to occur at one of the lines linking Jebba generating station to Jebba transmission station. The fault was cleared by disconnecting the line by means of a circuit breaker. Runge Kutta Method was then used to analyze the 330kV transmission network.

The critical clearing angle was found to be 166.376˚. The corresponding critical clearing time was 0.363s. After simulation, it was discovered that the system remained unstable.

Another critical clearing time of 0.1s was specified to see the system's reaction. The corresponding critical clearing time was found to be 12.85˚. Plots for the generator frequency, power output and voltage were generated. Results from these plots showed that the system remained stable.

Hence, it was deduced that faults on the network should be cleared as quickly as possible to avoid endangering the system. This can be achieved by means of protective devices and fault location algorithms. Other sophisticated control measures can be employed to achieve this objective.

ACKNOWLEDGEMENT

I wish to acknowledge professor A.O Ibe and Engr Omorogiuwa for their effortless contributions and corrections of this manuscript. I also wish to acknowledge my father Prof O.J Odia for proof reading my work and for his support.

REFERENCES

1. J.G. Duncan, Malukutla S. '*Power system analysis and design'* 4th edition international student edition, Canada. 2007.

2. C. Eze Focus: '*Power Outage Paralyses Operations at MM Airport*'. *thisday Online*, [internet] 10th May. Available at: http://www.thisdayonline.com/nview.php?id=172968]. 2010

3. Grid Code, '*The Grid Code for the Nigeria Electricity Transmission System.* ' Electrical power sector reform Act, version 01.2005.

4. A.O.Ibe ' *Power Systems Analysis'* Odus press 2002

5. P.Kundur, '*Power System Stability and Contro*l' Tata McGraw-Hill, New Delhi.1994

6. J.M Nadon, B.J Gelmine, E.D McLaughlin. '*Industrial Electricity*' Delmar publishers 5th edition, pp107.1994

7. I. A. W. Noor, M. Azah, '*Transient stability assessment of a power system using probabilistic neural network' 2008* American Journal of Applied Sciences.

8. *C. Okonji. Focus: 'Weak transmission threatens 6000MW target'. Compass news paper, Online, [internet] 24th June, 2010.*

9. C.C Okoro and Achugbu, '*Contigency Assessment of the Nigerian 330kV power grid*' 2007 Department of Electrical and Electronics Engineering, Faculty of Engineering University of Lagos, Akoka, Lagos, Nigeria.

10. Onohaebi. O. S. (2009) '*Power Outages in the Nigerian Grid*' Research Journal of applied sciences 4(1): 1-9

11. Operation Technology Inc, '*Electrical Transient Analyzer Program (ETAP)*' 2001

Analytic Formulae for Concrete Mix Design Based on Experimental Data Base and Predicting the Concrete Behavior Using ANN Technique

Mostafa A. M. Abdeen mostafa_a_m_abdeen@hotmail.com
Faculty of Engineering/Dept. of Engineering Mathematics and Physics
Cairo University
Giza, 12211, Egypt

Hossam Hodhod hossamhodhod@hotmail.com
Faculty of Engineering/Dept. of structural Engineering
Cairo University
Giza, 12211, Egypt

Abstract

The Local Egyptian practice in producing concrete for different structural applications is based on the known properties of cement. Cement has been produced locally under the Egyptian standards ES 372, 373 and 584 for ordinary, rapid hardening and sulphate resisting types. In 2007, the Egyptian standards issued ES 4756 that adopted the European standard EN 197 for producing cement. This resulted in new types of cements to replace the types that local construction companies used to apply for decades. Many doubts appeared about whether the rules applied for concrete mix proportioning are still valid. In the current research, an experimental investigation of concrete properties is made using two of the locally most common types of cements CEM I 32.5 R & CEM I 42.5 N. Slump, compressive strength, rebound number and ultrasonic pulse velocities were investigated for 64 mixes. The main parameters were type of cement, cement content, water content, and fine/coarse aggregate ratio. Data base was established for the mix proportions and corresponding properties. Analytic formulae are proposed for utilizing the collected data base for concrete mix design. Also, using the experimental data base presented in the current study, numerical approach, using one of the artificial intelligence techniques, is adopted to simulate the concrete behavior for different mix proportions. Artificial Neural Network (ANN) technique is developed in the present work to simulate the concrete slump and concrete compressive strength for different mix proportions at different ages for the two types of cement and then predict the concrete behavior for different mix proportions at ages rather than those investigated in the experimental work.

Keywords: Cement type, Concrete mix proportion, Concrete behavior, Modeling, Artificial neural network.

1. INTRODUCTION

Cement plays a vital role in construction industry. More than 90% of structures are made from reinforced concrete [1]. Besides, wall construction and finishing of surfaces is made using cement mortar. In 2007, Egyptian standards issued a new version of cement standard ES4756 that adopts solely the European norm EN197. This version included major changes in the concept of cement industry. Mainly, cement started to have a grade and rate of hardening in addition to its type. The term "Ordinary Portland cement OPC" is no longer correlated with strength or strength development. This drastic change dictated a comprehensive investigation of the properties of new types of cement. Results of such an investigation will be of major importance for Engineers and scientists since they will help to identify the properties of cement-based products, and to deal with any ill effects resulting from using these new types for some applications. The current paper represents a part of this targeted investigation [2, 3] applied to the local Egyptian cement.

Different concrete mixes are made using local materials with different proportions. Slump, compressive strength and non-destructive strength measurements were made and analyzed in order to identify the properties of concrete mixes using the new local cements and to establish a data-base for concrete mix-design and prediction of properties of different concrete mixes.

Since the experimental work needs a lot of effort, time and money, the need for utilizing new methodologies and techniques to reduce this effort, save time and money (and at the same time preserving high accuracy) is urged. Artificial intelligence has proven its capability in simulating and predicting the behavior of the different physical phenomena in most of the engineering fields. Artificial Neural Network (ANN) is one of the artificial intelligence techniques that have been incorporated in various scientific disciplines. Minns [4] investigated the general application of ANN in modeling rainfall runoff process. Ramanitharan and Li [5] utilized ANN with back-propagation algorithm for modeling ocean curves that were presented by wave height and period. Tawfik, Ibrahim and Fahmy [6] showed the applicability of using the ANN technique for modeling rating curves with hysteresis sensitive criterion. Kheireldin [7] presented a study to model the hydraulic characteristics of severe contractions in open channels using ANN technique. The successful results of his study showed the applicability of using the ANN approach in determining relationship between different parameters with multiple input/output problems. Abdeen [8] developed neural network model for predicting flow depths and average flow velocities along the channel reach when the geometrical properties of the channel cross sections were measured or vice versa. Allam [9] used the artificial intelligence technique to predict the effect of tunnel construction on nearby buildings which is the main factor in choosing the tunnel route. Allam, in her thesis, predicted the maximum and minimum differential settlement necessary precautionary measures. Abdeen [10] presented a study for the development of ANN models to simulate flow behavior in open channel infested by submerged aquatic weeds. Mohamed [11] proposed an artificial neural network for the selection of optimal lateral load-resisting system for multi-story steel frames. Mohamed, in her master thesis, proposed the neural network to reduce the computing time consumed in the design iterations. Abdeen [12] utilized ANN technique for the development of various models to simulate the impacts of different submerged weeds' densities, different flow discharges, and different distributaries operation scheduling on the water surface profile in an experimental main open channel that supplies water to different distributaries.

2. PROBLEM DESCRIPTION

To investigate and predict the behavior of concrete made from two of the locally most common types of cements CEM I 32.5 R & CEM I 42.5 N, experimental and numerical techniques will be presented in this study. The experimental program and its results will be described in detail in the following sections. After experimental presentation, analytic formulae are proposed for concrete mix design. The numerical models presented in this study utilized Artificial Neural Network technique (ANN) using the experimental data. Numerical models, then, can predict the performance of concrete for different mix proportions at different ages.

3. EXPERIMENTAL PROGRAM

There are many parameters figured for the investigation of cement application in concrete. Namely, type of cement, aggregate type and grading, cement and water contents are the most important. In order to limit the scope of the current investigation, the most common variations (alternatives) in the actual practice were assigned to the above mentioned parameters, CEM I 32.5 R and CEM I 42,5 N are the most common in the local Egyptian market. Desert siliceous gravel and sand were considered as aggregates. Sand to gravel ratio was considered as 1:2 (most widely used) and 1:1 (common for case of fine sand). Cement content ranges usually from 250 to 400 kg/m3. Water content ranges usually from 150 - 250 kg/m3. Four cement and water contents were used to cover the above mentioned ranges. Table (1) summarizes the Mix proportions for the investigated mixes in the current study. One can see that the selected parameters yielded sixty four mixes. For each of the mixes, slump, compressive strength at 3,7,28 and 56 days were measured. Some measurements of shmidt rebound numbers and ultrasonic pulse velocity were also made on concrete cubes before testing them in compression at different ages.

Mix No	Type of Cement	Cement Content (kg/m^3)	Water Content (kg/m^3)	Sand : Gravel
1 – 4	CEM I 32.5 R	250	120-160-200-240	1 : 1
5 – 8		300		
9 – 12		350		
13 – 16		400		
17 – 20		250		1 : 2
21 – 24		300		
25 – 28		350		
29 – 32		400		
33 – 36	CEM I 42.5 N	250	120-160-200-240	1 : 1
37 – 40		300		
41 – 44		350		
45 – 48		400		
49 – 52		250		1 : 2
53 – 56		300		
57 – 60		350		
61 – 64		400		

TABLE 1: Mix Proportions of Investigated Concrete Mixes

3.1 Concrete Materials

3.1.1 Cement

Two types of cement CEM I were used for the current study: CEM I 32.5 R and CEM I 42.5 N. These are locally produced according to Egyptian Standards ES4756 that complies with the EN 197.

3.1.2 Fine Aggregate

Local desert sand was used. The specific gravity, bulk density and fineness were measured. The sand has a specific gravity of 2.62, a bulk density of 1740 kg/m^3 and modulus of fineness of 3.3.

3.1.3 Coarse Aggregate

Local desert gravel was used in the current study. It has a specific gravity of 2.60, a bulk density of 1540 kg/m3, and a maximum nominal aggregate size of 25 mm.

3.1.4 Water

Tap water was used for mixing and curing concrete.

3.2 Test Specimens

Standard concrete cubes (150 mm size) were cast from each of the mixes shown in Table (1). Dry constituents were mixed first for about one minute in a tilting type 140 liter mixer. Then, water was added and mixing continued till homogeneous mixture was obtained. Slump was measured for the mix within 15 minutes after mixing. Then concrete was cast in the steel cube molds and vibrated using a vibrating table. Molds were covered with plastic sheets and stored in a humid room for 24 hours. Cubes were then de-molded and cured by immersion in water at about 23º C till the day of testing.

3.3 Test Results

3.3.1 Slump

Values of slump are shown in Tables (2) (a & b) for all mixes. One can easily see that results follow the well known trend where slump increases with increase of water content. In order to identify the effect of type of cement and sand: gravel ratio, slump values are plotted versus water content in Fig. (1). Two charts are shown; one for each type of cement. Data for sand : gravel ratio of 1:1 are shown in unfilled symbols whereas data for ratio of 1:2 are shown in filled symbols. One can easily see that increasing sand content reduces slump for all cases. Also, it can be seen that slump values are higher for cement CEM I 32.5 R. This is probably due to the high fineness of CEM I 42.5 N [13] that results in early hydration and, consequently, high water consumption. However, this was not expected to exceed the consumption of 32.5R (rapid setting).

Content			CEM-I 32.5 R		CEM-I 42.5 N	
Water W (kg/m^3)	**Cement C (kg/m^3)**	**Sand (S = G) (kg/m^3)**	**Slump (mm) Exp.**	**Slump (mm) ANN**	**Slump (mm) Exp.**	**Slump (mm) ANN**
120	250	1000	8.0	7.995	5.0	4.848
160		950	38.0	38.000	18.0	18.194
180		**925**		**70.376**		**37.409**
200		900	124.0	123.991	72.0	72.012
240		850	244.0	244.018	194.0	194.003
120	300	981	13.0	12.989	5.0	4.840
160		931	34.0	34.017	16.0	16.123
180		**906**		**56.024**		**36.229**
200		881	101.0	101.014	75.0	74.972
240		831	225.0	224.985	202.0	201.998
120	350	961	4.0	4.013	0.0	0.25563
160		911	30.0	29.986	21.0	20.890
180		**886**		**52.611**		**41.946**
200		861	90.0	89.993	71.0	71.029
240		811	215.0	215.007	184.0	183.999
120	400	941	0.0	0.001	0.0	0.2006
160		891	38.0	38.000	16.0	16.079
180		**886**		**65.511**		**33.197**
200		841	101.0	101.004	60.0	59.989
240		791	240.0	239.997	196.0	196.000
120	**450**	**921**		**9.910**		**5.988**
160		**871**		**64.847**		**30.639**
200		**821**		**126.733**		**88.235**
240		**771**		**253.927**		**228.975**

Note: data with **bold red** color represents the predicted ANN slump

TABLE 2(a): Slump results for sand: gravel ratio of 1: 1

Content			CEM-I 32.5 R		CEM-I 42.5 N	
Water W (kg/m^3)	Cement C (kg/m^3)	Sand S = G/2 (kg/m^3)	Slump (mm) Exp.	Slump (mm) ANN	Slump (mm) Exp.	Slump (mm) ANN
120	250	667	7.0	7.110	5.0	4.958
160		633	50.0	49.970	26.0	26.015
180		**616**		**134.992**		**56.661**
200		600	194.0	193.999	103.0	103.000
240		567	254.0	253.972	226.0	225.998
120	300	654	6.0	5.722	10.0	10.106
160		621	33.0	33.113	31.0	30.947
180		**604**		**102.126**		**56.367**
200		587	169.0	169.027	93.0	93.002
240		542	244.0	244.028	220.0	220.011
120	350	641	3.0	3.250	4.0	3.838
160		607	28.0	27.855	36.0	36.060
180		**590**		**72.568**		**62.272**
200		574	150.0	149.984	91.0	90.987
240		541	219.0	218.976	202.0	201.996
120	400	627	0.0	0.078	3.0	3.139
160		594	22.0	22.066	27.0	26.943
180		**577**		**55.670**		**51.313**
200		561	142.0	142.002	91.0	91.010
240		527	214.0	214.010	233.0	232.996
120	**450**	**613.0000**		**0.087**		**11.855**
160		**580.0000**		**8.779**		**47.772**
200		**547.0000**		**173.774**		**160.713**
240		**513.0000**		**247.906**		**240.125**

Note: data with **bold red** color represents the predicted ANN slump

TABLE 2(b): Slump results for sand: gravel ratio of 1: 2

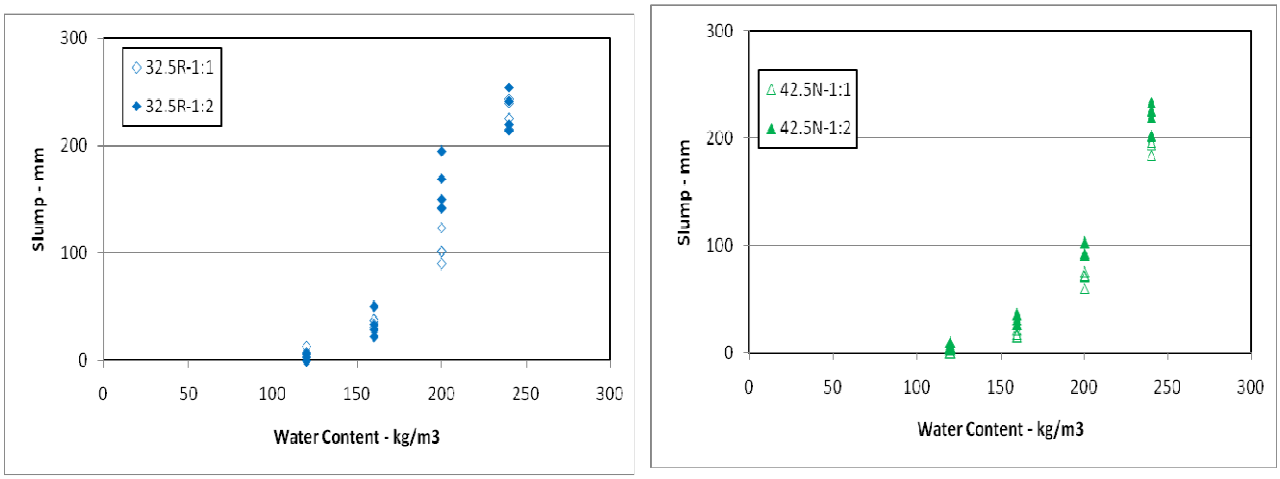

FIGURE 1: Slump versus Water Content for different types of cements and different sand: Gravel Ratios.

3.3.2 Compressive Strength

Compressive strength values for all mixes, at all ages, are presented in Figures (2-5). Each point represents the average result of three tested cubes. In the title of each chart the ratio following type of cement is the sand: gravel ratio. In the legend, data set is defined by cement content (in kg/m^3) followed by water content (kg/m^3). Lines represent artificial neural network (ANN) data presented later in this paper.

From figures, one can see that strength values increase with cement content, and with reduction of water content for the same cement content. Also, it is obvious that strength increases, slightly, with decrease of sand content. These observations comply with the known trend of strength variation for concrete mixes, and, therefore, indicate reliability of collected data. As a finding concerning the investigated new types of cements, one can see that for CEM I 42.5 N cement, strength development almost stops after 28 days and minor increase of strength occurs between 28 and 56 days. For CEM I 32.5 R cement, a significant increase of strength occurs between 28 and 56 days (almost 50%). This trend is not consistent with the designation R and N of cement type that dictates the early development of strength for R and late development for N.

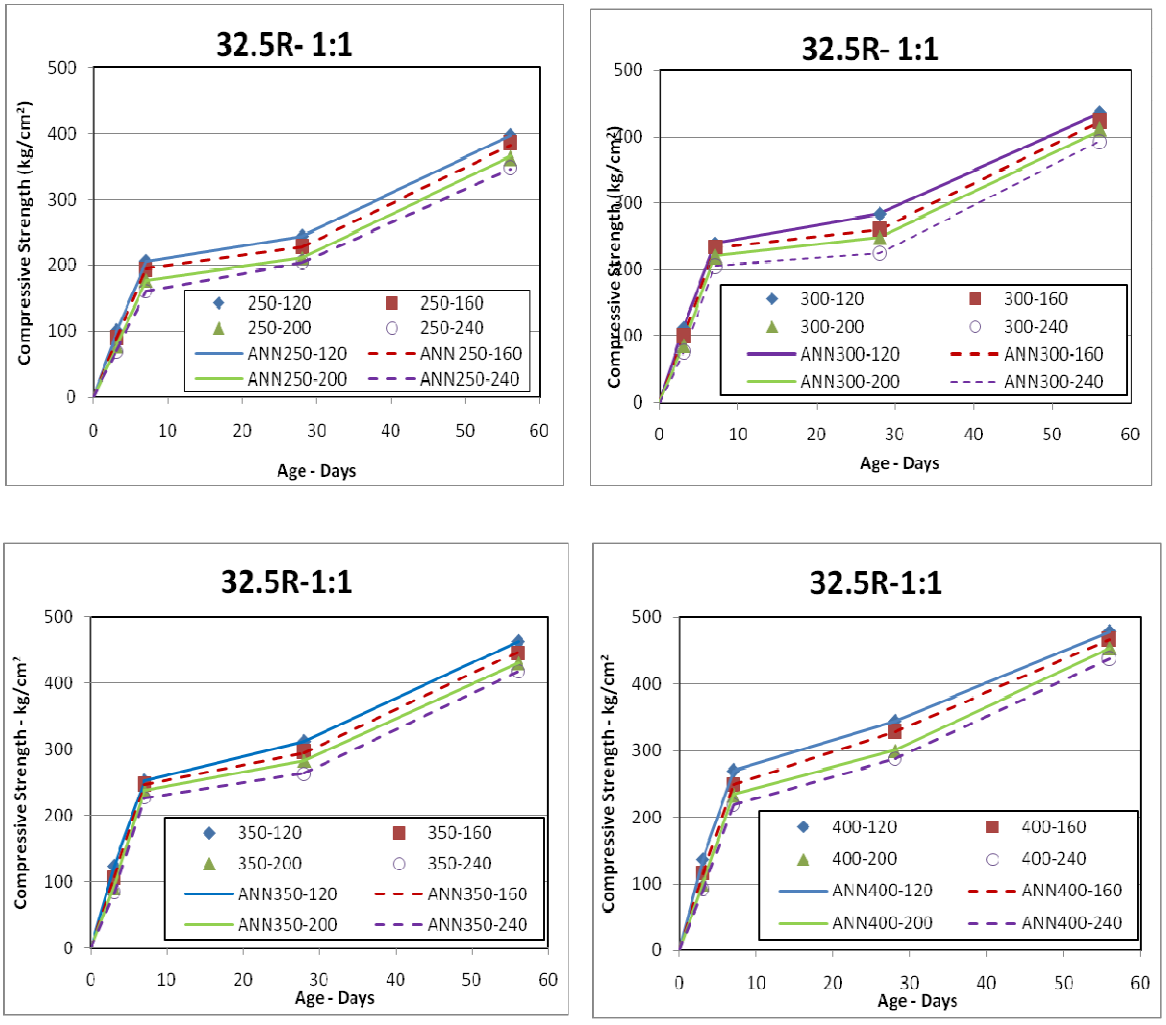

FIGURE 2: Development of Concrete Compressive Strength using CEM I 32.5 R and Sand: Gravel Ratio of 1:1 with different Cement and Water Contents.

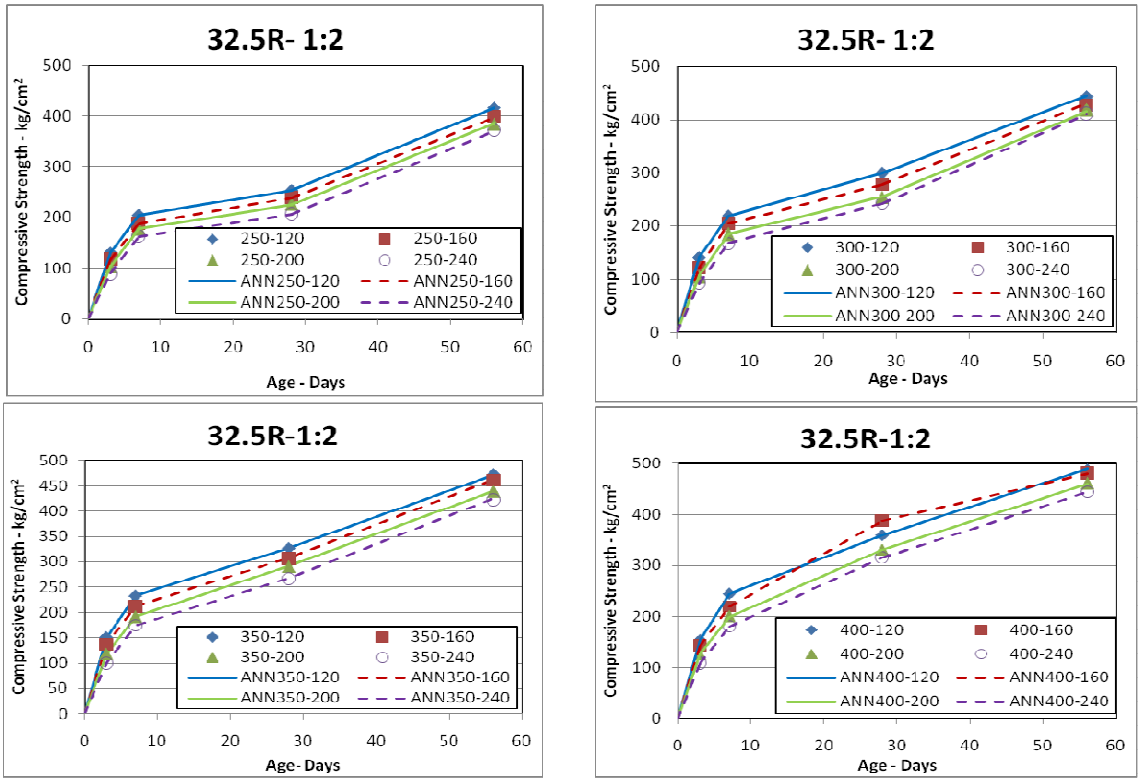

FIGURE 3: Development of Concrete Compressive Strength using CEM I 32.5 R and Sand: Gravel Ratio of 1:2 with different Cement and Water Contents.

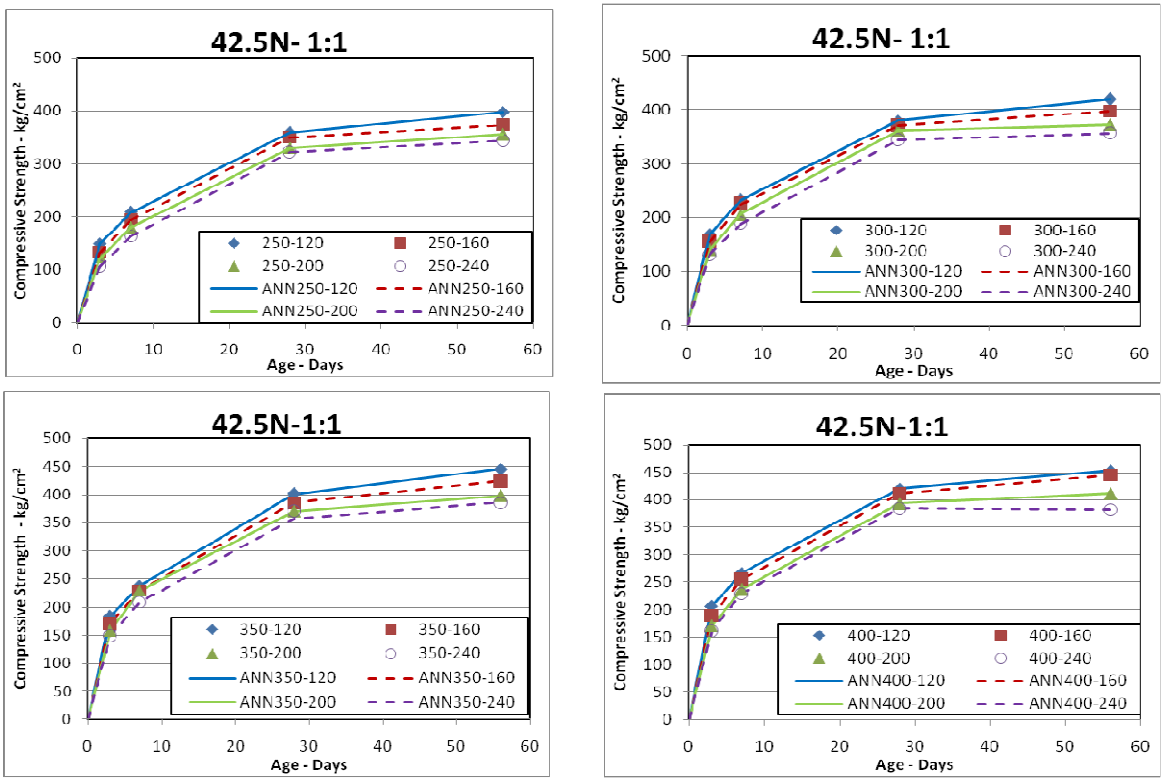

FIGURE 4: Development of Concrete Compressive Strength using CEM I 42.5 N and Sand: Gravel Ratio of 1:1 with different Cement and Water Contents.

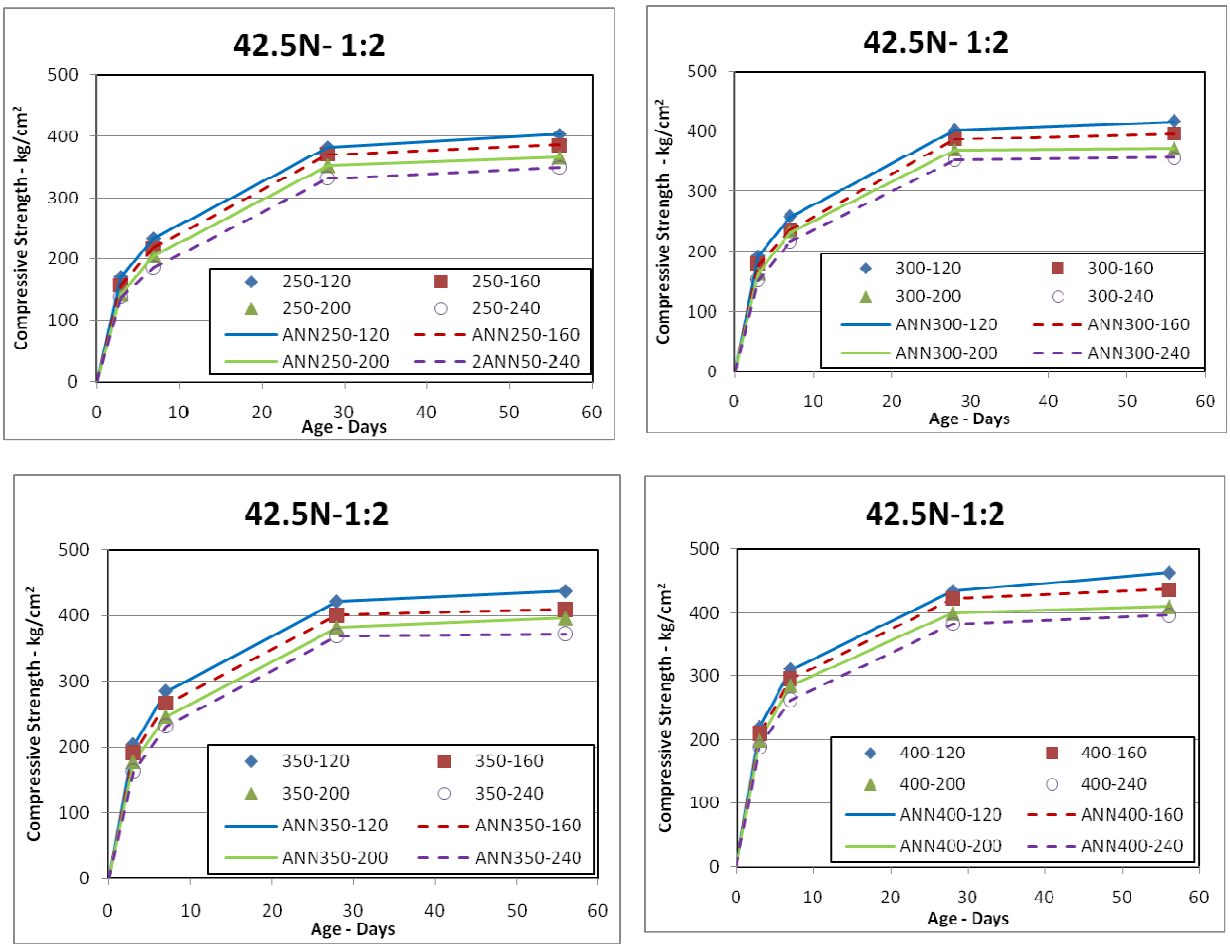

FIGURE 5: Development of Concrete Compressive Strength using CEM I 42.5 N and Sand: Gravel Ratio of 1:1 with different Cement and Water Contents.

The trend of strength development is consistent with the observed reduction of slump for CEM I 42.5 N, and the reported high fineness of this cement.

In order to evaluate the effect of cement content, data are presented in Fig. (6). Four charts are shown. In each chart, four series of data are presented: two for CEM I 32.5 R and two for CEM I 42.5 N. Filled symbols show the experimental results and unfilled ones show the ANN predictions, explained later in this paper. For each type of cement data for highest and lowest cement contents are presented together with highest and lowest water contents. One can see that, generally, for all cases, mixes with CEM I 32.5 R show lower strength than similar mixes with CEM I 42.5 N. At 56 days, however, mixes with 32.5 R cement show strength values higher than similar mixes with CEM I 42.5 N cement.

Strength values are plotted versus water/cement ratio (w/c) in Fig. (7). Two charts are shown in Fig. (7): one for each type of cement. Unfilled symbols represent mixes with sand/gravel ratio of 1:1, and filled symbols represent mixes with sand/gravel ratio of 1:2. It can be seen that the well known trend of strength reduction with increase of w/c ratio is fulfilled. There is also a slight effect of sand: gravel ratio on strength values. This is particularly true for later ages (28 days and higher).

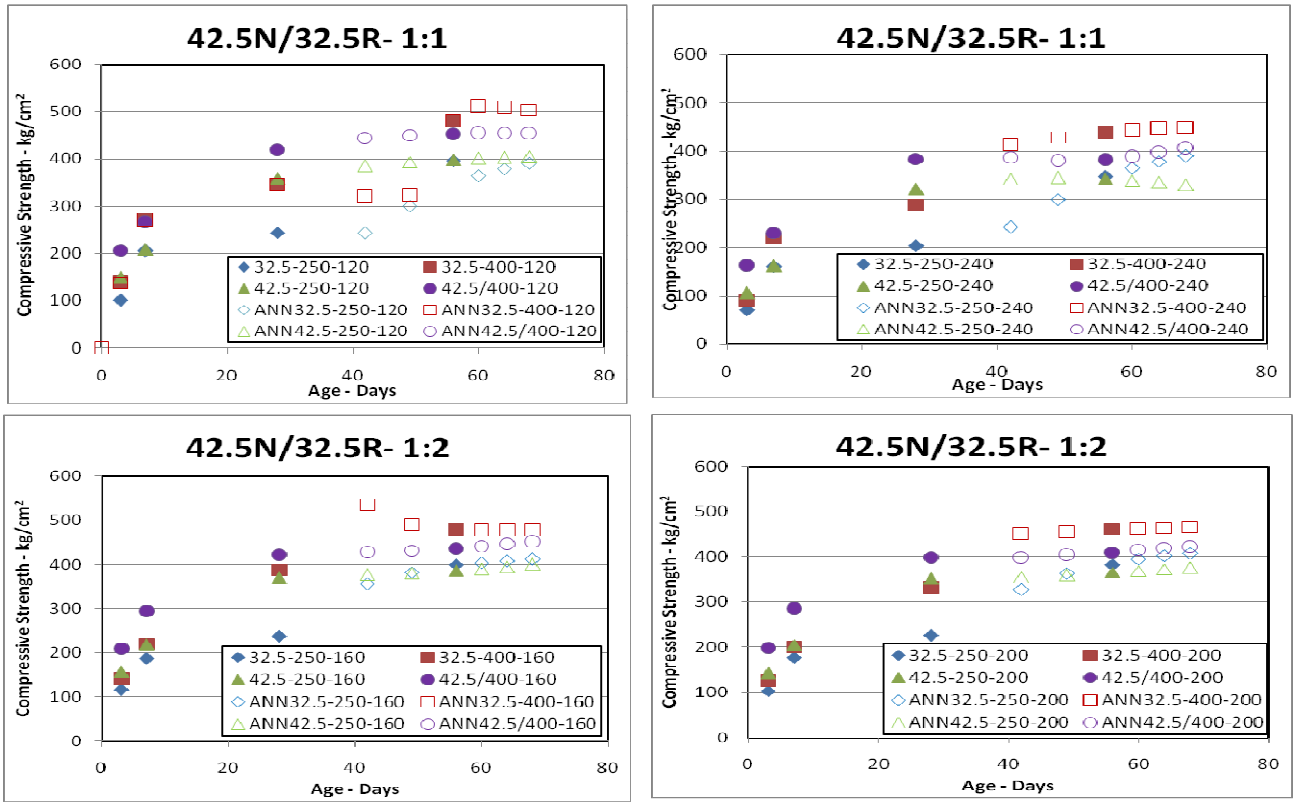

FIGURE 6: Comparison of Concrete Compressive Strength Development for CEM I 32.5 R and CEM I 42.5 N at different Cement and Water Contents.

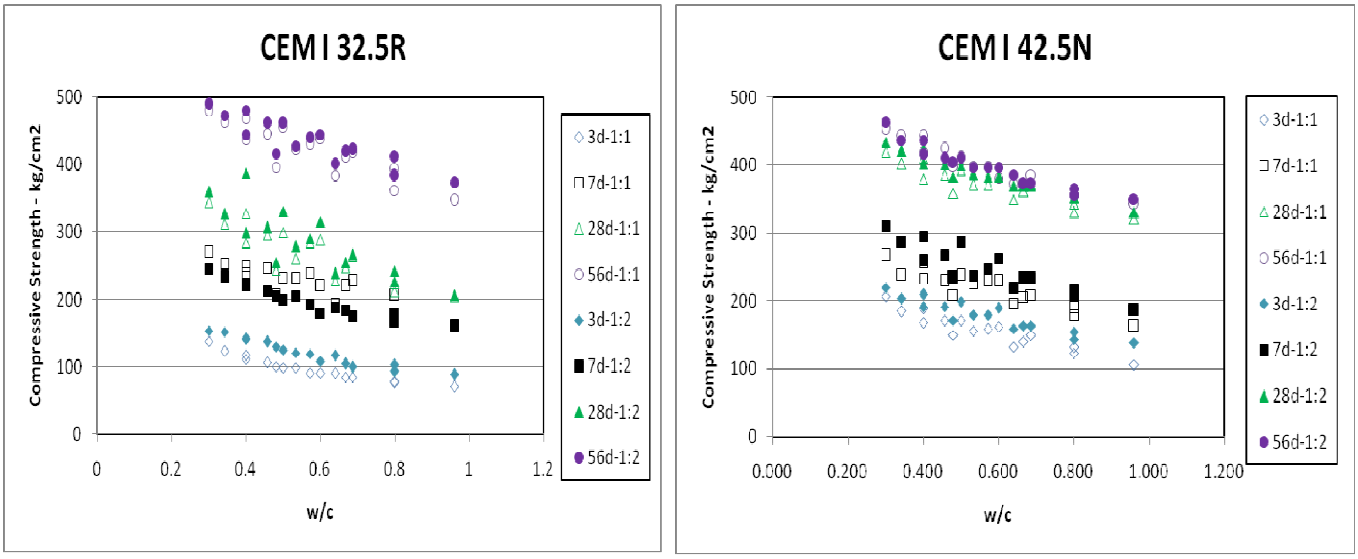

FIGURE 7: Concrete Compressive Strength versus Water/ Cement Ratio for different Mixes and Types of Cement.

3.3.3 Non-Destructive Testing (NDT)

Results of measuring Rebound number and ultrasonic pulse velocity are plotted versus measured compressive strength in Figs (8 - 11). The large filled symbols are used for measurements after 3 days; large unfilled symbols are used for 7-day measurements. Small filled and unfilled symbols are used for 28 and 56 day measurements, respectively. Some early age measurements are missing for concretes made from CEM I 32.5 R. This is due to some technical problems with measuring device at these specific ages. One can easily see that the correlation between compressive strength and rebound number or pulse velocity is an age dependent one. This is in good agreement with the known facts on NDT testing of concrete [14]. For rebound number (R_N) measurements on CEM I 32.5 R, one can see a slight increase in R_N for increased content of coarse aggregate. There is almost no effect of cement content on the correlation between compressive strength and rebound number at all ages for the two investigated types of cement. Ultrasonic pulse velocity showed similar trend to that of R_N, where it increases for increased coarse aggregate content with CEM I 32.5 R. There is no effect of cement content on correlation with compressive strength at all ages for the two investigated types of cement.

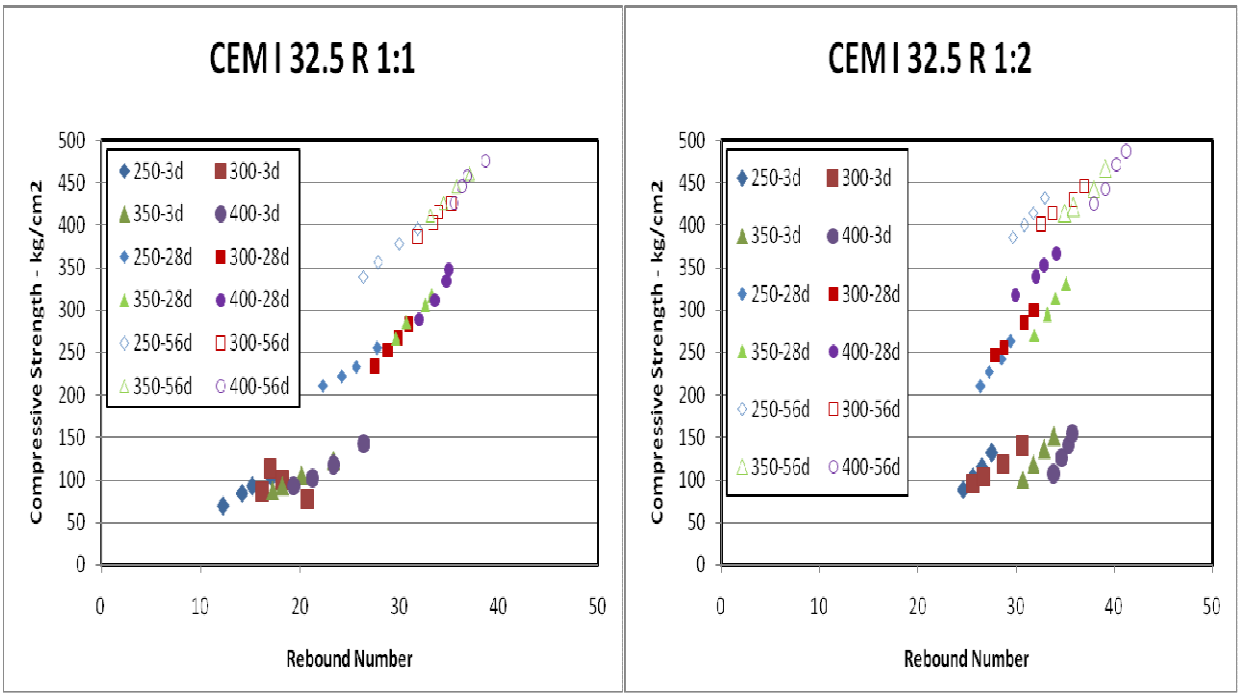

FIGURE 8: Rebound Number versus Compressive Strength at different ages and Cement Contents for CEM I 32.5 R and Sand: Gravel Ratios = 1:1 & 1:2

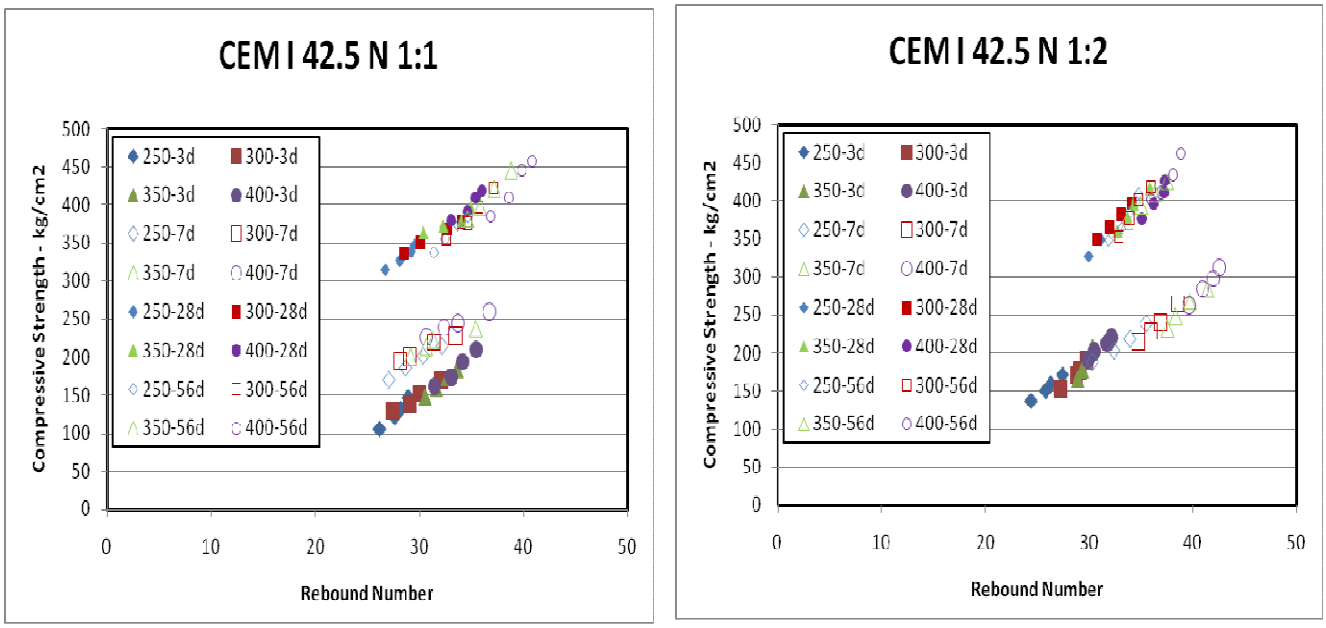

FIGURE 9: Rebound Number versus Compressive Strength at different ages and Cement Contents for CEM I 42.5 N and Sand: Gravel Ratios = 1:1 & 1:2

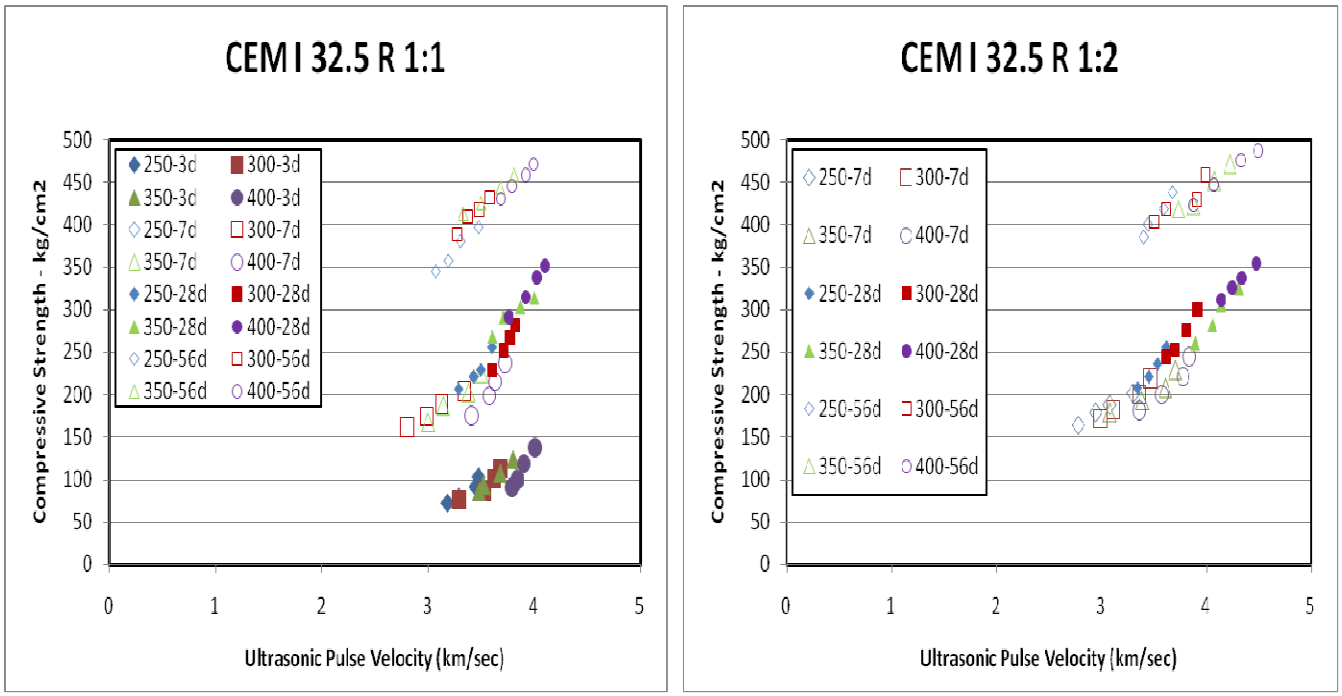

FIGURE 10: Ultrasonic Pulse Velocity versus Compressive Strength at different ages and Cement Contents for CEM I 32.5 R and Sand: Gravel Ratios = 1:1 & 1:2

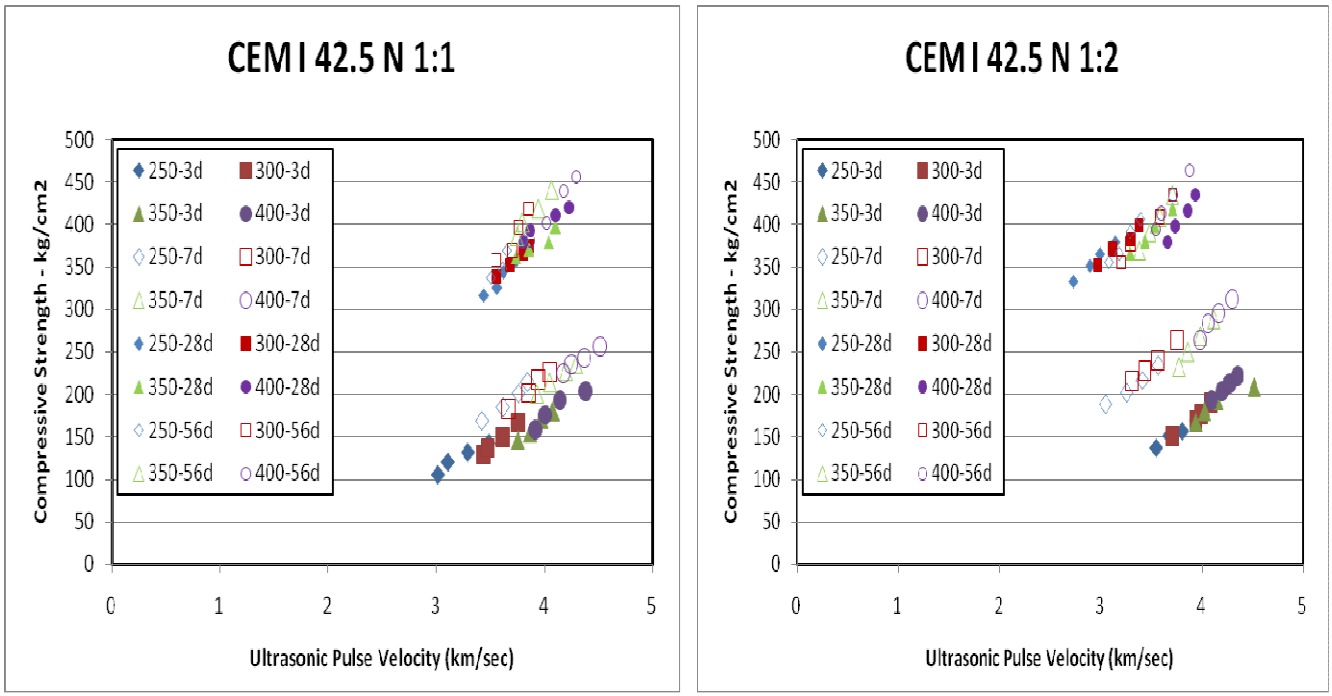

FIGURE 11: Ultrasonic Pulse Velocity versus Compressive Strength at different ages and Cement Contents for CEM I 42.5 N and Sand: Gravel Ratios = 1:1 & 1:2

4. ANALYTIC FORMULAE FOR MIX DESIGN

Usually mix design is made following the steps:

1) Given the required concrete slump (and the sand: gravel ratio), get water content (w) from the available database.
2) Given the target concrete compressive strength get the suitable water/cement (w/c) ratio from the available data base.
3) From the above two steps get cement content (c): c= w ÷ (w/c).
4) Applying the equation of absolute volume of concrete constituents, get the absolute volume of aggregate = 1000 – w – c/3.15.
5) Given aggregate specific gravity and sand: gravel ratio, get the sand and gravel contents.

Search in data base for steps 1 and 2 above is usually made through curves and tables. Although this graphical presentation of database can still be applied for the current database, formulae for such presentations are sought. The curves in Figs (1) and (7) were fitted to equations using the least mean square method. For the case of slump (S), the following equations were obtained:

$S = 294\ln(w) - 1432$ (R^2 = 0.834) for CEM I 32.5 R, Sand: Gravel = 1:2 (1)

$S = 259\ln(w) - 1265$ (R^2 = 0.787) for CEM I 32.5 R, Sand: Gravel = 1:1 (2)

$S = 346\ln(w) - 1677$ (R^2 = 0.896) for CEM I 42.5 N, Sand: Gravel = 1:2 (3)

$S = 310\ln(w) - 1507$ (R^2 = 0.847) for CEM I 42.5 N, Sand: Gravel = 1:1 (4)

Where: S = Slump in mm, w = water content (kg/m^3)
For the case of compressive strength, the following form was obtained

$$fc = A.e^{(-B*w/c)} \qquad w/c = [\ln(A) - \ln(fc)]/B \qquad (5)$$

Where fc = Compressive Strength (kg/cm^2), w/c = water/cement ratio.

A & B are constants depending on age of concrete (in days) and can be obtained from the following equations:

$$A = 116.7\ln(age) + 60.62 \quad (R^2 = 0.99) \quad \text{for CEM I 32.5 R} \tag{6}$$

$$A = 82.17\ln(age) + 188.3 \quad (R^2 = 0.971) \quad \text{for CEM I 42.5 N} \tag{7}$$

$$B = 0.94, 0.64, 0.78, 0.41 \quad \text{for CEM I 32.5 R at 3, 7, 28, 56 days, respectively.} \tag{8}$$

$$B = 0.80, 0.68, 0.38, 0.43 \quad \text{for CEM I 42.5 N at 3, 7, 28, 56 days, respectively.} \tag{9}$$

4.1 Analytic Example

Find the mix proportions for a concrete mix having 150 mm slump, and 28-day compressive strength of 300 kg/cm^2, given that sand: gravel ratio is 1 : 2, and cement type is CEM I 32.5 R.

From Eqn. (1),

150 = 294 ln (w) -1432 w = 217 kg/m3

From Eqn. (6),

A = 450

From Eqn. (8),

B = 0.78

From Eqn. (5),

w/c = 0.52 c = 217 / 0.52 = 417 kg/m^3

Absolute volume of aggregate = 1000-217-417/3.15 = 650 liter / m^3 of concrete
Weight of aggregate = 1690 kg (using specific gravity of 2.6 as measured early in this paper)

Mix Proportions = water: cement: sand: gravel = 217 : 417 : 560 : 1130 kg

Comparing this result with Table 2(b) and Fig. (3), one can see that the mix proportions are in good agreement with the experimental database.

5. NUMERICAL MODEL STRUCTURE

Neural networks are models of biological neural structures. Abdeen [8] described in a very detailed fashion the structure of any neural network. Briefly, the starting point for most networks is a model neuron as shown in Fig. (12). this neuron is connected to multiple inputs and produces a single output. Each input is modified by a weighting value (w). The neuron will combine these weighted inputs with reference to a threshold value and an activation function, will determine its output. This behavior follows closely the real neurons work of the human's brain. In the network structure, the input layer is considered a distributor of the signals from the external world while hidden layers are considered to be feature detectors of such signals. On the other hand, the output layer is considered as a collector of the features detected and the producer of the response.

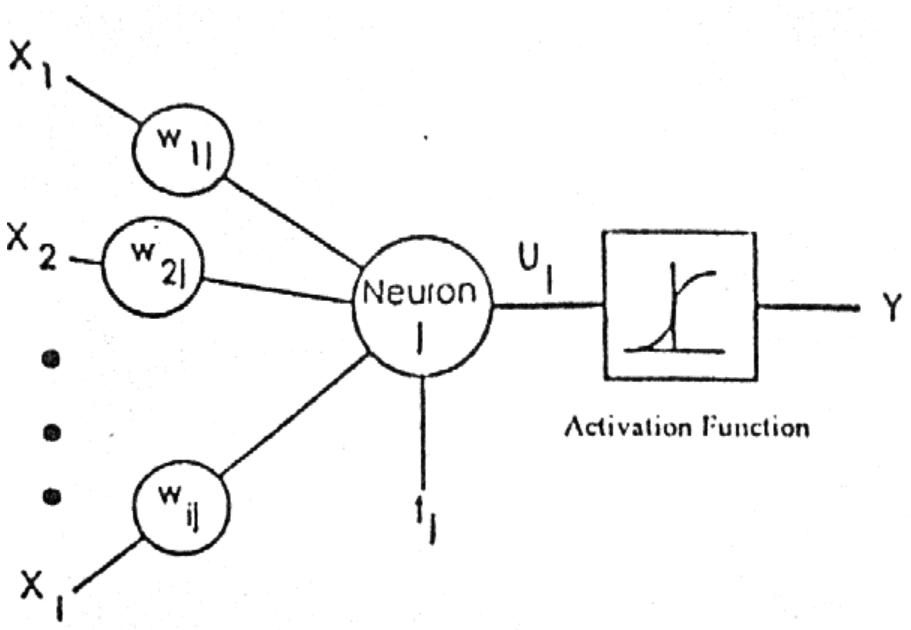

FIGURE 12: Typical picture of a model neuron that exists in every neural network

5.1 Neural Network Operation

It is quite important for the reader to understand how the neural network operates to simulate different physical problems. The output of each neuron is a function of its inputs (X_i). In more details, the output (Y_j) of the j^{th} neuron in any layer is described by two sets of equations as follows:

$$U_j = \sum\left(X_i w_{ij} \right) \tag{10}$$

And

$$Y_j = F_{th}\left(U_j + t_j\right) \tag{11}$$

For every neuron, *j*, in a layer, each of the *i* inputs, X_i, to that layer is multiplied by a previously established weight, w_{ij}. These are all summed together, resulting in the internal value of this operation, U_j. This value is then biased by a previously established threshold value, t_j, and sent through an activation function, F_{th}. This activation function can take several forms such as Step, Linear, Sigmoid, Hyperbolic, and Gaussian functions. The Hyperbolic function, used in this study, is shaped exactly as the Sigmoid one with the same mathematical representation, as in equation 12, but it ranges from – 1 to + 1 rather than from 0 to 1 as in the Sigmoid one (Fig. (13))

$$f(x) = \frac{1}{1+e^{-x}} \tag{12}$$

The resulting output, Y_j, is an input to the next layer or it is a response of the neural network if it is the last layer. In applying the Neural Network technique, in this study, Neuralyst Software, Shin [15], was used.

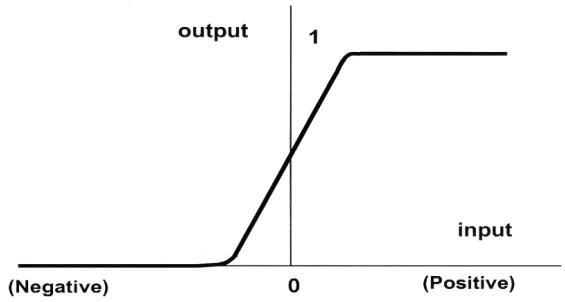

FIGURE 13: The Sigmoid Activation Function

5.2 Neural Network Training

The next step in neural network procedure is the training operation. The main purpose of this operation is to tune up the network to what it should produce as a response. From the difference between the desired response and the actual response, the error is determined and a portion of it is back propagated through the network. At each neuron in the network, the error is used to adjust the weights and the threshold value of this neuron. Consequently, the error in the network will be less for the same inputs at the next iteration. This corrective procedure is applied continuously and repetitively for each set of inputs and corresponding set of outputs. This procedure will decrease the individual or total error in the responses to reach a desired tolerance. Once the network reduces the total error to the satisfactory limit, the training process may stop. The error propagation in the network starts at the output layer with the following equations:

$$w_{ij} = w_{ij}^{'} + LR\left(e_j X_i\right) \tag{13}$$

And,

$$e_j = Y_j\left(1 - Y_j\right)\left(d_j - Y_j\right) \tag{14}$$

Where, w_{ij} is the corrected weight, $w_{ij}^{'}$ is the previous weight value, LR is the learning rate, e_j is the error term, X_i is the i^{th} input value, Y_j is the ouput, and d_j is the desired output.

6. SIMULATION MODELS

To fully investigate numerically the effect of concrete mix proportions at different ages on the performance of concrete, four numerical models are considered in this study, two for each type of cement (CEM-I 32.5 R and CEM-I 42.5 N). The models of each type of cement simulate the concrete slump and concrete compressive strength for different mix proportions at different ages.

6.1 Neural Network Design

To develop a neural network model to simulate the effect of concrete mix proportion on the performance of concrete, first input and output variables have to be determined. Input variables are chosen according to the nature of the problem and the type of data that would be collected in the field or from experiment. To clearly specify the key input variables for each neural network simulation model and its associated outputs, Table (3) is designed to summarize all neural network key input variables and output for the simulation models.

Model	Input Variables					Output
	Water	Cement	Sand	Gravel	Days	
Slump CEM-I 32.5 R	☑	☑	☑	☑		Slump
Compressive Strength CEM-I 32.5 R	☑	☑	☑	☑	☑	Comp. Strength
Slump CEM-I 42.5 N	☑	☑	☑	☑		Slump
Compressive Strength CEM-I 42.5 N	☑	☑	☑	☑	☑	Comp. Strength

TABLE 3: Key input and output variables for all ANN models

Several neural network architectures are designed and tested for all simulation models investigated in this study to finally determine the best network models to simulate, very accurately, the effect of mix proportions on the performance of concrete based on minimizing the Root Mean Square Error (RMS-Error).

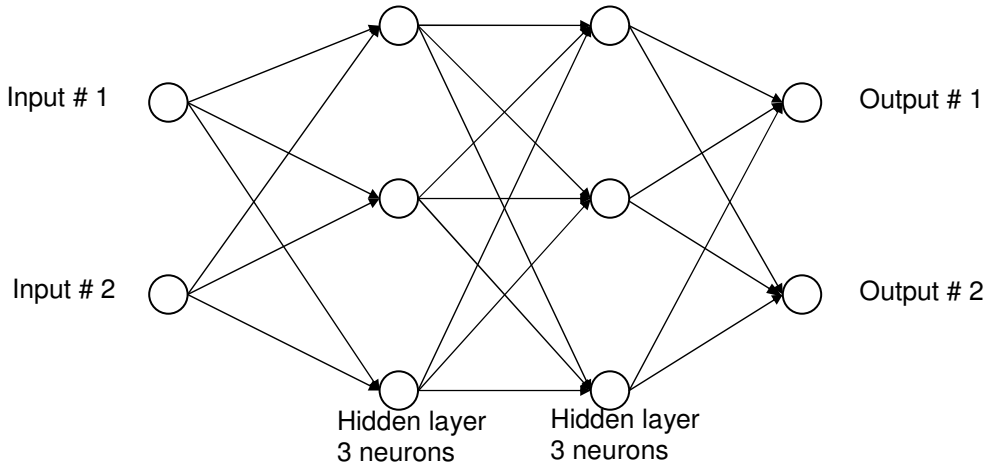

FIGURE 14: General schematic diagram of a simple generic neural network

Fig. (14) Shows a schematic diagram for a generic neural network. The training procedure for the developed ANN models, in the current study, uses the data for all the concrete mix proportions available from the experiments and then different mix proportions at different ages are used to test the power of prediction of the neural network models.

Simulation Model	No. of Layers	No. of Neurons in each Layer					
		Input Layer	First Hidden	Second Hidden	Third Hidden	Fourth Hidden	Output Layer
Slump CEM-I 32.5 R	4	4	8	6	-	-	1
Compressive Strength CEM-I 32.5 R	6	5	7	6	5	4	1
Slump CEM-I 42.5 N	5	4	8	6	4	-	1
Compressive Strength CEM-I 42.5 N	6	5	9	7	5	3	1

TABLE 4: The developed neural network models

Table (4) shows the final neural network models and their associate number of neurons. The input and output layers represent the key input and output variables described previously for each simulation model.

The parameters of the various network models developed in the current study are presented in Table (5), where these parameters can be described with their tasks as follows:

Learning Rate (LR): determines the magnitude of the correction term applied to adjust each neuron's weights during training process = 1 in the current study.
Momentum (M): determines the "life time" of a correction term as the training process takes place = 0.9 in the current study.
Training Tolerance (TRT): defines the percentage error allowed in comparing the neural network output to the target value to be scored as "Right" during the training process = 0.001 in the current study.
Testing Tolerance (TST): it is similar to Training Tolerance, but it is applied to the neural network outputs and the target values only for the test data = 0.003 in the current study.
Input Noise (IN): provides a slight random variation to each input value for every training epoch = 0 in the current study.
Function Gain (FG): allows a change in the scaling or width of the selected function = 1 in the current study.
Scaling Margin (SM): adds additional headroom, as a percentage of range, to the rescaling computations used by Neuralyst Software, Shin (1994), in preparing data for the neural network or interpreting data from the neural network = 0.1 in the current study.
Training Epochs: number of trails to achieve the present accuracy.
Percentage Relative Error (PRR): percentage relative error between the numerical results and actual measured value for and is computed according to equation (6) as follows:

$$PRE = (\text{Absolute Value } (ANN\_PR - AMV)/AMV)*100 \quad (15)$$

Where :
ANN_PR : Predicted results using the developed ANN model
AMV : Actual Measured Value
MPRE : Maximum percentage relative error during the model results for the training step.

Simulation Parameter	Slump (CEM-I 32.5 R)	Comp. Strength (CEM-I 32.5 R)	Slump (CEM-I 42.5 N)	Comp. Strength (CEM-I 42.5 N)
Training Epochs	489275	670443	323209	648395
MPRE	8.33	3.73	4.66	0.9
RMS-Error	0.0003	0.0016	0.0003	0.001

TABLE 5: Parameters used in the developed neural network models

6.2 Numerical Results

Numerical results using ANN technique are indicated with experimental data to simulate the concrete slump and concrete compressive strength for different mix proportions at different ages for the two types of cement.

6.2.1 Slump

Values of slump (experimental and numerical) are shown in Tables (2) (a & b) for all mixes for the two types of cement (CEM I 32.5 R & CEM I 42.5 N). The black color values are the ANN results during the training process. It is clear that ANN models presented in the current paper are very efficient for describing the slump property. The bold red color values are the predicted ANN results using the present model without the need to make any experiment. These predicted values are logic and in the range of the expected slump values. The ANN slump results shown in these Tables prove that the presented ANN models are very capable in simulating and predicting the slump property.

6.2.2 Compressive Strength

Compressive strength values (experimental and numerical) for all mixes, at all ages, are presented in Figures (2-6). Figures (2-5) show the numerical and experimental results during the training process of the present ANN models. One can see from these figures that the presented ANN models can accurately simulate the compressive strength property for all mixes at all ages for the two types of the cement. To check the power of the presented ANN models in predicting the compressive strength for all mixes at ages different than those used in the experiments, Figure (6) is drawn. In this Figure unfilled symbols represent the ANN predictions. It is clear that the presented numerical models using ANN technique are efficiently capable of predicting the compressive strength without the need to make a lot of experiments which will save time, effort and money.

7. CONCLUSIONS

Based on the results obtained from testing 64 concrete mixes with different types of cement, cement content, water content and sand/ gravel ratio, the following can be concluded:

- Concrete mixes with CEM I 42.5 N showed less slump than similar mixes with CEM I 32.5 R, and this was attributed to the high fineness of the former type as reported elsewhere.
- Concrete made from CEM I 32.5 R show early strength less than similar concrete with CEM I 42.5 N. However, after 28 days concrete with CEM I 32.5 R continue developing strength that exceed the strength of concrete with CEM I 42.5 N after 56 days.
- Non destructive testing techniques applied to concrete made from the two types of cement showed the known trend of measurements and showed almost no effect of Type of cements on the measured values.
- Some analytic formulae were proposed to correlate concrete properties and mix proportions of the collected database. These formulae were investigated as a basis for mix design and gave good results.
- The results of implementing the ANN technique in this study showed that this approach was capable of identifying relationship between different uncertain parameters with multiple input/output criterions. The presented designed ANN models in this study were very successful in simulating and predicting the concrete slump and concrete compressive strength for different mix proportions at different ages for the two types of cement (CEM I 32.5 R & CEM I 42.5 N).

8. ACKNOLEDGEMENT

The Authors would like to express their gratitude towards Prof. Dr. Farouk El-Hakim of 15th May institute for Civil and Arch. Engineering, and undergraduate students (4th year– civil) for the help they provided during the experimental part of this research.

9. REFERENCES

1. Neville, A.M. "*Properties of concrete*". John Wiley & Sons Ltd., London, 1997

2. Hodhod, H., Abdeen, M. A. M. "*A Comparative Study on Strength Evaluation of Cement Types: Effect of Specimen Shape and Type of Sand*". SciRP, ENGINEERING, 2(8): 2010

3. Zawam, M. and Hodhod, H. "*Effect of New Cement Types on Mechanical and Time-Dependent Properties of Concrete*", Proceedings of the ASCE 6th International Engineering and Construction Conference, Cairo, Egypt, 2010

4. Minns. "*Extended Rainfall-Runoff Modeling Using Artificial Neural Networks*". Proc. of the 2nd Int. Conference on Hydroinformatics, Zurich, Switzerland, 1996

5. Ramanitharan, K. and C. Li. "*Forecasting Ocean Waves Using Neural Networks*". Proceeding of the Second International Conference on Hydroinformatics, Zurich, Switzerland, 1996

6. Tawfik, M., A. Ibrahim, and H. Fahmy. "*Hysteresis Sensitive Neural Network for Modeling Rating Curves*". Journal of Computing in Civil Engineering, ASCE, 11(3): 1997

7. Kheireldin, K. A. "*Neural Network Application for Modeling Hydraulic Characteristics of Severe Contraction*". Proc. of the 3rd Int. Conference, Hydroinformatics, Copenhagen – Denmark, 1998

8. Abdeen, M. A. M. "*Neural Network Model for predicting Flow Characteristics in Irregular Open Channel*". Scientific Journal, Faculty of Engineering-Alexandria University, Alexandria, Egypt, 40 (4):539-546, 2001

9. Allam, B. S. M. "*Artificial Intelligence Based Predictions of Precautionary Measures for building adjacent to Tunnel Rout during Tunneling Process*". Ph.D. Thesis, Faculty of Engineering, Cairo University, Giza, Egypt, 2005

10. Abdeen, M. A. M. "*Development of Artificial Neural Network Model for Simulating the Flow Behavior in Open Channel Infested by Submerged Aquatic Weeds*". Journal of Mechanical Science and Technology, KSME Int. J., Soul, Korea, 20(10):2006

11. Mohamed, M. A. M., "*Selection of Optimum Lateral Load-Resisting System Using Artificial Neural Networks*", M. Sc. Thesis, Faculty of Engineering, Cairo University, Giza, Egypt, 2006

12. Abdeen, M. A. M. "*Predicting the Impact of Vegetations in Open Channels with Different Distributaries' Operations on Water Surface Profile using Artificial Neural Networks*". Journal of Mechanical Science and Technology, KSME Int. J., Soul, Korea, 22:1830-1842, 2008

13. Zawam, M. "*Evaluation of Physical, Mechanical, and Time Dependent Properties of New Cement Types in Concrete*", MSc Thesis, Cairo University, 2010

14. Malhotra, V.M. "*Testing Hardened Concrete: Nondestructive Methods*". ACI Monograph No. 9, USA, 1986.

15. Shin, Y. "Neuralyst^{TM} User's Guide", "*Neural Network Technology for Microsoft Excel*", Cheshire Engineering Corporation Publisher, 1994

Using Imperialist Competitive Algorithm to Find the Optimum Shape Design of Internally Pressurized Torispherical Dome Ends Based on Buckling Pressure

Behzad Abdi behzad.abdi@gmail.com
Faculty of Mechanical Engineering
University Technology Malaysia-UTM
81310 UTM, Skudai, Johor, Malaysia

Hamid Mozafari mozafari.h@gmail.com
Faculty of Mechanical Engineering
University Technology Malaysia-UTM
81310 UTM, Skudai, Johor, Malaysia

Amran Ayob amran@fkm.utm.my
Faculty of Mechanical Engineering
University Technology Malaysia-UTM
81310 UTM, Skudai, Johor, Malaysia

Abstract

In this paper, Imperialist Competitive Algorithm (ICA) and Genetic Algorithm (GA) are used to find the optimal form for torispherical dome ends under internal pressure load. According to fabrication and strength of material requirements, a group of compromised counters are studied. According to ASME Section VIII and BS5500 pressure vessel codes, a reasonable buckling pressure limit is proposed. Four-centered ellipse method is used to describe the geometry of the torispherical dome end that this method is commonly used in engineering drawing. A minimum weight optimization problem based on buckling pressure is studied. Two different size torispherical dome end examples are selected and studied. Imperialist Competitive Algorithm is found to be very efficient and easy to use for the applications, such as torispherical dome end and subjected to internally pressurized loading.

Keywords: Imperialist Competitive Algorithm, Genetic Algorithm, Four-Centered Ellipse Method, Torispherical, Buckling Pressure, Internal Pressure

1. INTRODUCTION

Pressure vessels are very important in shell structures and a majority of them are axisymmetric. Torispherical dome ends are frequently used as end closures on pressure vessels and different types of cylindrical containers which can be found in various fields, such as aerospace, food processing, chemical, nuclear, oil industries, and so on. In this paper, we are only concerned with the structural honesty of the dome ends of the pressure hull.

Designers are seeking for maximum strength of structure with minimum weight. Minimum weight design of cylindrical and conical shells have been studied in details [1-3]. It seems that, for external pressurized cased, the optimization of torispherical dome ends under buckling

constraints was attempted in [4-6]. But studies concerned with the optimal shape design of torispherical dome end which under internal pressure loading are still limit. In this paper, we looked for an optimal deign of torispherical dome end according to elastic – plastic buckling pressure.

The British pressure vessel code BS5500 gives the design pressure P_w of internally pressurized dome ends which is not allowed to exceed 1/8.33 of the elastic plastic buckling pressure P_b while for the ASME section VIII it is 1/19.4. Therefore, in this paper, reasonable buckling pressure range is proposed between $8.33P_w$ and $19.4P_w$.

By using four-centered ellipse, three commonly used dome geometries that namely hemispherical dome, ellipsoidal dome, and torispherical dome can be described [7]. This method is commonly used in engineering drawing and it is very useful in the design and construction of the dome structure.

Imperialist Competitive Algorithm (ICA) is a new socio – politically motivated global search strategy that has recently been introduced for dealing with different optimization task [8]. This evolutionary optimization strategy has shown great performance in both convergence rate and better global optima achievement [9-11]. In this paper, we used imperialist Competitive Algorithm in optimizing torispherical dome ends and compared it with the genetic algorithm results.

2. GEOMETRY OF TORISPHERICAL DOME ENDS

At first, consider an elastic torispherical dome end with constant thickness t (Figure 1) under static internal pressure. It can be assumed that there is not any flange and the torispherical dome end is fully clamped at the edge.

The geometry of torispherical dome end can be constructed by using the four-centered ellipse method (Figure 1).

If we know the ratio $K = \frac{b}{a}$, then the other parameter θ, ϕ, r, and R can be determined from the following equation:

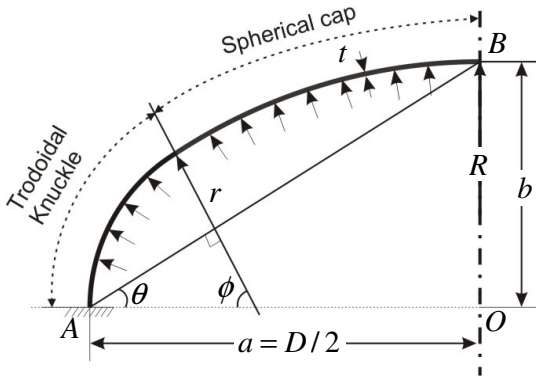

FIGURE 1: Geometry of torispherical dome end

$$\theta = \tan^{-1}\left(\frac{b}{a}\right) = \tan^{-1} K \tag{1}$$

$$\phi = \frac{\pi}{2} - \theta \tag{2}$$

$$r = \frac{a}{2}\left[\frac{1+\sin\theta-\cos\theta}{\cos^2\theta}\right] \tag{3}$$

$$R = \frac{a}{2\sin\theta}\left[1+\frac{1-\sin\theta}{\cos\theta}\right] \tag{4}$$

Finally, the total weight of torispherical dome end with constant thickness is [5, 6]

$$W = 2\pi\gamma t\left[r\omega\left(\frac{\pi}{2}-\Phi\right)+r^2\cos\Phi+\left(1-\cos\Phi\right)R^2\right] \tag{5}$$

Where

$$\omega = \frac{D}{2} - r = a - r \tag{6}$$

$$\Phi = \sin^{-1}\left(\frac{\omega}{R-r}\right) \tag{7}$$

And γ is the specific gravity.

In the [5, 6] Thickness t and the ratios $r/D, R/D$ were selected for the design variables of the optimum shape design of torispherical dome end. However, in this article, when the four-centered ellipse method is used, the radius of spherical cap R and the radius of toroidal knuckle r have certain relations which can be expressed as function of the angle of spherical cap θ and the ratio K. Therefore the thickness t and the ratio K are selected for design variables.

The choice of boundary values for the thickness t and the ratio K depends on practical application. From Harvey's study [14] in order to minimize the hoop stresses, the torispherical dome end must should a large knuckle radius. Must of pressure vessel contraction codes recognize this fact and therefore specify a minimum permissible knuckle radius. For instance, the British pressure vessel codes BS5500 and the ASME version VIII specify the minimum value of the knuckle radius as 6% of the crown radius. Therefore, the lower limit on the knuckle shallowness ($r/D = 0.06$) is chosen in this article. Blachut [5] showed that an unexpected drop in the buckling strength with the range $0.45 \le r/D \le 0.5$. Therefore, the range of r/D is selected to be $0.06 \le r/D \le 0.45$ in this paper.

3. MATHEMATICAL FORMULATION

An internally pressurized torispherical dome end is designed for the minimum weight objective satisfying specified design requirement. The manufacturing limitations on the geometric parameters and the mechanical properties of the shell material are the preassigned parameters for this design problem. The following optimization problem can then be formulated.

3.1 Cost function

Accompanying engineering demands for high pressure vessels with and without large sizes are often the economic ones of weight reduction to save materials, to enhance shipping and erection procedures and reduce fabrication costs. Therefore, cost function $F(\tilde{x})$ for weight is considered to be minimized in this paper

$$\text{Minimize} \quad F(\tilde{x}) = W_d / W_s$$

Where W_s is the weight of hemispherical dome end ($W_s = \frac{1}{2}\pi\gamma D^2 t$) and W_d is the weight of torispherical dome end.

3.2 Design variables

The dimensions of the torispherical dome end are selected as the independent design variables. These variables are:

(a) The thickness of torispherical dome end, $x_1 = t$

(b) The ratio of minor axis to the major axis, $x_2 = K = b/a = \tan\theta$

(c) The major axis of the torispherical dome end, $x_3 = a$

According to engineering design consideration, the length of major radius a is specified which must coincide with cylindrical shell at the junction. Therefore, there are two independent design variables taken for this problem. Therefore the vector $\tilde{x}$ will be given as

$$\tilde{x}_{opt} = (t, K)$$

3.3 Constraints

The lower and upper bounds are imposed on all the design variables. Based on the standard of practical design, a reasonable buckling pressure range is proposed. The BS5500 design pressure is not allowed to exceed $P_b / 8.33$, and the corresponding ratio for ASME is $P_b / 19.4$.

The constraints g_i are represented by the following:

(a) The lower bound on buckling pressure

$$g_1 = \frac{(P_L - P_b)}{P_b} \leq 0$$

Where P_b is the critical buckling pressure and P_L is the lower bound of critical buckling pressure, ($P_L = 8.33 P_w$ where P_w is the maximum work pressure).

(b) The upper bound on buckling pressure

$$g_2 = \frac{(P_b - P_U)}{P_U} \leq 0$$

Where P_U is the lower bound of critical buckling pressure. ($P_U = 19.4 P_w$)

(c) The lower bound on design variables

$$g_3 = \frac{(x^{Li} - x_i)}{(x^{Ui} - x^{Li})} \leq 0$$

Where x_i are design variables $(i = 1, 2)$, x^{Ui} is the upper bound value of design variable x_i and x^{Li} is the lower bound value of design variables x_i

(d) The upper bound on design variables

$$g_4 = \frac{(x_i - x^{Ui})}{(x^{Ui} - x^{Li})} \leq 0$$

4. IMPERIALIST COMPETITIVE ALGORITHM

Imperialist competitive algorithm (ICA) is a new evolutionary algorithm for optimization. This algorithm starts with an initial population. Each population in ICA is called country. Some of the best countries in the population selected to be the imperialists and the rest form the colonies of these imperialists. In this algorithm the more powerful imperialist, have the more colonies. When the competition starts, imperialists attempt to achieve more colonies and the colonies start to move toward their imperialists. So during the competition the powerful imperialists will be improved and the weak ones will be collapsed. At the end just one imperialist will remain. In this stage the position of imperialist and its colonies will be the same. The flowchart of this algorithm is shown in Figure 2 [11]. More details about this algorithm are presented in [8-13].

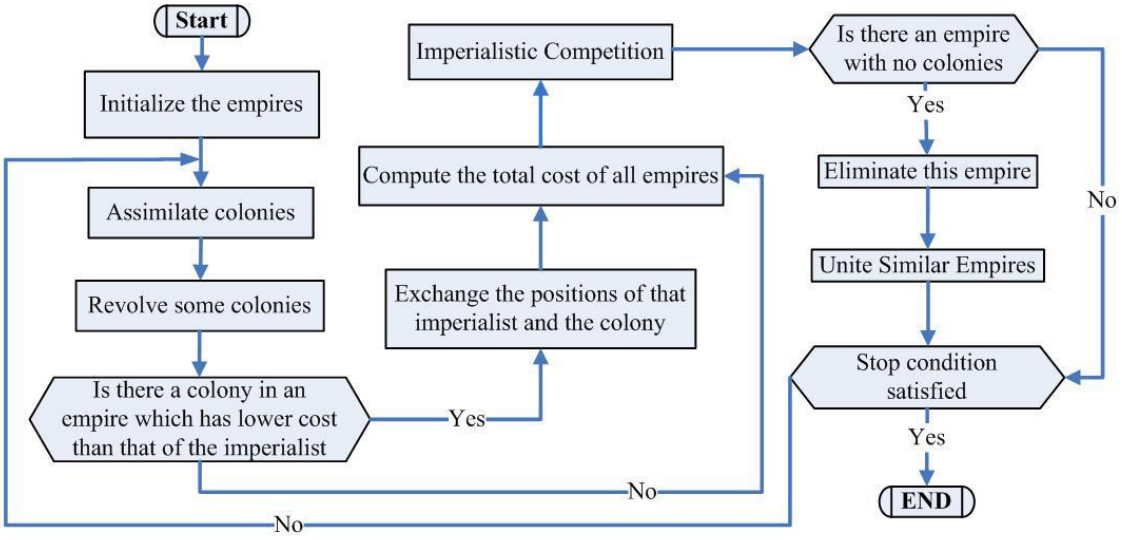

FIGURE 2: Flowchart of the imperialist competitive algorithm (ICA) [11].

5. MODEL DESCRIPTION

In this paper, two reference models of the torispherical dome end were considered. Both Models have the same poisson's ratio of 0.3 and the same elastic modulus of $3.0\times10^{7}\ lbf/in^{2}$. The fixed major axis a for model 1 is $63.98\,in$ and $91.73\,in$ for model 2. The principal dimensions for two references models are showed in table 1. The range of the ratio K is selected as $0.21 \le K \le 0.95$, and the range of thickness t as $50 \le D/t \le 150$. The preassigned lower and upper bound of design variables which were used in this paper are listed in table 2.

Torispherical dome	Model 1	Model 2
Length of major axis. a	63.98 in	91.73 in
Ratio of minor to major axis, $K = b/a$	0.61	0.53
Thickness, t	1.26 in	1.77 in
Radius of toroidal knuckle, r	29.28 in	34.35 in
Angle of toroidal knuckle, ϕ	58.62^{o}	61.99^{o}
Radius of spherical cap, R	95.91 in	156.83 in
Angle of spherical cap, θ	32.38^{o}	28.01^{o}

TABLE 1: The Principle Design Data of Reference Dome

Torispherical dome	Side constraint	Model 1	Model 2
Major axis. a	Fixed	63.98 in	91.73 in
Ratio of minor to major axis, $K = b/a$	Lower bound	0.21	0.21
	Upper bound	0.95	0.95
Thickness, t	Lower bound	0.85 in	1.22 in
	Upper bound	2.56 in	3.66 in

TABLE 2: The Upper and Lower Bounds of Design Variables

6. NUMERICAL RESULTS AND DISCUSSION

The numerical comparison between the results of the two optimal torispherical dome ends and two reference dome ends models are listed in table 3 and 4. Table3. The results in table 3 are optimized by using Genetic Algorithm (GA) and in table 4 we use Imperialist competitive algorithm (ICA) for optimization. Also, the comparisons between optimal dome ends and referenced dome ends are displayed in Figure 3 and Figure 4. For a hemispherical dome end, the thickness effects of the dome end to weight and the effect of ratio K to weight are showed in Figure 5 and Figure 6. In additional, for a hemispherical dome end, the thickness effects of the dome end to the buckling pressure is studied and showed in Figure 7 and table 5. Also, if thickness is kept constant, the effect of ratio K to the buckling pressure of torispherical dome end is also studied and the results are showed in Figure 8 and table 6. If the ratio K is kept constant, the effect of thickness to the buckling pressure is also studied and the results are showed in Figure 9 and table 7.

Torispherical dome	Model 1		Model 2	
	Ref. dome	Opt. dome (GA)	Ref. dome	Opt. dome (GA)
Length of major axis. a	63.98 in	63.98 in	91.73 in	91.73 in
Ratio of minor to major axis, $K = b/a$	0.61	0.64	0.53	0.64
Thickness, t	1.26 in	0.87 in	1.77 in	1.24 in
Radius of toroidal knuckle, r	29.28 in	31.42 in	34.35 in	45.04 in
Angle of toroidal knuckle, ϕ	58.62^o	57.39^o	61.99^o	57.39^o
Radius of spherical cap, R	95.91 in	91.82 in	156.83 in	131.66 in
Angle of spherical cap, θ	32.38^o	32.61^o	28.01^o	32.61^o
Total weight of dome end	913.06 lbf	644.4 lbf	2486.9 lbf	1887.8 lbf
Elastic – Plastic buckling pressure, P_b	8216.6 psi	2741.7 psi	6273.85 psi	2715.9 psi

TABLE 3: The numerical comparison table of torispherical dome ends

Torispherical dome	Model 1		Model 2	
	Ref. dome	Opt. dome (ICA)	Ref. dome	Opt. dome (ICA)
Length of major axis. a	63.98 in	63.98 in	91.73 in	91.73 in
Ratio of minor to major axis, $K = b/a$	0.61	0.65	0.53	0.65
Thickness, t	1.26 in	0.85	1.77 in	1.22
Radius of toroidal knuckle, r	29.28 in	32.14 in	34.35 in	46.09 in
Angle of toroidal knuckle, ϕ	58.62^o	56.98^o	61.99^o	56.98^o
Radius of spherical cap, R	95.91 in	90.57 in	156.83 in	129.84 in
Angle of spherical cap, θ	32.38^o	33.02^o	28.01^o	33.02^o
Total weight of dome end	913.06 lbf	634.1 lbf	2486.9 lbf	1870.9 lbf
Elastic – Plastic buckling pressure, P_b	8216.6 psi	2737.7 psi	6273.85 psi	2742.8 psi

TABLE 4: The numerical comparison table of torispherical dome ends

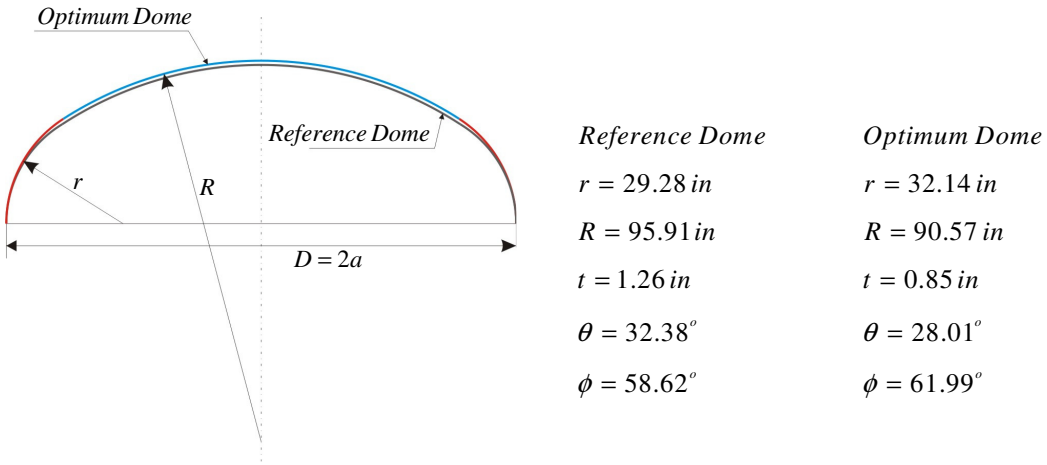

FIGURE 3: The dome configuration comparison of model 1 for minimum weight design

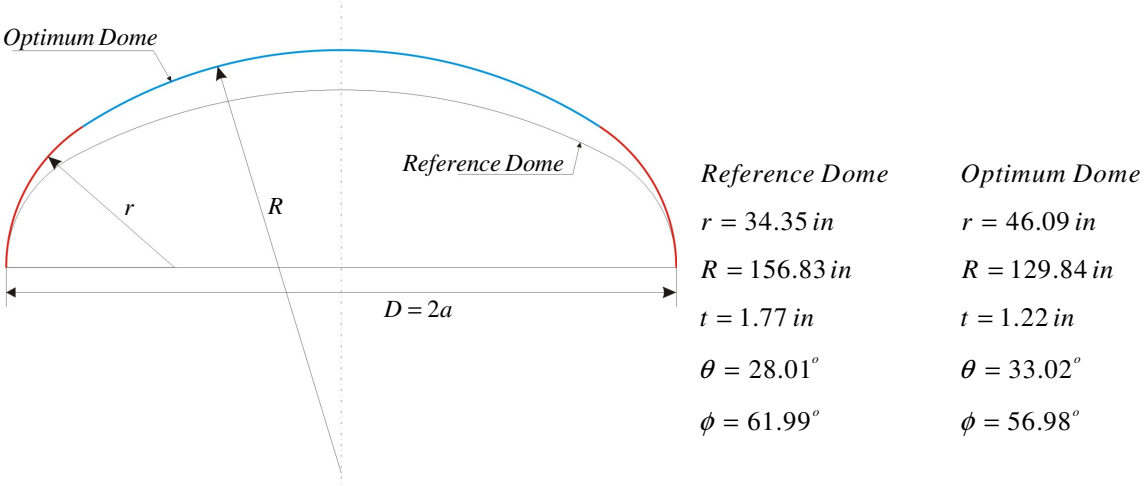

FIGURE 4: The dome configuration comparison of model 2 for minimum weight design

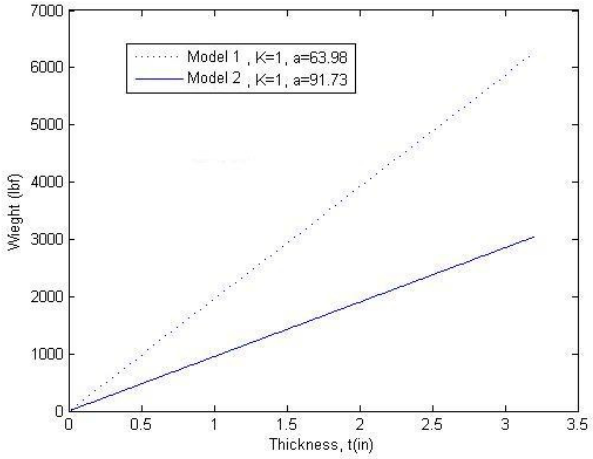

FIGURE 5: The weight via thickness of hemispherical dome end

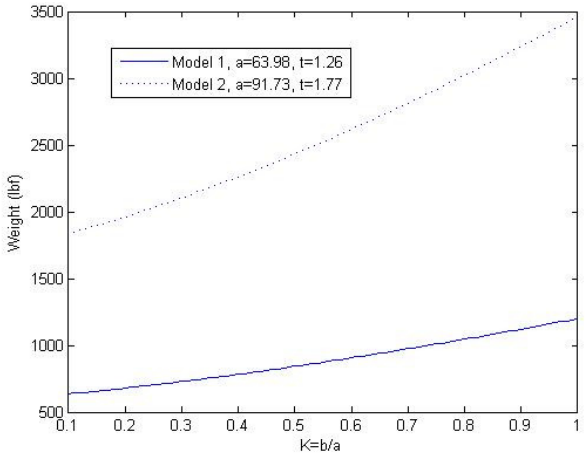

FIGURE 6: The weight via the slope K of torispherical dome end

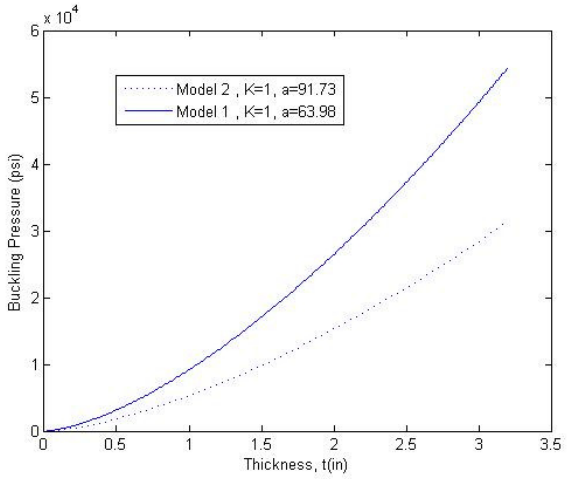

FIGURE 7: The buckling pressure via thickness of hemispherical dome end

Model 1 $K=1\ ,\ a=63.98\ in$		**Model 2** $K=1\ ,\ a=91.73\ in$	
$t\,(in)$	$P_b\,(psi)$	$t\,(in)$	$P_b\,(psi)$
0.2	718.7	0.2	450.4
0.4	2257	0.4	1301
0.6	4193	0.6	2419
0.8	6519	0.8	3756
1.0	9173	1.0	5285
1.2	12124	1.2	6986
1.4	15349	1.4	8845
1.6	18828	1.6	10850
1.8	22546	1.8	12992
2.0	26490	2.0	15265
2.2	30648	2.2	17661
2.4	35013	2.4	20176
2.6	39574	2.6	22804
2.8	44325	2.8	25542
3.0	49260	3.0	28386

TABLE 5: The buckling pressure table at some corresponding thickness of hemispherical dome end

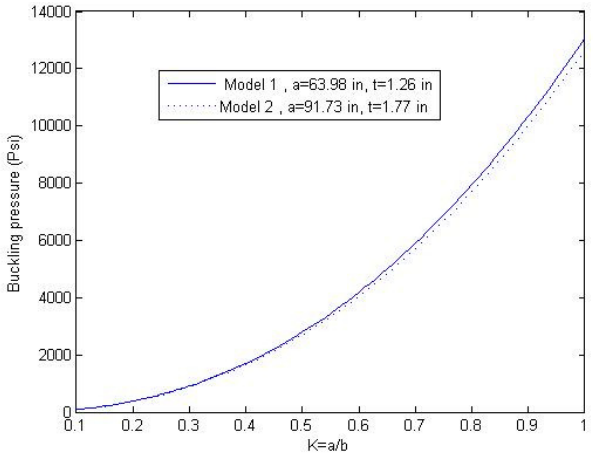

FIGURE 8: The Buckling Pressure via the Slope K of Torispherical Dome End

Model 1 $t=1.26\ ,\ a=63.98\ in$		**Model 2** $t=1.77\ ,\ a=91.73\ in$	
$K=b/a$	$P_b\,(psi)$	$K=b/a$	$P_b\,(psi)$
0.1	91.97	0.1	89.14
0.2	384.2	0.2	372.3
0.3	910.6	0.3	882.6
0.4	1703	0.4	1651
0.5	2787	0.5	2702
0.6	4182	0.6	4054
0.7	5902	0.7	5721
0.8	7954	0.8	7709
0.9	10341	0.9	10023
1.0	13064	1.0	12662

TABLE 6: The buckling pressure table at some corresponding thickness of hemispherical dome end

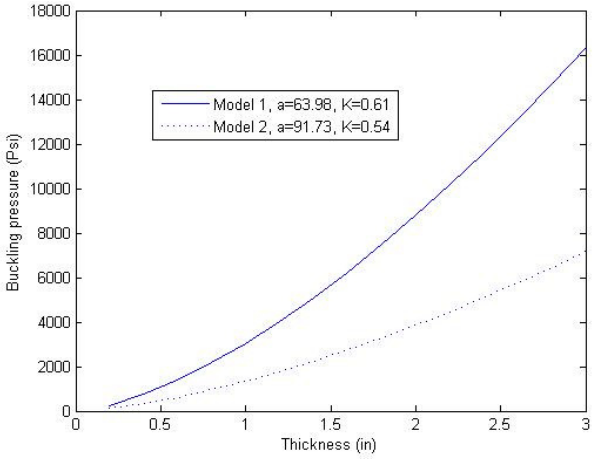

FIGURE 9: The buckling pressure via thickness of torispherical dome end

Model 1 $K = 1.61$, $a = 63.98\ in$		**Model 2** $K = 0.53$, $a = 91.73\ in$	
$t(in)$	$P_b\,(psi)$	$t(in)$	$P_b\,(psi)$
0.2	259.7	0.2	114.0
0.4	750.0	0.4	329.3
0.6	1394	0.6	612.4
0.8	2165	0.8	951.1
1.0	3047	1.0	1338
1.2	4027	1.2	1768
1.4	5099	1.4	2239
1.6	6254	1.6	2746
1.8	7490	1.8	3289
2.0	8800	2.0	3864
2.2	10182	2.2	4471
2.4	11632	2.4	5107
2.6	13147	2.6	5773
2.8	14725	2.8	6466
3.0	16365	3.0	7186

TABLE 7: The buckling pressure table at some corresponding thickness of hemispherical dome end

From table 3 and 4 and Figure 3 and 4, the ratio of K is found to be 0.64 for optimal model 1 and mode2 by using Genetic algorithm and it is found to be 0.65 for both of models when we use imperialist competitive algorithm (ICA), while the ratios of K are chosen as 0.61 and 0.53 for the reference models. The critical buckling pressure are $2741.7\ psi$ for optimum model 1 and $2715.9\ psi$ for optimum model 2 by using genetic algorithm and $2737.7\ psi$ and $2742.8\ psi$ for imperialist competitive algorithm (ICA) and for reference models being $8216.6\ psi$ and $6273.8\ psi$.

According to this fact that the ratios of K for the optimum models are bigger than that of reference models, the shape of the optimum dome ends of two models tend to be bigger than the reference models, while the buckling pressures are lower than the reference models. Because of we set the preassigned buckling pressure bound ($8.33P_w \le P_b \le 10.4P_w$) and select the minimum weight type of cost function, the weight is reduced by 29.4% for model 1 and

24.1% for model 2 when we optimized by genetic algorithm and 30% for model 1 and 24.7% for model 2 while imperialist competitive algorithm is our optimization method.

From table 7 and Figure 9, the critical buckling pressure for a constant ratio K torispherical dome end is to be raised with the increase of the thickness. Also, the other important factor of the total weight of the torispherical dome end is thickness. However, the larger the thickness, the greater the weight and this situation must be taken into account.

7. CONSLUSION & FUTURE WORK

The four-centered ellipse method is a very easy and good method to describing the shape of the torispherical dome end and it makes the shape optimization problem very easy. This methodology uses only two design variables: thickness and the ratio of minor axis to major axis K. Imperialist competitive algorithm is a very efficient and easy to use algorithm for optimization problems such as the optimization of torispherical dome end subject to internally pressurized loading and the results of imperialist competitive algorithm are very close to the results of genetic algorithm.

For future study, the optimum design of composite torispherical dome end may consider such factor as buckling pressure, strength, space use, manufacturing cost, safety, weight, and so on.

8. REFERENCES

1. A. Gaiewski, M. Zyczkowski. *"Optimal structural design under stability constraints".* In Mechanics of Elastic Stability (Edited by H. H. E. Leipholz and G. E.Oraras). Kluwer, 1988

2. J. Farkas. *"Optimum Design of Metal Structures"*. John Wiley, New York. 1984

3. J. Middleton and J. Petmska, *"Optimal pressure vessel shape design to maximize limit load*". Engng. Comput. 3, 287-294, 1988

4. E. H. Mansfield, "*An optimum surface of revolution for pressurized shell*". Int. J. Mech. Sci. 23, 57-62. 1981

5. J. Blachut, "*Search for optimal torispherical end closures under buckling constraints*". Int. J. Mech. Sci. 31, 623-633. 1989

6. J. Blachut, *"Optimally shaped torispheres with respect to buckling and their sensitivity to axisymmetric imperfections*" Comput. Struct. 29, 975-981, 1987

7. T. E. French, C. J. Vierckand and R. J. Foster, "*Engineering Drawing and Graphic Technology"*, 3rd edn. McGraw-Hill, 1987.

8. Atashpaz-Gargari, E., Lucas, C. *"Imperialist Competitive Algorithm: An algorithm for optimization inspired by imperialistic competition*", IEEE Congress on Evolutionary Computation, 4661–4667. 2007

9. Atashpaz-Gargari, E., Hashemzadeh, F., Rajabioun, R. and Lucas, C. *"Colonial Competitive Algorithm, a novel approach for PID controller design in MIMO distillation column process",* International Journal of Intelligent Computing and Cybernetics, 1 (3), 337–355. 2008

10. Rajabioun, R., Atashpaz-Gargari, E., and Lucas, C*., "Colonial Competitive Algorithm as a Tool for Nash Equilibrium Point Achievement"*. Lecture notes in computer science, 5073, 680-695. 2008

11. Lucas. C., Nasiri-Gheidari. Z., Tootoonchian. F*., "Application of an imperialist competitive algorithm to the design of a linear induction motor*", Energy Conversion and Management. 51, pp. 1407–1411. 2010

12. R. Rajabioun, E. Atashpaz-Gargari, C. Lucas., *"Colonial Competitive Algorithm as a Tool for Nash Equilibrium Point Achievement*" , Springer LNCS, Book Chapter, 2008

13. E. Hosseini Nasab, M.Khezri, M.Sahab Khodamoradi, E. Atashpaz Gargari., *"An application of Imperialist Competitive Algorithm to Simulation of Energy Demand Based on Economic Indicators: Evidence from Iran",* European Journal of Scientific ResearchVol.43 No.4, pp.495-506, 2010

14. J. F. Harvey, *"Pressure Component Construction: Design and Materials Application*". Van Nostrand Reinhold, New York. 1980

Intelligent Controller Design for a Chemical Process

Mr. Glan Devadhas G. glandeva@gmail.com
Research Scholar,
PRIST University,
Thanjavur

Dr.Pushpakumar S. spushpakumar@gmail.com
Former Principal,
Govt College of Engineering,
Kannur

Abstract

Chemical process control is a challenging problem due to the strong on-line non-linearity and extreme sensitivity to disturbances of the process. Ziegler – Nichols tuned PI and PID controllers are found to provide poor performances for higher-order and non–linear systems. This paper presents an application of one-step-ahead fuzzy as well as ANFIS (adaptive-network-based fuzzy inference system) tuning scheme for an Continuous Stirred Tank Reactor CSTR process. The controller is designed based on a Mamdani type and Sugeno type fuzzy system constructed to model the dynamics of the process. The fuzzy system model can take advantage of both a priori linguistic human knowledge through parameter initialization, and process measurements through on- line parameter adjustment. The ANFIS, which is a fuzzy inference system, is implemented in the framework of adaptive networks. The proposed ANFIS can construct an input-output mapping based on both human knowledge (in the form of fuzzy if-then rules) and stipulated input-output data pairs. In this method, a novel approach based on tuning of fuzzy logic control as well as ANFIS for a CSTR process, capable of providing an optimal performance over the entire operating range of process are given. Here Fuzzy logic control as well as ANFIS for obtaining the optimal design of the CSTR process is explained. In this approach, the development of rule based and the formation of the membership function are evolved simultaneously. The performance of the algorithm in obtaining the optimal tuning values has been analyzed in CSTR process through computer simulation.

Keywords*:* Ziegler – Nichols tuning, Fuzzy Logic, ANFIS, CSTR Process.

1. INTRODUCTION

System Modeling based on conventional mathematical tools (e.g., differential equations) is not well suited for dealing with ill-defined and uncertain systems. In contrast, a fuzzy inference system employing fuzzy if-then rules can model the qualitative aspects of human knowledge and reasoning processes without employing precise quantitative analysis. Some basic aspects of this approach are discussed below.

1) No standard methods exist for transforming human knowledge or experience into the rule base and database of a fuzzy inference system.
2) There is a need for effective method for tuning the membership functions (MF's) so as to minimize the output error measure or maximize performance index.

The regulation and control of CSTR process is a typical problem found in a variety of industries including pharmaceuticals, biotechnology and chemical processing. Normally in process control laboratories, the processes are subjected to load disturbances. ANFIS as well as Fuzzy provide a good regulation against sudden changes and restore the desired process state within a shortest possible time. There are many methods for tuning PID controllers. Some of them are Ziegler-Nichols (ZN), Cohen and Coon (CC), Internal Model Control (IMC) and Performance criteria optimization (PCO). Ziegler-Nichols tuning [1] is one of the most widely used method to tune the PID controllers. Tuning the controller by Ziegler-Nichols method does not provide optimum system response since they are dependent on the exact mathematical model of a process. Cohen and Coon method [2] requires limited process knowledge but it offers low damping and high sensitivity to the system. Internal model control [3] is easy to shape sensitivity function but for unstable plants it cannot be applied. The adaptive learning algorithm of Universal Learning Network (ULN) represents the modeling and control of nonlinear black box systems with large time delay [4]. The main difficulty in control is due to the disturbances and parameter uncertainties. The fuzzy modeling or fuzzy identification, first explored systematically by Takagi and Sugeno [5], has found numerous practical applications in control, prediction and inference [6], [7]. Rest of the paper is organized as follows.

System description is given in Section 2. Section 3 introduces the basics of fuzzy inference system. Section 4 describes the structures and learning rules of adaptive networks. Simulation is given in Section 5. Simulation Results are shown in Section 6.Section 7 concludes this paper with some extensions of this work.

2. SYSTEM DESCRIPTION

A chemical system common to many chemical processing plants, known as a continuous stirred tank reactor (CSTR), was utilised as a suitable test for, TSK Fuzzy control, ANFIS control and PID control. It suffices to know that within the CSTR two chemicals are mixed, and react to produce a product compound with concentration Ca(t). The temperature of the mixture is $\vartheta(t)$ .A schematic representation of the system is shown in Fig. 1.The reaction is exothermic, producing heat which acts to slow the reaction down. By introducing a coolant flow rate qc(t), the temperature can be varied and hence the product concentration controlled. This system can be described by the following nonlinear simultaneous differential equations1 which effectively combine the laws of chemical reaction and thermodynamics:

$${}^{\cdot}Ca(t) = Q(Ca0 - Ca(t))/V - k0Ca(t)e - E/R\vartheta(t) \quad \ldots\ldots\ldots\ldots\ldots\ldots\ldots\ldots\ldots\ldots\ldots\ldots(1)$$

$${}^{\cdot}\vartheta(t) = Q(\vartheta 0 - \vartheta(t))/V + k1Ca(t)e - E/R\vartheta(t) + k2qc(t)\ (1 - e - k3/qc\ (t))\ (\vartheta c0 - \vartheta(t))\ldots\ldots\ (2)$$

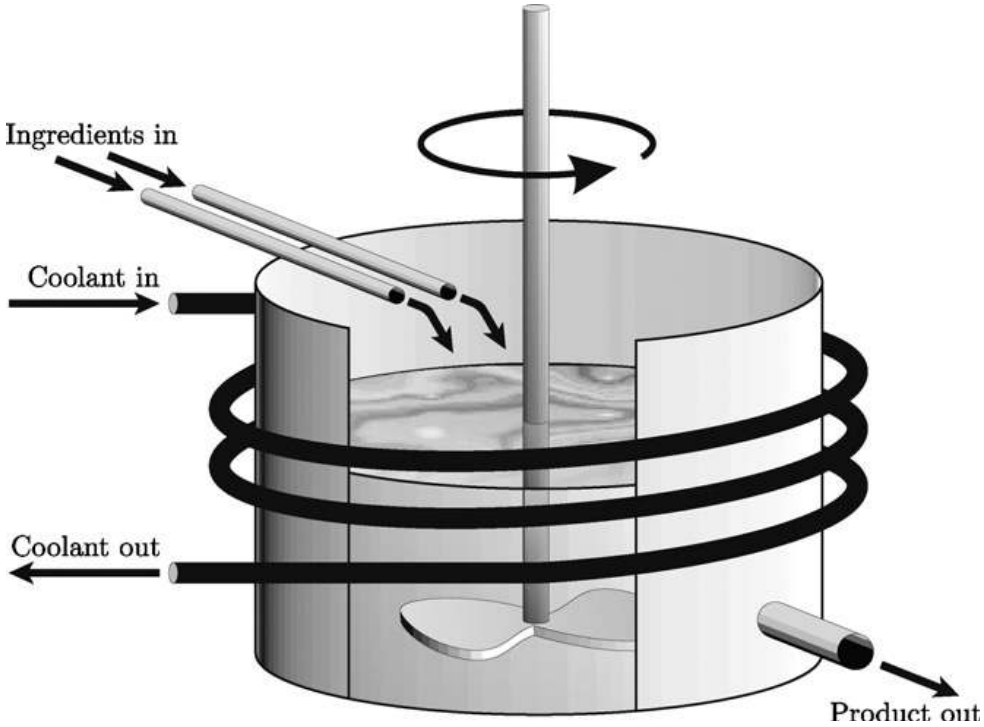

FIGURE 1: CSTR process

Parameter	Description	Nominal value
Q	Process flow rate	100 l/min
V	Reactor volume	100 l
k0	Reaction rate constant	7.2 × 1010 1/min
E/R	Activation energy	1 × 104 K
ϑ0	Feed temperature	350K
ϑC0	Inlet coolant temperature	350K
ΔH	Heat of reaction	−2 × 105 cal/mol
Cp, Cpc	Specific heats	1 cal/gK
ρ,ρc	Liquid densities	1 × 103 g/l
Ca0	Inlet feed concentration	1mol/l
ha	Heat transfer coefficient	7 × 105 cal

TABLE 1: The CSTR parameters

Consider the flow rate qc(t) as the input and product concentration Ca(t) as the output of the system. As seen from Fig. 2, the gain and damping of the system vary widely over the whole operating region, from 0.08 mol/l to 0.13 mol/l.

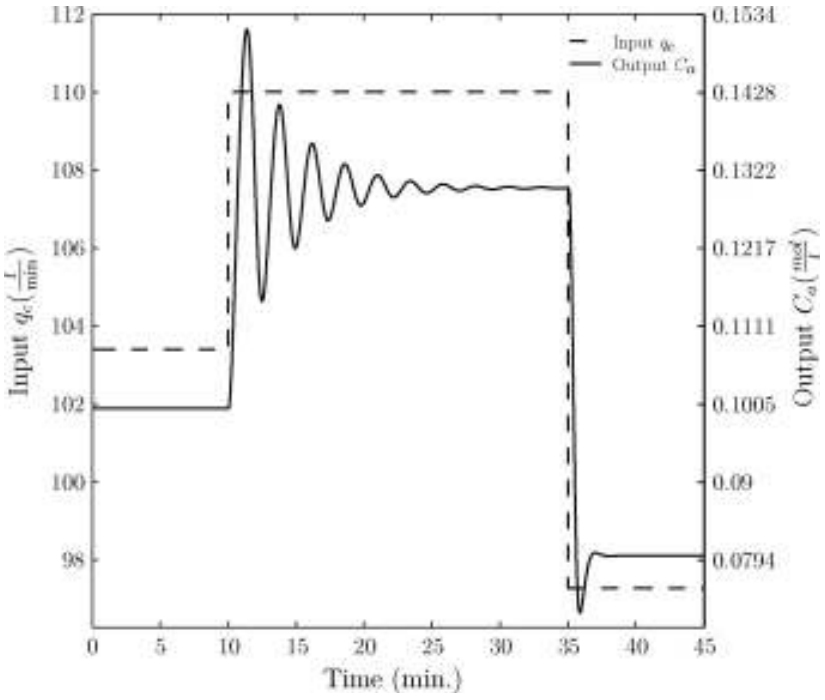

FIGURE 2: Open-loop step response of the CSTR

3. FUZZY INFERENCE SYSTEM

Fuzzy inference systems are also known as fuzzy-rule-based systems, fuzzy models, fuzzy associative memories (FAM).It is also known as fuzzy controllers when used as controllers. Basically a fuzzy inference system is composed of five functional blocks.

- a rule base containing a number of fuzzy if-then rules.
- a database which defines the membership functions of the fuzzy sets used in fuzzy rules.
- a decision-making unit which performs the inference operation of the rules.
- a fuzzification interface which transforms the crisp inputs into degrees of match of the linguistic variables.
- a defuzzification interface which transforms the fuzzy results of the interface into crisp output. Usually, the rule base and the database are jointly referred to as the knowledge base.

The overall output is the weighted average of each rule's crisp output induced by the rule's firing strength (the product or minimum of the degrees of match with the premise part) and output membership functions. The output membership functions used in this scheme must be monotonic functions [8]. The overall fuzzy output is derived by applying "max" operation to the qualified fuzzy outputs (each of which is equal to the minimum of firing strength and the output membership function of each rule). Various schemes have been proposed to choose the final crisp output based on the overall fuzzy output; some of them are centroid of area, bisector of area, mean of maxima, maximum criterion, etc [9],[10].

4. ADAPTIVE NETWORKS: ARCHITECTURES AND LEARNING ALGORITHM

This section introduces the architecture and learning procedure of the adaptive network which is in fact a superset of all kinds of feed forward neural networks with supervised learning capability. The basic learning rule of adaptive networks is based on the gradient descent and the chain rule, which was proposed by Werbos [11] in the 1970's. However, due to the state of artificial neural network research at that time, Werbos' early work failed to receive it's desired attention .

4.1 Architecture and Basic Learning Rule

An adaptive network is a multilayer feed forward network in which each node performs a particular function (node function) on incoming signals as well as a set of parameters pertaining to this node. The formulas for the node functions may vary from node to node, and the choice of each node function depends on the overall input-output function which the adaptive network is required to carry out. Note that the links in an adaptive network only indicate the flow direction of signals between nodes; no weights are associated with the links.

4.2 ANFIS: Adaptive-Network-based Fuzzy Inference System.

Functionally, there are almost no constraints on the node functions of an adaptive network except piecewise differentiability. Structurally, the only limitation of network configuration is that it should be of feed forward type. Due to these minimal restrictions, the adaptive network's applications are immediate and immense in various areas. We propose a class of adaptive networks which are functionally equivalent to fuzzy inference systems.

4.2.1. ANFIS Architecture

For simplicity, we assume the fuzzy inference system under consideration has two inputs x and y and one output z.

Suppose that the rule base contains two fuzzy if-then rules of Takagi and Sugeno's type [8].
Rule 1: If x is A_1 and y is B_1, then $f1 = p_1x + q_1y + r_1$ (3)
Rule 2: If x is A_2 and y is B_2, then $f_2= p_2x + q_2y + r_2$ (4)

Then the fuzzy reasoning is illustrated in Fig. 3 and the corresponding equivalent ANFIS architecture is shown in Fig. 4

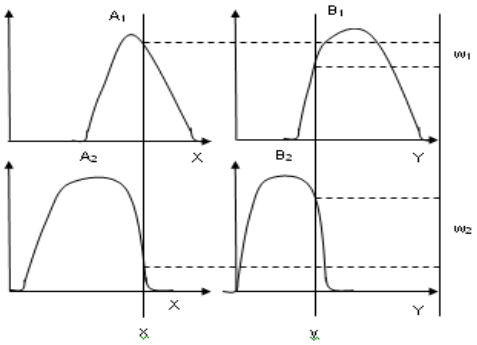

FIGURE 3: Fuzzy Reasoning

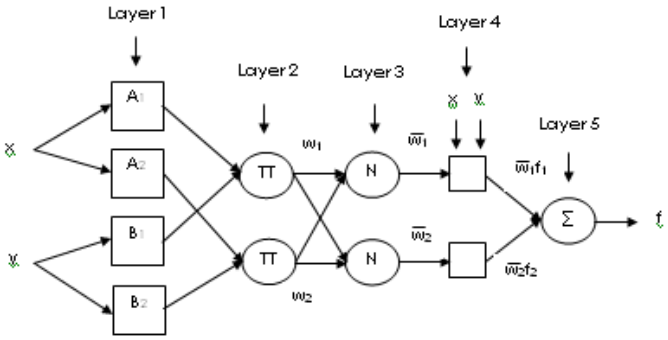

FIGURE4. Equivalent ANFIS

The node functions in the same layer are of the same function family as described in [12], [13].

Layer 1: Every node i in this layer is a square node with a node function:

$O_{1,i} = \mu A_i(x)$ for i = 1,2 or (5)
$O_{1,i} = \mu B_{i-2}(y)$ for i = 3,4 (6)

Where x (or y) is the input to node i, and A_i(or B_{i-2}) is the linguistic label (small , large, etc.) associated with this node function. In other words, $O_{1,i}$ is the membership grade of a fuzzy set A(= A_1,A_2,B_1 or B_2), and it specifies the degree to which the given input x (or y) satisfies the quantifier A. Usually we choose (x) to be bell-shaped function as :

$$\mu A_i(X) = \frac{1}{1+\left[\left(\frac{X-c_i}{a_i}\right)^2\right]b_i} \qquad (7)$$

Where {a_i, b_i, c_i} is the parameter set. As the values of these parameters change, the bell-shaped functions vary accordingly, thus exhibiting various forms of membership functions for a fuzzy set. Parameters in this layer are referred to as premise parameters.

Layer 2: Every node in this layer is a circle node labeled TT, whose output is the product of all the incoming signals:

$O_{2,i} = w_i = \mu A_i(x)\, \mu B_i(y)$ i = 1,2 (8)

Each node output represents the firing strength of a rule. (In fact, other T-norm operators that performs generalized AND can be used as the node function in this layer.)

Layer 3: Every node in this layer is a circle node labeled N. The ith node calculates the ratio of the ith rule's firing strength to the sum of all rules firing strengths:

$$O_{3,i} = \frac{w_i}{w_1 + w_2} \qquad i = 1,2 \quad (9)$$

For convenience, outputs of this layer will be called normalized firing strengths.

Layer 4: Every node i in this layer is a square node with a node function:

$O_{4,i} = \overline{w_i}\, f_i = \overline{w_i}\, (p_i x + q_i y + r_i)$ (10)

Layer 5: The single node in this layer is a fixed node labeled Σ that computes the overall output as the summation of all incoming signals
Overall Output is given by:

$$O_{5,i} = \frac{\sum w_i f_i}{\sum w_i} \qquad (11)$$

5. SIMULATION

5.1. Fuzzy logic control simulation

In this paper, we have presented a Fuzzy logic control for obtaining the optimal design of the CSTR process. In this approach, the development of rule base and the formation of the Gaussian membership function are evolved simultaneously. The fuzzy rules we have used in this work is shown in Fig 5. In order to extract the best crisp value for defuzzification, mean of maximum method is used. The performance of the algorithm in obtaining the optimal values of Fuzzy controller parameters has been analyzed in CSTR process through computer simulation.

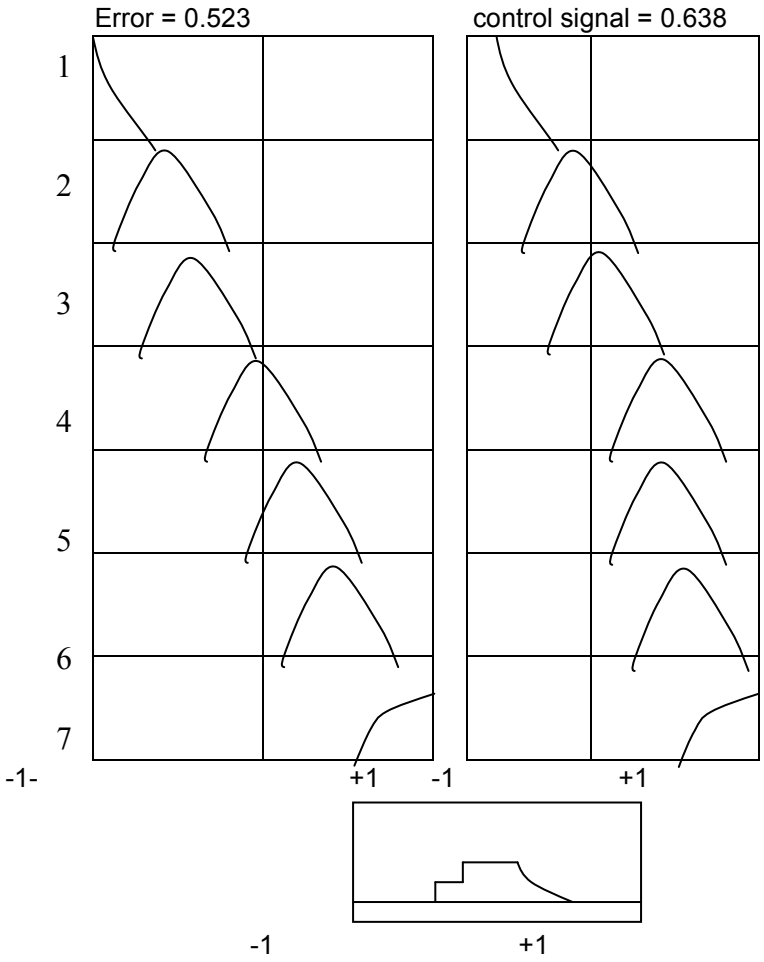

FIGURE 5: Fuzzy Rules

In this approach, the development of rule base and the formation of the membership function are evolved simultaneously. The input and output membership functions chosen for tuning are shown in Fig 6(a) and Fig 6(b) respectively.

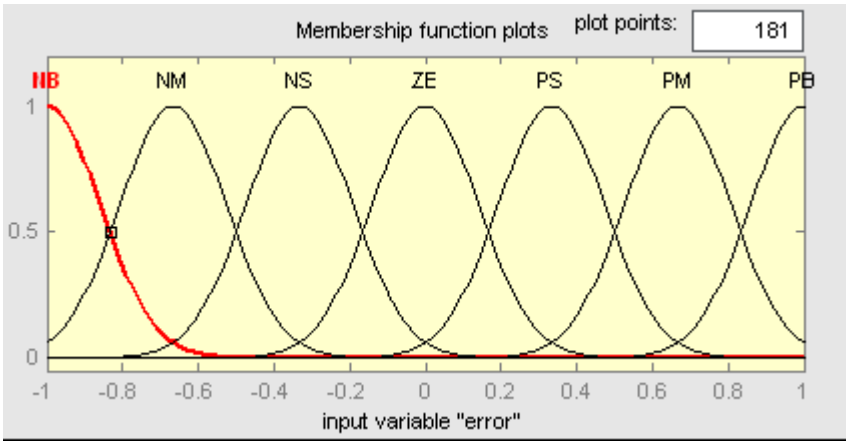

FIGURE 6 :(a). Input membership function plot

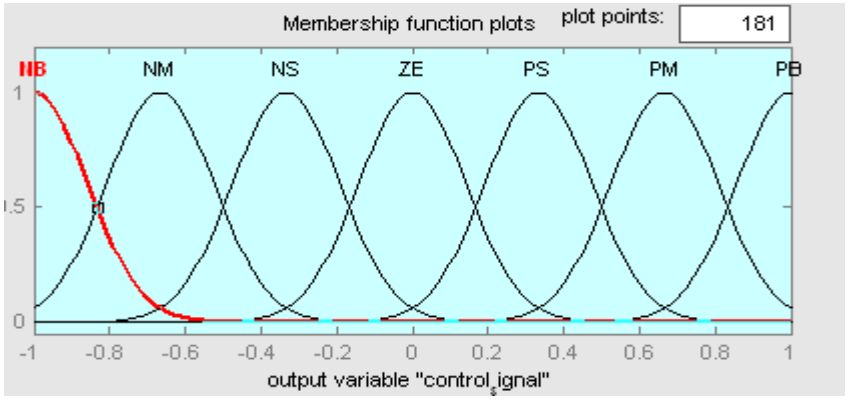

FIGURE 6(b). Output membership function plot

5.2. ANFIS simulation

Here an ANFIS tuning for obtaining the optimal design of the CSTR process is simulated. The ANFIS rules and model structure we have chosen in our work are shown in Fig 7 and Fig 8. It is found that the development of ANFIS makes the CSTR process more efficient. The configuration of ANFIS can be reduced and is smaller than Mamdani fuzzy system. The ANFIS model structure chosen has five layers. The performance of the algorithm has been analyzed in CSTR process through computer simulation.

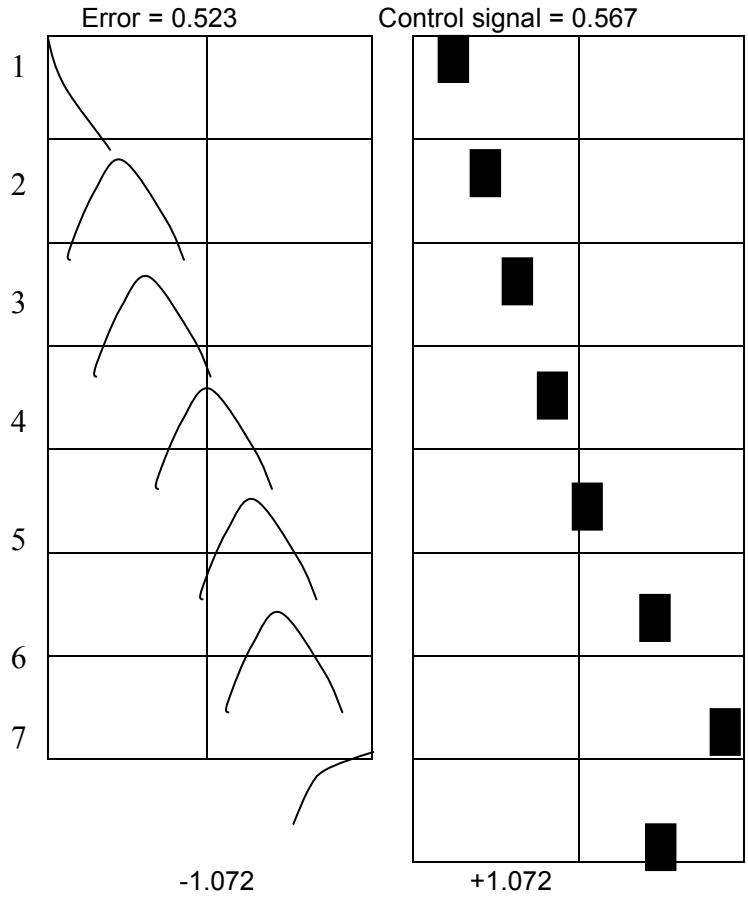

FIGURE 7: ANFIS Rules

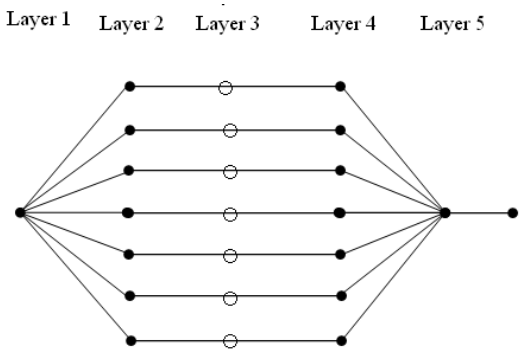

FIGURE 8: ANFIS Model Structure

6. SIMULATION RESULTS

The tuning of a CSTR process is carried out by both Fuzzy Logic as well as ANFIS. The development of ANFIS makes the CSTR process more efficient than that of using a fuzzy. The configuration of ANFIS can be reduced and made smaller than Mamdani fuzzy system. The responses of CSTR for temperature change which is the main disturbance using Z.N,fuzzy logic and ANFIS are shown in Fig 9. The response of CSTR for change in setpoint using Z-N,Fuzzy andANFIS are shown in Fig 10 and The simulation results are given in Table 2.It is seen from the table that that ANFIS tuned CSTR process

Gives the better performance in all aspects(Delay Time, Rise Time, Peak Time, Settling Time and Peak Overshoot).The fuzzy logic tuned CSTR process is better than Ziegler – Nichols tuned CSTR process.

Tuning Methods	Delay Time(Secs)	Rise Time (Secs)	Peak Time (Secs)	Settling Time (Secs)	Peak Overshoot(%)
Ziegler - Nichols	2	1	9.5	50	18
FuzzyLogic	1.2	0.8	7.5	32	14
ANFIS	0.8	0.6	6.0	20	8

TABLE 2 Comparison of various Tuning Methods

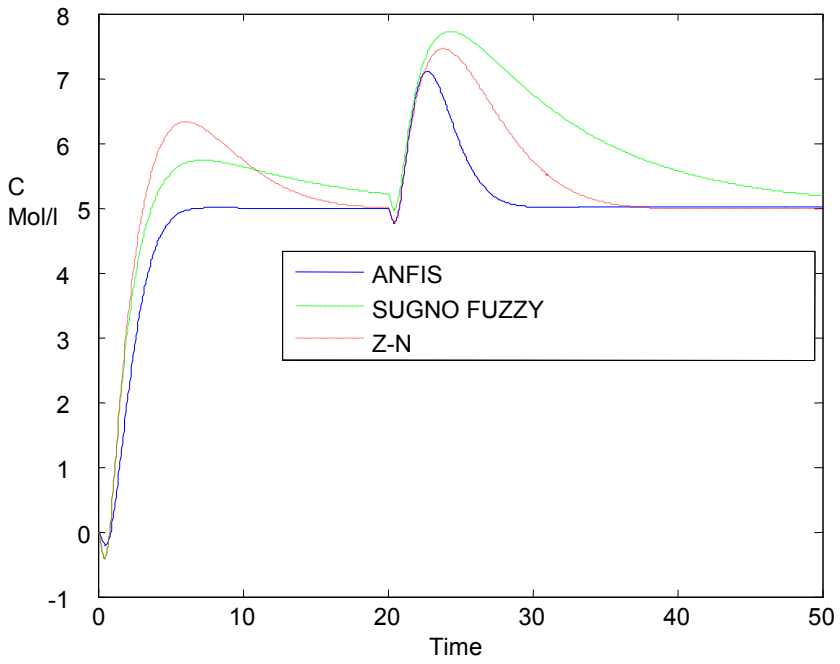

FIGURE 9: Response of CSTR process for Temperature change

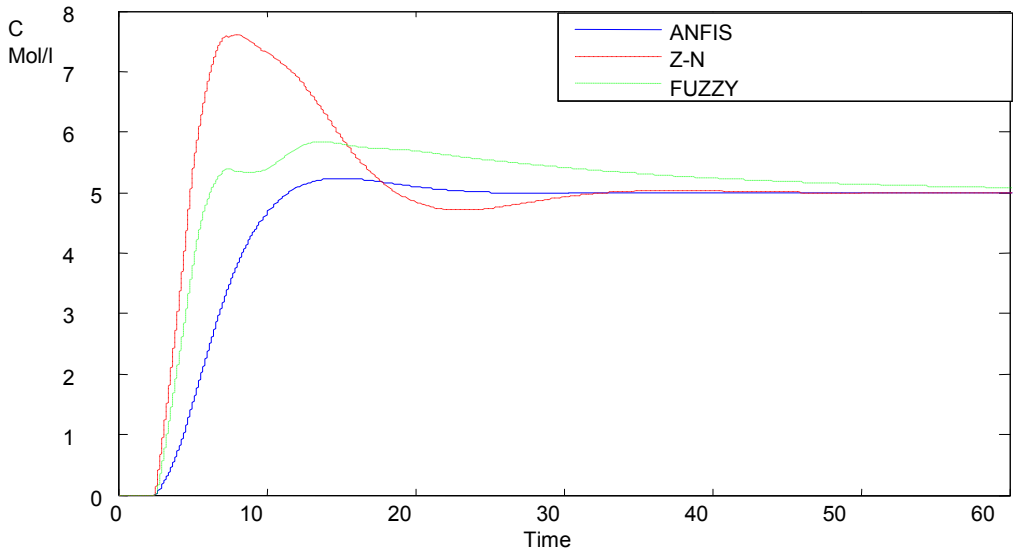

FIGURE10. Response of a CSTR Process for set point variations

7. CONCLUSION

We have described the tuning of an industrial CSTR process using Fuzzy – Logic control as well as ANFIS. This paper describes an intelligent method to tune the controller for a CSTR process. It also discuss the temperature variation and variation in concentration both are in interacting in nature are dealt with this intelligent method .

The controller developed here clearly give the solution of the MIMO process where both concentration and temperature are controlled simultaneously .

The tuning of the controller for CSTR process using Z-N, Fuzzy, and ANFIS for variations in concentration and temperature. Results show that the performance obtained by ANFIS method is better than Z-N and Fuzzy tuning methods. The ANFIS configuration is reduced and smaller than Fuzzy system. Simulation of response of CSTR for change in set point and temperature(disturbance) configuration are shown in Fig 10and Fig9..The performance are compared and tabulated in Table 2.

The ANFIS controller designed here gives better response than other methods [12],[14] &[17] in the simulation mode. This method incorporates the knowledge base system which makes it more intelligence.

Thus in this paper, the parameter notification is solved through the learning rule. By employing a proper learning procedure, the proposed process can refine the ANFIS model to obtain the tuning of the CSTR process.

8. REFERENCES

1. K.J. Astrom, & T. Hagglund, "*The future of PID control Control Engineering Practice",* pp.1163 -1175. 2001.

2. F. G. Shinskey, *"process control system: application, design and tuning"* (McGraw-Hill, 4th Ed., 1996).

3. K. Yamada, & K. Watanabe, "*A State Space Design Method of Stable filtered Inverse Systems and Its Application to H2 Suboptimal Internal Model Contro"l*, Proc. IFAC96,1996, pp.379-382.

4. A.P. Loh, K.O. Looi, & K.F. Fong, "*Neural network modeling and control strategies for a CSTR neutralization process",* Journal of Proc. Control, 6: 355-362.1995.

5. T. Takagi, & M. Sugeno, Fuzzy identification of systems and its applications to modeling and control,*IEEE Trans. Syst., Man, Cybern.,vol. 15*, pp. 116-132, 1985.

6. S. J. Qin, & G. Borders, *"A multiregion fuzzy logic controller for nonlinear process control",* IEEE Transactions on Fuzzy Systems, 2:74–81.1994,

7. Rajani K. Mudi, Chanchal Dey, & Tsu – Tian Lee, *"An improved auto – tuning scheme for PI controllers*", Journal of science Direct ISA Transactions ,47 : 45 – 52,2008.

8. T. Takagi, & M. Sugeno, "*Derivation of fuzzy control rules from human operator's control actions"*, Proc. IFAC Symp. Fuzzy Inform. Knowledge Representation and Decision Analysis, pp. 55-60. July 1983,

9. C.-C. Lee, "*Fuzzy logic in control systems: Fuzzy logic controller-Part I*." IEEE Trans. Syst., Man, Cybern., 20: 404 -418, 1990.

10. *"Fuzzy logic in control systems: Fuzzy logic controller-Part II".* IEEE Trans. Syst., Man, Cybern., 20: 419-435, 1990

11. P. Werbos, beyond regression: "*New tools for prediction and analysis in the behavioral sciences".* Doctoral diss. Harvard Univ., Cambridge, MA, 1974.

12. Luis E. Zarate, Peterson Resende, & M. Benjamin*," A Fuzzy Logic and Variable Structure Base Controller for CSTR Control*". Annual conference of IEEE, 2001.

13. "*Rule extraction using generalized neural networks*," Proc. 4th IFSA World Congress, July 1991.

14. Tipsuwanporn.V, S.Intajag, K.Witheephanich, N.Koetsam-ang and S.Samiamag, *"Neuro-Fuzzy Controller Design for Industrial Process Contro*l"s, PP :1656-1661, SICE 2004.

15. Toru Yamamoto and Sirish L. Shah, "*Design of a Performance-Adaptive PID controller",*.International conference on Networking,Sensing and Control IEEE 2007 pp547-552.2007.

16. Xiao-Feng Li, Jian Sun, Hui-Yan Wu, Wei-Dong Zong, *"Application of the fuzzy PID to the Power Plant*", IEEE 2007

17. Yun Li,Kiam Heong Ang and Gregory C.Y.Chong, "*PID Control System Analysis and Design – Problems, Remedies, and Future Directions*". IEEE control system magazine, February 2006 pp. 32-41,2006

18. Yamada.K, & K. Watanabe, "*A State Space Design Method of Stable filtered Inverse Systems and Its Application to H2 Suboptimal Internal Model Control"*, Proc. IFAC96, 1996, pp.379-382.1996

Applications of Circulation Control, Yesterday and Today

Jonathan Kweder jonathan.kweder@mail.wvu.edu
Center for Industrial Research Applications
West Virginia University
Morgantown, WV USA

Chad C. Panther chad.panther@mail.wvu.edu
Center for Industrial Research Applications
West Virginia University
Morgantown, WV USA

James E. Smith james.smith@mail.wvu.edu
Center for Industrial Research Applications
West Virginia University
Morgantown, WV USA

Abstract

Circulation control, an aerodynamic method of changing the properties of an airfoil, such as lift, camber and angle of attack, has been used in several unique ways since its inception, as an enhancement to fixed wing aircraft, in the 1960's. Early in the research venture, this technology was used on the main wing of an aircraft in conjunction with a Coandă surface, such as a rounded trailing edge or a deployable flap. Research during this time proved to be the foundation of the circulation control technology and showed that small amounts of exit jet velocity could have a large impact on the aerodynamics of an airfoil.

In the 1970's the inspirations that drove circulation control research changed from design work to optimization of the parameters which were found to have the most effect on circulation control. These studies included slot placement, favorable momentum coefficient, and pressurization benefits and determents. This research period also allowed for expansion of the uses of circulation control to submarine/hydrodynamic and rotary wing applications.

Newest research has brought on several propeller driven applications and the recent push for efficient renewable research has allowed circulation control research technologies to evolve into use in wind turbine and water turbine applications. The idea being that with circulation control the turbine can adapt easier to the changing wind velocity and direction and ultimately capture more power than an un-augmented turbine.

As with most new and novel technologies there is a process and time delay associated with their development and ultimate application. For some technologies the market, or the supporting hardware, are lacking and sometimes the technology has strong advocacies for yet to be fulfilled expectations. In most of these cases a strong idea will re-surface repeatedly until the art has matured, or the better solution is found. This

paper will focus on the previously developed circulation control research, from its beginnings, as used on fixed wing aircraft, following the progression, as this technology evolved through the past five decades, to its now more widely considered potential.

Keywords: Circulation Control, Lift Augmentation, Drag Reduction

NOMENCLATURE

AUV	*Autonomous Underwater Vehicle*	***NREL***	*National renewable Energy Laboratory*
c	*Airfoil Chord*	***NSRDC***	*Naval Ship Research and Development Center*
CC	*Circulation Control*	***NSWC***	*Naval Surface Warfare Center*
CCR	*Circulation Control Rotor/Rudder*	***R***	*Radius*
C_D	*Drag Coefficient*	***t***	*Airfoil Thickness*
C_L	*Lift Coefficient*	***TE***	*Trailing Edge*
C_m	*Moment Coefficient*	V_∞	*Freestream Velocity*
C_p	*Center-of-Pressure*	***VAWT***	*Vertical Axis Wind Turbine*
C_μ	*Momentum/Blowing Coefficient*	***V/STOL***	*Vertical/Short Take-Off Landing*
D	*Drag*	α	*Angle-of-Attack*
HAWT	*Horizontal Axis Wind Turbine*	$\Delta C_l/C_\mu$	*Lift Augmentation Factor*
L	*Lift*	ρ_∞	*Density*
LE	*Leading Edge*	Γ	*Circulation*
L/D	*Lift-to-Drag Ratio*	Ω	*Rotational Speed*
		μ	*Advance Ratio*

1. INTRODUCTION

Circulation control (CC) as a lift augmentation device is traditionally used on the main wing of an aircraft. This technology has been in the research and development phase for over sixty years, primarily for fixed wing aircraft with the early models referred to as “blown flaps.” The first reported use of blowing slots to control lift is attributed to H. Hagedorn and P. Ruden, in 1938, who noticed an unaccountable increase in lift at high blowing rates during investigations into boundary layer control on a flap [34]. Interest in active blowing systems increased with the advent of the turbojet engine, initially in Great Britain and France with a jet flap configuration. While the addition of energy near the surface of a lifting body can be used to increase lift, and thus circulation, by retarding boundary layer separation, most of the high lift applications are performed on specially designed wings where the addition of high velocity air can be used to control the boundary layer and to virtually extent the camber and the chord.

The flow of a fluid over curved surfaces has long been studied for a variety of applications. The most prevalent application of circulation control works by increasing the near surface velocity of the airflow over the leading edge (LE) and/or trailing edge (TE) of a specially designed aircraft wing using a series of blowing slots that eject high velocity jets of air [28]. These augmented wings normally have a rounded trailing edge, and eject the air tangentially, through these slots inducing the Coandă effect [38]. This phenomenon prolongs boundary layer separation while increasing circulation around the airfoil and thus increases the lift generated by the wing surface due to the relaxation of the Kutta condition. Initially, at very low blowing values, the jet entrains the boundary layer to prevent aft flow separation, and thus is a very effective form of boundary layer control (BLC) [20]. As blowing levels are increased, the jet continues to wrap around the Coandă surface causing a rise in the local static pressure. This pressure increase,

along with viscous shear stress, and centrifugal forces, lead to jet separation from the rounded TE resulting in a new stagnation point on the lower surface of the airfoil. The direct effect of altering streamlines and stagnation points around an airfoil is lift augmentation.

Historically, the main purpose of CC for fixed wing aircraft has been to increase the lift when large lifting forces and/or slow speeds are required, such as at take-off and landing. Wing flaps and slats are currently used during landing on almost all fixed wing aircraft and on take-off by larger jets. While flaps and slats are effective in increasing lift, they do so with a penalty of increased drag and added hardware. The benefit of the CC wing is that no extra drag is created from the movement of surfaces into the airflow around the wing and the C_L is greatly increased. Note that while a CC wing may have less hardware on the wing there is the obvious addition of pumping and plumbing hardware that often obviates the value of the additional lift for all but a few applications.

In past analytical trials, an elliptical airfoil shape was used to analyze the potential fluid flow, [49] for these applications. The original theoretical methods are only applicable for frictionless, incompressible fluids, thus not truly valid for complex CC flows, due to the compression of air at the blowing slot. In 1975, further research was completed using the Theodorsen method in a potential flow analysis of 20%t/c CC-ellipse (5% camber), with a modified circular TE [25]. The analytical results showed close agreement to Kind's experimental data [28]. A Coandă simulation was later conducted which under-predicted the decay of the maximum jet velocity [9].

From previous experimentation, four main benefits were achieved by using an active circulation control method on fixed wing aircraft to control moment augmentation [4] [21]. These benefits are:

1. Very small movement, or even non-moving, control surfaces are required [14],
2. Lift augmentation can be achieved, independent of the airfoil angle-of-attack, and can virtually change the airfoil's apparent camber/angle-of-attack
3. Jet turning angle no longer limited by physical jet exit angle/flap deflection angle [18],
4. Very high force augmentation can be achieved per unit blowing momentum input [20].

Following the application of this technology to fixed wing and rotary wing aircraft, it became increasingly more attractive to consider for other areas such as marine propellers and lifting surfaces, passenger and transport automobiles, as well as wind turbines and water turbines. The use of this technology has also been seen to advance other technologies because of the need for smart materials, such as for piezoelectric valves [46]. This literature survey contains research documented in other recent surveys [33] [57], as well as summarizes these previous studies and reviews the findings as they contribute to the further advancement of circulation control technology.

2. EARLY CC RESEARCH (1960'S-1970'S)

Circulation control has been implemented in various applications since its inception. Among these applications that have been studied in the past are high lift fixed wing aircraft, vertical/short take-off and landing aircraft (V/STOL), and anti-torque systems for rotorcraft.

In 1969, wind tunnel studies of three 20% t/c elliptical airfoils for stowed rotor applications were completed at the NSDRC. Several TE configurations were examined including three TE shapes (true ellipse, circular), TE radius (R/c = .019, .038), and chord-wise location of slot (x/c = 0.813, .922, .934). These results showed, that when the blowing coefficient is varied ($0 \leq C_\mu \leq 0.32$) and angle of attack is held constant, a violent LE stall occurs only correctable with a compensational change in the α, called an α-stall [57]. A second stall phenomenon occurs when the C_μ is held fixed and α is varied through a number of positions ($\pm 10^o$). This test also produced a TE stall which was not nearly as severe as the aforementioned LE stall.

In 1969, a series of testing scenarios of V/STOL and landing vehicles was conducted at Washington University in order to study the low speed applications and wind tunnel capabilities. It was shown through this study that, there is a minimum speed, determined by wind tunnel geometry, in which the flow seems to breakdown and the testing is no longer valid. Testing below this minimum tunnel velocity produces

recirculation flow within the tunnel which is also shown to be a function of the downwash, configuration of this model and relative size of the model [41].

In 1970, at West Virginia University (WVU), a study was conducted on two circulation controlled cambered airfoils, for fixed wing aircraft applications, Model A (20% elliptic/c ellipse, 5% camber, and true elliptical TE) and Model B (20% elliptic/c ellipse, 5% camber and a modified circular TE R=5.8%c) in the hopes of proving that the addition of a high velocity jet of air ejected tangentially around the airfoil would produce a greater lifting force on the airfoil due to the Kutta-Joukowski theorem. This theorem, shown in Equation 1, states that the overall circulation (Γ) around the airfoil is directly related to the lifting force (L) when expressed in terms of the freestream velocity (V_∞) and fluid density (ρ_∞) of the free stream flow [26].

$$L = \rho_\infty V_\infty \Gamma \qquad \textbf{EQUATION 1}$$

It was found that Model A produced a lift-to–drag ratio (L/D) of 30 and Model B produced a ratio of 55 proving that circulation impacted the lift directly, and the experiments also determined that the TE shape is the major parameter that should be considered when dealing with a CC airfoil. For low freestream velocity (Re ≤ 500K) a circular/rounded TE shape provides better lift augmentation ($\Delta C_l/C_\mu$) while at high freestream velocities (Re > $1x10^6$), an elliptical TE shape is the optimal choice.

Very few stall experimentations were conducted in past work with circulation control airfoils, however, studies were conducted on a 20% t/c elliptical airfoil (5% camber) and the momentum coefficient (C_μ) was varied from 0.006 to 0.119, with a constant free stream velocity (V_∞) of 100 m/sec [26]. Stall angles of this airfoil were increased from nine to fourteen degrees through this range of C_μ. This stall study did not, however, take into account LE or TE separation effects, only the effects of the entire suction surface of the airfoil. This airfoil's TE was also unaltered, so the Kutta Condition still held true.

The pitching moment (C_m) and center-of-pressure (C_p) of the experimental model are very important parameters when testing the stall angles in a wind tunnel environment. In 1970, two models were examined for the change in the pitching moment and center of pressure. The results concluded that at three different angles of attack, neither of these two parameters is significantly affected by a change in lift coefficient [26].

In a follow-up study conducted at WVU, Model B, from the experimentation conducted by Harness, was examined in greater depth as to how the rounded trailing edge of the airfoil impacts the addition of lifting forces on the aerodynamic body, for fixed wing aircraft ([36]. Through this study it was shown that the airfoil tested could attain a maximum C_L of 4.58 with a C_μ of 0.17. The author also claims that the rounded TE radius of 5.8% c was as optimal a design as could be used on this particular airfoil. The author further states that the rounded trailing edge is the most important parameter when dealing with CC airfoils.

In 1971, research was conducted to design a non-deflecting stern plane for a submarine, by applying CC technology. This was one of the first instances where an application of CC technology was studied for a purpose other than fixed wing aircraft [12]. Elliptic hydrofoil sections with a rounded trailing edge were used for this experiment. Each of the models had upper and lower tangential blowing slots. The same profile of the existing stern plane was used to minimize any additional interference. A second design is also mentioned with end plates added to reduce induced drag which showed an overall improved performance. Studies showed that the stern plane with CC activated provided a reliable solution to submarine stability, however, optimizing the endplates by adding camber to increase the aspect ratio was predicted to make an even better improvement.

This work allowed for the creation of a non-dimensional relationship to be established between ejection slot height, airfoil chord, and trailing edge radius. This information became important in choosing an airfoil profile for CC applications, as there was a region where the Coandă operation was most effective. This idea, postulated by Englar, can be seen in Figure 1, where airfoils which were designed to fall within the shaded region would be able to take more advantage of the benefits of the CC technology than ones which fell outside of this region.

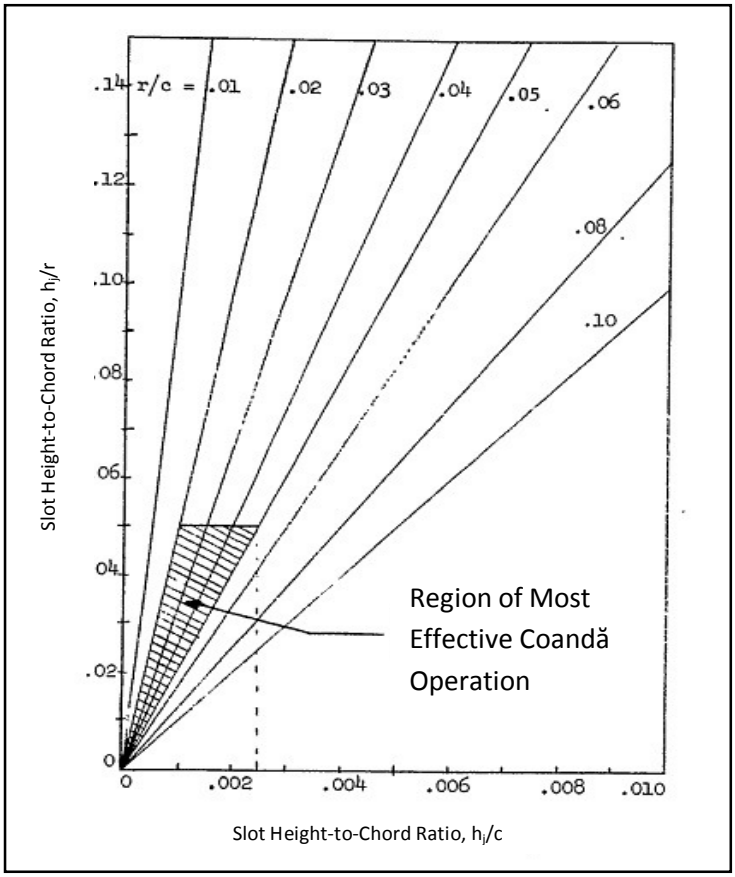

FIGURE 1. Englar's Original Hypothesis of the Region of Most Effective Coandă Operation [11].

Adding to the studies conducted by Harness and Myer, further experimentation of Model B was conducted in 1972 using the principle of unsteady flow to study the effect of pulsing the CC jets on and off in a repetitive manner [27]. This investigation showed that modulating the air to feed the exit jets provided a 25% decrease in mass flow rate and still provided a 15% overall increase in C_L. This study further indicated that the feasibility of CC for use in fixed wing aircraft was not as dependant as previously thought on the addition of large weight additions of mass from regulation and pressurization equipment.

With the introduction of CC to rotary aircraft, a study conducted at WVU was done on a shrouded propeller in order to attempt to increase the static thrust of the propeller. The apparatus in this study used CC theory and the addition of blowing slots around the propeller shroud to change the effective velocity and pressure of the flow that the rotor interacts with [7]. The results of this study concluded that the CC shroud produced the effect of being a cambered shroud while CC was activated, as well as, successfully increasing the overall thrust produced by the motor at increasing C_μ.

CC was applied to a helicopter rotor model in 1973, and tested by means of installing the model into a wind tunnel. This “first generation” helicopter application demonstrated the use of CC over the entire rotor field as well as demonstrating rotor trim, lift augmentation, and maneuver moment generation through the use of cyclic blowing [56]. This was one of the first steps into applying circulation control principles to rotary powered aircraft.

The second instance of attempting to apply CC principles to rotating bodies was made in 1973 at the Naval Surface Warfare Center (NSWC). This study examined the inherent issues with using CC on a rotor, such as, boundary layer separation due to an adverse pressure gradient, the inaccuracy of measurements, and the use of flow visualization methods. This study showed that the use of pressure taps on the model to measure lift and drag forces, is a more accurate way of collecting the necessary two-dimensional data and more practical than using a conventional force balance method [10].

Again in 1975, two-dimensional CC wing sections were examined and found to produce maximum lifting coefficients of three times that of an unaltered airfoil with a sharp TE [15]. These models were fabricated using the existing NACA shape profiles (NACA 66-210 and NACA 64A-212), removing the sharp TE and replacing one profile with a rotated flap configuration and the other profile with a circular TE of radius 0.875 inches. At various angles of attack ($-16^{\circ} \leq \alpha \leq 15^{\circ}$) and momentum coefficients ($0 \leq C_{\mu} \leq 0.24$), the modified NACA 66-210 and NACA 64A-212 models produced C_L values of 5.5 and 5.95 respectively, at a C_{μ} of 0.20.

At the Aviation and Surface Effects Department, in conjunction with the David W. Taylor NSRDC a 15% t/c CC elliptical airfoil section with slots at both LE and TE blowing slots was evaluated in a subsonic wind tunnel. The goal was to determine its potential for use in conjunction with a high-speed (300-400 knot) helicopter rotor system. Fore-and-aft slot utilization was determined by local flow direction over the blade as it revolved around the azimuth. Aerodynamic performance was not affected by the addition of an un-blown LE slot except beyond the usable positive α range. Some loss in lift and an increase in drag were noted in the results. At equal plenum pressures, simultaneous blowing from the LE and TE slots resulted in a decrease in C_L, an increase in C_D, and a more positive C_m when compared to TE blowing alone [40].

Another series of evaluations were performed on a 20% t/c CC-ellipse in 1975, for use on fixed wing aircraft. In this testing scenario, an elliptical airfoil was tested at subsonic speeds in a two dimensional wind tunnel environment which produced C_L of 5 while C_{μ} was 0.24. This C_L showed a similar improvement in the L/D of the activated circulation control model, reaching a maximum value of 30 [3].

In the mid 1970's, a theoretical analysis was completed on arbitrary airfoils, augmented to include CC capabilities in order to predict the blowing slot characteristics for a given airfoil at given operating conditions. This research proved to have a powerful effect on the study of CC in that it used potential flow, laminar boundary layer, turbulent boundary layer and turbulent wall jet theories applied together in order to approximate the geometry needed for the CC exit slots [25]. The application of these aerodynamic theories to circulation control provided a basis in which to design an augmented airfoil for a specific use without the need for several failed designs, including physical tests, and ultimately redesigns of the particular CC airfoil.

Another rotary application of CC was conducted at the David W. Taylor NSRDC in 1976, where hardware was applied to a high speed helicopter blade and tested during reverse blowing conditions (i.e. while the rotor is in retreat in comparison to the freestream velocity along the rotary path). This study involved wind tunnel testing of an elliptical airfoil (root section: 20%t/c, 5%camber, tip section: 15%t/c, 0%camber) with both LE and TE blowing slots in which CC was activated and seen to improve the overall performance of the helicopter during hover applications and through advance ratios of 4.0 [42]. This system also proved beneficial while flying through the critical advance ratio of 0.7. Equation 2 defines the advance ratio (μ) of the rotor, using the freestream velocity (V_{∞}) related to the rotational speed (Ω) and radius of the propeller (R).

$$\mu = \frac{V_{\infty}}{\Omega R} \qquad \textbf{EQUATION 2}$$

In the late 1970's circulation control was applied and used on the TE of a fixed wing aircraft, specifically on the A-6 flight demonstrator [16] to achieve larger C_L values at times of need such as take-off and landing. Wind tunnel testing was completed using a NACA 64A008.4 (modified) model and test case ranges included ($0 \leq C_{\mu} \leq 0.30$) and ($-4^{\circ} \leq \alpha \leq 22^{\circ}$) at a Re of 1.9×10^6. In this testing, C_L of 6.5 was found in two-dimensional testing, and a three-dimensional C_L was found to be a factor of 2.2 greater than non-blowing cases ($C_{\mu}=0$).

FIGURE 2. A-6 Flight Demonstrator [42].

In 1976, the inaugural CC flight demonstrator was built and flown at WVU. The pioneer plane was equipped with a retractable Coandă surface on the TE of the aircraft, as shown in Figure 3 [30]. It was found that CC flap deployment increases the wing chord by 20% for increased performance with blowing. The flap is articulated with a bell crank but is not rigidly connected to the piano hinge at the sharp TE. Its sliding connection allows the rounded TE to thermally expand up to ½" when the hot gas bleed air is routed from the auxiliary turbine situated in the rear seat of the aircraft. The flight test of this aircraft produced lift augmentation increases of the local C_L value from 2.1 to 5.3 with a C_μ of 0.12.

FIGURE 3. Trailing Edge Coandă Surface Extended From WVU Flight Demonstrator [30].

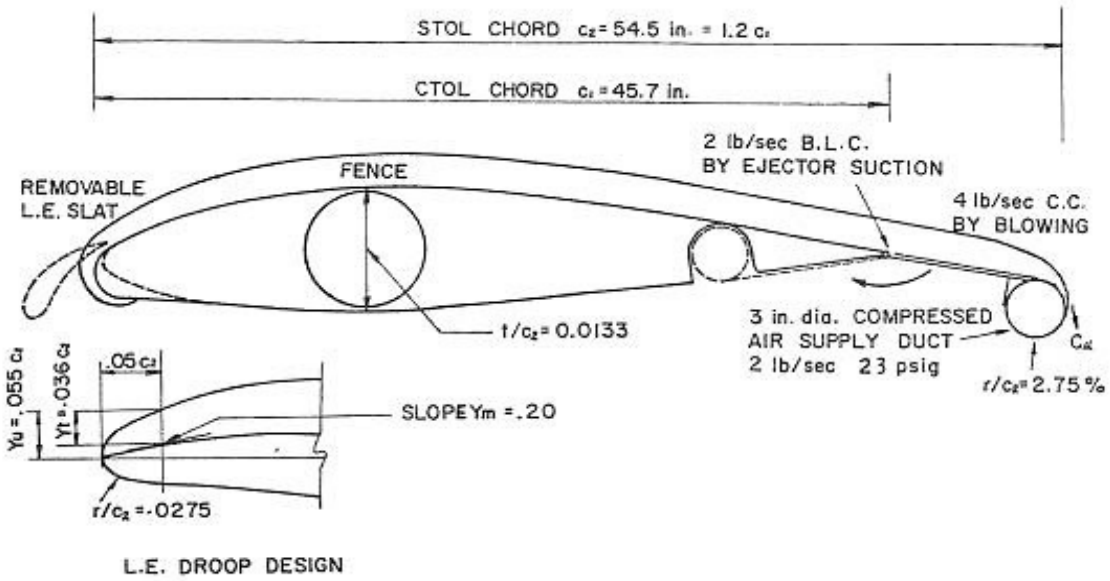

FIGURE 4. Schematic of Trailing Edge Coandă Configuration of WVU Flight Demonstrator [30].

3. MID-CYCLE OF CC RESEARCH (1980'S)

As the development of CC technologies continued, research and experimentation gained regard in the scientific community. With the new understanding of CC technology, its application and uses of CC technologies began to expand from simply being an addition to existing aircraft to being a significant design factor to improve performance of rotary powered aircraft. Also gaining interest was novel ways of pressurizing for the CC plenums located inside the airfoils, as it was shown that the addition of large scale pumping devices often negated the value the additional lifting forces achieved by adding circulation control.

With the introduction of CC rotor blades, in the 1970's, a study was designed to look at the differences in the noise levels of using such high lift devices in place of conventional helicopter blades. The testing models used were the circulation control rotor (ejects high velocity jets of air tangentially around a rounded trailing edge), X-Wing (designed to stop mid-flight and act as a fixed wing at high forward speeds, while utilizing CC technology on the upper surface), and a control scenario (a conventional helicopter rotor). In studies which used similar rotational speeds, advance ratios, and forward speeds, the X-Wing rotor showed the most promise for eliminating blade/vortex noise as well as impulse noise, both common with conventional helicopter rotors. In testing the CCR, it was found that there was an abundance of broadband noise at high blowing velocities which produced high decibel levels while testing [35].

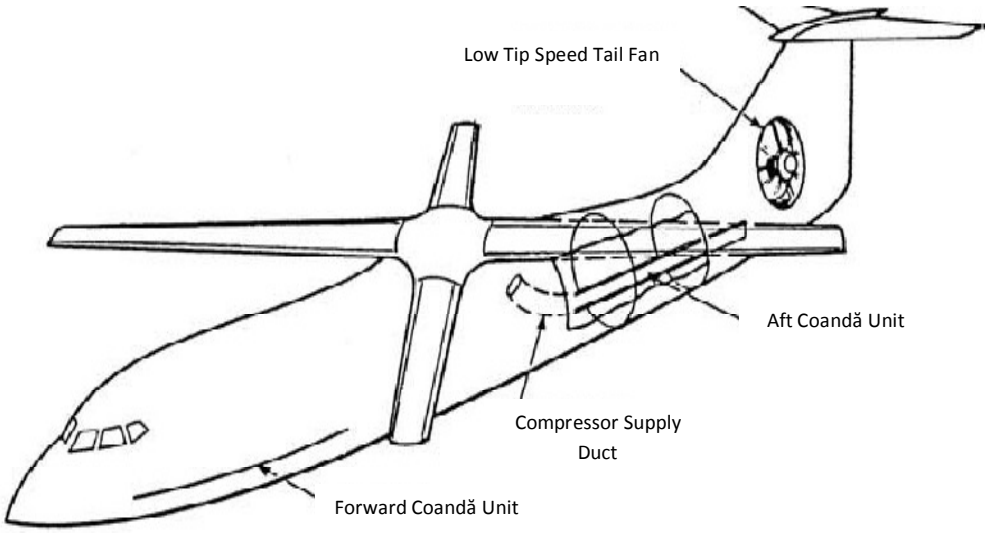

FIGURE 5. X-Wing Configuration and Supply Compressor.

A study conducted at WVU optimized the wall jet velocity used for CC applications in STOL aircraft. The information found in this experiment showed that the addition of a Coandă surface and jet ejectors improved the CC performance. This study also showed that the need for a "stowable" Coandă surface needed to be examined and implemented so that the CC surface would be able to be taken out of the flow during cruise conditions when the high values for lift were not needed [31].

Two-dimensional wind tunnel tests were conducted on a 20% t/c elliptic airfoil which was equipped with both forward and reverse blowing slots. This model was tested between momentum coefficient values of 0.0 to 0.4, and included some tests with leading edge slot activation. The results of this study contributed fundamental knowledge to the understanding of the behavior of Coandă surfaces and Coandă flows. This research proposed that the exit jet is a flow of highly concentrated vortices and may explain the strong entrainment experienced with Coandă flows [52].

In 1986, a 15% t/c ellipse with interchangeable TEs was studied in Stanford University's low-speed wind tunnel in order to obtain C_L and C_μ data to compare to the NSRDC studies completed several years previous [43]. Although a similar model was used, a leading edge activation slot was added to the model as well as a wall blowing slot was introduced at 0.85 x/c to reduce the three-dimensional effects on the model 3D effects are large in part caused by extreme pressure gradients at the junction of the model and endplates/tunnel walls.

Testing was conducted with the LE and TE slots activated. LE slot activation was shown to induce a positive lift enhancement at high blowing rates ($C_\mu \geq 0.10$). Two types of flow fields were observed due to the LE activation. In one situation, the flow folded over the top leading edge and the second showed the jet continued over the lower surface. The combination of dual slot activation showed the availability of a positive lift enhancement, although further investigation needed to be completed [43].

During a three year stretch during the mid 1980's, a series of experiments were conducted by NSRDC (1984) and Lockheed Martin (1987), the first of which attempted to redirect the engine thrust of an aircraft to be used to deflect the flow around a Coandă surface on the TE of a wing. An above wing mounted propulsive device was used in this wind tunnel experiment, and in a series of full-scale tests a deflection angle of 90 degrees was achieved, producing a C_L of almost 6.0 [17]. This system also achieved lift augmentation equal to, or in some cases greater than, that of the multi-flap systems commonly used in commercial aircraft and offered this similar augmentation without the addition of weight and complexity of several moving parts. In 1987, the upper jet deflection apparatus was combined with a flow entraining system (CC wing) which demonstrated the ability of the exhaust flow and the circulation control jet to work together to increase the lifting capability of the aircraft even further than the experiments conducted in 1984, resulting in a C_L upwards of 7.0 [17].

1987 brought about a study which combined laser velocimetry measurement and surface pressure measurement of aerodynamic forces on an airfoil model with a circular wall jet. This model had a slot thickness-to-chord ratio of 0.002 and was examined at momentum coefficients of 0.1 and 0.03. Using both of these methods to measure the aerodynamic forces provided a background in which to accurately validate and generate CFD data [39].

Secondly, in 1987, the effects of blown jets on the aerodynamic forces of cambered elliptical airfoils were studied using models with a chord of 0.66m a span of 0.51m and an ejection slot height of 0.005m. Each of these three models examined a different effect of the application of circulation control technologies to an airfoil model. One model used a single plenum to supply air to the circulation control slot, while a second model used two plenums, supplying air to two ejection slots. The results measured from these models were compared to reveal that the use of two blown jets is more effective than a single blown slot in some cases. The fourth model, "the rotating cylinder" model proved that the relative location of the two jets also had an impact on the aerodynamic forces and the maximum C_L/C_D ratio was obtained by limiting the flow of the second slot to allow the first slot to attain flow attachment [24].

After completing the previous study [31] of CC in attempting to optimize the jet velocity, the next step in the process of studying this technology at WVU was to analyze the thrust savings that CC could provide to aircraft using high lift wings. It was found that high lift devices such as CC and boundary layer control (BLC) apparatuses have a distinct upper C_L limit that can be achieved. Any attempt to exceed this optimum C_L, as in high speed applications, would cause rapid deterioration of the BLC objectives [32].

4. NEWEST CC RESEARCH (1990'S–2000'S)

In this section, CC techniques are shown to have become more predictable, as well as, they are shown to be productive in several previously unresearched scenarios, including water/other fluid mediums, vehicular uses other than aircraft (i.e. tractor trailers and automobiles), and wind turbines. It can also be shown that the future uses of CC are expansive, in comparison to the original ideas for the uses of this technology. Further research in this period includes the ability to reduce the amount of additional hardware to the original system and attempts to enhance the control of the system, or increase its effectiveness.

In an assessment of using a stopped rotor in conjunction with CC in the early 1990's, a study was performed to analyze and predict the effects of the addition of CC. This study produced a software tool which predicts trade-offs in sizing appropriate to stopped rotor systems based on horsepower, forward flight speed, mass flow requirements as well as it predicts some of the transition performance expectations while the aircraft travels at high speeds [48].

In 1996, the Circulation Control Rudder (CCR) was tested in an attempt to improve hydrodynamic characteristics of control surfaces found on ships. Water-channel testing of a modified NACA 0015 was completed at Wuhan Transportation University in Wuhan, China; 2-D and 3-D aerodynamic coefficients were analyzed at various momentum coefficients ($0 \leq C_\mu \leq 0.63$ and AoA ($0^\circ \leq \alpha \leq 24^\circ$), Results showed that the lift developed by a CC section can be easily and rapidly changed simply by varying the supply of blowing water [47]. The section shape facilitated the attainment of high structural stiffness. This method was able to generate a large lift force at small or even zero angle of attack while using only minimal values of C_μ (≤ 0.05).

A second scenario was tested in this experimentation which included the endplates and longitudinal v-grooves engraved in the Coandă surface. A high C_L was produced by the CCR with trailing-edge jet blowing at a zero degree angle of attack, and the lift coefficient of the CCR at a fixed angle of attack increased with jet momentum. The maximum of L/D occurred at zero degree angle of attack. Based on this, it could be used in ships to improve the maneuvering performance, especially when the ship sails at low speed. When reaching its maximum L/D, the lift decreased abruptly with further increasing jet momentum, known as C_μ-stall. With endplates installed, the C_D and L/D characteristics were improved, and the lift at relatively large α increased. Also, with the introduction of longitudinal v-grooves, the lift and drag forces were smaller, but the lift-to-drag ratio was shown to be greater [47].

In 1996, at the Georgia Tech Research Institute (GTRI), a new application of CC was envisioned. It was hypothesized that because the modern ground vehicle, automobiles and long haul tractor trailers, are influenced greatly by vortex shedding and separated flow fields, the addition of CC technologies might positively impact the fuel consumption and efficiency of these vehicles. In such applications, lower levels of C_μ would be used as BLC, rather than lift augmentation, to reduce separation, decreasing the vehicle's C_d leading to a direct improvement in fuel economy. In the push for greater fuel economy and reduction of the use of fossil fuels, the application of CC technologies to ground vehicles is just one of many solutions being considered. Wind tunnel tests of a generic fiberglass automobile model, showed a 35% reduction in overall drag in comparison to an already streamlined vehicle without circulation control. Another facet of this research concluded that the application of lower surface blowing, as opposed to upper surface activation can provide an increase in down-force on the vehicle as well as reducing the instability of the automobile while in a yawing motion, thus showing that active blowing can be used to restore the lateral stability of the model [19].

Although CC technology was first envisioned to be a productive system for enhancing lift in any fluid medium the vast majority of studies up until the mid 1990's examined the system within the constraints of using airflow as the pressurized fluid medium. In 2004, a water tunnel experiment was conducted in the Large Cavitation Chamber, located in Memphis, TN. This study used a circulation controlled wing having a 20% elliptic cross section, an aspect ratio of 2, and both upper and lower surface jet exit slots. This model also employed a slight amount of taper, overall, 0.76 from root to tip. Unlike the previous tests which use air as the pressurization medium, this model provided a visual representation of the behavior of the exit jet at various angles of attack and plenum pressures [44]. One unique finding of this particular research was the fact that when cavitation was forced to occur on the Coandă surface, there was no abrupt stall of the airfoil. The model showed signs of a slow, even decrease in the lifting forces. This indicated that the reduction of the pressure around the exit jet and Coandă surface, while decreasing the lifting force as expected, will not become detrimental, and will still allow the propeller, or airfoil to produce a lifting force, even at conditions of higher speed, greater depth/altitude, and increased pressure. Also shown in this study was the availability to produce a positive lifting force at a geometric pitch angle of negative 40 degrees. In comparison to ship surfaces of the same geometry, this particular CC augmented rudder produced a lifting coefficient of 3.0.This lift increase was nearly double that of its counterpart [44].

The effects of pulsed vortex generator jets on a naturally separating low-pressure turbine boundary layer were studied in 2002 at the Advanced Flight Systems Department of Lockheed Aeronautical Systems Company. These vortex generator jets were pulsed over a wide range of frequencies at constant amplitude. The resulting wake loss coefficient versus pulsing frequency data documented a minimal dependency on amplitude. Vortex generator jets were shown to be highly effective in controlling the location of laminar boundary layer separation. This behavior suggested that some economy of jet flow may be possible by optimizing the pulse frequency for a particular application. At higher pulsing frequencies, when the flow is fully dynamic, the boundary layer was dominated by periodic shedding and separation bubble migration [8]. This study opened the door to research into pulsing flow circulation control applications as well as conservation of onboard CC pressurization.

Pneumatic control and distributed engine technologies were explored by NASA Langley Research Center in 2003 as a means to maximize performance of a new civil aircraft concept called the Personal Air Vehicle [29]. A morphing nacelle was designed capable of enhancing propulsive efficiency throughout the flight envelope. Initial experimental investigation of this technology used CC applied at the inlet and exit nozzle of a shrouded fan, similar to previous experiments conducted at WVU [7]. A powered model shrouded fan was tested on a static thrust cell at GTRI in order to quantify any performance brought by CC enhancements.

Tests were conducted both in and out of ground effect, determining the effectiveness of the CC adaption to enhance propulsive efficiency. The tests showed that the inlet CC device was effective at alleviating inlet stall in static operation but showed limited performance enhancements. This technology did, however, prove to be effective at reducing peak ground pressure when operating at greater heights. An enhanced mass flow into the nacelle was noted with CC activation, showing a possible propulsive efficiency augmentation to be considered for further research.

In 2004, again at the NSWC, an elliptic airfoil section (17%t/c, 1% camber) was evaluated to determine the low speed characteristics of performance. This model was tested with both upper and lower CC surface blowing slots and at a zero angle of attack so as to analyze the blowing efficiency of the system. This model produced a C_L of 3.6 during employment of the upper slot exit jet, while the lower slot produced a C_L of -4.0. This result shows that using a negatively effective camber on a circulation control airfoil produces a greater lift augmentation ratio and lifting force [3].

Similar studies to that of the fiberglass model automobile were conducted in 2005; however, the circulation control system was directly applied to a tractor trailer and examined in real use conditions, driving on the interstate. With the use of heavy vehicles to transport goods, and the fact that a typical tractor trailer averages 175,000 miles a year, fuel costs alone average upwards of $40,000 each year [21]. The application of circulation control technologies to these types of vehicles, although a small benefit in comparison to traditional CC applications can be quite meaningful.

The preliminary tests of this type of application were conducted in a wind tunnel environment in order to get an idea of the practicality and feasibility. The next step in the testing process lead to an actual tractor trailer being retro-fitted with appropriate circulation control hardware along the length and around the back door of the trailer. A second replica tractor trailer was also examined in order to produce a baseline comparison test.

The results show that activation of certain blowing slots can reduce drag (in the wind tunnel model) of up to 84% by preventing the flow separation at the rear end of the vehicle. It was also noted that the activation of top blowing slots, only, can increase the lifting force experienced by the wheels of the automobile and thus increase its fuel economy [23]. Several ideas for the supply of circulation control pressurized air, without the addition of heavy, complicated aftermarket parts, include a turbo/super charge onboard or already existing auxiliary engines (such as cabin generators and refrigeration motors).

In 2006, a rapid predictive method was studied for the implementation of circulation control techniques at the GTRI. In this study, two-dimensional circulation control performance calculations were made using the Navier-Stokes Equations for fluid flow. Coupled with a computer code to compute and predict circulation control airfoil characteristics, this method set out to predict the interaction between variables involved with circulation control systems. Using flow visualization, quantitative, and qualitative methods, it was possible to compare the aerodynamic forces achievable by adding circulation control. Although the particular experiment is only useful for selected ranges of variables such as pressure and density, the overall modeling can be used to predict the effect of adding circulation control to a model operating at any range of variables, so long as the variable are all called out at the beginning of the simulation [37].

Later in 2006, the aerodynamic performance of a wind turbine rotor equipped with circulation enhancement technology was investigated using a three-dimensional unsteady viscous flow analysis [51]. This study used a trailing-edge blowing slot and a gurney flap on the model. The National Renewable Energy Laboratory (NREL) horizontal axis wind turbine was used as the baseline configuration. At low wind speed (7 m/s) where the flow is fully attached, it was shown that a Coandă jet at the trailing edge of the rotor blade is effective at increasing circulation resulting in an increase of lift and the thrust force in the chord direction. An increased amount of net power generation compared to the baseline configuration was also seen for moderate blowing coefficients ($C_\mu \leq 0.075$). The application of a passive Gurney flap was found to increase the bound circulation and produce increased power in a manner similar to the Coandă jet. At high wind speed (15 m/s) where the flow separated, both the Coandă jet and gurney flap become ineffective in increasing the performance.

In the interest of forwarding the study of circulation control effects in alternate fluid mediums, an experiment was conducted at the University of Strathclyde, England, implementing a modified marine propeller duct with circulation control capabilities. The study focused on using this propeller duct to eliminate the use of conventional control planes on autonomous underwater vehicles (AUV's). The use of this altered propeller duct indicated an effective increase of the maneuvering force produced, of about 600%, and also increased the efficiency of the overall ability to maneuver the craft by 9.5% over the ability of the conventional lifting surfaces [53]. This study further showed the availability of a CC application to a wider array of uses, particularly uses involving hydrodynamics and other water applications.

In 2006, at WVU, a conceptual design of a new helicopter blade, with the addition of both LE and TE blowing slots, was studied, in the hopes of using this technology to reduce or eliminate the need for a swash-plate design. This application uses CC slots on the helicopter blades to increase the lifting forces of the aerodynamic surfaces, thus increasing the payload of the system while eliminating the need to articulate the blade angle continuously throughout the rotation of the blade. This new design would eliminate many mechanical complexities associated with the aforementioned swash plate configuration. Although this design is still in the development stages, it predicts that the reliance on the major limiting factor and failure point of helicopters, the swashplate, can be reduced or even eliminated [5].

Further research work was conducted at NSWC in 2006, on the dual LE and TE slotted CC wing, in the Large Cavitation Channel in Memphis, TN. In order to measure the performance of the 20% t/c elliptic airfoil (rounded trailing edge) force measurements via a 6-component load cell balance and laser Doppler velocimetry data was taken in the wake of the airfoil [10]. An extensive number of tests were run in order to produce characteristic loading of the model due to angle-of-attack, slot exit velocity, and cavitation impact. With the results of this test documented, a computational model was envisioned to be built, simulated, and compared to the data found in testing in order to get a general understanding of the effect of CC on several different cross-sectional hydrodynamic surfaces.

In another study of a unique implementation of circulation control sciences, active (leading edge and trailing edge slots and exit jets) and passive (Gurney Flap) CC systems were applied to a horizontal axis wind turbine (HAWT). In the application of a leading edge, the results showed that at high wind speeds the enhancement with circulation control techniques breaks down and is no longer applicable. When the "passive" Gurney Flap system as well as the trailing edge activated slot were employed on the model, a circulation increase around the airfoil was observed and the overall power generation capabilities experienced a net increase over the unaltered model.

The activation of trailing edge blowing slots proved to have a larger aerodynamic force output as well as a larger power output available than the model employing a "passive" Gurney flap system. However, the application of the Gurney flap without the need for an external pumping system gives it versatility in applications where no additional weight or added complex hardware is allowable [50]. This selected study, although focusing on HAWT configurations, can also be implemented in vertical axis wind turbines (VAWT) as well as water turbines and coaxial, multi-stage compressors.

A more recent testing scenario, of near surface actuation circulation control for use on a rotorcraft main rotor was conducted at WVU [6]. Again, in this scenario, an external compressor was used to pressurize the plenums of the experimental model to 10-15 psig, resulting in a slot exit velocity of 1000 ft/s. The circulation control velocity has a bearing on several factors including slot height, slot length and plenum pressure. As with Englar's work, this study produced results which proved a lift coefficient in excess of 5.0 is achievable. Also in this work, the response times of a circulation control model of a 10:1 elliptical airfoil was determined to be 55-60 ms.

In 2009, a research program emphasized the development of CC active flow control concepts for high-lift augmentation, drag control, and cruise efficiency. The ability to consistently predict advanced aircraft performance requires improvements in design tools to include these advanced concepts. Validation of these tools was based on experimental methods applied to complex flows that go beyond conventional aircraft modeling techniques.

The experimental data highlighted the physics of separation and circulation related to activation of CC on high lift and drag-control airfoils [22]. Lift coefficients over 8 at $\alpha=0°$ was demonstrated, as well as a drag increase or decrease by variation in blowing. In analysis of these test results, existing CFD codes were employed to assist in evaluation of tunnel effects, such as wall interference, wall juncture flows, possible 3-dimensional interference, and resulting induced downwash.

Finally in 2009, preliminary studies were conducted at West Virginia University to add circulation control technology to a vertical axis wind turbine (VAWT). Selection of a circulation control airfoil to be used on an H-Type VAWT Performance predictions were studied after adding circulation control to a computationally simulated model. C_μ values of 0%, 1%, and 10% were studied over a range of solidity ratios, 0.01-0.4. It was found that the overall power output performance of the turbine would be increased 24% at a blowing coefficient of 10% [54]. This work continued through the implementing a momentum

model of the wind turbine in order to begin developing the control algorithms needed to use circulation control most efficiently around the turbine blade's path. The initial two-dimensional version of the model proved successful in modeling the interaction and effects of the turbine and its wake region [55]. Below in Figure 6, the model of the VAWT is shown which shows the vortex production at the 90 and 270 degree position of the rotation, as well as the wake confinement to the original diameter of the turbine.

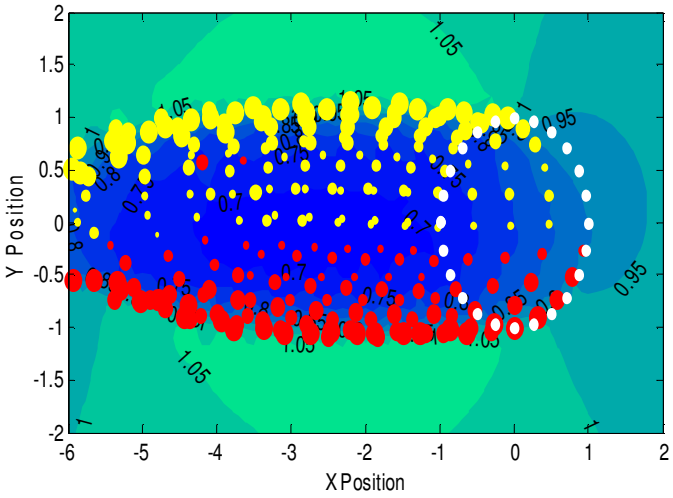

FIGURE 6: Vortex Model Velocity Field with Vortices and Blade Positions [55].

Through the study of the applications of circulation control and previous experimentation, it was possible to add further specific airfoils to Englar's original three dimensional airfoil comparison study in 1971 to see exactly where all the models and applications fall in comparison to the "region of most effectiveness," see Figure 7, below. In this figure, the previous noted work has been added to show how each compares to the most effective circulation control region. This figure can be very powerful in selecting future airfoils for circulation control applications, as the most important airfoil dimensions (h_j, c, and r) are related to one another. This reduces the need to research an airfoil profile in a wind tunnel environment before selecting the appropriate model for the application.

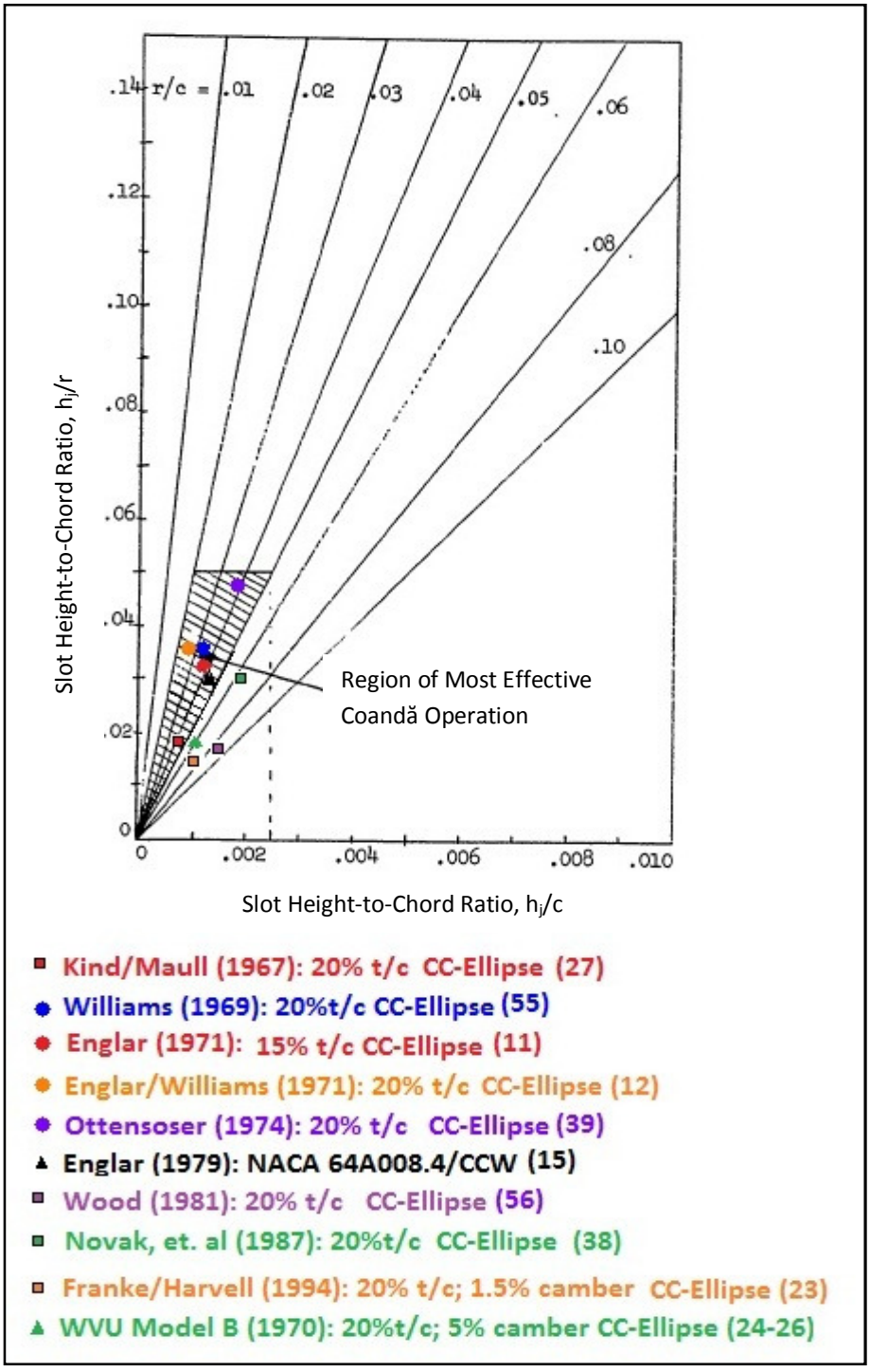

FIGURE 7. Notable Airfoils used in Past Research and their Comparison to "The Region of Most Effectiveness" [11].

It is the summary of all of the work conducted over the past five decades that will provide the future researcher with the background needed to apply what has been discovered. Several of these graphical models can be generated from the wealth of research that has been conducted.

5. CONCLUSIONS

Through the study of previous experimentation, it was possible to see the development of circulation control technology from its early years of use on fixed wing aircraft, into rotary application and hydrodynamic uses and finally to see an interest in conducting studies for use in renewable energies. A research map of the applications and the directions in which this technology has been adapted can clearly be observed in this study and a natural progression as to what research still needs to be completed to help make circulation control a viable lift enhancement device for aircraft, automobiles, hydrodynamic applications, and wind turbines. With the data collected in this study, several other baseline and design aid figures, similar to Figure 7, can be generated in order to help further the advancement of circulation control technology and ensure that this science moves toward implementation.

There is also evidence leading to the realization that CC technology has effectively expanded the range of operational conditions for such devices. Maybe the technology, or the state of the art, has finally arrived.

6. REFERENCES

[1] Abbott, I.H., Von Doenhoff, A. E., Theory of Wing Sections, Dover Publications, Inc, New York, NY, 1959.

[2] Abramson, J. "Two-Dimensional Subsonic Wind Tunnel Evaluation of a 20-Percent-Thick Circulation Controlled Airfoil." David W. Taylor Naval Ship Research Center, Bethesda, MD, 1975.

[3] Abramson, J. "Characteristics of a Cambered Circulation Control Airfoil Having Both Upper and Lower Surface Trailing Edge Slots." Naval Surface Warfare Center – Carderock Division, Bethesda, MD, 2004.

[4] Ambrosiani, J.P., "Analysis of a Circulation Controlled Elliptical Airfoil," Doctorate of Philosophy Dissertation, Department of Mechanical and Aerospace Engineering, West Virginia University, Morgantown, WV, 1971.

[5] Angle II, G.M., Huebsch, W.W., Prucz, J.C., Smith, J.E. "Circulation Controlled, Fixed-Root Helicopter Concept." American Helicopter Society 62nd Annual Forum, Phoenix, AZ, 2006.

[6] Angle II, G.M., "Aerodynamic Benefits of Near-Surface-Actuated Circulation Control Blowing Slots for Rotorcraft Use," Doctorate of Philosophy Dissertation, Department of Aerospace Engineering, West Virginia University, Morgantown, WV, 2008.

[7] Ashworth, J.C. "An Experiment Investigation of a Circulation Controlled Shrouded Propeller." Master of Science Thesis, Department of Mechanical and Aerospace Engineering, West Virginia University, Morgantown, WV, 1973.

[8] Bons, J.P., Sondergaard, R.B., Rivir, R.B., The Fluid Dynamics of LPT Blade Separation Control Using Pulsed Jets." *Journal of Turbomachinery*, Vol. 124, Issue 1, 2002.

[9] Churchill, R.A. "Coandă Effect Jet Around a Cylinder with an Interacting Adjacent Surface," Doctorate of Philosophy Dissertation, Department of Aerospace Engineering, West Virginia University, Morgantown, WV, 1992.

[10] Donnelly, M.J., Cutbirth, J.M., Rogers, E.O., Jessup, S.D., Park, J.T. "Hydrodynamic Performance of a Dual-Slotted Circulation Control Wing of Low Aspect Ratio," Naval Surface Warfare Center, Carderock Division, Hydrodynamics Department Report, TR-2006-031, Bethesda, MD, 2006.

[11] Englar, R. J., "Two-Dimensional Subsonic Wind Tunnel Tests of Two 15-Percent Thick Circulation Control Airfoils," David W. Taylor Naval Ship Research and Development Center Technical Note AL-211, Washington, DC, 1971.

[12] Englar, R.J., Williams, R.M., "Design of a Circulation Control Stern Plane for Submarine Applications." David W. Taylor Naval ship Research and Development Center, Bethesda, MD, 1971.

[13] Englar, R.J., Williams, R.M. "Test Techniques for High Lift, Two-Dimensional Airfoils with Boundary Layer and Circulation Control for Application to Rotary Wing Aircraft." Canadian Aeronautics and Space Journal, Vol. 19, No. 3, 1973.

[14] Englar, R.J., "Subsonic Two-Dimensional Wind Tunnel Investigation of the High Lift Capability of Circulation Control Wing Sections." David W. Taylor Naval ship Research and Development Center, Bathesda, MD, 1975.

[15] Englar, R.J., "Experimental Investigation of the High Velocity Coandă Wall Jet Applied to Bluff Trailing Edge Circulation Control Airfoils," David W. Taylor Naval Research and Development Center Report 4708, September 1975.

[16] Englar, R.J., "Development of the A-6/Circulation Control Wing Flight Demonstrator Configuration." David W. Taylor Naval Ship Research and Development Center, Bethesda, MD, 1979.

[17] Englar, R.J., Nichols, J.H., Harris, M.J., Eppel, J.C., Shovlin, M.D., "Circulation Control Technology Applied to Propulsive High Lift Systems." Society of Automotive Engineers, Aerospace Congress and Exposition, Long Beach, CA, 1984.

[18] Englar, R.J., "The Application of Circulation control Pneumatic Technology to Powered-lift STOL Aircraft." Advanced Flight Systems Department, Lockheed Aeronautical Systems Company, Marietta, GA, 1987.

[19] Englar, R.J., Smith, M.J., Neibur, C.S., Gregory, S.D., "Development of Pneumatic Aerodynamic Concepts for Control of Lift, Drag and Moment plus Lateral/Directional Stability of Automotive Vehicles." Georgia Tech Research Institute Journal of Technology, Atlanta, GA, 1996.

[20] Englar, R.J., "Overview of Circulation Control Pneumatic Aerodynamics: Blown force and Moment Augmentation and Modification as Applied Primarily to Fixed Wing Aircraft," Proceedings of the 2004 NASA/ONR Circulation Control Workshop, NASA CP-2005-213509, Pages 23-66, 2005.

[21] Englar, R.J., "Pneumatic Aerodynamic Technology to Improve Performance of Automotive Vehicles." American Institute of Aeronautics and Astronautics, Inc. 2005.

[22] Englar, R.J., Jones, G.S., Allan, B.G., Lin, J.C., "2-D Circulation Control Airfoil Benchmark Experiments Intended for CFD Code Validation." American Institute of Aeronautics and Astronautics, 47th Aerospace Sciences Meeting Including the New Horizons Forum and Aerospace Exposition, Orlando, FL, 2009.

[23] Englar, R.J., "The Application of Pneumatic Aerodynamic Technology to Improve Performance and Control of Advanced Automotive Vehicles." Georgia Tech research institute: Aerospace, Transportation and Advanced Systems Lab, Atlanta, GA, 2009.

[24] Franke, M.E., Harvell, J.K., "Wind Tunnel Studies of Circulation Control Elliptical Airfoils." Air Force Institute of Technology, Tech #N88-17598, Wright-Patterson Air Force Base, Dayton, OH, 1987.

[25] Gibbs, E.H., "Analysis of Circulation Controlled Airfoils," Doctorate of Philosophy Dissertation, Department of Mechanical and Aerospace Engineering, West Virginia University, Morgantown, WV, 1975.

[26] Harness, G.S., "An Experimental Investigation of a Circulation Controlled Cambered Elliptical Airfoil," Master of Science Thesis, Department of Aerospace Engineering, West Virginia University, Morgantown, WV, 1970.

[27] Holt, D.J., "Circulation Controlled Airfoil with Pulsed Flow." Master of Science Thesis Department of Mechanical and Aerospace Engineering, West Virginia University, Morgantown, WV, 1972.

[28] Kind, R.J., Maul, D.J., "An Experimental Investigation of a Low-Speed Circulation-Controlled Aerofoil," The Aeronautical Quarterly, Vol. XIX, May, 1968.

[29] Kondor, S., Englar, R.J., Moore, M. "Experimental Investigation of Circulation Control on a Shrouded Fan," American Institute of Aeronautics and Astronautics, 21st Applied Aerodynamics Conference, Orlando, FL, 2003.

[30] Loth, J.L., Fanucci, J.B., Roberts, S.C., "Flight Performance of a Circulation Controlled STOL Aircraft." *Journal of Aircraft*, American Institute of Aeronautics and Astronautics, Vol. 13, No. 3, 1976.

[31] Loth, J.L., Boasson, M. "Circulation Control STOL Wing Optimization," *Journal of Aircraft*, American Institute of Aeronautics and Astronautics, Vol. 21 No. 2, February, 1984.

[32] Loth, J.L., Funk, M.S., "Thrust Savings Limitations with Blown high Lift Wings." AIAA/AHS/ASEE Aircraft Design, Systems and Operations Meeting, St. Louis, MO, 1987.

[33] Loth, J.L, Browning, P., Posada, A., "Engineering Solutions for Circulation Control Applications." Society of Automotive Engineers, AeroTech Congress and Exhibition, Grapevine, TX, 2005.

[34] Maskell, E.C., Spence D.A., "A Theory of the Jet Flap in Three Dimensions," *Proceedings of the Royal Society of London, A Mathematical and Physical Sciences Series*, Vol. 251, No. 1266, 1959.

[35] Mosher, M., "Acoustics of Rotors Utilizing Circulation Control." American Institute of Aeronautics and Astronautics Journal of Aircraft, Vol. 20, No. 11, 1981.

[36] Myer, D.P., "An Investigation of a Circulation Controlled Cambered Elliptical Airfoil with a Rounded Trailing Edge," Master of Science Thesis, Aerospace Engineering Department, West Virginia University, Morgantown, WV, 1972.

[37] Naqvi, M.A., "Prediction of Circulation Control Performance Characteristics for Super STOL& STOL Applications." Doctorate of Philosophy Dissertation, Georgia Institute of Technology, 2006.

[38] Newman, B.G. "The Deflexion of Plane Jets by Adjacent Boundaries – Coandă Effect," Boundary Layer Flow Control, Pergamon Press, Vol. 1, 1961.

[39] Novak, C.J., Cornelius, K.C., Roads, R.K., "Experimental Investigations of the Circular Wall Jet on a Circulation Control Airfoil." American Institute for Aeronautics and Astronautics, 25th Aerospace Sciences Meeting, Reno, NV, 1987.

[40] Ottensoser, J. "Two-Dimensional Subsonic Evaluation of a 15-Percent Thick Circulation Control Airfoil with Slots at Leading and Trailing Edges." David W. Taylor Naval Ship Research and Development Center, Bethesda, MD, 1974.

[41] Rae Jr., W.H., Shindo, S., "Comments on V/STOL Wind Tunnel Data at Low Forward Speeds." Washington University, Seattle, WA, 1969.

[42] Reader, K.R., Wilkerson, J.B., "Circulation Control Applied to a High Speed Helicopter Rotor." David W. Taylor Naval Ship Research and Development Center, Bethesda, MD, 1976.

[43] Rodman, L.C., Wood, N.J., "Verification of Performance for a Low-Speed 15% Elliptical Circulation Control Airfoil," Stanford University, Stanford CA, 1986.

[44] Rogers, E.O., Donnelly, M.J., "Characteristics of a Dual-Slotted Circulation Control Wing of Low Aspect Ratio Intended for Naval Hydrodynamic Applications." American Institute of Aeronautics and Astronautics, 42nd Aerospace Sciences Meeting, Reno, NV, 2004.

[45] Seif, M.S, Tavakoli, M.T., "New Technologies for Reducing Fuel Consumption in Marine Vehicles," XVI SORTA Symposium, Croatia, 2004.

[46] Smith, J.E., Loth, J.L., Craven, R.P.M., Bond, R., "Piezoelectric Actuators for Circulation Controlled Rotorcraft," US Patent 6,425,553 B1. 2002.

[47] Songlin, Z., Zianfu, W. "Experimental Investigation of a High-Lift Rudder-Circulation Control Rudder." *Journal of International Shipbuilding Progress*, Vol. 43, No. 436, 1996.

[48] Tai, J.C., Mavris, D.N., Schrage, D.P., "An Assessment of a Reaction Driven Stopped Rotor/Wing Using Circulation Control in Forward Flight." American Institute of Aeronautics and Astronautics, World Aviation Congress, Los Angeles, CA, 1996.

[49] Theodorsen, T., "Theory of Wing Sections of Arbitrary Shape," NACA-TR-411, 1931.

[50] Tongcitpakdee, C., "Computational Studies of the Effects of Active and Passive Circulation Enhancement Concepts on Wind Turbine Performance." Doctorate of Philosophy Dissertation, School of Aerospace Engineering, Georgia Institute of Technology, 2007.

[51] Tongcitpakdee, C., Benianirat, S., Sankar, L.N., "Numerical Studies of the Effects of Active and Passive Circulation Enhancement Concepts on Wind Turbine Performance." *Journal of Solar Energy Engineering*, American Society of Mechanical Engineers, Vol. 128, No. 4, 2006.

[52] Wood, N.J., "The Aerodynamics of Circulation Control Aerofoils." Joint Institute for Aeronautics and Astronautics, Stanford University, Stanford, CA, 1986.

[53] Ward, C.C., "Circulation Control technique on a Marine Propeller Duct." Master of Science Thesis, department of Naval Architecture and Marine Engineering, University of Strathclyde, Glasgow, U.K., 2006.

[54] Wilhelm, J.P., Pertl, E.D., Pertl, F.A., Smith, J.E. "Performance Predictions of a Circulation Controlled-Vertical Axis Wind Turbine with Solidity Control," American Society of Mechanical Engineers, Energy Sustainability Conference, San Francisco, CA, 2009.

[55] Wilhelm, J.P., Panther, C.C., Pertl, F.A., Smith, J.E. "Vortex analytical Model of a Circulation Controlled Vertical Axis Wind Turbine," American Society of Mechanical Engineers, Energy Sustainability Conference, San Francisco, CA, 2009.

[56] Wilkerson, J.B., Reader, K.R., Linck, D.W., "The Application of Circulation Control Aerodynamics to a Helicopter Rotor Model." American Helicopter Society, 29th Annual Forum, Washington, D.C., 1973.

[57] Williams, R.M., "Some Aspects on Rotor Circulation Control." CAL/AVLABS 3rd Symposium of Rotary Wing and V/STOL Aircraft, Buffalo, NY, 1969.

[58] Wood, N. J., "The Aerodynamics of Circulation Control Aerofoils," Stanford University Technical Report (SU-JIAA TR-41), Stanford, CA, 1981.

Lift Augmentation for Vertical Axis Wind Turbines

Gerald M. Angle II gerald.angle@mail.wvu.edu
Post Doctoral Fellow/Department of Mechanical and
Aerospace Engineering/Center for Industrial Research Applications
West Virginia University
Morgantown, WV 26506-6106, USA

Franz A. Pertl franz.pertl@mail.wvu.edu
Program Coordinator/Department of Mechanical and
Aerospace Engineering/Center for Industrial Research Applications
West Virginia University
Morgantown, WV 26506-6106, USA

Mary Ann Clarke maclarke@math.wvu.edu
Assistant Professor/Department of Mathematics
West Virginia University
Morgantown, WV 26506-6310, USA

James E. Smith james.smith@mail.wvu.edu
Professor and Director/Department of Mechanical and
Aerospace Engineering/Center for Industrial Research Applications
West Virginia University
Morgantown, WV 26506-6106, USA

Abstract

The concept of harnessing wind power has been around for centuries, and is first recorded by the Persians in 900 AD. These early uses of wind power were for the processing of food, particularly grinding grains, and consisted of stationary blades around a horizontal axis, the precursor to today's horizontal axis wind turbines (HAWT). Technology for these wind mills was essentially the same until the 1930's when advances in aircraft propeller theories were applied to the blades of the turbine. During this development period, which has since remained basically unchanged, the design push was for increasingly larger propellers requiring heavy and costly transmissions, generators, and support towers to be installed.

An alternative concept to the HAWT was developed by Georges Darrieus [1], which utilized a vertical shaft and is known as a vertical axis wind turbine (VAWT). The scientific development of the concept did not gain strong attention until the 1970's due to the perceived low efficiency of this style. This perception was due in part to the portion of the blade's rotary path that is adverse to the generation of power. This efficiency loss can be minimized by the mechanical movement of the blade, relative to the airflow during the upwind portion of the blades' rotational path. Since, circulation control can alter the forces generated by an airfoil, it could be used to increase the efficiency of a VAWT by increasing

the torque produced on the downwind portion of the path, while removing the need for a physical change in angle of attack.

With the recent upturn in petroleum costs and global warming concerns, interest in renewable energy technologies have been reinvigorated, in particular the desire for advanced wind energy technologies, including the application of lift augmentation techniques. One of these techniques is to utilize circulation control to enhance the lifting capacity of the blades based on the location of the blade in the turbine's rotation. Though this technology can be applied to any wind turbine, whether horizontal or vertical axis, this paper focuses on the application of circulation control for VAWT's due primarily to reduced hardware complexities and to increase the performance of this design thus helping to level the playing field between the two styles. This performance enhancement coupled with the ability to locate the primary components near the ground allows for easier installation, troubleshooting, maintenance, and future improvement of the circulation control sub-system.

By varying the circulation control performance with the blade position, the coefficient of performance, C_p, of the wind turbine can be altered. This variation in C_p resembles a change in the effective solidity factor, the non-dimensional characteristic that accounts for the number of turbine blades, chord length, and turbine radius. The solidity factor is typically used in the design of a wind turbine with its peak performance occurring at various tip speed ratios, at different solidity factors.

Prior to the construction of physical models, numerical methods, namely a vortex model, was used to estimate the performance enhancement potential of the blade force augmentation via circulation control. These results were then used to construct and test a wind tunnel blade section model to obtain lift and drag values for a full range of rotational angles. These results were then supplied to the vortex model which indicated that through the addition of circulation control to the blades of a vertical axis wind turbine a wider coefficient of performance curve can be achieved, similar to a change in the solidity factor of the wind turbine.

Keywords: Circulation Control, Vertical Axis Wind Turbine, Vortex Model.

1. INTRODUCTION

The maximum power extractable from wind at a specified velocity flowing through a turbine area, A, is defined by the Betz limit, 16/27. This limit has been derived by considering the momentum loss between the upstream and downstream velocities, V_1 and V_2, respectively, as shown in Eq. (1).

$$P = \frac{1}{2}\rho A\left(\frac{V_1+V_2}{2}\right)\left(V_1^2 - V_2^2\right) \quad (1)$$

The maximum extractable power of ~59% of the available power occurs when V_2 (downstream) is approximately one third of V_1 (upstream). Substituting the free stream velocity, V_∞, into Eq. (1), results in Eq. (2) for the maximum power extractable from a wind according to the Betz limit, relative to the overall power available in the wind. The coefficient of performance, C_p, defined in Eq. (3), is a representation of the ratio of actual power produced-to-maximum power available in the wind.

$$P_{\max} = \frac{16}{27}\left(\frac{1}{2}\right)\rho A V_\infty^{\,3} \tag{2}$$

$$C_p = \frac{\left(1+\frac{V_2}{V_1}\right)\left[1-\left(\frac{V_2}{V_1}\right)^2\right]}{2} \tag{3}$$

The theoretical maximum coefficient of performance, 16/27, is never achieved by practical wind turbines due to the irregularities in the wind speed and other environmental factors. A more realistic value for the C_p for existing wind turbines range from 30-50%, or 51-85% of the Betz limit. Thus, the power extracted by a wind turbine can be defined based on an efficiency, η, density, ρ, the turbine's capture area and the wind velocity as is shown in Eq. (4). This definition of efficiency is with respect to the Betz limit, thus if the coefficient of performance is 0.45, the efficiency is 76%. The power produced depends on the wind-speed cubed, thus it is important to know the wind speed of the intended site in order to predict the power capacity of a wind turbine. This study is based on the H-Shaped Darrieus Vertical Axis Wind Turbine as previously investigated by Kuhlke [2], Migliore [3], and Migliore et al. [4].

$$P_\eta = \eta\frac{16}{27}\left(\frac{1}{2}\right)\rho S V_\infty^{\,3} \tag{4}$$

2. IMPLEMENTED VORTEX MODEL

The approach taken to evaluate the performance of the VAWT was to use the vortex model by combining the Kutta-Joukowski law, Eq. (5), with the aerodynamic lift force exerted by the blade per unit span, Eq. (6). By equating these two relationships, the influence of the lift force on the air surrounding the VAWT, can be investigated using Eq. (7).

$$L' = \rho V \Gamma \tag{5}$$

$$L' = \frac{1}{2}\rho V^2 c C_\ell \tag{6}$$

$$\Gamma = \frac{1}{2} V c C_\ell \tag{7}$$

However, the aerodynamic forces change with angle-of-attack, thus the circulation created by the wind turbine blade is also dependent on the angle-of-attack, and consequently dependent upon the rotational location of the turbine blade with respect to the direction of the wind plus the tip speed ratio. The vortex model incorporates a time dependent analysis, taking small time steps to analyze the wind turbine performance. Each blade has an associated "bound vortex", Γ_B, with a strength based on the lift force of the current conditions (angle-of-attack, speed, etc) which moves with the blade, around the turbine. As the strength of the bound vortex changes from time step, *NT*, to time step, *NT-1*, the difference between the vortex strength defines the strength of the vortex that is shed, Γ_S, as is illustrated in FIGURE 1 and defined in Eq.(8).

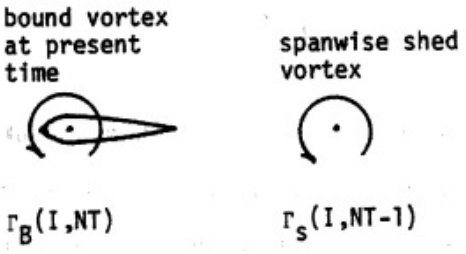

FIGURE 1: Diagram of the Spanwise Shed Vortex, Strickland, et al. [5].

$$\Gamma_s(i, NT-1) = \Gamma_B(i, NT-1) - \Gamma_B(i, NT) \tag{8}$$

The induced velocity at a point (i, j) in the flow, due to a single vortex can be found using Eq.(9). In complex flows, such as for the VAWT, the induced velocity is determined based on the sum of all the vortex strengths, bound and shed, in the spanwise direction and is due to the lift generation, i.e. trailing vortices, as shown in Eq. (10).

$$\vec{V}_p = \frac{\Gamma}{4\pi}\int_{\ell}\frac{\vec{r}\times d\vec{\ell}}{r^3} \tag{9}$$

$$\vec{V}(i,j) = \sum_{k=1}^{NE}\sum_{\ell=1}^{NT-1}\vec{V}_p\Big|_{trailing\ \ vortices} + \sum_{k=1}^{NE-1}\sum_{\ell=1}^{NT}\vec{V}_p\Big|_{spanwise\ \ vortices} \tag{10}$$

After prediction of the induced velocities, the bound vortex strength was updated using Eq. (7) along with the new velocities, which were then used to update the induced velocity using Eq. (9). Note that this relationship is only valid outside of a given radius, “core” of the vortex. The velocity at the edge of the vortex core, V_c, if found using Eq. (11), the corresponding radius, h_c, is defined by Eq. (12). FIGURE 2 illustrates the velocity profile in the vicinity of a vortex, where a zero velocity is imposed at the core center and a linear profile is applied to the calculated velocity at the edge of the core. Strickland, et al. [5] notes that the core velocity is independent of the $\Delta\theta$ angle when the step is reasonably small; however, the core radius is proportional to the angular increment. Eq. (13) was used to represent the velocity near the core as a single function, as done by Pawsey [6], rather than the piecewise function of Strickland, et al. [5], resulting in the profile shown in FIGURE 3.

$$V_c = \frac{1}{2}\frac{\Gamma}{R(\Delta\theta)} \tag{11}$$

$$h_c = \frac{R(\Delta\theta)}{\pi} \tag{12}$$

$$V_c = \frac{\Gamma h}{2\pi\left(h^2 + \left(\frac{R\,\omega\Delta t}{2\pi}\right)^2\right)} \tag{13}$$

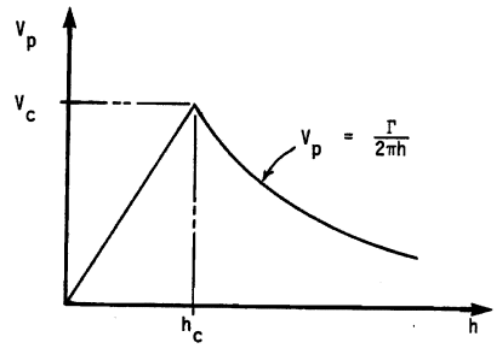

FIGURE 2: Velocity Profile of Vortex with Viscous Core, Strickland, et al. [5]**.**

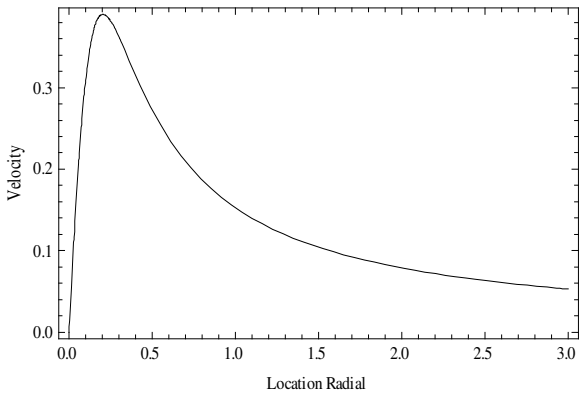

FIGURE 3: Representation of the Velocity Profile with $R = 1$ using Eq. 13 from Pawsey [6].

A vortex is shed from the blade at every time step in the analysis, and is transmitted downstream by the induced velocity due to all vortices in the flow field. The shed vortices are transmitted downstream until they exit the analytical space, generally five rotor diameters downstream, which allows for the visualization of multiple revolutions of the wind turbine.

As the resultant velocity, U_R, is determined, the tangential force per unit length, F_t', acting in the direction of motion and the normal force per unit length, F_n', can be determined using Eqs. (14) and (15), respectively. The non-dimensional version of these relationships, F_t^+ and F_n^+, Eqs. (16) and (17), are non-dimensionalized with respect to the freestream velocity, U_∞.

$$F_t' = \frac{1}{2} C_t \rho c U_R^2 \tag{14}$$

$$F_n' = \frac{1}{2} C_n \rho c U_R^2 \tag{15}$$

$$F_t^+ = \frac{F_t'}{\frac{1}{2}\rho c U_\infty^2} = C_t \left(\frac{U_R}{U_\infty} \right)^2 \tag{16}$$

$$F_n^+ = \frac{F_n'}{\frac{1}{2}\rho c U_\infty^2} = C_n \left(\frac{U_R}{U_\infty} \right)^2 \tag{17}$$

Eq. (18) defines the torque produced by one element (blade) based on the tangential force per unit length, as well as its non-dimensional form. The power coefficient (coefficient of performance) at each time step is determined by Eq. (19) for an individual blade. To obtain the coefficient of performance for the entire rotor the average value for a complete revolution is found from Eq. (20), based on the number of time increments, *NTI*, and the number of elements, *NE*, (blades).

$$T_e^+ = \frac{F_t'}{RU_\infty^2} = \frac{1}{2}\left(\frac{c}{R}\right)F_t^+ \tag{18}$$

$$C_{p_{element}} = T_e^+ \frac{U_T}{U_\infty} \tag{19}$$

$$C_p = \frac{1}{NTI}\sum_{1}^{NTI}\sum_{1}^{NE-1} C_{p_{element}} \tag{20}$$

The coefficient of performance is dependent on the solidity factor, σ, as well as the tip speed ratio, λ, as shown in FIGURE 4 for an unaltered NACA 0012 blade cross-sectional shape. As the solidity factor is increased the low tip speed ratio performance in increased, where a maximum Cp of approximately 0.42 is achieved at solidity factors of 0.2 and 0.4. However, at low tip speed ratios the peak coefficient of performance is decreased while an increasing coefficient of performance can be achieved at higher tip speeds. For example, a solidity of 0.1 reaches a Cp of zero at a tip speed of 10.5, whereas a solidity of 0.2 reaches zero at just over a tip speed ratio of 8. FIGURE 4 represents a series of plots for solidity factors, σ, from 0.0125 to 0.8 over the range of tip speed ratios, λ, up to 12. These curves represent the potential power capture ratios for a given solidity factor wind turbine, where the designer would select the single curve that would result in the greatest energy capture for the given wind conditions of the intended site.

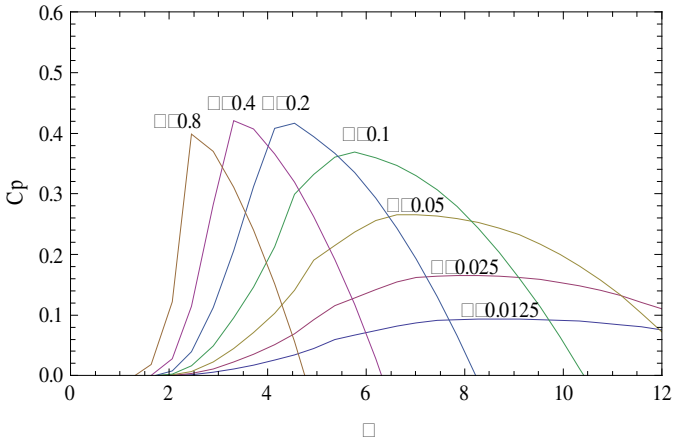

FIGURE 4: Coefficient of Performance using a NACA0012 Airfoil at Re = 300,000, for various σ Values, McGrain, et al. [7]**.**

3. APPLICATION BACKGROUND OF CIRCULATION CONTROL

The initial research and later applications of circulation control technologies were for short take-off, fixed-wing aircraft which were initially built and tested in the late 1960's and 1970's. This phenomenon re-energizes the boundary layer near the trailing edge, as shown in FIGURE 5, of an airfoil with a rounded trailing edge which enhances the circulation around the wing. Introducing a blowing jet tangent to the surface, either inclined or rounded, creates a pressure force deflecting the jet towards the surface, as introduced by Newman [8]. For a rounded surface, such as a cylinder as investigated by Churchill [9], or a modified trailing edge of an airfoil as studied by

Ambrosiani [10], Englar [11], Kind [12], Kind and Maull [13], and Myer [14], to name a few of the many investigators, this pressure force overcomes the centrifugal (inertial) force of the jet. As the jet flow travels along the surface, the pressure force decreases until the inertial force is greater, at which point flow separates from the surface.

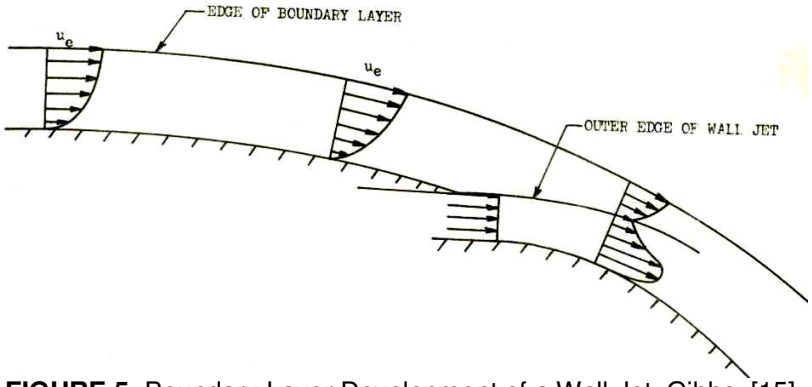

FIGURE 5: Boundary Layer Development of a Wall Jet, Gibbs, [15].

The blown jet in turn entrains the freestream airflow, effectively altering the interaction of the airfoil with the surrounding fluid. This change in effective shape alters the lift and drag performance of the airfoil. The amount of change in the aerodynamic forces is a function of the blowing coefficient which is a non-dimensional ratio of jet momentum to the freestream momentum. The blowing coefficient, C_μ, is a function of the density, ρ, velocity, V, of the jet and free-stream as prescribed by the subscripts j and ∞, respectively, and slot height, h, chord length, c, and the span of the jet and turbine blade, b_j and b_s, respectively, as is shown in Eq. (21).

$$C_\mu = \frac{\rho_j V_j^2 b_j h}{\frac{1}{2}\rho_\infty V_\infty^2 b_s c} \tag{21}$$

In the prior fixed wing circulation control studies, the change in lift coefficient of the airfoil was found to be dependent on the ratio of velocities; jet and freestream, V_j and V_∞. Eq. (22) is an empirical fit created by Loth and Boasson [16] to describe the circulation control lift enhancement. Combining Eq. (21) and Eq. (23) yields a relationship of the change in lift coefficient, as a function of the blowing coefficient, slot height, and chord length.

$$\Delta C_L = 40\left(\frac{h}{c}\right)^{0.64}\left(\frac{V_j}{V_\infty} - 1\right) \tag{22}$$

$$\Delta C_L = 40\left[\left(\frac{h}{c}\right)^{0.14}\sqrt{\frac{\rho_\infty C_\mu}{2\rho_j}} - \left(\frac{h}{c}\right)^{0.64}\right] \tag{23}$$

4. AERODYNAMIC PERFORMANCE MODIFICATIONS

Circulation control was initially considered such that the open blowing slots near the trailing edge of the airfoil are in the direction of the lift force. In other words, when the airfoil is at positive angles-of-attack, the blowing slot on the upper surface of the airfoil will be opened, and at negative angles-of-attack the lower surface blowing slot is opened. In order to simulate this transition the data from 0 to 180 degrees was inverted and applied from 0 to -180 degrees as shown in **FIGURE 6** for the lift coefficient and **FIGURE 7** for the drag coefficient.

The lift and drag coefficient plots in **FIGURE 6** and **FIGURE 7** were based on the data presented by Pawsey [6] as the non-circulation controlled performance. Circulation control enhancement of the lift, as described by Loth and Boasson [16] in Eq. 21, and the corresponding increase in induced drag, was applied at angles of attack ranging from -15 to 15 degrees, which is the only region where circulation control blowing is currently applied in these idealized lift and drag curves. In this range, a considerable increase in lift coefficient can be achieved which can in turn be utilized to enhance the performance of the wind turbine. The increased enhancement will be most beneficial during low tip speed ratio operation, which provides a wider range of useful wind speeds.

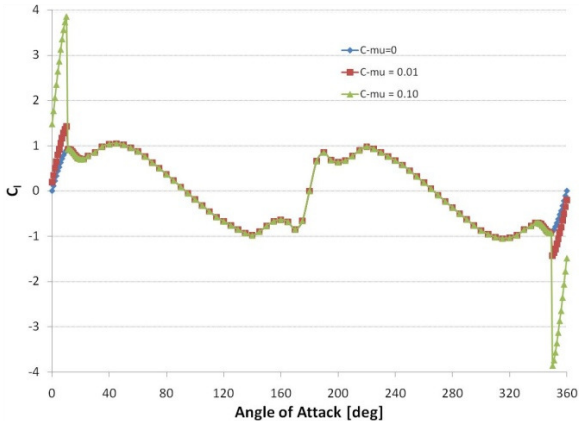

FIGURE 6: Lift Coefficient Determined for the Blowing Coefficients of 0, 0.01, and 0.10.

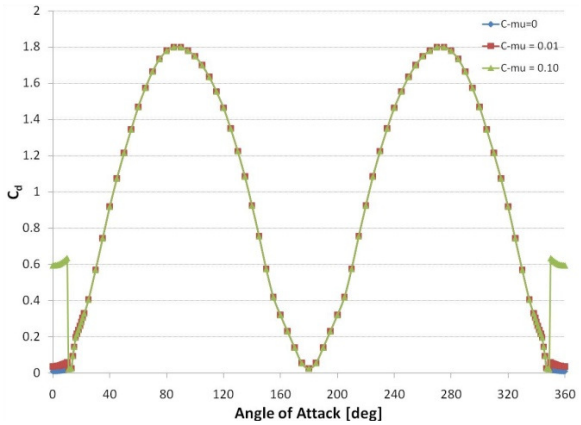

FIGURE 7: Drag Coefficient Determined for the Blowing Coefficients of 0, 0.01, and 0.10.

Since the application of circulation control requires a modification to the trailing edge of the airfoil, and existing literature has no general theory for the precise prediction of the augmented aerodynamic forces for this application, an experiment was undertaken to expand the understanding of parameters which influence the performance of circulation control. A model was developed based on the NACA 0018 airfoil with a 9 inch chord-length. The airfoil model was modified by creating a rounded trailing edge, with ~0.015 inch blowing slots located at the vertical apex of the cylindrical trailing edge. This modification resulted in a physical chord length of 8 inches and a thickness ratio of 20.3% for the test model and is shown in **FIGURE 8**, as installed in the West Virginia University Closed Loop Wind Tunnel. This test specimen was tested at a variety of air speeds and over the required range of angles of attack. The results obtained were in the form of lift and drag coefficient curves.

FIGURE 8: Experimental Set-up of the Modified NACA 0018 Airfoil Model, as Tested in the WVU Closed Loop Wind Tunnel

5. RESULTS AND CONCLUSIONS

The lift and drag curves resulting from the experiments are shown in FIGURE 9 and **FIGURE 10**, respectively, are the key results of the tests on the modified NACA 0018 airfoil. These results indicate an increase in the lift coefficient, at zero degrees for the non-blown C_l = 0, and for blowing at a C_μ = 0.10 resulted in a lift coefficient of approximately 1; and as expected the drag was also found to increase. These lift augmentation curves are approximately one half the values documented by previous investigations Englar [11], Gibbs [15], and Harness [17]. The limited performance of the circulation control in the current research was attributed to the smaller trailing edge radius incorporated into the NACA 0018 Circulation Control model. This decrease in lift augmentation potential was deemed acceptable due to the penalties associated with large profile drag of a large diameter trailing edge. This trade-off will be considered in future work.

FIGURE 11, shows the vortex model predictions with the various blowing coefficients against the inverse of the tip speed ratio, which reveals that the blowing coefficient has a similar influence on the performance of the wind turbine as the various potential solidity factors, compared to FIGURE 4 in that the shape of the curve is slightly modified in width and location of the peak. The benefit of using circulation control is that the blades' performance can be changed on the fly during operation of the wind turbine, which is not possible with a non-augmented blade. A computerized system can be incorporated to customize the circulation control blowing coefficient to maximize the performance over a wide range of tip speed ratios. In lieu of using the site specific wind conditions needed to estimate the annual energy gain, the area under the C_p-λ curve can be used to represent the comparative difference in the annual energy production independent of the site specific wind conditions. The area under the "*Base"* curve was found to be 0.0423 and the *"Variable* σ*"* curve was found to be 0.0654. Allowing the circulation control augmented wind turbine to effectively capture energy at the peak performance coefficient over a range of blowing conditions, yields approximately a 50% increase in the area under the performance curve. It is important to note that this is an idealized measure of the performance over a range of wind speeds and may not reflex the gains in total power generated in the actual wind conditions and have yet to account for the power required to supply the blown air and other performance factors

of the circulation control. Some of these factors include the maximum blowing coefficient, the tip speed ratio when circulation control is phased out, as well as the duration of the blowing.

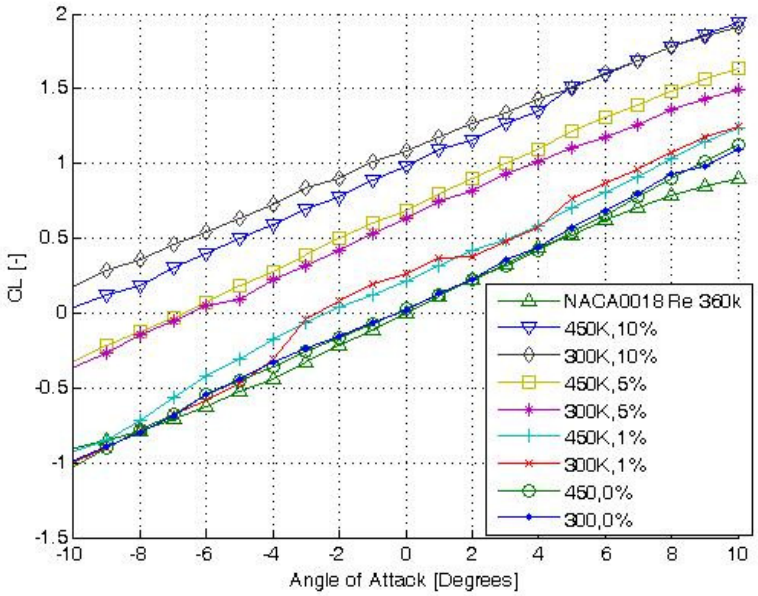

FIGURE 9: Experimentally Determined Lift Coefficient Curves for the Circulation Control Augmented NACA 0018.

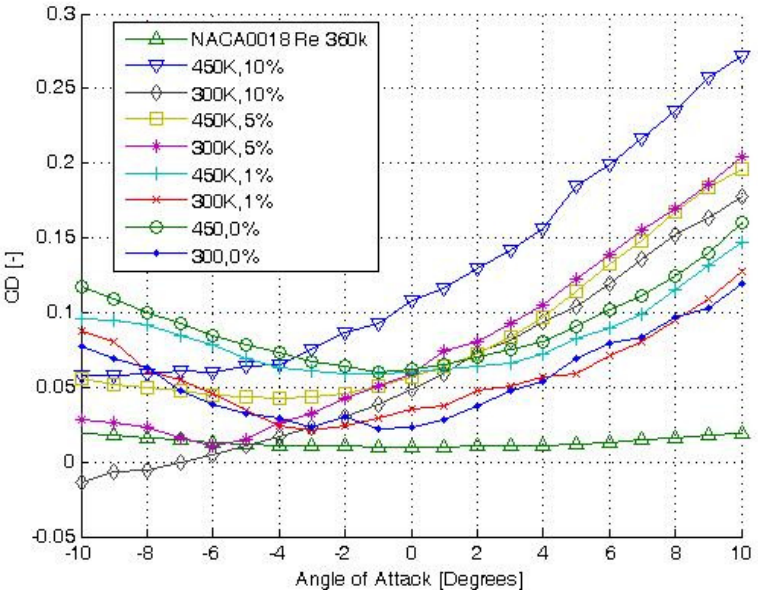

FIGURE 10: Experimentally Determined Drag Coefficient Curves for the Circulation Control Augmented NACA 0018.

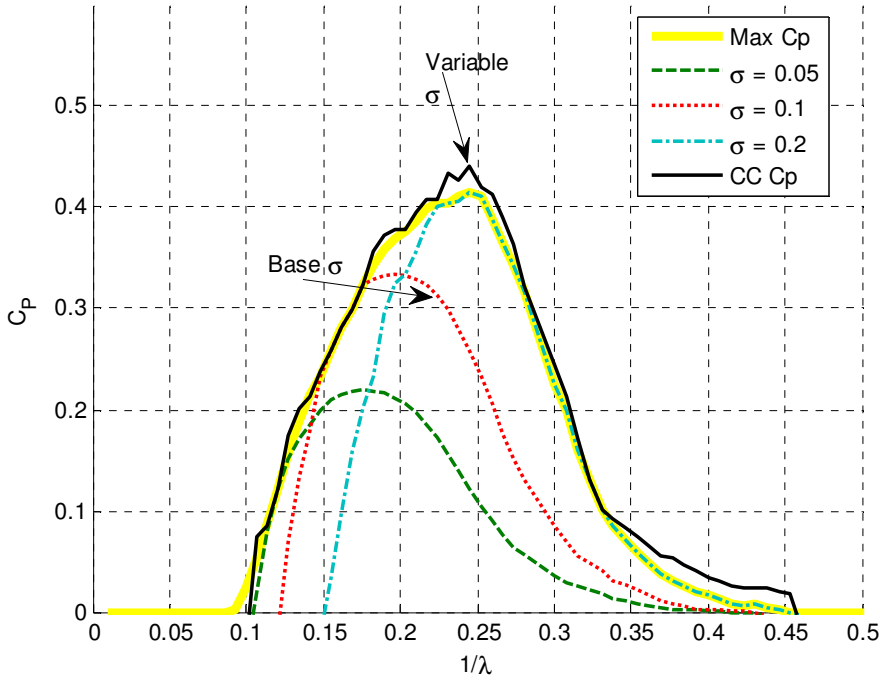

FIGURE 11: Estimated Performance for Solidity Factor of 0.1 with Blowing for the Investigated Blowing Coefficients, Wilhelm [18].

From the projected performance of the circulation control augmented vertical axis wind turbine, FIGURE 11, the regions of the world upon which large wind turbines can be installed can be increased. Large wind turbines, generally referred to as "Utility Size", tend to operate at a fixed rotational speed and are directly connected to the electrical grid. Consequently, as the wind speed varies the tip speed ratio also varies, resulting in a change in the coefficient of performance. The adaptation of circulation control to the wind turbine has been simulated and yields a potential method to alter the performance curve of the wind turbine to tailor the performance to the current wind conditions of the site. In consistent wind environments this adaptation provides less benefit. However, in environments with predominant wind at a variety of speeds the use of circulation control can potentially enhance the turbine performance by 5% to 50%. The amount of improvement due to circulation control depends on the engineering trade-offs of the maximum blowing coefficient, tip speed ratio at which blowing is phased out, wind distribution, height of the blown jet, duration of the blowing (% of the blades path), and the span of the blowing jet (% of the turbine rotor height).

These results lead to the conclusion that circulation control has a potential impact on the future of wind turbines, particularly VAWT's, and should be further evaluated by experimental means, particularly methods to enhance the jets interaction with the flow such as ejectors or injectors near the jet. Another issue which needs further examination is the power required to provide the compressed air to the blowing slots. The estimated power can be experimentally determined for the various blowing coefficients and used to develop the upper and lower limits of when to apply the circulation control and how to manipulate the flow rate to maximize the energy capture while minimizing the power required and making the concept cost effective.

6. NOMENCLATURE

Symbol	Meaning
A	Turbine Rotor Area
A_{shaft}	Internal Ducting Area of Shaft
b_j	Span of Jet
b_s	Span of Turbine Blade

c	Chord Length of Blade
C_l	Lift Force Coefficient
C_n	Normal Force Coefficient
C_p	Coefficient of Performance
$C_{P_{element}}$	Coefficient of Performance per Element Span
C_t	Tangential Force Coefficient
C_μ	Blowing Coefficient
$d\ell$	Incremental Length
F_n'	Normal Force per Unit Span
F_n^+	Non-Dimensional Normal Force per Unit Span
F_t'	Tangential Force per Unit Span
F_t^+	Non-Dimensional Tangential Force per Unit Span
h	Height of the Blowing Slot
HAWT	Horizontal Axis Wind Turbine
h_c	Radial Height of a Vortex
L'	Lift per Unit Span
P	Power
P_{max}	Maximum Power
P_η	Power Incorporating Compressor Efficiency
r	Radial Location
R	Turbine Radius
S	Blade Area
T_e^+	Non-Dimensional Torque per Blade Element
U_R	Resultant Velocity
U_T	Tangential Velocity
V_1	Upstream Wind Speed
V_2	Downstream Wind Speed
VAWT	Vertical Axis Wind Turbine
V_c	Velocity at Edge of Vortex Core
V_j	Jet Velocity
V_∞	Wind Speed
ΔC_l	Change in Lift Coefficient Due to Circulation Control
Δt	Time Step
$\Delta\theta$	Angular Step
η	Compressor Efficiency
Γ	Circulation
Γ_B	Bound Circulation
Γ_s	Shed Circulation
λ	Tip Speed Ratio
ρ	Density
σ	Solidity Factor
ω	Rotational Speed of Turbine

7. REFERENCES

[1] Georges Jean Marie Darrieus, "Turbine Having Its Rotating Shaft Transverse to the Flow of the Current," 1,835.018, December 1931.

[2] K.A. Kuhlke, "An Experimental Investigation of the WVU Straight Bladed Darrieus Wind Turbine," Morgantown, WV, MS Thesis 1978.

[3] P.G. Migliore, "A Free-Vortex Model with Numerical Solution for the Unstead Lifting Characteristics of Straight Bladed Darrieus Wind Turbines," Morgantown, WV, Ph.D.

Dissertation 1978.

[4] P. G. Migliore, W. P. Wolfe, and R. E. Walters, "Aerodynamic Tests of Darrieus Turbine Blades," 1980.

[5] J. H. Strickland, B. T. Webster, and T. Nguyen, "A Vortex Model of the Darrieus Turbine: An Analytical and Experimental Study," Alburquerque, NM, 1980.

[6] N.C.K. Pawsey, *Development and Evaluation of Passive Variable-Pitch Vertical Axis Wind Turbines. Diss.* New South Wales: University of New South Wales, 2002.

[7] David McGrain, Gerald M Angle II, Jay P Wilhelm, Emily D Pertl, and James E Smith, "Circulation Control Applied to Wind Turbines," , San Francisco, CA, USA, 2009.

[8] B.G. Newman, "The Deflexion of Plane Jets by Adjacent Boundaries - Coanda Effect," in *Boundary Layer and Flow Control, Vol. 1.*: Pergamon Press, 1961, p. 232.

[9] R. A. Churchill, "Coanda Jet Around a Cylinder with an Interacting Adjacent Surface," Morgantown, WV, Ph.D. Dissertation 1992.

[10] J. P. Ambrosiani, "Analysis of a Circulation Controlled Elliptical Airfoil," Morgantown, WV, Ph.D. Dissertation 1971.

[11] R.J. Englar, "Two-Dimensional Subsonic Wind Tunnel Tests of Two 15-Percent Thick Circulation Control Airfoils," Tech. Note AL-211 1971.

[12] R. J. Kind, "A Calculation Method for Circulation Control by Tangential Blowing Around a Bluff Trailing Edge," *Aeronautical Quarterly*, p. Vol. XIX, 1968.

[13] R J Kind and D J Maull, "An Experimental Investigation of a Low-Speed Circulation-Controlled Aerofoil," *Aeronautical Quarterly Vol. XIX*, pp. 170-182, May 1968.

[14] Danny P. Myer, "An Experimental Investigation of a Circulation Controlled Cambered Elliptical Airfoil with a Rounded Trailing Edge," Morgantown, WV, MS Thesis 1972.

[15] E.H. Gibbs, "Analysis of Circulation Controlled Airfoils," Morgantown, WV, Ph.D. Dissertation 1975.

[16] J. L. Loth and M. Boasson, "Circulation Contol STOL Wing Optimization," *Journal of Aircraft*, pp. Vol. 21 No. 2 pp. 128-134, 1983.

[17] Gregory S. Harness, "An Experimental Investigation of a Circulation Controlled Cambered Elliptical Airfoil," Morgantown, WV, MS. Thesis 1970.

[18] Jay P. Wilhelm, "Power Envelope Expansion using a Solidity Matching Scheme for a Circulation Controlled Vertical Axis Wind Turbine," Morgantown, WV, PhD Dissertation 2010.

[19] C. Trevelyan, "Application of Circulation Control Aerofoils to Wind Turbines," Leicestershire, UK, Ph.D. Dissertation 2002.

Manufacture of a Biodegradable Detergent on Small Scale

Abdulla A.Aziz A.Majeed abuwaelhb@yahoo.com
Faculty of Engineering,
I Department of Mechanical Engineering,
University of Aden, Yemen
Aden, Yemen

Jairam Singh jsinghaden@yahoo.com
Faculty of Engineering,
Department of Mechanical Engineering,
University of Aden, Yemen
Aden, Yemen

Abstract

This paper deals with an aggregate planning for a small scale production unit using a network flow model for full utilization of its capacity to meet the changing forecasted demand .The formulation of the problem is done by using the given inventory capacity with backorders by making a trade-off among inventory costs , backlog costs, production and subcontracting costs. The total cost function and the constraint inequalities were developed assuming the cost functions to be linear. The parameters of objective function and the constraints were estimated from the economics of the plant. The values of the work force, overtime, backlog, amount subcontracted were determined for a planning horizon of six months using an LP computer package. This method of production scheduling took care of the fluctuating demand utilizing the full capacity of the plant.

Keywords: Production scheduling, Operations Management, Supply chain Management.

1. INTRODUCTION

The goal of the IJCSS is to publish the most recent results in the development of information technology. Soaps are the earliest form of detergents, though at present, the term detergent is used for synthetic detergents derived from petroleum products. Due to tremendous strides in petrochemical industries, propylene became available which was polymerized to propylene tetramer that became the major feedstock for the manufacture of synthetic surfactant known as Linear Alkyl Benzene Sulphonate (LABS). To improve the detergency of powders, certain other components known as builders, synergizers, fillers and brighteners, etc. are also added. The surfactants have molecular structure that have hydrophilic groups on one end and hydrophobic groups on the other end which imparts the special characteristics of soil removal from the surface of the clothes [4,5].

2. The Production Process of an Anionic Detergent

Synthetic detergents are cleansing agents which have all the properties of soaps, but which actually does not contain any soap. These can be used both in soft and hard water as they give foam even in hard water some of the detergents give foam even in ice cold water.

The propylene tetramer dodec-1-ene can be made to add onto a benzene ring in presence of hydrogen chloride and aluminum chloride catalyst - a variation of Fridal-Crafts reaction as shown below:

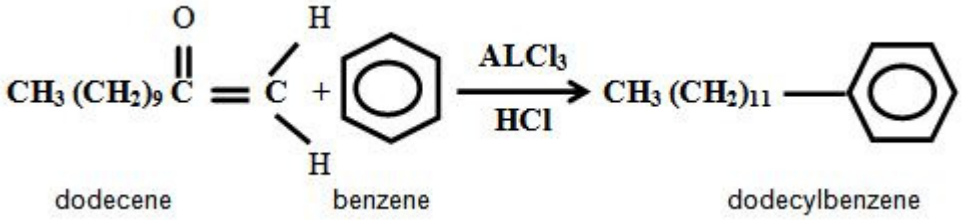

The dodecylbenzene is sulphonated by refluxing it with concentrated sulphuric acid. The form of sulphuric acid is (HO)2 SO2 i.e. an oxoacid with two –OH groups and two oxygen atoms attached to a central sulphur atom. The actual electrophile is SO3 and the overall reaction may be represented as

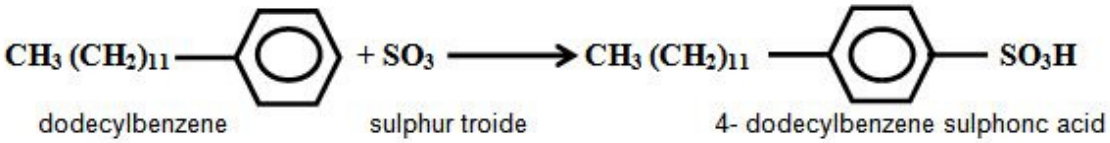

This is neutralized by sodium hydroxide to form the sodium salt, which is the detergent.

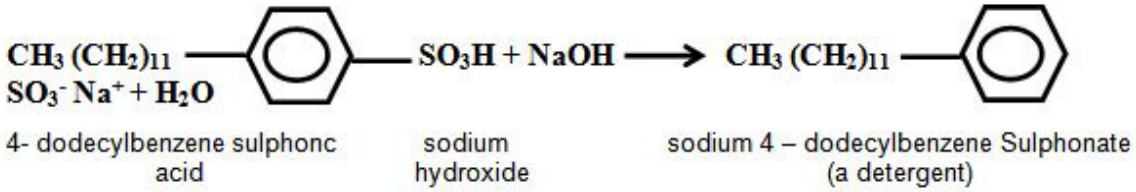

Here, the reactions used are essentially those which can be carried out in the laboratory, although the conditions vary somewhat. The sulphur trioxide gas (hard to handle in the laboratory) is used rather than sulphuric acid for the sulphonation step. This detergent makes up around 10% by weight of most commercial washing powders. This detergent sodium 4-dodecylbenzene sulphonate has the 12-carbon side chain attached by a Friedel-Crafts reaction is biodegradable. Bacteria such as Escherichia coli can degrade this detergent.
Small scale production of detergent powder is done by mixing 15 to 40 percent active surfactant known as acid slurry with rest of the additives in an Amalgamator and a slurry milling machine. Then it is pulverized in a pulverizer. Then the stuff is ground in either a disintegrater or a centrifugal type of grinding machine. Then packaging is done as required by the consumers [5].

3. Aggregate Planning for Production

An aggregate planning is a process by which company determines levels of production capacity, subcontracting, inventory, stock outs and even pricing over specified time horizon, the goal of aggregate planning is to satisfy demand in a way that maximizes profit. Generally, the demand rate varies over time and the associated problem becomes a dynamic planning problem [1,2,3,6] but it is assumed to remain the same during a fixed period stated in the planning time horizon.

The following are some of the alternatives available for planning to meet the fluctuating demands.

1. Build inventories during the period of peak demand in anticipation of higher demand rates later in the planning periods.
2. Carry backorders during the periods of peak demands.
3. Use overtime in peak periods or under time in slack periods to vary output while holding workforce and facilities constant.

4. Use subcontracting in peak periods.
5. Vary capacity by changing the size of the workforce through hiring and firing.
6. Vary capacity through changes in plants and equipment. Since we typically are concerned with planning horizon less than a year, we usually shall assume that facilities are fixed and thus this alternative is not available to the planner.

The optimal combination of these alternatives involves proper trade-offs between the following types of costs:

1. Production costs which include any out-of-pocket costs that is associated with production rate.
2. Inventory holding costs.
3. Shortage losses associated with backorders and lost sales.
4. Costs of increasing and decreasing workforce levels. These include hiring and training costs and separation pay and other losses associated with firing or laying off workers.
5. Costs of deviating from normal capacity through use of overtime or under time.

4. The Network Flow Model

In general, the fundamental trade-offs available to an aggregate planner are among the following:

1. Capacity (regular time, overtime, subcontracting).
2. Inventory.
3. Backlog / lost sales.

An aggregate plan that decreases one of these costs typically results in an increase of the other two. In this sense, the costs represent a trade-offs. To lower inventory cost the planner must increase capacity costs or backlog costs. Arriving at a most profitable trade-offs is the goal of an aggregate planning [8,10]. It is interesting to observe that the aggregate planning problem can be conceptualized as a network model with backorders as indicated in the network flow diagram in Fig.1.

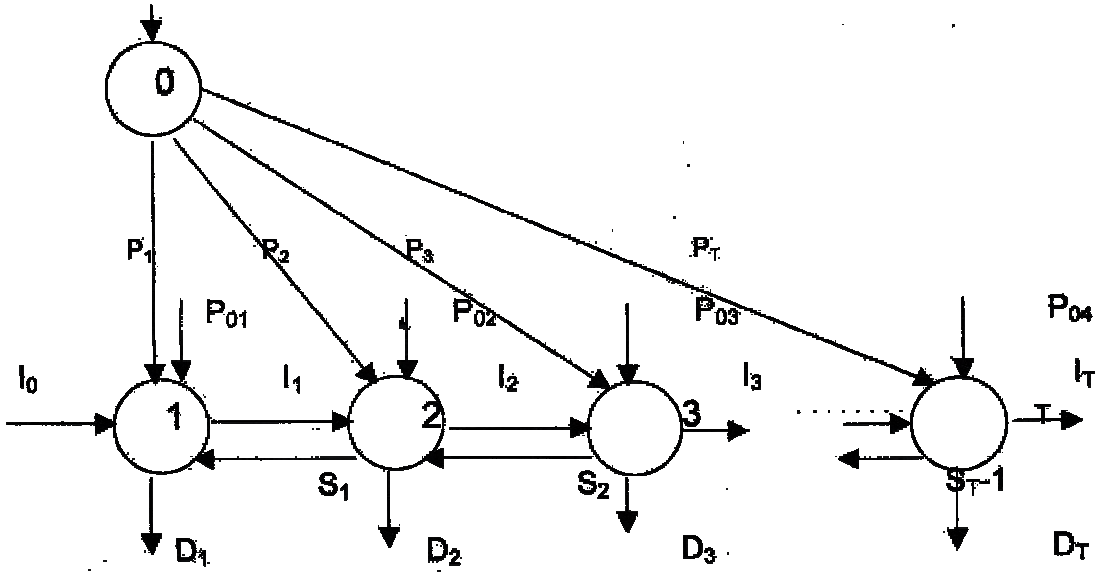

FIGURE 1: Network Flow Model With Backlogging

4.1 Decision Variables

The following decision variables are defined for the aggregate planning model:
W_t = Workforce size in man - hours for the month t; t = 1, 2, 3…., T.
H_t = number of employees hired in man-hours at the beginning of the month t; t=1, 2,…..T.
L_t = number of employees laid off at the beginning of the month t; t = 1, 2….., T.
P_t = number of units produced in month t, t = 1, 2,…..T.

I_t = inventory at the end of the month, t = 1, 2,…..,T.
S_t= number of units stock out / backlogged at the end of month t; t = 1, 2,…..,T.
P_{st}= number of units subcontracted for the month t; t = 1, 2,….,T.
O_t= number of overtime man-hours in month t; t = 1, 2,…..,T.

4.2 Parameters of the Problem

C_t= unit material cost in the period t; t= 1, 2,…….,T.
h_t= inventory carrying cost per unit held in the period t; t = 1,2,……..,T.
TT_t = backorder cost per unit carried from period t to t +1.
m = number of man-hours required to produce one unit of product.
L_t = cost of one regular labour per man-hour.
e_t =cost of hiring and training per unit of labour.
e^t = cost of laying off one worker.
D_t = demand in the period t.
C_{st}= cost of subcontracting per unit.

4.3 Formulation

The values of demand, D_t, are specified by the demand forecast which is fluctuating each month of the planning horizon [7,9]. The objective function is to minimize the total cost incurred during the entire planning horizon. The cost incurred includes regular labour cost, overtime labour cost, cost of hiring and training, cost of laying off, cost of holding inventory, cost of stocking out, cost of subcontracting and material cost. The objective function turns out to be

$$z = \sum_{t=1}^{T} [\, L_t W_t + e_t H_t + e^t L_t + 1.5\, L_t O_t + h_t J_t + \pi_t S_t + C_{st} P_{ot} + C_t P_t \,] \quad \textbf{(1)}$$

to be minimized subject to the following constraints. It is intended to give a high level customer service having met all their demands.

i. Workforce constraint

The workforce size W_t in any period t, is dependent upon the workforce size in the previous period (t-1) and number of workers hired in the period t and the number of workers fired in the period t.
Therefore

$$W_t = W_{t-1} + H_t - L_t \quad \text{for } t = 1,2,\ldots\ldots T.$$

The starting workforce is given to be W_o. Then

$$W_t = W_o + \sum_{t=1}^{T} = (H_t - L_t) \quad \textbf{(2)}$$

ii. Capacity Constraint

In each period, the amount produced in house cannot exceed the capacity of the plant available including overtime. This constraint limits the internal production based on three shifts and overtime subcontracted production is not included in this constraint. Let us say that the total production of the plant is X units per month and total man-hours required per month are Y. Then man-hours required per unit of production is Y/X
Therefore,

$$P_t <= Y/X\, W_t + Y/X\, O_t \quad \textbf{(3)}$$

iii. Inventory balance constraint

This set of constraints balances inventory at the end of each period. Net demand for the period t is obtained as a sum of current demand D_t and the previous backlog S_{t-1} .This demand is either filled with the current production P_t and/or subcontracted from outside, P_{st} and the previous inventory, I_{t-1}. In some cases, we make a provision of inventory in the period t, I_t and some backlog in the period t, S_t. Hence, the constraint turns out to I be

$$I_{t-1} + P_t + P_{st} = D_t + S_{t-1} + I_t - S_t;\ t=1,2,\ldots..\ T. \quad \textbf{(4)}$$

The starting inventory I_0, may be known and sometime the ending inventory may also be required.

iv. Overtime constraint

This set of constraints requires that no employee should work more than a specified man-hours as overtime each month for efficient working. Let us say that not more than l0 percent of the total man-hours is allowed as over time.

Then

$$O_t = 0.10\, W_t \;, t = 1.2,\ldots\ldots \quad T \qquad \textbf{(5)}$$

v. Backlog constraint

Sometimes more backlog creates a lot of problem to the reputation of the company. Therefore, some restriction is imposed on the level of backlog but it is not a mathematical requirement at all. Let us say that not more than 10 percent of the total demand can be backlogged, then the constraint assumes the form as.

$$S_t = 0.10\, D_t \,; t = 1.2,\ldots\ldots T. \qquad \textbf{(6)}$$

vi. Workforce Constraint

Generally all the production organizations have some permanent workers (skilled and unskilled) and they work minimum for one shift and maximum for three shifts. In this problem, not less than one shift is desired as a special case.

Therefore,

W_t => man-hours available per month per shift **(7)**

vii. Warehouse constraint

Another constraint is the capacity of the warehouse.

$$I_t = c_w \qquad \textbf{(8)}$$

The problem boils down to minimizing Eq. (1) to subject to the conditions stated in Eqs. (2) to (7). The values of the parameters are estimated from the economics of the plant.

5. Case Study

An aggregate planning of a Detergent Manufacturing Company for a plant Capacity of 12.5MT per month per shift.

An aggregate plan has been developed for this company that has to satisfy the following forecasted demand, as given in the Table 1.

Month	Forecasted Demand, kg.
July	16,000
August	30,000
September	32,000
October	38,000
November	22,000
December	22.000

TABLE 1: Forecasted Demand of the company

The required workers and their wages, the raw materials required for manufacture to the full capacity of the plant per shift are worked out as shown in Appendix 1. The company has a starting inventory in the month of July of 10,000 kg.

Estimation of the Parameters

Estimation of regular labour wages

From the plant economics [5] (Appendix I), it is obvious that five workers are paid at the rate YR 40,000 per month for working 8 hours a day and 25 days a month. Therefore labour wage per man-hour, L_t

L_t= YR 40/man-hour.

Overtime cost is one and a half times the regular cost.

Cost of hiring and firing

The cost of hiring and training a worker is one and a half times the normal wage rate i.eYR60.00 per man-hour and cost of firing a worker is double that of hiring. Therefore

e_t =YR 60 per man-hour.

e^t =YR 80 per man-hour.

Estimating the cost of Inventory and stock out

The rent of the store including watchman's wages is YR 30,0000/ for storing 15000kg of detergent. Therefore, inventory-holding cost per kg per month is YR 2/kg/month. If the demand is not met, it is backlogged which is estimated to cost YR 80 kg including loss of goodwill.

Estimation of material cost and cost of subcontracting

It is clear from appendix I that the cost of raw materials for producing 12,500 kg of detergent is YR 400,600. Therefore,

C_t = 400,000/12,500 =YR 40 per kg.

It is assumed that if we get the detergent from a sister concern, it will cost more the double, that is,

C_{st}= YR 100/kg

Determination of the decision variable

The complete formulation can be written as follows after subsisting the values of ft parameters.

To minimize

$$Z= [40W_t + 60H_t + 80L_t + 60O_t + 21_t + 80S_t + 40P_t + 100P_{st}] \quad \textbf{(9)}$$

Subject to

$$\textbf{Workforce: } W_t = W_{t-1} + H_t - L_t \quad \textbf{(10)}$$

$$\textbf{Production Capacity: } P_t <= 12.5\ W_t + 12.5\ O_t \quad \textbf{(11)}$$

$$\textbf{Inventory: } I_{t-1} + P_t + P_{St} = D_t + S_{t-1} + I_t - S_t \quad \textbf{(12)}$$

$$W_t >= 1000 \quad \textbf{(13)}$$

$$\textbf{Inventory Capacity: } I_t <= 15000 \quad \textbf{(14)}$$

$$\textbf{Backlog: } S_t <= 0.10\ D_t \quad \textbf{(15)}$$

The objective function and the constraints are linear functions of the variables. Therefore, the solution to the problem can be obtained by solving it as a linear programming problem [9]. A standard L.P.P package is available as TORA which has been used to find the solution as given below. The solution of the problem from July to December for the entire planning horizon is given in the Table 2.

Period	Inventory I_t	Hired H_t	Laid off L_t	Work force W_t	Overtime O_t	Backlog S_t	Production P_t	Subcontract P_{st}
0	10000	0	0	0	0	0	0	0
1	0	0	0	1000	0	0	6000	0
2	0	0	0	2400	480	0	30000	0
3	0	0	0	2400	480	2000	30000	0
4	0	0	0	3000	0	500	37500	0
5	0	0	0	2000	600	0	22000	0
6	0	0	0	2000	600	0	22000	0

TABLE 2: Aggregate plan for 6 month-horizon

6. Results and Discussion

The forecasted demand of the detergent in a detergent manufacturing company is given in Table 1. This shows that the demand is fluctuating every month and it varies from 16000 kg/month to 32000 kg/month. In this production scheduling problem a number of decisions variables are involved as discussed in the section 4.1. A linear programming model was developed including a decision variable known as subcontracting, P_{st}. After solving the formulated linear programming problems, the complete solution is given in Table 2. The results show that the firm can manage the demand by manipulating the overtime variable, O_t, and subcontracting is not required. In order to meet the demand if subcontracting variable is high, then cost of production will increase. This may demand the expansion of the plant capacity instead of subcontracting. This type of production scheduling will help in understanding whether expansion is economical or not. The case study considered here as an example shows that subcontracting for given six month's horizon of scheduling is zero. This indicates that at the moment the capacity expansion may not be desirable but in future if the demand increases then an analysis of a trade off between subcontracting and expansion of the plant is required to take appropriate decisions.

7. Conclusions

Surprisingly, many companies do not go for an aggregate planning instead rely on orders from their distributors or warehouses to determine their production schedules. These orders are actually driven either by an actual demand or through inventory management algorithms .If a company has no trouble in efficiently meeting the demands this way, then lack of aggregate planning may not significantly harm the company. However, when the capacity utilization increases and capacity becomes an issue, relying on orders to set the production schedules can lead to a capacity bottleneck. When utilization is high, the probability of supplying all the orders as they arrive is low. Therefore, manager should resort to aggregate planning to best utilize the capacity to meet the forecasted demands. Aggregate plans are based on forecasts of future demands that are always subject to errors. Therefore, the aggregate plans need to have some flexibility. The network flow method of aggregate planning helps to develop an aggregate plan formulation amenable to a linear programming solution which involves sensitivity analysis. This provides a tool to calculate the cost of expanding the capacity during peak periods clubbed with the costs when the demands are lower than expected. This might lead to postponing the capacity expansion decision. This paper shows that an aggregate planning will be a powerful tool to manage periodic higher demands without expanding the capacity of the plant.

8. References

1. Debels, D. and M. Vanhoucke, "A Finite Capacity Production Scheduling Procedure for Belgian Steel Company", Paper Provided by Ghent University, Faculty of Economics and Business Administration, Belgium, Oct. 2006.

2. Varela, L.R. and J.N. Aparicio."An XML knowledge Base Systems for Scheduling Problems", Conference Internet Computing Systems – IICS, pp 63-64, 2002.

3. Carison, D. "Modeling with XML Applications with UML: Practical e-Business Applications". Innovative Internet Computing Systems – IICS. 2001.

4. Chopra, S. and P.Meindl, "Supply Cain Management." Prentice Hall (USA) 2001, pp 40-45.

5. Katra, M. and R. Pura, "Detergent Cake and Powder", Engineers India Research Institute, pp 31-43, 2000.

6. Hines, P. "Creating World Class Suppliers." Cardiff University Press (U.K.), p.100, 1999.

7. Artiba, A. and S. Elmaghraby, "Planning and Scheduling of Productions Systems". Innovative Internet Computing Systems – IICS, 1997.

8. Dobler , W.D. and D.N. Burt, "Purchasing and Supply Management ."McGraw Hill Co. NewYork, pp. 15-20, 1996.

9. Taha, H. A. "Operations Research," Macmilian Publishing Co., New York, pp.1-30, 1989.

10. Johson, L.A.and D. Montgomary, "Operations Research in Production Planning, Inventory and Forecasting," Wiley & Sons, pp.115-120, 1974.

11. Appendix

Manufacturing Economics of 12.5 WIT per Month Capacity Plant [2]

Basis:
Rated capacity: 500 kg per day.
Number of working days : 25 days per month.
Number of hours per shift: 8
Currency: Yemeni Rials.

Cost of Land Building

Land area, 1000 square meter @ YR 220 per square meter:	YR 220,000
Covered area, 50 square metre @ 4.800YR per square metre:	YR 240,000
Boundary wall, gate and miscellaneous:	YR 24,000
Total	YR 484,000

Plant and Machinery

1.	Amalgamator, 150 kg per shift; No.1:	
2.	Milling machine,150 kg per shift, No. 1: Gross amount for items 1 and 2:	YR 280,000
3.	Empty drum for storage, @ YR 800per drum, No. 5:	YR 4,000
4.	Neutralizer (Kettle of stainless steel):	YR 60,000
5.	Blender (Semi- automatic, capacity: 100 kg per hour ,No. 1:	YR 120,000
6.	Pulverizing machine , capacity :100 kg per hour ,No. 1:	YR 100,000
7.	Weighing machine, No. 1:	YR 40,000
8.	Miscellaneous items, like blowers, trolleys and bag sewing m/c:	YR 60,000
9.	Small Furnace:	YR 20,000
10.	Laboratory equipment:	YR 20,000
	Total	YR 724,000

Other Fixed Assets

Installation costs for water, electricity and fuel	YR 20,000

Total Capital Cost

Land and building	YR 484,000
Plant and machinery	YR 724,000
Other fixed assets	YR 20,000
Total	YR 1,228,000

Raw Materials Required per Month

1.	Acid slurry(LABS),575 kg @ YR 720 per kg:	YR 92,000
2.	Sodium triphosphate,1175 kg @ YR 88 per kg:	YR 103,400
3.	Carboxy methyl cellulose,375 kg @YR 600 per l:	YR 225,000
4.	Optical whitening agent 5 kg @YR 640 per kg:	YR 3,200
5.	Foam booster 25 kg @ 160 per kg:	YR 4,000
6.	Sodium silicate 125 kg @ YR 20 per kg:	YR 2,500
7.	Sodium sulphate 412.5 kg @ YR 32 per kg:	YR 13,200
8.	Acid slurry * 300 kg @YR 160 per kg:	YR 48,000

9.	Soda ash 1000 kg @ 28per kg:	YR 42,000
10.	Sodium silicate * 1000 kg @ YR 16per kg:	YR 16,000
11.	Marble chips 7200 kg @ YR 4per kg:	YR 28,800
12.	Packaging material:	YR 25,000
	Total:	YR 400,600

An Intelligent Approach for Handover Decision in Heterogeneous Wireless Environment

Manoj Sharma neelmanoj@gmail.com
Research Scholar, Faculty of Engineering & Technology
Maharishi Dayanand University
Rohtak,Haryana,India-124001

Dr. R.K. Khola manoj_brcm@yahoo.com
Professor, Department of Electronics & Communication Engg.
P.D.M College of Engineering
Bahaadurgarh, Haryana, India-124507

Abstract

Vertical handoff is the basic requirement of the convergence of different access technologies. It is also the key characteristic and technology of overlay wireless network with appropriate network interfaces. The integration of diverse but complementary cellular and wireless technologies in the next generation wireless networks requires the design of intelligent vertical handoff decision algorithms to enable mobile users equipped with contemporary multi-interfaced mobile terminals to seamlessly switch network access and experience uninterrupted service continuity anywhere and anytime. Most existing vertical handoff decision strategies are designed to meet individual needs that may not achieve a good system performance. In this paper an intelligent approach is used for vertical handover decision. The intelligence is based on the fuzzy logic approach. So here, fuzzy logic is used for network selection and decision making for vertical handover.

Keywords: Heterogeneous wireless network, Fuzzy logic, Fuzzification, Crisp value, Mobility Management.

1. INTRODUCTION

With the development of wireless communication technology, the service of wireless communication networks is upgrading extremely fast. Presently, there are many kinds of wireless networks available to fulfill different needs and requirements of mobile users. When users are roaming among various wireless networks, such as Wireless LANs and 3G, the interconnection of these different networks has become a problem. While a mobile terminal (MT) crosses the coverage boundary of two different systems, its ongoing connection must be seamlessly switched to a new network with a guaranteed QoS. Such a cross-system transfer of an ongoing connection is usually referred to as inter-system, or vertical handover.

Unlike a horizontal handoff that only occurs within the same network [1], a vertical handoff occurs in the heterogeneous wireless network when a mobile user changes its connection between different networks. The vertical handoff can happen in two ways. The first is Upward Vertical Handover. This occurs from a network with small coverage and high data rate to a network with wider coverage and lower date rate. The second one is Downward Vertical Handover. This occurs in the opposite direction. This occurs from a network with wide coverage and low data rate to a network with small coverage range and high data rate.

The traditional horizontal handoff research is emphasized on the received signal strength (RSS) evaluation of the mobile host (MH). However, in the case of vertical handoff, RSS evaluations and comparisons are insufficient for making an optimized vertical handoff decision. Many other metrics, such as service type, monetary cost, network conditions, system performance, mobile node conditions and user preferences, should be taken into consideration [2].
Now there is a need of vertical handover decision handover algorithm which will make the connection alive during the handoff session. In this paper we have proposed an handoff decision algorithm based on fuzzy logic.

2. SURVEY OF RELATED WORKS

Related work on vertical handoff has been presented in recent research literature. Several papers have addressed designing architecture for hybrid networks, such as the application-layer session initiation protocol (SIP) [3], the hierarchical mobility management architecture proposed in [4], and the *P*-handoff protocol [5]. However, these papers focused on architecture design and did not address the handoff decision point or the vertical handoff performance issues.
W. Zhang, in [6], proposes that the vertical handoff decision is formulated as a fuzzy multiple attribute decision-making (MADM) problem. Fuzzy logic is used to represent the imprecise information of some attributes of the networks and the preferences of the user. In [7], Pramod Goyal, and S. K. Saxena proposes the *Dynamic Decision Model,* for performing the vertical handoffs to the "Best" interface at the "best" time moment, successfully and efficiently. They proposed *Dynamic Decision Model* for VHO which adopts a three phase approach comprising Priority phase, Normal phase and Decision phase. Lorenza Giupponi and Jordi Pérez-Romero in [8] propose an innovative mechanism to perform joint radio resource management (JRRM) based on neuron-fuzzy in heterogeneous radio access networks. The proposed fuzzy neural JRRM algorithm is able to jointly manage the common available radio resources operating in two steps. The first step selects a suitable combination of cells built around the three available Radio Access Technology (RAT), while the second step chooses the most appropriate RAT to which a user should be attached. The proposed algorithm allows implementing different operator policies as well as technical and subjective criteria, such as the operator and user preferences when performing the RAT selection by means of appropriate inference rules and a multiple decision mechanism. In [9] Liu Xia, et. al proposes a novel vertical handoff decision algorithm for overlay wireless networks consisting of cellular and wireless local area networks (WLANs). The target network is selected using a fuzzy logic-based normalized quantitative decision algorithm. Rami Tawil, et. al in [10] proposes a Trusted Distributed Vertical Handover Decision (T-DVHD) scheme for the fourth generation wireless networks. The main goals of the T-DVHD are to decrease the processing delay and to make a trust handoff decision in a heterogeneous wireless environment. In [11] Imed Lassoued, et. al proposes a novel methodology to evaluate the performance of vertical handoff mechanisms. They proposed a framework that allows to simulate realistic scenarios and to evaluate the entire vertical handoff mechanisms in a coherent manner. The proposed methodology takes into account the users preferences, the applications requirements, the mobile terminal context and the operator constraints. In [12] Ben-Jye Chang and Jun-Fu Chen propose a cross-layer-based polynomial regression predictive RSS approach with the Markov decision process (MDP) based optimal network selection for handoff in heterogeneous wireless networks was proposed. The proposed approach consists of a two-phase procedure. In the first phase, a predictive RSS based on the polynomial regression with a hysteresis algorithm is proposed to predict whether a mobile node moves closer to or away from the monitored wireless network. In the second phase, the handoff cost is determined based on the MDP analysis. The candidate network with the lowest handoff cost is selected as the optimal handoff network.

3. TRIGGER MANAGEMENT SYSTEM

There are many events which affects the mobile device in heterogeneous wireless environment. After surveying the literature [13], [14]–[15], we identified more than one hundred different types of network events related to mobility management. These triggers and events can be cluster, regardless of the underlying communication technology, based on groups of events related to changes in network topology and routing, available access media, radio link conditions, user

actions and preferences, context information, operator policies, quality of service (QoS) parameters, network composition, and security alerts. In the mobility management, triggers can be classified and filtered based on five criteria: type, origin, occurrence/frequency, event persistence, and temporal constraints [16]. For example, we identified three trigger types based on whether an event may, will, or must force a HO. Origin corresponds to the entity that produces the trigger, for example, the radio access component. With respect to frequency of occurrence, an event may be either periodic (such as, network measurements) or asynchronous (such as, the availability of a new network access or a security alert). Finally, events can be either transient or persistent, and they may be associated with a real-time constraint. There are different types of events related to mobility management and vertical handover. The events that relate to application layer mobility management includes changes in QoS parameters, user preferences and security alerts. The events of network topology and routing information relates to transport and network layer. The events of radio link conditions, link parameters and available media bandwidth are some of the events that relate to the link and physical layers.
The figure 1 shows the events and triggers of different layers in mobility management [16]. Trigger management in mobility management gives a facility to improve delays and errors. Now consider the case where mobile has registered for a set of events, like available bandwidth, link status, network load etc. Now when the network load starts exceeding then after a certain threshold level, a trigger will be generated to describe the condition of the network load. This will make the mobile node to take a prior decision to switch to other available network.

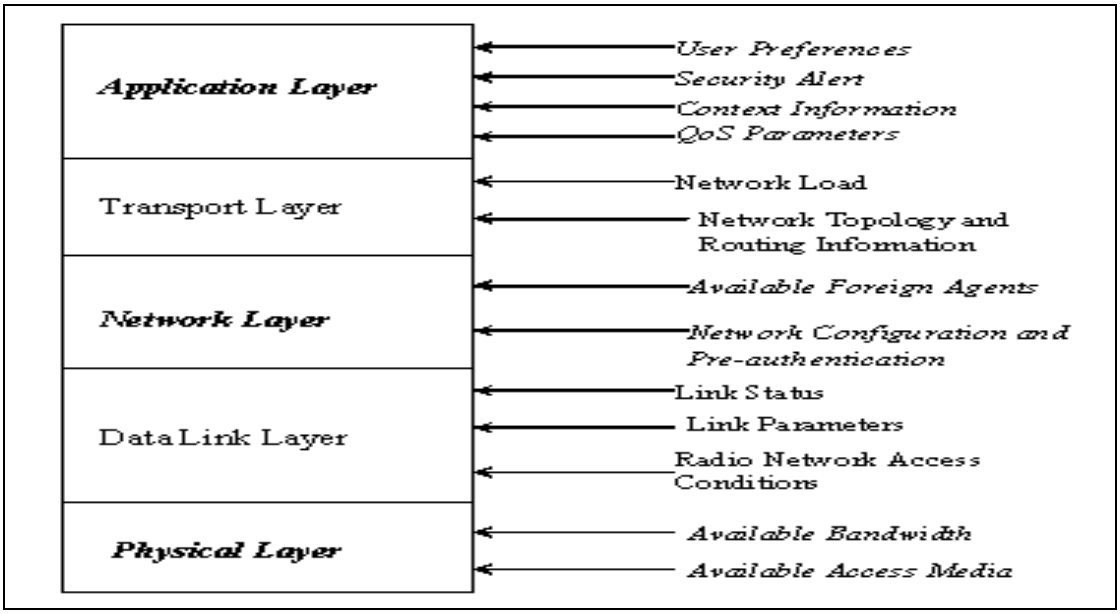

FIGURE 1: Event and Triggers of Different Layer in Mobility Management.

4. FUZZY INFERENCE SYSTEM

Fuzzy logic can be viewed as a theory for dealing with uncertainty about complex systems, and as an approximation theory. This perspective shows that fuzzy has two objectives (a) To develop computational methods that can perform reasoning and problem solving tasks that requires human intelligence and (b) To explore an effective trade-off between precision and the cost in developing an approximate model of a complex system.
Now in order to design a fuzzy logic system one has to be able to describe the operations linguistically. In other words one has to:

- Identify the inputs and outputs using linguistic variables. In this step we have to define the number of inputs and output terms linguistically.
- Assign membership functions to the variables. In this step we will assign membership functions to the input and output variables.

- Build a rule base. In this step we will build a rule base between input and output variables. The rule base in a fuzzy system takes the form of IF---AND---OR, THEN with the operations AND, OR, etc.

The fuzzy inference system is shown in Figure 2 which shows the input, output and fuzzy rules.

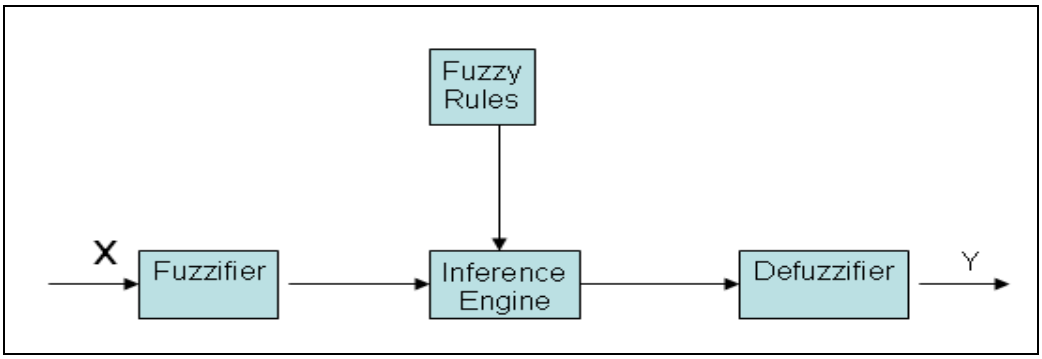

FIGURE2: The Fuzzy Inference System

5. ARCHITUCTURE OF PROPOSED INTELLIGENT HANDOVER DECISION MODEL

Heterogeneous access through multiple network interfaces is the current trend in the new generation of mobile devices. Managing the complexity of different access schemes, amount of bandwidth and cell coverage in multiple-interface devices is becoming a critical aspect to face. Namely, with multiple-mode mobile devices it is necessary to provide seamless mobility support not only during changes of cells of the same access network, but also during movement between access technologies. So we need vertical handover to use the best characteristic of any technology at one time and another at any other time. This handover decision should be intelligent enough to take the decision spontaneously. As for real time applications we need more bandwidth and connection must be alive all the time so decision should be intelligent which cater QoS requirement and witching among networks should be at right time.

Here we propose a model which gathers events from link layer, network layer and transport layer and takes decision based on fuzzy rules.

For our model we choose different variables, i.e.

• Signal Strength
• Network load
• Available Bandwidth

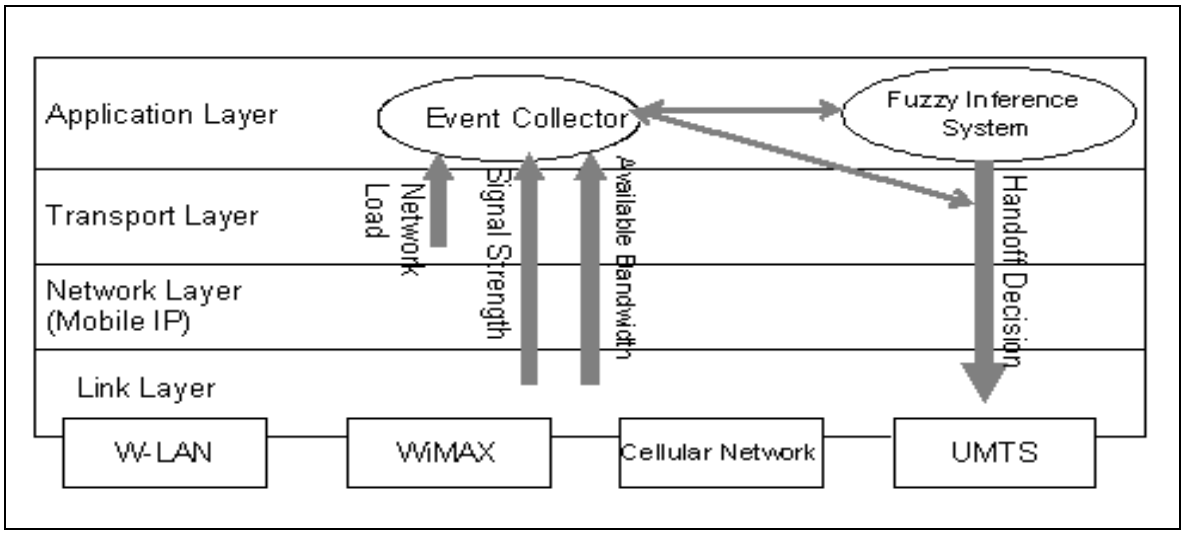

FIGURE3: Proposed Handover Decision System

Figure 3 shows the model for handover decision system. It represents 4 layers of the OSI model, which are in more focus in this model. Link layer triggers the changes in interface signal strength and the bandwidth provided by the operator company. Network layer supports mobility in heterogeneous environment and Transport layer represents network load. Network load can be observed by checking congestion or flow of packets at transport layer. The values of the events generated by event generator are feed to the fuzzy inference system. The output of the fuzzy system is the handover decision.

Event collector in application layer will collect events from different layers, i.e., if the available bandwidth is less than the required bandwidth then that interface will generate event that will be collected by Event collector. Then all these events and triggers are forwarded to fuzzy expert system as crisp input, then the information from the rule base is taken and inputs are evaluated. Event collector maintains states of every interface variable for further processing and also maintains final output selection that is returned from fuzzy expert system.

6. SYSTEM SIMULATION AND RESULTS

For system simulation Sugeno Fuzzy Inference system was used. Fuzzy inference collects input values of signal strength, network load and available bandwidth from event collector as crisp inputs and then evaluates them according to rules. The crisp input is then evaluated using rule base. The composed and aggregated output of rules evaluation is defuzzified and crisp output is obtained. Figure 4, 5, and 6 shows the fuzzy input variable for the available bandwidth, network load and Signal strength respectively. Each of the fuzzy variables has three subsets. These sets are mapped to the corresponding Gaussian membership functions. Since here we are using the fuzzy input variables and each of them has three subsets so there are 3^3 =27 rules. These rules are given in the Appendix.

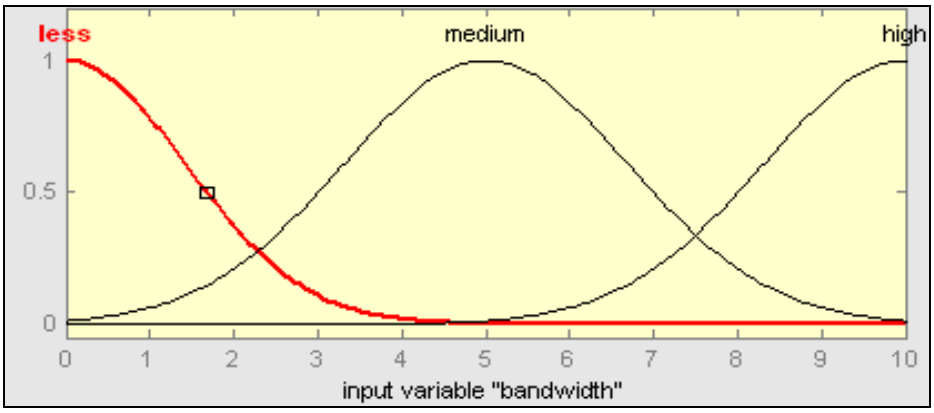

FIGURE4: Fuzzy Input Variable “Available Bandwidth”

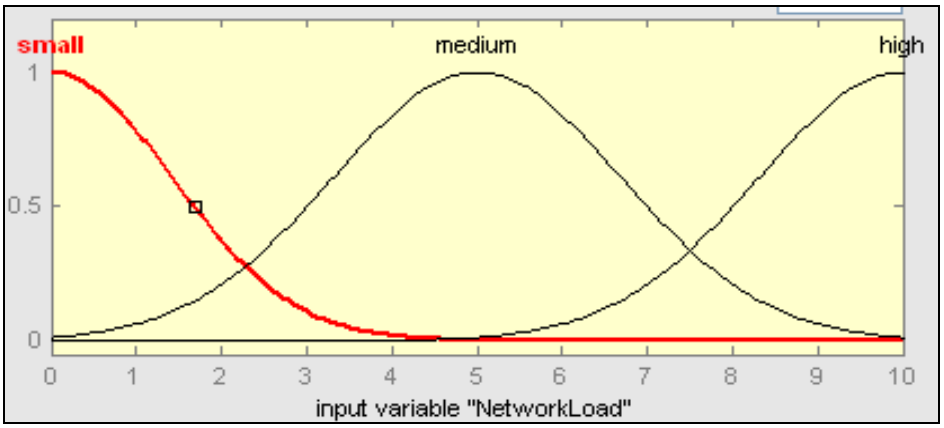

FIGURE5: Fuzzy Input Variable “Network Load”

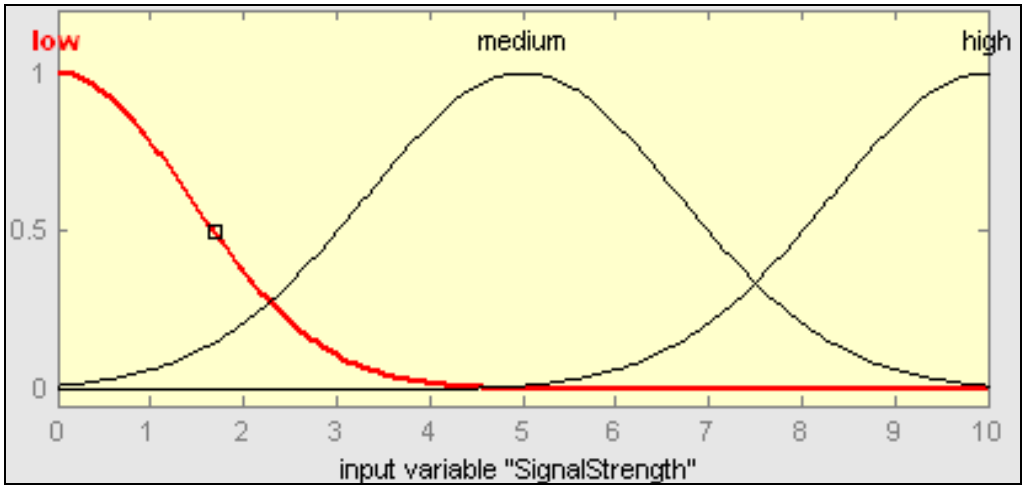

FIGURE6: Fuzzy Input Variable “Signal Strength”

The fuzzy set values for the output decision variable Handoff Decision are NO, Probably Yes (PY) and Yes (Y). The universes of discourse for the variable Handoff is defined from 0 to 1.
Now let us consider a mobile device currently in a W-LAN network. All the network interface variables, i.e. Network Load, Available bandwidth and Signal Strength of the current network are known. Now as the device moves from one place to another where cellular network and UMTS

networks are available, the device interface for cellular network and UMTS starts receiving signals. As the new signals are received, the triggers of its variable will be generated. The device will evaluate network variables of current network with the new one make a decision of vertical handover depending on current application requirement.
Now the crisp inputs of network variables are entered in the fuzzy inference system trough which they pass to the rule base to evaluate the output crisp value for network selection.

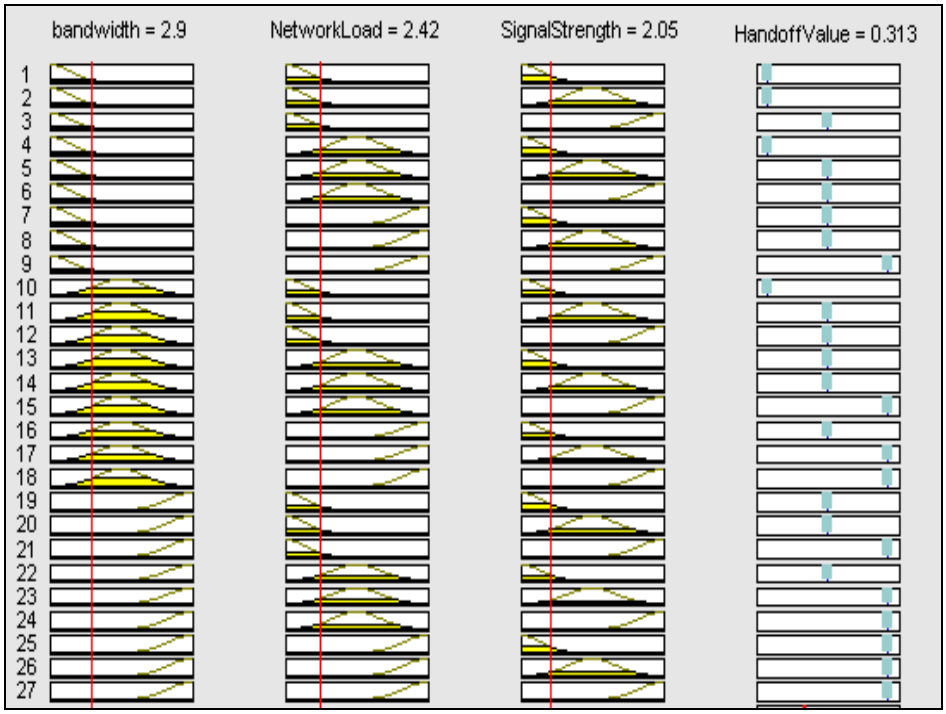

FIGURE 7: Rule Base for W-LAN Network

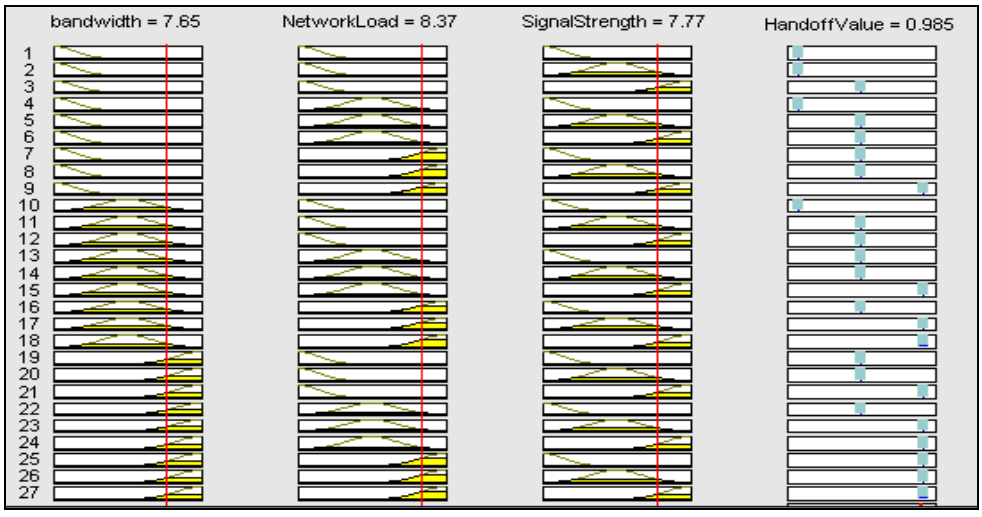

FIGURE 8: Rule Base for UMTS Network.

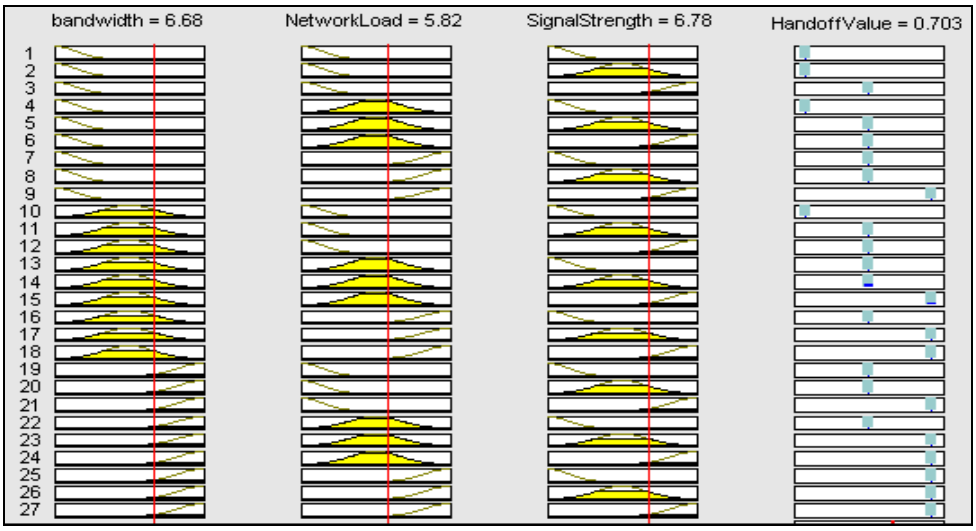

FIGURE 9: Rule Base for Cellular Network

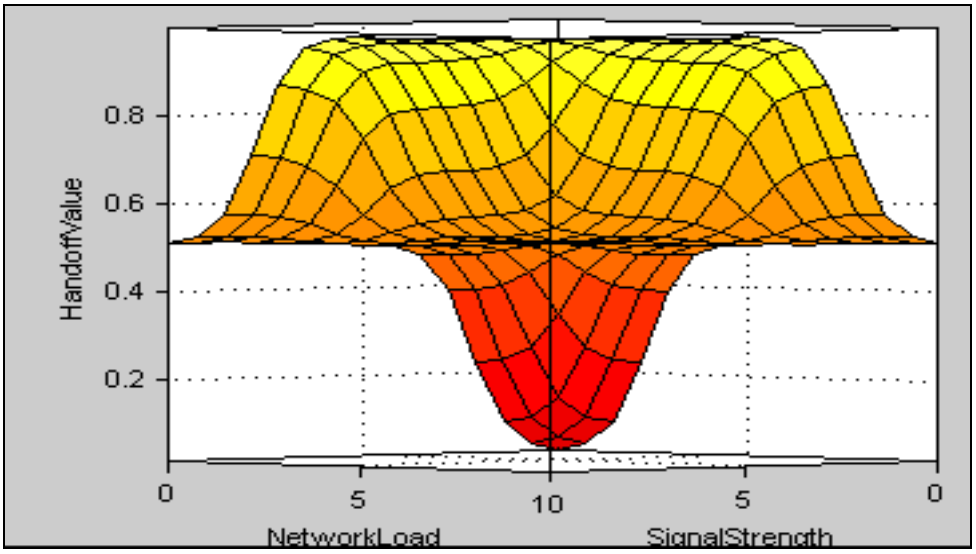

FIGURE 10: Surface Curve Between Network Load, Signal Strength and Handoff Value

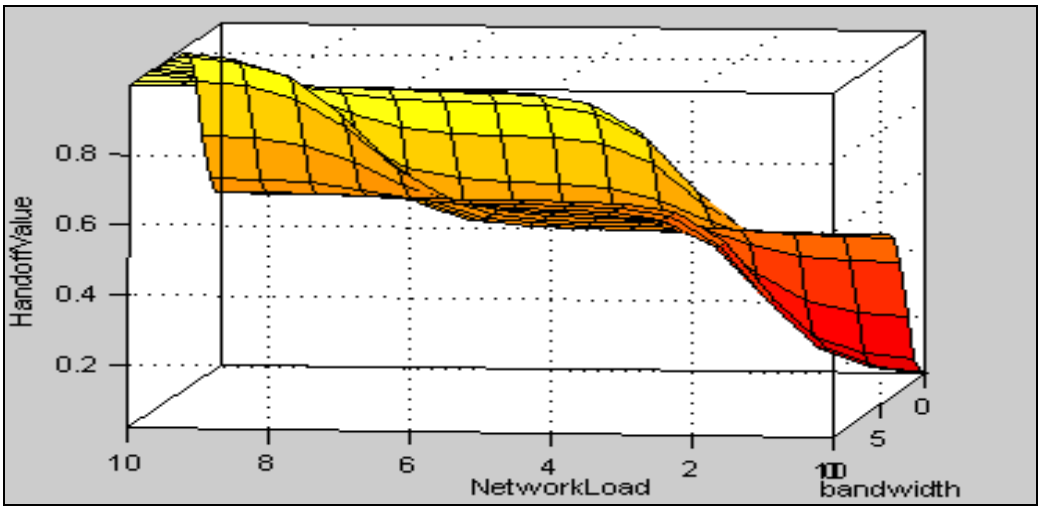

FIGURE 11: Surface Curve Between Network Load, Available Bandwidth and Handoff Value.

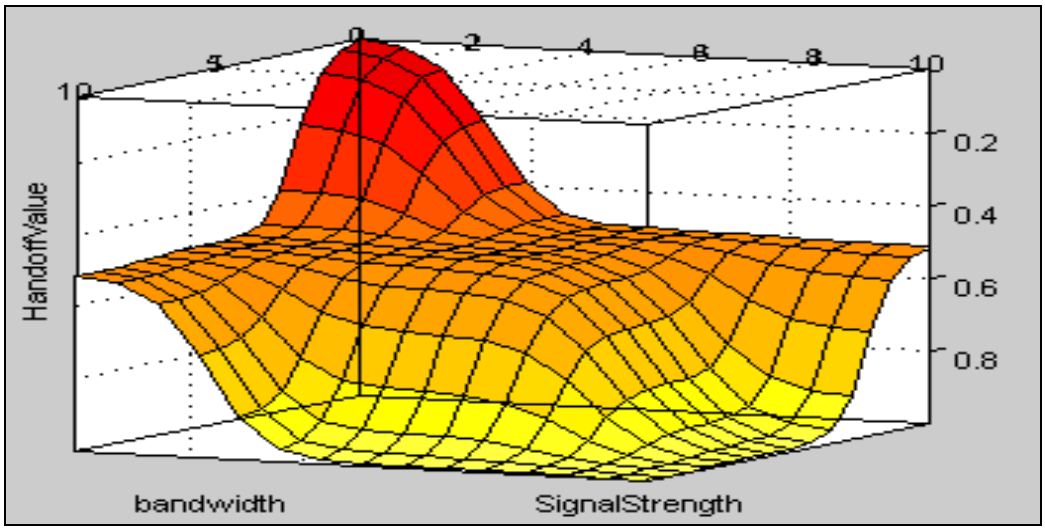

FIGURE 12: Surface Curve Between Signal Strength, Available Bandwidth and Handoff Value.

Now consider for example, that the crisp input value of current W-LAN network for network variable Bandwidth, Network Load and Signal Strength be 2.29, 2.42 and 2.05 respectively. As the device moves from one place to another where Cellular Network and UMTS are available. The input crisp value of new network i.e. for UMTS the value for network variables Bandwidth, Network Load and Signal Strength is 7.65, 8.37 and 7.77 and similarly for cellular network the input crisp value are 6.68, 5.82 and 6.78 respectively. Now putting these values to the Sugeno fuzzy expert system, the crisp output for network selection is obtained for W-LAN, UMTS and Cellular Network. Figure 7, 8 and 9 shows the rules evaluation phase of fuzzy expert system for W-LAN, UMTS and Cellular Networks respectively. Figure 10, 11 and 12 shows the surface curves between Network Load, Available Bandwidth, Signal Strength and Handoff Values.
Crisp output obtained from networks from fuzzifier is forwarded to the comparator to make final decision about the interface selection. From the above example, the crisp value of handoff output for W-LAN is .313 (No), for UMTS is .985 (Yes) and for Cellular Network is .703 (PY). So UMTS will be selected.

7. CONCLUSION

Here an intelligent approach is proposed to find out the vertical handover decision in multi network environment. The Sugeno Fuzzy Inference system is used to find the decision for vertical handover. The inference use the crisp input values for network parameters such as available bandwidth, network load and signal strength. The value of these network parameters are generated by event generator and are feed fuzzy inference system. The output of the fuzzy system is handover decision. In this way an intelligent decision will be taken based on output values.

8. REFERENCES

[1] Q-A. Zeng and D. P. Agrawal, "Modeling And Efficient Handling Of Handoffs In Integrated Wireless Mobile Networking", IEEE Transactions on Vehicular Technology, Vol. 51, No.6, Nov. 2002, pp. 1469-1478.

[2] McNair, J. and Fang Zhu, "Vertical Handoffs In Fourth-Generation Multinetwork Environments", IEEE Wireless Communications, vol. 11, no. 3, 2004, pp. 8-15.

[3] W.Wu, N.Banerjee, K. Basu, and S. K. Das, "SIP-Based Vertical Handoff between WWANs and WLANs," IEEE Wireless Communications, vol. 12, no. 3, pp. 66–72, 2005.

[4] H. Badis and K. Al-Agha, "Fast and Efficient Vertical Handoffs In Wireless Overlay Networks," in Proceedings of IEEE International Symposium on Personal, Indoor and Mobile Radio Communications (PIMRC '04), vol. 3, pp. 1968–1972, Barcelona, Spain, September 2004.

[5] J. Tourrilhes and C. Carter, "P-Handoff: A Protocol for Fine-Grained Peer-To-Peer Vertical Handoff," in Proceedings of the 13th IEEE International Symposium on Personal, Indoor, and Mobile Radio Communications (PIMRC '02), vol. 2, pp. 966– 971, Lisbon, Portugal, September 2002.

[6] W. Zhang, "Handover Decision Using Fuzzy MADM In Heterogeneous Networks," in Proc. IEEE WCNC, Atlanta, GA, Mar. 2004, pp. 653–658.

[7] Pramod Goyal, and S. K. Saxena, "A Dynamic Decision Model For Vertical Handoffs Across Heterogeneous Wireless Networks" proceedings of World Academy of Science, Engineering & Technology Vol. 31 July 2008, pp 677-682.

[8] Lorenza Giupponi, Jordi Pérez-Romero, "A Novel Approach for Joint Radio Resource Management Based On Fuzzy Neural Methodology" IEEE Transactions on Vehicular Technology, Vol. 57, No. 3, May 2008. pp 1789-1805.

[9] Liu Xia, Ling-ge Jiang and Chen He, "A Novel Fuzzy Logic Vertical Handoff Algorithm with Aid of Differential Prediction and Pre-Decision Method" Proceedings of IEEE International Conference on Communications ICC' 07 pp 5665-5670.

[10] Rami Tawil, Jacques Demerjian, Guy Pujolle, " A Trusted Handoff Decision Scheme For The Next Generation Wireless Networks" International Journal of Computer Science and Network Security, VOL.8 No.6, June 2008 pp.174-182.

[11] Imed Lassoued, Jean-Marie Bonnin, Zied Ben Hamouda and Abdelfettah Belghith, "A Methodology For Evaluating Vertical Handoff Decision Mechanisms" proceedings of IEEE Seventh International Conference on Networking, 2008, ICN 2008, pp 377-384.

[12] Ben-Jye Chang and Jun-Fu Chen, "Cross-Layer-Based Adaptive Vertical Handoff with Predictive RSS in Heterogeneous Wireless Networks" IEEE Transactions on Vehicular Technology Vol. 57, No. 6, November 2008, pp 3679-3692.

[13] P. Prasad, W. Mohr, and W. Konhuser, Third Generation Mobile Communication Systems. Boston: MA: Artech House Publishers, 2005.

[14] Jochen Eisl et al, "Mobility Architecture & Framework - D4.2 Core Report," 2005, IST-2002-507134-AN/WP4/D4.2.

[15] E. Casalicchio, V. Cardellini, and S. Tucci, "A Layer-2 Trigger To Improve Qos In Content And Session-Oriented Mobile Services," in Proceedings of the 8th ACM international Symposium on Modeling, Analysis and Simulation of Wireless and Mobile Systems, Montral, Quebec, Canada, OCT 2005, pp. 95–102.

[16] J. Makela and K. Pentikousis, "Trigger Management Mechanisms", IEEE 2nd International symposium on wireless pervasive computing, 2007.

APPENDIX

RULES: The rule blocks contain the control strategy of a fuzzy logic system. Each rule block confines all rules for the same context. A context is defined by the same input and output variables of the rules. The rules 'if' part describes the situation, for which the rules are designed. The 'then' part describes the response of the fuzzy system in this situation.

IF			**THEN**
AVAILABLE BANDWIDTH	*NETWORK LOAD*	*SIGNAL STRENGTH*	*HANDOFF DECISION*
Less	Small	Low	NO
Less	Small	Medium	NO
Less	Small	High	PY
Less	Medium	Low	NO
Less	Medium	Medium	PY
Less	Medium	High	PY
Less	High	Low	PY
Less	High	Medium	PY
Less	High	High	YES
Medium	Small	Low	NO
Medium	Small	Medium	PY
Medium	Small	High	PY
Medium	Medium	Low	PY
Medium	Medium	Medium	PY
Medium	Medium	High	YES
Medium	High	Low	PY
Medium	High	Medium	YES
Medium	High	High	YES
High	Small	Low	PY
High	Small	Medium	PY
High	Small	High	YES
High	Medium	Low	PY
High	Medium	Medium	YES
High	Medium	High	YES
High	High	Low	YES
High	High	Medium	YES
High	High	High	YES

CALL FOR PAPERS

Journal: International Journal of Engineering (IJE)
Volume: 4 **Issue:** 6
ISSN:1985-1553
URL: http://www.cscjournals.org/csc/description.php?JCode=IJE

International Journal of Engineering (IJE) is devoted in assimilating publications that document development and research results within the broad spectrum of subfields in the engineering sciences. The journal intends to disseminate knowledge in the various disciplines of the engineering field from theoretical, practical and analytical research to physical implications and theoretical or quantitative discussion intended for both academic and industrial progress.

Our intended audiences comprises of scientists, researchers, mathematicians, practicing engineers, among others working in Engineering and welcome them to exchange and share their expertise in their particular disciplines. We also encourage articles, interdisciplinary in nature. The realm of **International Journal of Engineering (IJE)** extends, but not limited, to the following:

To build its International reputation, we are disseminating the publication information through Google Books, Google Scholar, Directory of Open Access Journals (DOAJ), Open J Gate, ScientificCommons, Docstoc and many more. Our International Editors are working on establishing ISI listing and a good impact factor for IJE.

IJE List of Topics:
The realm of International Journal of Engineering (IJE) extends, but not limited, to the following:

- Aerospace Engineering
- Biomedical Engineering
- Civil & Structural Engineering
- Control Systems Engineering
- Electrical Engineering
- Engineering Mathematics
- Environmental Engineering
- Geotechnical Engineering
- Manufacturing Engineering
- Mechanical Engineering
- Agricultural Engineering
- Chemical Engineering
- Computer Engineering
- Education Engineering
- Electronic Engineering
- Engineering Science
- Fluid Engineering
- Industrial Engineering
- Materials & Technology Engineering
- Mineral & Mining Engineering

- Nuclear Engineering
- Petroleum Engineering
- Telecommunications Engineering
- Optical Engineering
- Robotics & Automation Engineering

IMPORTANT DATES

Volume: 4
Issue: 6
Paper Submission: November 31, 2010
Author Notification: January 01, 2011
Issue Publication: January /February 2011

CALL FOR EDITORS/REVIEWERS

CSC Journals is in process of appointing Editorial Board Members for ***International Journal of Engineering (IJE)***. CSC Journals would like to invite interested candidates to join **IJE** network of professionals/researchers for the positions of Editor-in-Chief, Associate Editor-in-Chief, Editorial Board Members and Reviewers.

The invitation encourages interested professionals to contribute into CSC research network by joining as a part of editorial board members and reviewers for scientific peer-reviewed journals. All journals use an online, electronic submission process. The Editor is responsible for the timely and substantive output of the journal, including the solicitation of manuscripts, supervision of the peer review process and the final selection of articles for publication. Responsibilities also include implementing the journal's editorial policies, maintaining high professional standards for published content, ensuring the integrity of the journal, guiding manuscripts through the review process, overseeing revisions, and planning special issues along with the editorial team.

A complete list of journals can be found at http://www.cscjournals.org/csc/byjournal.php. Interested candidates may apply for the following positions through http://www.cscjournals.org/csc/login.php.

Please remember that it is through the effort of volunteers such as yourself that CSC Journals continues to grow and flourish. Your help with reviewing the issues written by prospective authors would be very much appreciated.

Feel free to contact us at coordinator@cscjournals.org if you have any queries.

Contact Information

Computer Science Journals Sdn BhD
M-3-19, Plaza Damas Sri Hartamas
50480, Kuala Lumpur MALAYSIA

Phone: +603 6207 1607
+603 2782 6991
Fax: +603 6207 1697

BRANCH OFFICE 1
Suite 5.04 Level 5, 365 Little Collins Street,
MELBOURNE 3000, Victoria, AUSTRALIA

Fax: +613 8677 1132

BRANCH OFFICE 2
Office no. 8, Saad Arcad, DHA Main Bulevard
Lahore, PAKISTAN

EMAIL SUPPORT
Head CSC Press: coordinator@cscjournals.org
CSC Press: cscpress@cscjournals.org
Info: info@cscjournals.org

COMPUTER SCIENCE JOURNALS SDN BHD
M-3-19, PLAZA DAMAS
SRI HARTAMAS
50480, KUALA LUMPUR
MALAYSIA